



KATHOLIEKE UNIVERSITEIT  
**LEUVEN**

Arenberg Doctoral School of Science, Engineering & Technology  
Faculty of Engineering  
Department of Mechanical Engineering

# **Efficient Runge-Kutta Discontinuous Galerkin Methods Applied to Aeroacoustics**

Thomas TOULORGE

Dissertation presented in partial  
fulfillment of the requirements for  
the degree of Doctor  
in Engineering



# Efficient Runge-Kutta Discontinuous Galerkin Methods Applied to Aeroacoustics

**Thomas TOULORGE**

Jury:

Prof. dr. ir. P. Van Houtte, chair

Prof. dr. ir. W. Desmet, promotor

Dr. ir. W. De Roeck

Prof. dr. ir. J. Meyers

Prof. dr. ir. H. De Gerssem

Prof. dr. ir. J.-F. Remacle

(Université Catholique de Louvain)

Prof. dr. R. Abgrall

(Université de Bordeaux & INRIA, France)

Prof. dr. ir. S. Rebay

(Università degli Studi di Brescia, Italy)

Dissertation presented in partial fulfillment of the requirements for the degree of Doctor of Engineering

February 2012

© Katholieke Universiteit Leuven – Faculty of Engineering  
Celestijnenlaan 300B - Box 2420, B-3001 Heverlee(Belgium)

Alle rechten voorbehouden. Niets uit deze uitgave mag worden vermenigvuldigd en/of openbaar gemaakt worden door middel van druk, fotocopie, microfilm, elektronisch of op welke andere wijze ook zonder voorafgaande schriftelijke toestemming van de uitgever.

All rights reserved. No part of the publication may be reproduced in any form by print, photoprint, microfilm or any other means without written permission from the publisher.

D/2012/7515/18  
ISBN 978-94-6018-479-6

# Acknowledgements

After a bit more than four years, I am obtaining my Ph.D. If I enjoyed my time as doctoral student, it is not only for the satisfaction of the work realized, but also for the people that I have met.

First, I would like to express my sincere gratitude to my supervisor, Prof. Wim Desmet. I realize it is a risk to hire a doctoral student with an untypical career path like mine. Therefore, I appreciate the trust and continuous support he showed from the beginning.

I am also grateful to the members of my supervisory committee, Prof. Herbert De Gerssem, Prof. Johan Meyers and Prof. Jean-François Remacle, who provided me with advice on specific technical topics and at the same time helped me to situate my work in a broader perspective. I am glad that they showed interest in my research, and that they gave me the opportunity to present it outside KU Leuven. I am thankful to the additional members of my doctoral jury as well: grazie al Professor Stefano Rebay, et merci au professeur Rémi Abgrall, for the time and effort they invested in evaluating my thesis and in attending the preliminary defense in Leuven. I appreciated their positive attitude towards my work and their useful feedback.

Among the members of my doctoral jury, Dr. Wim De Roeck deserves special thanks for being there every time I had a question, whether it was scientific or not, and for always being willing to share his experience. I would also like to thank the other members of the aeroacoustics group: Yves, Bart, Maarten, Leandro and Hervé. I appreciated the scientific collaboration with them, and the friendly atmosphere of the office is one of the reasons why I have felt at home at KU Leuven.

My gratitude extends for the same reasons to all the collaborators and friends I made in the MOD group and in the PMA division. With them, I enjoyed the daily events (lunches at ALMA) as much as the less frequent ones (biennial ISMA receptions), the intellectual stimulation (acoustic researcher's meetings)

as much as the less intellectual one (contested squash matches). Thanks, then, to Bert, Karel, Bart, Elke, Onur, Alex, Maira, Leopoldo... And so many others who will, I hope, forgive me for not mentioning them here. Among all of them, I owe special thanks to Bert Pluymers, for his friendliness and for the role he played in finding the funding for the completion of this Ph.D. I am also grateful to the administrative staff (Karin, Lieve, Ann...) and to all those who made my life at KU Leuven easier not only by performing their duties efficiently, but also by treating me nicely.

Outside KU Leuven, I greatly enjoyed the meetings for the European project AETHER<sup>1</sup>, which I suppose is also due to the personality of Prof. Christophe Schram. Some of the fellows, like Paula and Korcan, have become good friends. I am particularly grateful to Prof. A. (Mico) Hirschberg and to Dr. Joachim Golliard for their kind help and suggestions concerning my work.

Finally, I am thankful to all the beloved ones who have been with me during these four years. In particular, thanks to my friends, my family and Claudia for the constant support they gave me.

---

<sup>1</sup>I gratefully acknowledge the financial support of the European Commission through the Marie-Curie Research and Training Network “AETHER”, Contract Nr. MRTN-CT-2006-035713.

# Abstract

The simulation of aeroacoustic problems sets demanding requirements on numerical methods, particularly in terms of accuracy. Runge-Kutta Discontinuous Galerkin (RKDG) schemes are increasingly popular for such applications, because they converge at an arbitrarily high order rate, they can deal with complex geometries, and they are amenable to parallel computing. However, they are still considered to be computationally costly. The work presented in this thesis aims at improving the computational efficiency of RKDG methods for linear aeroacoustic applications.

The first part of the work is dedicated to the study of the stability and accuracy properties that affect the performance of RKDG methods applied to hyperbolic problems. An analysis technique inspired by the classical von Neumann method is used to determine the stability restrictions of the schemes, as well as their accuracy properties in terms of dissipation and dispersion. It is first used to investigate the influence of the element shape on CFL conditions with triangular grids, in order to improve the determination of the maximum allowable time step in practical simulations. Alternative methods to the CFL conditions are also devised for this purpose. Moreover, Runge-Kutta schemes specifically designed to maximize the computational efficiency of RKDG methods for wave propagation problems are derived.

The second part of the work deals with the application of RKDG methods to linear aeroacoustics. RKDG formulations for the linearized Euler and Navier-Stokes equations are introduced, along with validation cases. Then, higher-order treatments of curved wall boundaries, needed to fully benefit from the efficiency of high-order RKDG methods in aeroacoustic propagation problems, are studied. Finally, the methods developed in this work are used in a hybrid approach to characterize the acoustic behaviour of orifices in plates under grazing flow. The results show a clear qualitative improvement over the existing analytical approaches.



# Beknopte Samenvatting

De simulatie van de aero-akoestische problemen stelt hoge voorwaarden aan numerieke methoden, in het bijzonder voor de nauwkeurigheid. Runge-Kutta Discontinue Galerkin (RKDG) methoden worden steeds populairder voor dergelijke toepassingen, omdat ze convergeren voor een willekeurige hoge orde, complexe geometrieën kunnen behandelen, en geschikt zijn voor parallele berekeningen. Ze worden echter nog beschouwd als erg rekenintensief. Het werk gepresenteerd in dit proefschrift is gericht op het verbeteren van de computationele efficiëntie van RKDG methoden voor lineaire aero-akoestische toepassingen.

Het eerste deel van het werk is gewijd aan de studie van de stabiliteits- en nauwkeurigheidseigenschappen, die de prestaties van RKDG methoden voor hyperbolische problemen beïnvloeden. Een analysetechniek, geïnspireerd door de klassieke von Neumann methode, wordt gebruikt om de stabiliteitgrenzen van de schema's, evenals om de nauwkeurigheid op het gebied van dissipatie en dispersie te bepalen. Deze techniek wordt eerst gebruikt om de invloed van de vorm van elementen op de CFL voorwaarden met driehoekige roosters te onderzoeken, met het oog op het verbeteren van de bepaling van de maximaal toegelaten tijdstap in toegepaste simulaties. Alternatieve methoden voor de CFL voorwaarden zijn tevens ontworpen voor dit doel. Bovendien worden Runge-Kutta schema's ontworpen, die de rekenefficiëntie van RKDG methoden maximaliseren voor golfvoortplantingsproblemen.

Het tweede deel van het werk behandelt de toepassing van RKDG methoden op lineaire aero-akoestiek. RKDG formuleringen voor de gelineariseerde Euler en de gelineariseerde Navier-Stokes vergelijkingen worden voorgesteld, en toegepast op enkele validatiegevallen. Vervolgens worden hogere orde behandelingen van gebogen wanden bestudeerd, die nodig zijn om de efficiëntie van hoge orde RKDG methoden in aero-akoestische voortplantingsproblemen volledig tot zijn recht te laten komen. Tot slot worden de in dit werk ontwikkelde methoden gebruikt in een hybride methodologie om het akoestisch

gedrag van openingen in platen onder scherende stroming te karakteriseren. De resultaten vertonen een duidelijke kwalitatieve verbetering ten opzichte van de bestaande analytische benaderingen.

# Abbreviations

<b>CAA</b>	Computational AeroAcoustics
<b>CFD</b>	Computational Fluid Dynamics
<b>CFL</b>	Courant-Friedrichs-Levy
<b>DG</b>	Discontinuous Galerkin
<b>DGM</b>	Discontinuous Galerkin Method
<b>DNS</b>	Direct Numerical Simulation
<b>DoF</b>	Degree of Freedom
<b>FDM</b>	Finite Difference Method
<b>FEM</b>	Finite Element Method
<b>FVM</b>	Finite Volume Method
<b>LES</b>	Large Eddy Simulation
<b>ODE</b>	Ordinary Differential Equation
<b>PDE</b>	Partial Differential Equation
<b>RANS</b>	Reynolds-Averaged Navier-Stokes
<b>RK</b>	Runge-Kutta



# List of Symbols

$\Delta t, \Delta t^*$	Time step, maximum time step
$\Delta x$	Element size in one dimension
$\chi$	Element curvature parameter
$\tilde{\delta}_F$	Scaled non-dimensional end correction (due to mean flow)
$\gamma$	Mesh quality measure
$\gamma_k$	Coefficient of the polynomial RK amplification factor
$\kappa$	Normalized computational cost
$\lambda_m$	Eigenvalue in stability analysis
$\mu$	Dynamic viscosity
$\nu, \nu^*$	Courant number, maximum Courant number
$\Omega$	Computational domain
$\partial T_i$	Face (or edge) of element $T$
$\phi$	Test function
$\varphi^T$	Basis function in element $T$
$\rho, \rho_0$	Density, mean flow density
$\theta$	Advection direction (angle)
$\xi, \xi$	Coordinate, vector of coordinates in the reference space
$\mathbf{a}$	Advection vector
$\mathbf{A}$	Flux Jacobian in the LEE and the LNSE

$\mathcal{B}_p^T$	Polynomial basis in element $T$
$\mathbf{C}$	Non-uniform mean flow matrix in the LEE or the LNSE
$c_0$	Sound velocity
$\mathbf{f}$	Flux vector
$\widehat{\mathbf{f}}^{\partial T_i}$	Vector of unknowns for the numerical flux on face $\partial T_i$
$\mathbf{f}^{\mathbf{v}}$	Viscous fluxes in the LNSE
$\mathbf{f}_r^T$	Vector of unknowns for the r-th component of the flux in element $T$
$h$	Element size
$H$	Plate and orifice thickness
$\mathbf{K}^T$	Stiffness matrix of element $T$
$\mathbf{k}$	Wave number
$\mathbf{L}$	Semi-discrete spatial operator
$\mathbf{L}$	Matrix of eigenvectors in characteristic decomposition
$L$	Orifice length
$L_{tu}$	Tube width
$\mathbf{M}^T$	Mass matrix of element $T$
$\mathbf{M}^{\partial T_i}$	(Mass) Matrix of face $\partial T_i$
$\mathbf{n}^{\partial T_i}$	Normal to face $\partial T_i$
$N_p$	Dimension of the polynomial approximation
$p, p_0$	Pressure, mean flow pressure
$p$	Order of the polynomial approximation
$q$	Order of the RK scheme
$\mathbf{q}^T$	Vector of unknowns for the variable in element $T$
$R$	Reference element
$R(z)$	Polynomial RK amplification factor
$\tilde{r}_F$	Scaled non-dimensional acoustic resistance (due to mean flow)

$R_{up}, R_{down}$	Upstream edge radius, downstream edge radius
$\mathbf{w}^s$	Auxiliary variables in the LNSE
$S$	RK stability region
$\mathbf{S}$	Source term of the LEE or the LNSE
$T$	Element
$u, u_0$	Velocity, mean flow velocity
$w$	Characteristic variable of the LEE or LNSE
$x, \mathbf{x}$	Coordinate, vector of coordinates in the physical space
$Z, Z_0$	Impedance, specific impedance



# Contents

<b>Acknowledgements</b>	<b>i</b>
<b>Abstract</b>	<b>iii</b>
<b>Contents</b>	<b>xiii</b>
<b>I Introduction</b>	<b>1</b>
<b>1 Introduction</b>	<b>3</b>
1.1 Computational Aeroacoustics . . . . .	3
1.1.1 Aeroacoustics . . . . .	3
1.1.2 Computational Aeroacoustics . . . . .	4
1.2 Numerical Methods for Linear Aeroacoustics . . . . .	6
1.2.1 Linear Aeroacoustics . . . . .	6
1.2.2 Requirements for Numerical Methods . . . . .	7
1.2.3 Spatial Discretization Techniques . . . . .	8
1.2.4 Time Discretization Techniques . . . . .	11
1.3 Research Goals . . . . .	12
1.4 Outline of the Thesis . . . . .	14

<b>II</b>	<b>Stability and Accuracy of RKDG Methods</b>	<b>17</b>
<b>2</b>	<b>Runge-Kutta Discontinuous Galerkin Methods</b>	<b>19</b>
2.1	Derivation of RKDG Methods . . . . .	19
2.1.1	Discontinuous Galerkin Space Discretization . . . . .	20
2.1.2	Runge-Kutta Time Discretization . . . . .	26
2.2	Stability and Accuracy of RKDG Methods . . . . .	28
2.2.1	Dispersion Relation of the Spatial Scheme . . . . .	29
2.2.2	Accuracy . . . . .	31
2.2.3	Stability . . . . .	31
2.3	Conclusion . . . . .	32
<b>3</b>	<b>CFL Conditions on Triangular Grids</b>	<b>35</b>
3.1	Context . . . . .	35
3.2	Method . . . . .	36
3.2.1	Exploration of Triangle Shape . . . . .	36
3.2.2	RKDG Method . . . . .	39
3.3	Results . . . . .	41
3.3.1	Advection Velocity and Numerical Flux . . . . .	41
3.3.2	CFL Conditions . . . . .	46
3.4	Examples . . . . .	51
3.5	Conclusion . . . . .	54
<b>4</b>	<b>Alternatives to CFL Conditions</b>	<b>59</b>
4.1	Introduction . . . . .	59
4.2	Straight Elements . . . . .	60
4.2.1	Maximum Dissipation Method . . . . .	60
4.2.2	Mapping Method . . . . .	68

4.2.3	Examples . . . . .	70
4.3	Curved Elements . . . . .	73
4.3.1	Study of the Stability with Curved Elements . . . . .	73
4.3.2	Qualitative Assessment of the Curvature Effect in 2D . . . . .	75
4.3.3	Influence of the Curvature in 1D . . . . .	75
4.4	Conclusion . . . . .	79
<b>5</b>	<b>Optimized Runge-Kutta Schemes for Wave Propagation Problems</b>	<b>81</b>
5.1	Context . . . . .	81
5.2	Computational Efficiency . . . . .	82
5.2.1	Definition of the Problem . . . . .	82
5.2.2	Cost Measure . . . . .	83
5.2.3	Error Measure . . . . .	84
5.3	Optimized RK Schemes . . . . .	84
5.3.1	Optimization Objectives . . . . .	84
5.3.2	Existing RK Schemes . . . . .	85
5.3.3	Optimization of RKDG Performance . . . . .	87
5.4	Examples . . . . .	97
5.4.1	2D Advection Test . . . . .	97
5.4.2	Acoustic Properties of an Elliptical Muffler . . . . .	98
5.5	Conclusion . . . . .	100
<b>III</b>	<b>RKDG Methods for Aeroacoustics</b>	<b>103</b>
<b>6</b>	<b>RKDG Methods Applied to Aeroacoustics</b>	<b>105</b>
6.1	Linear Equations in Aeroacoustics . . . . .	105
6.1.1	Linearized Euler and Navier-Stokes Equations . . . . .	106

6.1.2	Modes of Fluctuation and Characteristics . . . . .	109
6.2	DG Method for Linear Aeroacoustic Equations . . . . .	112
6.2.1	Discretization . . . . .	112
6.2.2	Boundary Conditions . . . . .	114
6.2.3	High-Order Interpolation . . . . .	115
6.3	Implementation and Verification . . . . .	120
6.3.1	Implementation . . . . .	120
6.3.2	Grid Convergence . . . . .	121
6.3.3	Boundary Conditions . . . . .	122
6.3.4	Non-Uniform Flow . . . . .	125
6.4	Conclusion . . . . .	126
<b>7</b>	<b>Curved Boundary Treatments for Aeroacoustic Propagation</b>	<b>129</b>
7.1	Introduction . . . . .	129
7.2	Higher-Order Wall Boundary Treatments . . . . .	130
7.2.1	Wall Treatments . . . . .	131
7.2.2	Mesh Generation and Robustness . . . . .	131
7.3	Results . . . . .	133
7.3.1	Acoustic Scattering by a Cylinder . . . . .	133
7.3.2	Sound Propagation around a High-Lift Airfoil . . . . .	137
7.3.3	Acoustic Scattering by a Sphere . . . . .	142
7.3.4	Transmission Loss of a Muffler . . . . .	145
7.4	Conclusion . . . . .	148
<b>8</b>	<b>Acoustic Characterization of Orifices Under Grazing Flow</b>	<b>151</b>
8.1	Introduction . . . . .	151
8.1.1	Context . . . . .	151
8.1.2	Impedance and Related Quantities . . . . .	153

8.2	Method . . . . .	155
8.2.1	Impedance Measurement and Configuration . . . . .	155
8.2.2	Cases . . . . .	157
8.2.3	Numerical Methodology . . . . .	159
8.3	Results . . . . .	163
8.3.1	Verification . . . . .	163
8.3.2	Geometry Variations . . . . .	169
8.4	Conclusion . . . . .	171
<b>IV Conclusion</b>		<b>173</b>
<b>9 Conclusion</b>		<b>175</b>
9.1	Summary and Achievements . . . . .	175
9.1.1	Method Description . . . . .	175
9.1.2	RKDG Stability Restrictions . . . . .	176
9.1.3	Optimized RK Schemes . . . . .	177
9.1.4	Curved Wall Treatments for Aeroacoustics . . . . .	178
9.1.5	Application to a Linear Aeroacoustics Case . . . . .	178
9.2	Perspectives for Future Research . . . . .	179
9.2.1	General Computation Strategy . . . . .	179
9.2.2	Time Discretization . . . . .	180
9.2.3	Applications . . . . .	181
<b>V Appendix</b>		<b>183</b>
<b>A Runge-Kutta Amplification Factor Coefficients</b>		<b>185</b>
A.1	Jameson and Standard RK Schemes . . . . .	185

A.2	Third-Order RK Schemes . . . . .	185
A.3	One-Step Fourth-Order RK Schemes . . . . .	186
A.4	Two-Step Fourth-Order RK Schemes . . . . .	186
<b>B</b>	<b>Maximum Courant Number Results for Triangular Grids</b>	<b>189</b>
B.1	Results for the Lax-Friedrichs Flux . . . . .	189
B.2	Results for the Upwind Flux . . . . .	196
<b>C</b>	<b>Useful Data on the Optimized RK Schemes</b>	<b>203</b>
C.1	RKF84 Scheme . . . . .	203
C.2	RKC73 Scheme . . . . .	210
C.3	RKC84 Scheme . . . . .	217
C.4	Element Size Constraint . . . . .	224
	<b>Bibliography</b>	<b>227</b>
	<b>Curriculum Vitae</b>	<b>243</b>
	<b>List of Publications</b>	<b>245</b>

# **Part I**

# **Introduction**



# Chapter 1

## Introduction

### 1.1 Computational Aeroacoustics

#### 1.1.1 Aeroacoustics

Aeroacoustics can be defined as the field concerned with the interaction between aerodynamic flows and acoustic fields. This interaction includes the generation and absorption of sound by flow features, as well as the acoustic propagation through moving and often non-uniform fluid media.

The history of aeroacoustics is inseparable from that of its industrial applications. It can be traced back to the pioneering work of Lighthill [93, 94] in the early 1950's, triggered by the concerns over the noise produced by the jet engines of that time [95]. Jet noise remained the prime subject of study in aeroacoustics until the mid-1970's, when the noisy turbojet engines had been replaced with more quiet high-bypass-ratio turbofan engines [144]. In order to further reduce the noise level emitted by conventional airplanes, as well as novel aircraft designs, the scientists and engineers then turned their attention towards airframe and propeller noise [142], that involve different physical phenomena. At the same time, the interest for studying and controlling flow-generated sound diffused to the automotive industry [142], wind power generation [142], HVAC and other applications involving complex pipe systems [40] and even musical instruments [40]. Nowadays as ever, the development of aeroacoustics

as a science and its application for engineering purposes are mainly driven by a growing customer demand for acoustic comfort, and stricter regulations integrating the noise issue into more general environmental considerations.

Until the 1980's, the dominant approach to aeroacoustic problems was the so-called *acoustic analogy* pioneered by Lighthill [93, 94]. It consists in splitting the Navier-Stokes equations, that model all fluid phenomena including acoustics, into a wave operator and a source term. The limited sound production region can then be considered as a set of equivalent acoustic sources depending only on the aerodynamic variables, and a classical radiation and/or scattering problem can be solved to calculate the acoustic field in the rest of the domain. One of the most important achievements of this theory is the prediction that the power of the sound generated by turbulence varies with the eighth power of the flow velocity. The analogy was extended in the following decades, most notably to include the effect of solid walls [36] and surfaces in arbitrary motion [49]. At that point, the knowledge of the aerodynamic variables for use in the analogies, as well as the understanding of the basic physical mechanisms of sound generation, were mainly coming from experimental data or semi-analytical derivations [48].

## 1.1.2 Computational Aeroacoustics

With the advent of computational methods in the 1990's, aeroacoustics entered a "second golden age", according to Lighthill [96]. Although the great impact of numerical methods on the field of fluid dynamics was promising, it is now generally acknowledged that applying directly the methods of Computational Fluid Dynamics (CFD) to aeroacoustic problems has had a limited success [35, 133, 142, 144].

### Computational Challenges

The relative failure of traditional CFD numerical methods is due to a number of challenges that distinguish the field of Computational Aeroacoustics (CAA) from typical fluid dynamics problems [35, 133, 142]:

**Time dependence** The generation of sound is an intrinsically unsteady process. At the modeling level, Reynolds-Averaged Navier-Stokes (RANS) simulations are thus irrelevant, and unsteady RANS modeling is generally too limited [142]. At the numerical level, the broadband nature of flow-generated noise, including high-frequency components, sets challenging accuracy requirements on the numerical method: if the scheme requires

more than a few Degrees of Freedom (DoF's) per wavelength to resolve acoustic waves, the number of DoF's needed to correctly predict the high-frequency acoustic field in the whole domain becomes prohibitively large.

**Propagation distance** CAA is most often used to simulate the radiation of flow-generated sound in the mid- and far-field. In order to predict the correct sound level and directivity, the numerical schemes shall introduce minimal dissipation and dispersion errors.

**Magnitude disparity** The radiation efficiency of aeroacoustic sources is very low: for low-Mach-number flows, only a fraction of the flow energy (typically a ratio of five or six orders of magnitude) is transformed into sound. Thus, the amplitude of the acoustic fluctuations is much smaller than the mean flow, which represents an additional constraint on the numerical accuracy.

**Length scale disparity** Finally, the typical length of flow features is usually much smaller than the acoustic wave length (with a ratio similar to the Mach number for turbulence noise). This may result in a prohibitive computational cost, if all length scales are resolved directly in the same computation.

These considerations call for the development of specific computational methods for CAA, with a strong emphasis on accuracy.

## **Direct and Hybrid Approaches**

In this context, two main computational approaches to aeroacoustic problems coexist. They are applied to different problems, for different purposes.

The direct approach consists in computing both the unsteady flow and the generated sound in one simulation by solving the compressible Navier-Stokes equations. Ideally, this is performed by Direct Numerical Simulation (DNS), i.e. with no further modeling than the plain compressible flow equations. Because of the lack of modeling approximations, the direct methodology with DNS is the method of choice for studying the physical phenomena of sound generation, and for obtaining benchmark solutions used to assess sound generation models. However, its computational cost is very high, so that it is applicable only to simple flows at relatively low Reynolds number [35], even with high-performance computing resources. The use of Large-Eddy Simulation (LES), that models the smallest dissipative flow scales while still resolving the more dynamically important scales, relaxes the computational requirements but is still hardly feasible for industrial-size cases. Moreover, the effect of the subgrid

modeling on the generated sound is not yet fully mastered. A more detailed review of the direct methodology in CAA can be found in Ref. [35, 142].

On the contrary, the hybrid approach consists in separating the flow simulation, often performed only in the limited region of sound production, from the computation of the acoustic field. This methodology takes advantage of the disparity in length scale and domain extent, by enabling to use different numerical methods for the two calculations. Many combinations are possible. The acoustic analogies mentioned in Sec. 1.1.1 can be applied to the unsteady flow computed by DNS or LES, that may be either compressible or incompressible. In some cases, the flow can be obtained through vortex methods [35], or even steady RANS simulations augmented with a stochastic model for the reconstruction of the turbulent fluctuations from the averaged turbulent variables [142]. The acoustic field is computed analytically only in case of free-field radiation or very simple scattering problems, otherwise the numerical methods of classical acoustics are used. When the mean flow in the mid- and far-field is non-uniform, many authors resort to linearized flow equations, mainly the linearized Euler equation and its variants, to simulate the acoustic propagation [35]. In some methods based on compressible flow computations, the determination of the acoustic sources involves separating the hydrodynamic part of the flow solution from the acoustic part by means of filtering techniques [37, Chap. 6].

## 1.2 Numerical Methods for Linear Aeroacoustics

### 1.2.1 Linear Aeroacoustics

This work focuses on computational methods for linear aeroacoustic problems. The main application of such methods is the simulation of acoustic propagation in non-uniform mean flows, including convection, refraction and scattering effects. They can of course be applied to a wide range of problems in the framework of hybrid methodologies, but they can also be used independently for the passive acoustic characterization of objects subject to flows, such as duct systems. The most obvious governing equations for linear propagation problems in non-uniform mean flows are the linearized Euler Equations (LEE). However, they inconveniently support unstable vortical modes that tend to be triggered in sheared mean flows. The lack of viscous diffusion and non-linear saturation effects may let the instabilities overwhelm the acoustic solution. In order to avoid this problem, several authors have proposed alternative governing equations, in combination with appropriate source terms [28, 46, 115, 125]. Nevertheless, the plain LEE have the interesting

ability of modeling generalized scattering phenomena, including the scattering of vortical or entropic fluctuations into sound [35].

As mentioned in Sec. 1.1.2, the physical mechanisms of aerodynamic sound generation are unsteady in essence, and the resulting acoustic field is of broadband nature in most aeroacoustic problems. This suggests a time-domain formulation of the governing equations. In the literature, time-dependent models dominate to the point that most recent review articles on CAA do not even mention frequency-domain methods [35, 91, 133, 142]. This may be partly explained by the historical link of the aeroacoustic community with fluid dynamics rather than with acoustics, but the efficiency of time-domain simulations compared to frequency-domain simulations has also been put in evidence [26, 56]. Therefore, the work described in this thesis focuses on the time-domain formulation of linear aeroacoustic equations.

## 1.2.2 Requirements for Numerical Methods

We are thus concerned with numerical methods for hyperbolic systems of Partial Differential Equations (PDE's), that include the equations of linear aeroacoustics, and more generally all systems of PDE's governing convection and wave propagation phenomena. As explained in Sec. 1.1.2, aeroacoustic problems set high accuracy requirements on the numerical schemes, which can be expressed in terms of dissipation and dispersion errors. Such requirements are shared by other kind of wave propagation problems, so that the numerical methods used to simulate those phenomena are often eligible for application to aeroacoustics.

When using any numerical scheme, a trade-off is to be made between accuracy and computational cost. The accuracy is usually improved by refining the computational mesh, i.e. increasing the number of DoF's in a fixed computational domain, which requires more computation time and memory. A numerical method can be characterized by its *convergence rate*, that is, the dependence of the error on a grid parameter inversely proportional to the number of DoF's. If the dependence is asymptotically equivalent to a polynomial of degree  $q$  as the number of DoF's tends to infinity, the method is said to have an (algebraic) *convergence order* of  $q$  [21, Chap. 2]. If  $q$  is unbounded (i.e. the error decreases faster than polynomially with the number of DoF's), the method is said to have *spectral* (or *exponential*) *convergence* [21, Chap. 2]. The classical CFD methods are of order 2: while they are efficient for the typically low accuracy required by fluid dynamics problems, their error decreases too slowly with respect to the number of DoF's, so that the cost becomes prohibitive for the high accuracy needed to solve wave propagation

problems, as mentioned in Sec. 1.1.2. For instance, Astley et al. [7] mention orders of magnitude of 10 million grid points for axisymmetric models and 35 billion grid points for full 3D models of large turbofan intakes, based on the accuracy of classical second-order methods. Thus, most of the numerical schemes used in the field of aeroacoustics are high-order methods (i.e. methods of convergence order  $q > 2$ ).

Another desirable feature of a numerical method is its flexibility with respect to the geometry of the computational domain. Some methods can only operate on *structured* grids, i.e. grids for which the position of the DoF's can be indexed in a system of Cartesian, rectilinear or curvilinear coordinates. Even if multi-domain (or multi-block) strategies extend their possibilities, such grids are very tedious or even impossible to generate for the complex geometries found in industrial problems. On the other hand, irregular tessellations of simple shapes (generally simplices), known as *unstructured* grids, can be more easily created by modern meshing software, even for complex geometries.

Finally, the suitability of a numerical method to parallel computation is regarded as an important aspect. Nowadays, large computation resources are made available through massively-parallel machines, that are generally communications-limited: the data transfer between processors is slow compared to their computation power. Most numerical methods are based on local approximations, so that they can be naturally parallelized by partitioning the domain. However, the scaling of the computational efficiency with the degree of parallelization is much better with compact methods, that use as little non-local information as possible.

With these criteria in mind, we review various numerical methods designed for solving systems of hyperbolic PDE's, in order to select the most appropriate for linear aeroacoustic problems.

### 1.2.3 Spatial Discretization Techniques

We first examine the numerous spatial discretization methods available for hyperbolic conservation laws, that could be applied to linear aeroacoustics.

#### Finite Volume Methods

Finite Volume Methods (FVM) are the methods of choice in CFD. They are routinely used in both academic and industrial contexts to solve a broad range of fluid dynamics problems, and can be run efficiently on massively parallel computers. However, the attempts to apply the classical, second-order FVM to

aeroacoustic problems succeeded only partially (see for instance Ref. [68]), due to the excess of numerical dissipation and dispersion introduced by the schemes. FVM optimized for aeroacoustics have been introduced [109] and applied to rotorcraft noise prediction [141]. Loh and Lin [99] applied a third-order FVM to internal acoustic propagation and cavity noise radiation benchmark problems. Second-order finite volume schemes of increased accuracy have been shown to work for simple acoustic problems [50, 100]. However, the development of these methods for aeroacoustics and their demonstration on complex problems has not been carried out, to our knowledge.

### **Boundary Element Methods**

Boundary Element Methods (BEM) are mature numerical methods that are very commonly applied to frequency-domain acoustics both at academic and industrial levels. Their main advantage is that they require the discretization of the scatterers only, instead of a whole volume domain mesh. They lead to relatively small, though dense, linear systems. However, they rely on the availability of a fundamental solution of the PDE being discretized, so that they are only suited to uniform mean flows [7]. Moreover, their time-domain formulation raises implementation issues, in addition to the usual difficulties related to the evaluation of singular integrals [144].

### **Spectral Methods**

Spectral methods are very popular in the field of CFD, particularly for applications requiring very high accuracy, as the study of turbulence through DNS. Their most interesting property is obviously their exponential convergence rate for both dissipation and dispersion errors [83], that make them particularly appropriate for aeroacoustics. However, they suffer from a lack of geometrical flexibility, due to the global nature of the underlying approximation. This difficulty can be alleviated by means of multi-domain methods [84, 86]. Spectral methods have been applied to simple aeroacoustic cases [18, 73, 85, 103, 126] as well as many other wave propagation problems.

### **Residual Distribution Schemes**

Residual Distribution Schemes (RDS), or Fluctuation Splitting Methods, are a family of schemes that combine aspects of FVM and FEM. They are well-suited to unstructured grids, and have high-order convergence capabilities. Their genuine multi-dimensional upwinding nature ensures good dissipation and

dispersion properties [79]. They have very recently been applied to aeroacoustic propagation problems [79].

### **Finite Difference Methods**

Finite Difference Methods (FDM) are probably the most popular schemes in the field of aeroacoustics. While classical schemes were found to be unsuitable for aeroacoustic problems, families of central explicit [131], compact [76] and upwind [98] stencils have been specifically designed to optimize the dissipation and dispersion properties. In addition to their computational efficiency, FDM are easy to implement and relatively amenable to parallelization. However, they can only be formulated on structured grids. Detailed reviews of this class of methods and its numerous aeroacoustic applications can be found in Refs. [35, 91, 133].

### **Continuous Finite Element Methods**

The classical, continuous class of Finite Element Methods (FEM) is widely used for frequency-domain wave problems and has been successfully applied to fluid dynamics, but is subject to very little attention for time-domain wave propagation problems [77]. Yue and Guddati [148] devised a formulation with improved accuracy for plain transient acoustics. To our knowledge, the only documented application of continuous FEM to time-domain aeroacoustics is the discretization of the wave equation for Lighthill's analogy [45]. These methods are naturally suited to unstructured grids. However, the classical FEM formulation is unstable when applied to convection-dominated problems, for which more complex stabilized formulations must be used. Moreover, their parallel efficiency mainly relies on the performance of parallel linear solving techniques, due to the strong coupling between elements.

### **Discontinuous Galerkin Methods**

The Discontinuous Galerkin Method (DGM) combines aspects from different discretization techniques mentioned above. They are based on local polynomial approximations, as in continuous FEM, and can thus be used on unstructured grids. The order of the approximation is arbitrarily high, similarly to spectral methods. Unlike continuous FEM, approximations on neighbouring elements are allowed not to coincide on the shared element boundary, and the coupling is realized through a numerical flux formulation, in the manner of FVM. This weak coupling ensures efficient parallel computation capabilities, although the

discontinuity at element boundaries implies additional DoF's. The accuracy of DGM has been thoroughly studied and characterized in terms of dissipation and dispersion [4, 55, 70, 72]. Unsurprisingly, this discretization technique is increasingly popular for aeroacoustic propagation problems [8, 14, 16, 20, 38, 42, 118, 119].

## 1.2.4 Time Discretization Techniques

In this section, we review the different possibilities for the time discretization. The semi-discrete equations resulting from the space discretization can be integrated by implicit or explicit Ordinary Differential Equation (ODE) solvers, following a method of lines. Alternatively, the time can be discretized with the same scheme as spatial dimensions.

### Explicit Schemes

Explicit time integration schemes calculate the solution at a later time directly through formulas depending explicitly from the solution at earlier times. They are easy to implement, and computationally efficient for convergence order up to four. However, they have the drawback of being conditionally stable: the Courant-Friedrichs-Levy (CFL) condition, that sets a maximum bound on the time step, may lead to large computation times in the case of stiff semi-discrete problems. In the literature, the vast majority of time integration schemes applied to linear CAA is explicit, with a preference for Runge-Kutta (RK) schemes, and to a lesser extent multi-step Adams-Bashford methods [35, 91, 132, 142]. Recent attempts to use more flexible explicit time discretization methods include schemes of ADER and Lax-Wendroff type [42, 116], as well as local time stepping techniques [97].

### Implicit Schemes

On the other hand, implicit schemes determine the solution at a later time by solving a linear system that depends on the solution at earlier times. Although its implementation is more complex, this method allows for much larger time steps than explicit schemes, and can even be unconditionally stable. The larger time step usually compensates the additional computation time required to solve the linear system, but the method requires a global system matrix formulation that makes efficient parallelization more difficult. Above all, the most widely used implicit methods lack accuracy, and show low-order convergence. To our knowledge, no plain implicit time integration scheme has

been applied to aeroacoustic propagation, but hybrid implicit-explicit methods could be of interest to mitigate the effects of grid-induced stiffness (i.e. the stiffness of the semi-discrete operator caused by the broad range of element size in the computational domain) [78].

### Space-Time Discretization

Another possibility is to use the same discretization scheme for the time as for the spatial dimensions, that is, to discretize the continuous equations directly in space-time. To our knowledge, such method has not been applied to aeroacoustic propagation yet, but a space-time approach using a scheme such as DGM could bring the flexibility of unstructured discretization to the time dimension [2, 47, 111, 140].

## 1.3 Research Goals

From the discussion on numerical methods in Sec. 1.2, it emerges that the numerical method combining DG space discretization and explicit RK time integration fulfills the requirements for application to linear aeroacoustic problems: it is flexible with respect to the geometry, provides high-accuracy solutions through high-order convergence, and can be efficiently parallelized. Additional benefits are the *hp*-refinement possibilities offered by the arbitrary order of the local polynomial approximation associated to unstructured grids, and the easy specification of boundary conditions through the numerical flux formulation. The RKDG method was introduced and analyzed by Cockburn and Shu [30, 31, 32], and has since been successfully applied to a broad range of problems, including aeroacoustic propagation [8, 14, 20, 38, 118, 119]. This work is set in the continuation of Reymen [122].

However, the RKDG method suffers from some shortcomings, and numerical methods based on finite difference schemes are still considered computationally more efficient. In particular, RKDG methods can be criticized on two points:

1. The time step restriction due to the conditional stability of the explicit RK scheme is very restrictive, compared to finite difference schemes. The maximum time step can be orders of magnitude smaller than the characteristic time scale of the physical phenomena to be simulated, which leads to a high computation time.
2. The discontinuous nature of the DG discretization implies that the approximation at inter-element boundaries is double-valued. This means

that more DoF's are used to represent the solution, compared to a continuous approximation of the same order. These additional DoF's can be regarded as a waste of memory and computation time.

The restriction on the time step can probably not be radically relaxed without changing the profound nature of the numerical method. However, a significant improvement may be obtained by filling two gaps in the current knowledge of RKDG methods. First, the dependence of the time step restriction on the computational grid in multiple spatial dimensions is not well understood, above all with unstructured grids. Consequently, users of RKDG methods can evaluate the maximum allowable time step only inaccurately, and they prefer to set a significantly suboptimal time step for safety. A more accurate quantification of the stability restriction would thus help them to set up more efficient simulations in practice. Second, none of the RK schemes that are currently used in RKDG methods were designed for this purpose. Specifically optimized RK scheme may bring an efficiency gain.

The problem of the additional DoF's due to discontinuities at element boundaries can be mitigated by increasing the order of the polynomial approximation. Indeed, the number of DoF's required for an approximation of order  $p$  varies like  $p$  in 1D,  $p^2$  in 2D and  $p^3$  in 3D. Thus, the ratio of the number of DoF's required to represent the solution on the element boundary to the total number of DoF's in the element decreases when  $p$  increases. In a more general perspective, DG discretizations of higher order are expected to be more efficient than those of lower order, because they require less DoF's for the same accuracy. However, the error due to the discretization of the domain boundary may become dominant at high order. Improved boundary treatment are thus needed to fully benefit from the efficiency of high-order schemes.

With these considerations in mind, the work described in this thesis aims at:

- Improving the understanding of the stability restriction of RKDG methods, and providing methods for the evaluation of the maximum allowable time step with unstructured grids,
- Deriving RK schemes that are specially designed to optimize the computational efficiency of RKDG methods,
- Proposing advanced treatments of curved wall boundaries for aeroacoustic applications,
- Applying the improved RKDG method to a linear aeroacoustic problem of scientific and practical relevance.

## 1.4 Outline of the Thesis

This dissertation is composed of four main parts.

Part I comprises this introductory **Chap. 1**.

Part II deals with the study of the stability and accuracy properties of RKDG methods for hyperbolic equations, that impact directly their intrinsic efficiency:

**Chap. 2** introduces the RKDG method from a theoretical point of view, and shows efficient implementation techniques. It also describes a method for the analysis of RKDG methods in terms of stability and accuracy, which is used subsequently in the thesis.

**Chap. 3** presents a study of the CFL conditions that characterize the stability restrictions of RKDG methods on triangular grids. This study sheds light on the dependence of the maximum allowable time step on the shape of the elements, and provides guidelines for the determination of the time step in practical simulations.

**Chap. 4** reports on methods for evaluating the stability of RKDG methods by more advanced means than the CFL conditions. It contains algorithms for the calculation of the time step in practical simulations.

**Chap. 5** deals with the derivation of RK schemes specifically designed for RKDG methods. Three new schemes that maximize the computational efficiency of RKDG methods are presented.

Part III focuses on the application of the RKDG method to linear aeroacoustics:

**Chap. 6** introduces the linearized Euler and linearized Navier-Stokes equations, that govern linear aeroacoustic problems. It discusses the specifics of the RKDG method applied to these equations, and presents the validation of the method on simple cases.

**Chap. 7** describes higher-order treatments of curved wall boundaries in aeroacoustic propagation simulations. It shows, with various examples, that these treatments are required to fully benefit from the efficiency of high-order RKDG simulations.

**Chap. 8** presents a concrete application of the RKDG method in the framework of a hybrid approach. The method is used to characterize the acoustic behaviour of orifices in plates subject to grazing flow. The numerical methodology proves valuable in producing realistic results that theoretical models are unable to predict.

Finally, in Part IV, **Chap. 9** summarizes the outcome of the investigations reported in this thesis, and gives perspectives for future research.



## **Part II**

# **Stability and Accuracy of RKDG Methods**



## Chapter 2

# Runge-Kutta Discontinuous Galerkin Methods

This chapter is dedicated to the derivation and the analysis of RKDG methods in terms of stability and accuracy. The equations governing the propagation and linear generation of sound in non-uniform flows, that are introduced in Chap. 6, belong to the category of hyperbolic conservation laws. Here, we consider only the scalar advection equation, that is the simplest equation of this kind, in order to provide a clear description of the numerical method. Moreover, most of the analysis of RKDG methods for the scalar advection equation can be generalized to hyperbolic systems of practical interest, which makes it the equation of choice for the evaluation and optimization of the schemes, like in the work presented in Chap. 5, 3 and 4.

### 2.1 Derivation of RKDG Methods

In this section, we present the method of lines combining discontinuous Galerkin schemes for the spatial discretization with Runge-Kutta time integrators, as introduced by Cockburn and Shu [32]. This approach takes advantage of the computational efficiency of explicit integration methods for moderately stiff PDE's, such as those used in the field of CAA that presented in Part III.

Considering an arbitrary domain  $\Omega$  in  $d$  spatial dimensions, the scalar advection equation can be formulated in a general form as:

$$\frac{\partial q}{\partial t} + \nabla \cdot \mathbf{f} = 0 \quad (2.1)$$

where  $q \in L^2(\Omega)$  is the unknown,  $t$  is the time,  $\mathbf{x}$  is the vector of space coordinates, and  $\mathbf{f} = q\mathbf{a}$  is the flux vector,  $\mathbf{a}$  being the advection vector. The boundary conditions are assumed to correspond to a well-posed problem, and their numerical treatment will not be detailed in this section.

## 2.1.1 Discontinuous Galerkin Space Discretization

### Discontinuous Galerkin Formulation

The derivation of the space discretization scheme starts by multiplying Eq. (2.1) by a test function  $\phi$  and integrating it over a subset  $T$  of  $\Omega$ , to obtain the weak formulation:

$$\int_T \left[ \frac{\partial q}{\partial t} + \nabla \cdot \mathbf{f} \right] \phi \, d\mathbf{x} = 0 \quad \forall \phi \in L^2(\Omega)$$

where the divergence term can be integrated by parts, resulting in:

$$\int_T \frac{\partial q}{\partial t} \phi \, d\mathbf{x} - \int_T \mathbf{f} \cdot \nabla \phi \, d\mathbf{x} + \int_{\partial T} \mathbf{f} \cdot \mathbf{n} \phi \, d\mathbf{x} = 0 \quad \forall \phi \in L^2(\Omega) \quad (2.2)$$

where  $\partial T$  is the boundary of  $T$  and  $\mathbf{n}$  is the outgoing unit normal to  $\partial T$ .

Then, we consider the subdivision  $\mathcal{S}_h = \{T\}$  of the computational domain  $\Omega$  into elements  $T$ . The finite element subspace  $V_h \in L^2(\Omega)$  associated to  $\mathcal{S}_h$  is defined as:

$$V_h = \{ \phi \in L^2(\Omega) : \phi|_T \in \mathcal{P}_p(T) \quad \forall T \in \mathcal{S}_h \}$$

where  $\mathcal{P}_p(T)$  is the space of polynomial functions of degree at most  $p$  on  $T$ . For simplex elements (i.e. segments in 1D, triangles in 2D and tetrahedra in 3D), one has:

$$N_p = \dim \mathcal{P}_p(T) = \frac{\prod_{r=1}^d (p+r)}{d!}$$

It is important to note that there is no assumption on the continuity of a function  $\phi \in \mathcal{S}_h$  between elements, unlike the classical FEM. Following the

Galerkin method applied to the weak formulation of Eq. 2.2, an approximation  $q_h \in \mathcal{P}_p(T)$  of  $q$  is sought such that for all  $T \in \mathcal{S}_h$ :

$$\int_T \frac{\partial q_h}{\partial t} \phi \, d\mathbf{x} - \int_T \mathbf{f}_h \cdot \nabla \phi \, d\mathbf{x} + \int_{\partial T} \widehat{f}_h \phi \, d\mathbf{x} = 0 \quad \forall \phi \in V_h \quad (2.3)$$

where  $\mathbf{f}_h = q_h \mathbf{a}$ , and  $\widehat{f}_h$  is the so-called *numerical flux* [32].

The presence of the approximation  $\widehat{f}_h$  of  $\mathbf{f} \cdot \mathbf{n}$  in the boundary integral term is made necessary by the fact that  $q_h$  is not uniquely defined on the element boundaries  $\partial T$  interior to the computational domain  $\Omega$ . It also allows to prescribe the boundary conditions in a weak sense where  $\partial T$  is a boundary of  $\Omega$ . The expression of  $\widehat{f}_h$  as a function of  $q_h$  is thus a key ingredient of the numerical scheme. A numerical flux function is generally required to fulfill two properties [6]:

- Consistency:  $\widehat{f}_h = f|_{\partial T}$  for any smooth function  $f$  that satisfies the Dirichlet boundary conditions (if any),
- Conservation:  $\widehat{f}_h$  is single-valued on  $\partial T$ .

A basic idea is to use a numerical flux  $\widehat{f}_h$  that depends only on the two values  $q_h^-$  and  $q_h^+$  of  $q_h$  on elements  $T^-$  and  $T^+$  that locally share  $\partial T$ , respectively. A possibility is the central flux:

$$\widehat{f}_h = \frac{1}{2} (\mathbf{f}_h^- + \mathbf{f}_h^+) \cdot \mathbf{n}$$

This formulation yields a conservative scheme which fails to damp the spurious modes of the system, so that it is rarely used in practical simulations. Therefore, it will be disregarded in this work. A valid alternative is the Lax-Friedrichs flux:

$$\widehat{f}_h = \frac{1}{2} [(\mathbf{f}_h^- + \mathbf{f}_h^+) \cdot \mathbf{n} - \|\mathbf{a}\| (q_h^+ - q_h^-)] \quad (2.4)$$

where the second term stabilizes the scheme by adding dissipation,  $\|\mathbf{a}\|$  being a particular choice of the dissipative constant. Another option is upwind flux:

$$\widehat{f}_h = \begin{cases} \mathbf{f}_h^- \cdot \mathbf{n}, & \mathbf{a} \cdot \mathbf{n} \geq 0 \\ \mathbf{f}_h^+ \cdot \mathbf{n}, & \mathbf{a} \cdot \mathbf{n} < 0 \end{cases} \quad (2.5)$$

Both choices fulfill the conditions required for stability and convergence to the exact solution [32]. They are the most widely used to solve linear PDE's, the Lax-Friedrichs flux because of its simplicity and low computational cost, and the upwind flux because of its optimal dissipation properties.

Then, a basis  $\mathcal{B}_p^T = \{\varphi_j^T, j = 1 \dots N_p\}$  of  $\mathcal{P}_p(T)$  is introduced. We can express in this basis the restrictions  $q_h^T$ ,  $\mathbf{f}_h^T$  and  $\widehat{f}_h^T$  of  $q_h$ ,  $\mathbf{f}_h$  and  $\widehat{f}_h$  respectively on  $T$ :

$$\begin{aligned} q_h^T(\mathbf{x}, t) &= \sum_{j=1}^{N_p} q_j^T(t) \varphi_j^T(\mathbf{x}) \\ \mathbf{f}_h^T(\mathbf{x}, t) &= \sum_{j=1}^{N_p} \mathbf{f}_j^T(t) \varphi_j^T(\mathbf{x}) \\ \widehat{f}_h^T(\mathbf{x}, t) &= \sum_{j=1}^{N_p} \widehat{f}_j^T(t) \varphi_j^T(\mathbf{x}) \end{aligned} \quad (2.6)$$

The choice of representing  $q_h^T$ ,  $\mathbf{f}_h^T$  and  $\widehat{f}_h^T$  in the same basis  $\mathcal{B}_p^T$  is made for the sake of an easy and efficient implementation. However, it may be problematic in case the advection vector  $\mathbf{a}$  is not uniform, because then  $q_h^T \mathbf{a} \notin \mathcal{P}_p(T)$ , and  $\mathbf{f}_h^T$  is a lower-order approximation of  $q_h^T \mathbf{a}$ . This problem, that often occur in practical applications of DG methods, is tackled in Sec. 6.2.3.

Substituting Eq. (2.6) into Eq. (2.3), and taking successively each basis function  $\varphi_j^T$  as test function  $\phi$  yields:

$$\begin{aligned} \int_T \sum_{j=1}^{N_p} \frac{\partial q_j^T}{\partial t} \varphi_j^T \varphi_k^T d\mathbf{x} - \int_T \sum_{j=1}^{N_p} \mathbf{f}_j^T \varphi_j^T \cdot \nabla \varphi_k^T d\mathbf{x} \\ + \int_{\partial T} \sum_{j=1}^{N_p} \widehat{f}_j^T \varphi_j^T \varphi_k^T d\mathbf{x} = 0, \quad k = 1 \dots N_p \end{aligned}$$

Separating the computation of the boundary integral term for each face  $\partial T_i$  of  $T$  gives:

$$\begin{aligned} \sum_{j=1}^{N_p} \frac{\partial q_j^T}{\partial t} \int_T \varphi_j^T \varphi_k^T d\mathbf{x} - \sum_{j=1}^{N_p} \mathbf{f}_j^T \cdot \int_T \varphi_j^T \nabla \varphi_k^T d\mathbf{x} \\ + \sum_{i=1}^b \sum_{j=1}^{N_p} \widehat{f}_j^{\partial T_i} \int_{\partial T_i} \varphi_j^T \varphi_k^T d\mathbf{x} = 0, \quad k = 1 \dots N_p \end{aligned} \quad (2.7)$$

where  $b$  is the number of faces of the element, and  $\widehat{f}_j^{\partial T_i}$  are the components of the restriction  $\widehat{f}_h^{\partial T_i}$  of  $\widehat{f}_h^T$  on  $\partial T_i$ . For simplex elements,  $b = d + 1$ . Expressed

in Cartesian coordinates, Eq. (2.7) can be recast in matrix form:

$$\mathbf{M}^T \frac{\partial \mathbf{q}^T}{\partial t} - \sum_{r=1}^d \mathbf{K}_r^T \mathbf{f}_r^T + \sum_{i=1}^b \mathbf{M}^{\partial T_i} \widehat{\mathbf{f}}^{\partial T_i} = \mathbf{0} \quad (2.8)$$

where  $r$  is the  $r$ -th Cartesian coordinate and  $\mathbf{q}^T$ ,  $\mathbf{f}_r^T$  and  $\widehat{\mathbf{f}}^{\partial T_i}$  represent vectors collecting all components  $q_j^T$ ,  $a_r q_j^T$  and  $\widehat{f}_j^{\partial T_i}$  respectively,  $a_r$  being the  $r$ -th Cartesian component of  $\mathbf{a}$ . The element mass matrix  $\mathbf{M}^T$ , the element stiffness matrices  $\mathbf{K}_r^T$  and the face matrices  $\mathbf{M}^{\partial T_i}$  are defined as:

$$\begin{aligned} \mathbf{M}_{kj}^T &= \int_T \varphi_k^T \varphi_j^T d\mathbf{x} \\ (\mathbf{K}_r^T)_{kj} &= \int_T \frac{\partial \varphi_k^T}{\partial x_r} \varphi_j^T d\mathbf{x} \\ \mathbf{M}_{kj}^{\partial T_i} &= \int_{\partial T_i} \varphi_k^T \varphi_j^T d\mathbf{x} \end{aligned} \quad (2.9)$$

Eq. (2.8) can be expressed for all elements in the computational domain and assembled in a more general form as:

$$\frac{d\mathbf{q}}{dt} = \mathbf{L}(t) \mathbf{q}(t) \quad (2.10)$$

where  $\mathbf{q}$  is the vector concatenating  $\mathbf{q}^T$  for all elements  $T \in \mathcal{S}_h$ , and  $\mathbf{L}$  is the spatial semi-discrete operator.

## Implementation Details

To complete the numerical scheme, the polynomial basis  $\mathcal{B}_p^T$  needs to be defined for all  $T \in \mathcal{S}_h$ . This is conveniently done by mapping each element  $T$  in the computational domain onto a reference element  $R$ , following the *quadrature-free* [9] technique:

$$\mathcal{M}^T : \begin{array}{l} R \rightarrow T \\ \boldsymbol{\xi} \mapsto \mathbf{x} \end{array}$$

We also introduce the parametrization  $\overline{\mathbf{x}}^{\partial T_i}$  of the face  $\partial T_i$  needed to calculate the face matrices in Eq. (2.9), and define the mapping  $\mathcal{M}^{\partial T_i}$  of  $\partial T_i$  onto the corresponding face  $\partial R_i$  of  $R$ :

$$\mathcal{M}^{\partial T_i} : \begin{array}{l} \partial R_i \rightarrow \partial T_i \\ \overline{\boldsymbol{\xi}}^i \mapsto \overline{\mathbf{x}}^{\partial T_i} \end{array}$$

The Jacobian matrices of  $\mathcal{M}^T$  and  $\mathcal{M}^{\partial T_i}$  are defined respectively as  $J^T = \frac{\partial \mathbf{x}}{\partial \boldsymbol{\xi}}$  and  $J^{\partial T_i} = \frac{\partial \bar{\mathbf{x}}^{\partial T_i}}{\partial \bar{\boldsymbol{\xi}}^i}$ , and the change of variables in Eq. (2.9) yields:

$$\begin{aligned} \mathbf{M}_{kj}^T &= \int_R \varphi_k \varphi_j |J^T| d\boldsymbol{\xi} \\ (\mathbf{K}_r^T)_{kj} &= \sum_{s=1}^d \int_R (J^T)_{sr}^{-1} \frac{\partial \varphi_k}{\partial \xi_s} \varphi_j |J^T| d\boldsymbol{\xi} \\ \mathbf{M}_{kj}^{\partial T_i} &= \int_{\partial R_i} \varphi_k \varphi_j |J^{\partial T_i}| d\bar{\boldsymbol{\xi}}^i \end{aligned} \quad (2.11)$$

The specification of  $\mathcal{B}_p^T$  for all  $T \in \mathcal{S}_h$  is thus reduced to the definition of a unique polynomial basis  $\mathcal{B}_p = \{\varphi_j, j = 1 \dots N_p\}$  on the reference element  $R$ . Moreover, if  $J^T$  is constant over the element (which is the case for triangles with straight edges, or tetrahedra with plane faces), the Jacobian terms can be taken out of the integrals in Eq. (2.11) to give:

$$\begin{aligned} \mathbf{M}^T &= |J^T| \mathbf{M}^R \\ \mathbf{K}_r^T &= \sum_{s=1}^d (J^T)_{sr}^{-1} |J^T| \mathbf{K}_s^R \\ \mathbf{M}^{\partial T_i} &= |J^{\partial T_i}| \bar{\mathbf{M}}^{\partial R_i} \end{aligned} \quad (2.12)$$

with:

$$\begin{aligned} \mathbf{M}_{kj}^R &= \int_R \varphi_k \varphi_j d\boldsymbol{\xi} \\ (\mathbf{K}_s^R)_{kj} &= \int_R \frac{\partial \varphi_k}{\partial \xi_s} \varphi_j d\boldsymbol{\xi} \\ \bar{\mathbf{M}}_{kj}^{\partial R_i} &= \int_{\partial R_i} \varphi_k \varphi_j d\bar{\boldsymbol{\xi}}^i \end{aligned} \quad (2.13)$$

Given that the reference element  $R$  and the basis  $\mathcal{B}_p$  are defined as part of the scheme, the matrices  $\mathbf{M}^R$ ,  $\mathbf{K}_s^R$  and  $\bar{\mathbf{M}}^{\partial R_i}$  can be precomputed analytically, hence the name of *quadrature-free* technique. Then, one just needs to store the Jacobians  $J^T$  and  $J^{\partial T_i}$  in memory during the computation, instead of storing the element matrices  $\mathbf{M}^T$ ,  $\mathbf{K}_r^T$  and  $\mathbf{M}^{\partial T_i}$ , that can be retrieved through Eq. 2.12. This represents a significant gain in memory storage.

For elements in which  $J^T$  is not constant, such as curvilinear simplices, the integrals in Eq. (2.11) must be computed by quadrature and stored in memory during the computation. In this work, Gauss-Legendre quadrature rules of order  $p+2$  are used, which ensures sufficient accuracy for elements of geometric order 2 (i.e. quadratic mappings  $\mathcal{M}^T$  and linear Jacobians  $J^T$ ). Note that an alternative method could be to include the non-constant Jacobian  $J^T$  in the approximation  $q_h^T$ , so that it would disappear from the integrals in Eq. (2.11), and the quadrature-free technique would still be possible. However, this would come at the price of an accuracy loss, as it would prevent the solution from being approximated up to order  $p$ . Another consequence of using elements with curved faces is that the normal  $\mathbf{n}$  is not constant over  $T$ : as  $\widehat{f}_h^T \in \mathcal{P}_p(T)$ , the terms  $\mathbf{f}_h$  in the numerical flux expressions of Eq. (2.4) and Eq. (2.5) are not approximated up to order  $p$ . This can be fixed, at the expense of additional storage, by defining additional face matrices that include the normals  $\mathbf{n}^{\partial T_i}$  to  $\partial T_i$ :

$$\left(\mathbf{M}_{kj}^{\partial T_i}\right)_r = \int_{\partial R_i} \varphi_k \varphi_j n_r^{\partial T_i} |J^{\partial T_i}| d\bar{\xi}^i$$

and reformulating the boundary integral term. For instance, Eq. (2.8) becomes, with the Lax-Friedrichs of Eq. (2.4):

$$\begin{aligned} \mathbf{M}^T \frac{\partial \mathbf{q}^T}{\partial t} - \sum_{r=1}^d \mathbf{K}_r^T \mathbf{f}_r^T \\ + \sum_{i=1}^b \frac{1}{2} \left[ \sum_{r=1}^d \mathbf{M}_r^{\partial T_i} \left( \mathbf{f}_r^{T_i^+} + \mathbf{f}_r^T \right) - \|\mathbf{a}\| \mathbf{M}^{\partial T_i} \left( \mathbf{q}^{T_i^+} - \mathbf{q}^T \right) \right] = \mathbf{0} \end{aligned}$$

where  $T_i^+$  is the element sharing the face  $\partial T_i$  with  $T$ .

Following Hesthaven and Warburton [58, 60], the basis functions  $\varphi_j$  are defined as basis Lagrange polynomials of order  $p$  on the reference element  $R$ . Thus, the unknowns  $q_j^T$  are the values of  $q_h^T$  taken at a set of nodes in  $R$ . Provided that this nodal set includes enough points located on  $\partial R$ , this facilitates considerably the computation and the integration of the numerical flux  $\widehat{f}_h$ , because the trace of  $q_h^T$  on  $\partial T$  is immediately available [60]. Although the choice of  $\mathcal{B}_p^T$  does not influence the basic properties of the DG space operator in principle, it has been shown that the quality of the interpolation strongly affects the conditioning of the mass matrix  $\mathbf{M}^T$  that has to be inverted, above all at high order  $p$ . Therefore, the Lagrange-Gauss-Lobatto points are chosen as nodal set on the 1D segment, and specially optimized nodal sets are used on the triangle [57] and on the tetrahedron [59]. The computation of the

integrals involving  $\varphi_j$  does not rely on an explicit definition of the Lagrange basis functions  $\varphi_j$ . Instead, the element matrices are computed in a polynomial basis that is orthogonal and analytically integrable in  $R$ , and transformed back to the nodal basis through Vandermonde matrices based on the interpolation properties of Lagrange polynomials [58, 60].

## 2.1.2 Runge-Kutta Time Discretization

Following the method of lines, Eq. (2.10) is integrated in time as an ODE by means of a  $s$ -stage Runge-Kutta scheme:

$$\begin{aligned} \mathbf{dq}^{(1)} &= \mathbf{L}(t_n, \mathbf{q}_n) \\ \mathbf{dq}^{(i)} &= \mathbf{L}\left(t_n + c_i \Delta t, \mathbf{q}_n + \Delta t \sum_{j=1}^{i-1} a_{ij} \mathbf{dq}^{(j)}\right), \quad i = 2 \dots s \quad (2.14) \\ \mathbf{q}_{n+1} &= \mathbf{q}_n + \Delta t \sum_{i=1}^s b_i \mathbf{dq}^{(i)} \end{aligned}$$

where  $\Delta t = t_{n+1} - t_n$  is the time step, and  $\mathbf{q}_n$  and  $\mathbf{q}_{n+1}$  represent the value of  $\mathbf{q}$  at time  $t_n$  and  $t_{n+1}$  respectively. The coefficients  $a_{ij}$ ,  $b_i$  and  $c_i$  can be summarized in matrix/vector form by the Butcher tableau:

$$\begin{array}{c|c} c & A \\ \hline & b^T \end{array}$$

By definition:

$$c_i = \sum_{j=1}^s a_{ij}$$

In this work, only explicit self-starting schemes are considered:

$$a_{ij} = 0, \quad j \geq i$$

thus  $c_1 = a_{11} = 0$ .

For the scheme to be third-order accurate, the RK coefficients must fulfill the conditions [22]:

$$\sum_{i=1}^s b_i = 1 \quad (2.15a)$$

$$\sum_{i=1}^s b_i c_i = \frac{1}{2} \quad (2.15b)$$

$$\sum_{i=1}^s b_i c_i^2 = \frac{1}{3} \quad (2.15c)$$

$$\sum_{i,j=1}^s b_i a_{ij} c_j = \frac{1}{6} \quad (2.15d)$$

among which Eq. (2.15a) and (2.15b) are required for first and second order of accuracy respectively. For fourth-order accuracy, the coefficients are subject to the additional constraints [22]:

$$\sum_{i=1}^s b_i c_i^3 = \frac{1}{4} \quad (2.16a)$$

$$\sum_{i,j=1}^s b_i c_i a_{ij} c_j = \frac{1}{8} \quad (2.16b)$$

$$\sum_{i,j=1}^s b_i a_{ij} c_j^2 = \frac{1}{12} \quad (2.16c)$$

$$\sum_{i,j,k=1}^s b_i a_{ij} a_{jk} c_k = \frac{1}{24} \quad (2.16d)$$

The RK scheme can be characterized in terms of accuracy and stability by applying it to integrate the model equation:

$$\frac{dq}{dt} = \lambda q$$

during a time step  $\Delta t = t_{n+1} - t_n$ . This results in the complex amplification factor [22]:

$$R(z) = \frac{q_{n+1}}{q_n} = 1 + zb^T (I - zA)^{-1} \mathbf{1} \quad (2.17)$$

with  $z = \lambda \cdot \Delta t$ . The stability is determined by the condition:

$$|R(z)| \leq 1$$

and the *stability region* of the RK scheme is defined as the locus  $S = \{z : |R(z)| \leq 1\}$ . For a scheme of order  $q$ , the polynomial  $R(z) = \sum_{k=0}^s \gamma_k z^k$  is subject to the constraints [22]:

$$\gamma_k = \frac{1}{k!}, \quad k = 1 \dots q \quad (2.18)$$

These conditions are sufficient to guarantee the order of accuracy  $q$  with linear, homogeneous and autonomous systems of ODE's [10]. However, the linear equations governing wave propagation problems are often solved in practice with time-dependent, nonlinear source terms, so that it is necessary to consider the full sets of non-linear order conditions such as Eq. (2.15) and Eq. (2.16), in which the linear conditions of Eq. (2.18) are included.

The implementation of a RK scheme following Eq. (2.14) obviously requires the storage of  $sN$  floating-point numbers in memory, where  $N$  is the number of unknowns in  $\mathbf{q}$ . However, several authors have developed alternative formulations [23, 146] that are only equivalent to a subset of all possible RK schemes allowed by Eq. (2.14), but reduce the storage requirement to  $2N$ .

## 2.2 Stability and Accuracy of RKDG Methods

Stability and accuracy are the two basic properties that govern the performance of RKDG methods. It is thus necessary to quantify them in order to determine and optimize the limits of the numerical method, as done in Chap. 3, 4, and 5.

Strong theoretical results, obtained in the framework of convergence proofs, exist in the literature. The original analysis of the DG method gave an error bound in  $O(h^p)$ , where  $h$  is the element size. This was later improved to  $O(h^{p+1/2})$ , and even  $O(h^{p+1})$  with particular constraints on the grid. Further details on these results can be found in Ref. [149]. Concerning stability, the RKDG method was shown to be linearly stable under a CFL condition [33] that limit the allowable time step. However, these accuracy and stability bounds only provide theoretical estimates, and numerical studies are necessary to obtain practical guidelines.

In this section, a methodology similar to the one presented in Ref. 89 and 90 is developed, for the analysis of the stability and the accuracy of the schemes derived in Sect. 2.1. The main difficulty lies in the determination of the dispersion relation for the spatial scheme, which is explained first.

## 2.2.1 Dispersion Relation of the Spatial Scheme

The first step is to notice that the DG spatial schemes derived in Sect. 2.1 are linear: when applied to the linear continuous Eq. (2.1), they yield a linear semi-discrete Eq. (2.10). Thus, the spatial scheme can be entirely characterized by the spectral properties of the semi-discrete operator  $\mathbf{L}$ .

In this analysis, we focus on the impact of choices in the spatial scheme (such as the type of numerical flux or the order  $p$ ), and the influence of the shape of individual elements, excluding other aspects like the effect of boundary conditions. Therefore, an unbounded domain is considered (in practice, periodic boundary conditions are imposed), and grids made up only of congruent elements are used: in 1D, the grids are simply uniform, and in 2D, they consist of a structured assembly of periodic patterns, as illustrated in Fig. 2.1.

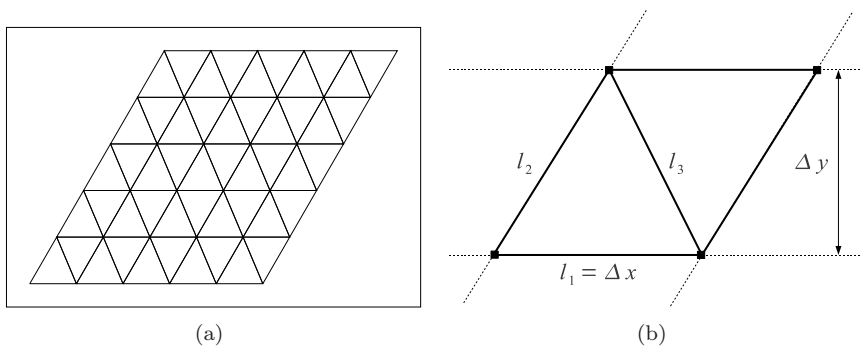


Figure 2.1: Structured grid (a) and sketch of the periodic pattern of elements (b) used for stability and accuracy analysis.

However, the accurate quantification of the accuracy and stability properties of the spatial scheme requires a high number of elements, and thus a high number of unknowns, particularly in 2D and at high order  $p$ . The computation cost of the eigenvalue problem scales like the cube of the dimension of  $\mathbf{L}$ , thus it can become prohibitive.

Therefore, it is preferable to analyze the spatial scheme by means of a classical technique that is similar to the von Neumann (or Fourier) method commonly used with finite difference stencils. It basically consists in comparing the behaviour of harmonic waves between the discrete and the continuous equations. The method is explained here with one spatial dimension, starting from the

solution of the continuous Eq. (2.1):

$$q(x, t) = \tilde{q}e^{i(kx - \omega t)} \quad (2.19)$$

with the physical dispersion relation  $k = \frac{\omega}{a}$ , the advection velocity  $a$  being constant over the whole domain  $\Omega$ . The elements  $T = [x_i, x_{i+1}]$ , that are all of equal size  $\Delta x$ , can be indexed with  $i$ . Thus, the matrices in Eq. (2.9) are the same for all  $T$ , and Eq. (2.8) can be rewritten as:

$$\mathbf{M} \frac{\partial \mathbf{q}^i}{\partial t} - \mathbf{K} \mathbf{f}^i + \mathbf{M}^R \widehat{\mathbf{f}}^R - \mathbf{M}^L \widehat{\mathbf{f}}^L = \mathbf{0} \quad (2.20)$$

where  $R$  represents the right face of element  $i$  (i.e. the point  $x = x_i + 1$ ), and  $L$  represents the left face of element  $i$  (i.e. the point  $x = x_i$ ). Assuming a solution in the form of Eq. (2.19) and  $a > 0$ , the periodicity can be exploited to express the numerical fluxes as:

$$\begin{aligned} \widehat{\mathbf{f}}^R &= a \mathbf{q}^i \\ \widehat{\mathbf{f}}^L &= a \mathbf{q}^{i-1} = a e^{-ik\Delta x} \mathbf{q}^i \end{aligned}$$

that is valid for both Lax-Friedrichs fluxes and upwind fluxes in 1D. Eq. (2.20) can then be rewritten as:

$$\frac{d\mathbf{q}^i}{dt} = \mathbf{L}(k) \mathbf{q}^i \quad (2.21)$$

with

$$\mathbf{L}(k) = \mathbf{M}^{-1} a (\mathbf{K} - \mathbf{M}^R + \mathbf{M}^L e^{-ik\Delta x}) \quad (2.22)$$

Inserting Eq. (2.19) into Eq. (2.21) leads to an eigenvalue problem that stands for the dispersion relation of the spatial scheme: the eigenvalues  $\lambda_m(k)$  of  $\mathbf{L}(k)$  represents the numerical approximation of  $i\omega$  for a solution of wavenumber  $k$ . The eigenvalues  $\lambda_m(k)$  that correspond to *physical* modes are those that approximate best the continuous dispersion relation, whereas the others are associated to *spurious* modes that are highly damped [3, 69]. The  $\lambda_m(k)$  have to be computed for many values of  $k$ , but as the  $\mathbf{L}(k)$  is defined on one element, it has dimensions of only  $N_p \times N_p$ , so that the analysis is still much faster than assembling the operator  $\mathbf{L}$  and solving the eigenproblem for a whole grid. With several spatial dimensions, the operator  $\mathbf{L}(\mathbf{k})$ , where the wavenumber  $\mathbf{k}$  is a vector, can be defined in a similar way on a pattern of elements.

Apart from the wavenumber  $\mathbf{k}$ , the operator  $\mathbf{L}(\mathbf{k})$  depends on the advection  $\mathbf{a}$ , the geometry of the elements through  $J^T$ , the type of numerical fluxes  $\widehat{f}_h$ , and the basis functions  $\varphi_j$ . It can be shown that the particular choice of  $\varphi_j$  does not affect the eigenvalues  $\lambda_m$ , as long as the basis  $\mathcal{B}_p^T$  spans the same polynomial space  $\mathcal{P}_p(T)$ , i.e. for the same order  $p$  [20]. The rest of the parameters influence the stability and accuracy properties of the scheme.

## 2.2.2 Accuracy

The error due to the spatial discretization can be defined as [117]:

$$E_{space}(k, \Delta t) = \frac{e^{\lambda_m(k)t}}{e^{i\omega t}}$$

and  $|E_{space}|$  is the dissipation part of the error, while  $\arg(E_{space})$  is the dispersion part.

For the analysis of the temporal scheme, the function  $R(z)$ , defined in Sect. 2.1.2, is applied to Eq. (2.21). The error due to the time scheme alone can be defined as [117]:

$$E_{time}(k, \Delta t) = \frac{e^{R(\lambda_m(k)\Delta t)}}{e^{\lambda_m(k)\Delta t}}$$

with  $|E_{time}|$  the dissipation part of the temporal error, and  $\arg(E_{time})$  the dispersion part.

The error for the fully discrete scheme is then:

$$E_{total}(k, \Delta t) = \frac{e^{R(\lambda_m(k)\Delta t)}}{e^{i\omega\Delta t}} = E_{space}(k, \Delta t) \cdot E_{time}(k, \Delta t) \quad (2.23)$$

where  $|E_{total}| = |E_{space}| |E_{time}|$  and  $\arg(E_{total}) = \arg(E_{space}) + \arg(E_{time})$  are the total dissipation and dispersion error respectively.

## 2.2.3 Stability

Unlike implicit schemes, explicit RK integrators feature a stability threshold that the time step  $\Delta t$  shall not exceed for the scheme to remain stable. The stability restriction, illustrated in Fig. 2.2, is expressed for the fully discrete scheme as:

$$|R(\lambda_m \cdot \Delta t)| \leq 1, \quad \forall \lambda_m \quad (2.24)$$

From the theory of the method of lines, this condition is known to be necessary and sufficient only if  $\mathbf{L}$  is normal ( $\mathbf{L}^t \mathbf{L} = \mathbf{L} \mathbf{L}^t$ ) [121]. In the general case, Relation (2.24) is only a necessary condition for absolute stability, the sufficient condition being more complex [87, 121]. However, it provides an excellent guideline for the choice of  $\Delta t$  [60, Chap. 4, p. 95].

In practice, a simple bisection method is used to find the maximum allowable time step  $\Delta t^*$  for stability. The method iteratively reduces the bracket interval

$[\Delta t_{low}, \Delta t_{high}]$  subject to the conditions:

$$\begin{cases} |R(\lambda_m \cdot \Delta t_{low})| \leq 1, & \forall \lambda_m \\ \exists \lambda_m : |R(\lambda_m \cdot \Delta t_{high})| > 1 \end{cases}$$

In 1D, the stability constraint can be expressed as the so-called CFL condition:

$$\nu = a \frac{\Delta t}{\Delta x} \leq \nu^* = a \frac{\Delta t^*}{\Delta x} \quad (2.25)$$

in which the maximum allowable Courant number  $\nu^*$  depends only on the numerical method, that is, on the order  $p$  of the polynomial approximation in the spatial DG scheme and on the RK scheme.

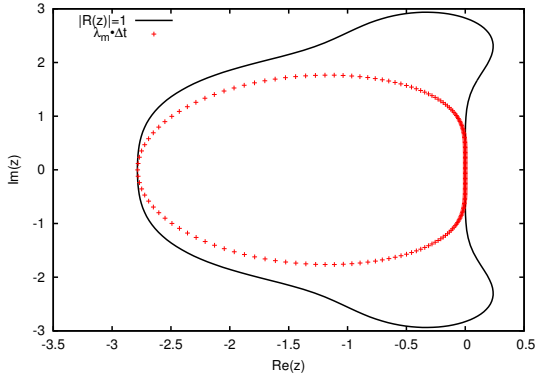


Figure 2.2: Illustration of the stability condition in 1D for  $p = 2$ , with the standard fourth-order RK scheme: the values  $\lambda_m \cdot \Delta t$  all lie within the RK stability region  $S = \{z : |R(z)| \leq 1\}$ .

## 2.3 Conclusion

In this chapter, we have presented the derivation and the analysis of the RKDG method that is used throughout this thesis. Both the spatial and the temporal discretization schemes have been established from a theoretical point of view in Sect. 2.1. The efficient implementation of the method has also been considered, mentioning in particular the quadrature-free technique and nodal basis functions for the spatial DG scheme, and low-storage RK schemes for time integration. In Sect. 2.2, we have introduced a von Neumann-like method that can be used to quantify the accuracy and stability of the RKDG method.

The parameters that influence the performance of the scheme through these two properties have been identified.

The details provided in this chapter put in evidence the benefits of the RKDG methods mentioned in Chap. 1. The order of convergence depends only on the order  $p$  of the polynomial approximation, that can be freely chosen. Moreover, the compact nature of the DG scheme, due to the loose coupling between neighbouring elements, is preserved by the explicit character of the RK scheme. The only operation that is non local to the element, namely the calculation of the numerical flux, is computationally cheap because it only involves the trace of the solution on faces, whereas the local operations, that include integrations over the whole element, are more expensive. This makes the method very amenable to parallelization. Finally, the numerical fluxes also allow us to easily prescribe the boundary conditions in a weak manner, without any need for ghost unknowns like with finite difference stencils.



## Chapter 3

# CFL Conditions on Triangular Grids

In this chapter, the relation between the shape of 2D triangular elements and stability restrictions is investigated in a systematic way, with the aim of providing CFL conditions that could be used to set the time step in practical simulations. The method described in Sec. 2.2 is used to analyze numerically the stability of RKDG methods on grids composed of congruent elements, so that a given element shape can be associated to a stability limit. This method is applied to a broad range of triangle shapes, and results are presented in the form of values for the maximum Courant number, calculated with different geometrical parameters for the element size. Conclusions are drawn on the ability of each size measure to take into account the influence of element shape in the CFL condition. The study is repeated for two types of numerical fluxes, namely the Lax-Friedrichs flux and the upwind flux, and several RK schemes that are commonly used with DG space discretization, in order to provide fairly general results.

### 3.1 Context

As mentioned in Sec. 2.2.3, the RKDG method is subject to stability restrictions that are illustrated by the well-known Courant-Friedrichs-Levy (CFL) Inequality (2.25). In the context of a general multi-dimensional

hyperbolic system, the CFL condition can be written as:

$$\nu = \|\mathbf{a}\| \frac{\Delta t}{h} \leq \nu^* \quad (3.1)$$

where  $h$  is the element size, and  $\|\mathbf{a}\|$  represents the magnitude of the largest characteristic velocity of the hyperbolic system (i.e. the advection velocity in the case of a simple advection equation). The maximum Courant number  $\nu^*$  depends on the spatial and time discretization methods. In practice, this relation imposes a superior bound on the time step, thus limiting the computational efficiency of the numerical method.

With one spatial dimension, a DG space discretization using polynomials of degree  $p$ , associated to a  $(p + 1)$ -stage RK time integrator of order  $p + 1$ , was formally proven to be stable under Condition (3.1) with:

$$\nu^* = \frac{1}{2p + 1}$$

up to  $p = 2$  [30], this condition being optimal for  $p = 0$  [32] and  $p = 1$  [31]. Moreover, numerical evidence was given that these values are less than 5% smaller than the optimal CFL limit for  $p \geq 2$  [32]. Kubatko et al. [89] studied the linear stability of stage-exceeding-order SSP RK schemes with DG spatial discretization, and gave values for the maximum Courant number, for  $p \leq 3$ .

In the case of multiple spatial dimensions, the conditional stability of the method was demonstrated in Ref. 33. However, no clear link between the element geometry and the stability bound was put in evidence. In practice, engineers and researchers use Condition (3.1) in 2D and 3D to determine the maximum time step to be set in their simulations, choosing empirically a measure for the element size  $h$ . The analysis of Ref. 89 was extended to 2D [90] for two structured triangular grid configurations, and a grid parameter  $h$  was proposed. However, that work does not address the influence of the element shape on the stability bounds. The work described in this chapter aims at filling this gap, by quantifying the impact of the element shape on the CFL condition with different element size measures  $h$ , for several variants of the numerical method (numerical fluxes, RK scheme).

## 3.2 Method

### 3.2.1 Exploration of Triangle Shape

To determine the dependence of the stability bound on the triangle shape, the von Neumann-type stability analysis procedure introduced in Chap. 2 is

applied to various grids made up of periodic patterns (see Fig. 2.1(b)). As in Ref. 89 and 90, a harmonic wave assumption is used to formulate a semi-discrete operator  $\mathbf{L}(k)$  depending on the wavenumber  $k$ , thus avoiding the need to assemble the operator for a whole grid containing a large number of elements. The eigenvalues  $\lambda_m(k)$  of  $\mathbf{L}(k)$  are then computed, and a bisection method is applied to find the maximum time step  $\Delta t^*$  satisfying the stability condition  $|R(\lambda_m \cdot \Delta t)| \leq 1$  for all eigenvalues  $\lambda_m(k)$ , where  $R(z)$  is the amplification factor of the RK scheme. The procedure is extensively described in Sec. 2.2. A key point of the method is that in each grid, all elements are congruent, so that a stability limit can be associated to each element shape. The influence of the element shape on the stability restriction can thus be investigated by repeating the stability analysis for various grids representing a broad range of element shapes, which is not carried out in Ref. 89 and 90.

In order to explore triangle shapes in a systematic way, consider first that a triangle is uniquely determined by specifying the length of its three sides  $l_1$ ,  $l_2$  and  $l_3$ . Now, consider two similar triangles differing only by a scale factor  $\alpha$ : it can be deduced from Eq. (2.8) and (2.11) that the semi-discrete operator  $\mathbf{L}$  is inversely proportional to  $\alpha$ . Thus,  $l_1$  is fixed:

$$l_1 = \Delta x$$

and only two independent parameters ( $l_2, l_3$ ) need to be studied. The choice of  $\Delta x$  is arbitrary, here it is set to 2 for  $l_1$  to be equal to the length of the corresponding side  $[-1, 1]$  in the reference triangle  $R$ . Furthermore,  $l_2$  and  $l_3$  are interchangeable, so that only half of the two-parameter space needs to be explored:

$$l_2 \geq l_3$$

Finally, the triangle inequalities:

$$l_1 \leq l_2 + l_3$$

$$l_2 \leq l_1 + l_3$$

reduce the region to be explored as illustrated in Fig 3.1. In order to characterize the triangle shapes in a simple manner, a measure  $\gamma$ , that is commonly used for grid quality assessment in meshing methods, is chosen:

$$\gamma = 2 \frac{r_{inner}}{r_{circum}}$$

where  $r_{inner}$  is the radius of the inscribed circle and  $r_{circum}$  is the radius of the circumcircle of the triangle. Fig. 3.2 shows the value of the grid quality

measure as a function of  $l_2$  and  $l_3$ . A set of 52 points, indicated in Fig. 3.2, is chosen in the parameter space  $(l_2, l_3)$ , spanning a large variety of triangle shapes, as the grid quality measure  $\gamma$  varies from 0.031 to 1, with a mean of 0.45. The actual shape of these 52 triangles is illustrated in Fig. 3.3.

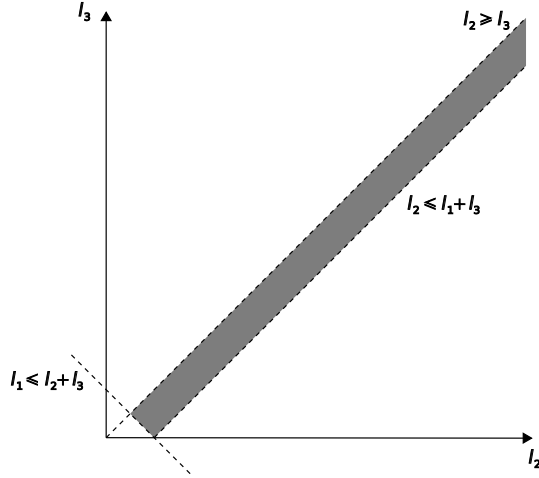


Figure 3.1: Parameter space  $(l_2, l_3)$ . The region to be effectively explored is colored in grey.

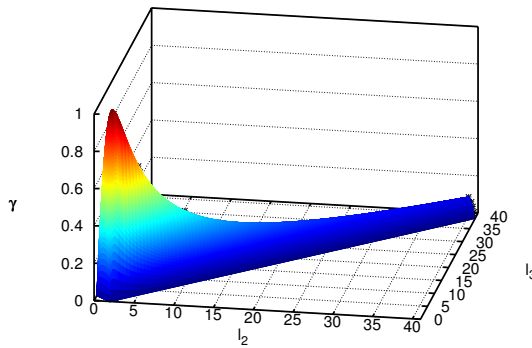


Figure 3.2: Mesh quality measure  $\gamma$  in function of the triangle side lengths  $l_2$  and  $l_3$ . Black stars represent the position of the chosen triangles in the parameter space  $(l_2, l_3)$ .

### 3.2.2 RKDG Method

As shown in Sec. 2.2.3, the maximum time step allowed for stability depends both on the eigenvalues  $\lambda_m$  of the semi-discrete operator  $\mathbf{L}$  and the choice of the RK scheme. In this section, we explain which aspects of the space and time discretization methods affect the stability bound, and the choices made to obtain results that can be applied to practical simulations. Two areas of application, where the use of RKDG methods is becoming popular, are particularly targeted, namely linear wave propagation problems and non-linear problems. It is to be noted that with non-linear equations, conditions for linear stability are usually more restrictive than those for non-linear stability, but the method must be linearly stable to prevent round-off errors from ruining the high-order accuracy [32]. Thus, the CFL conditions presented in Sec. 3.3 may be of interest for both linear and non-linear applications.

#### Space Discretization

It can be deduced from Eq. (2.8) and (2.11) that, apart from the grid, the operator  $\mathbf{L}$  depends on the basis functions  $\varphi_j$  and the numerical flux  $\hat{f}_h$ . Nevertheless, as mentioned in Sec 2.2.1, it can be shown [20] that the choice of  $\varphi_j$  does not influence the eigenvalues  $\lambda_m$  of  $\mathbf{L}$ , as long as the basis  $\mathcal{B}_p^T$  spans the

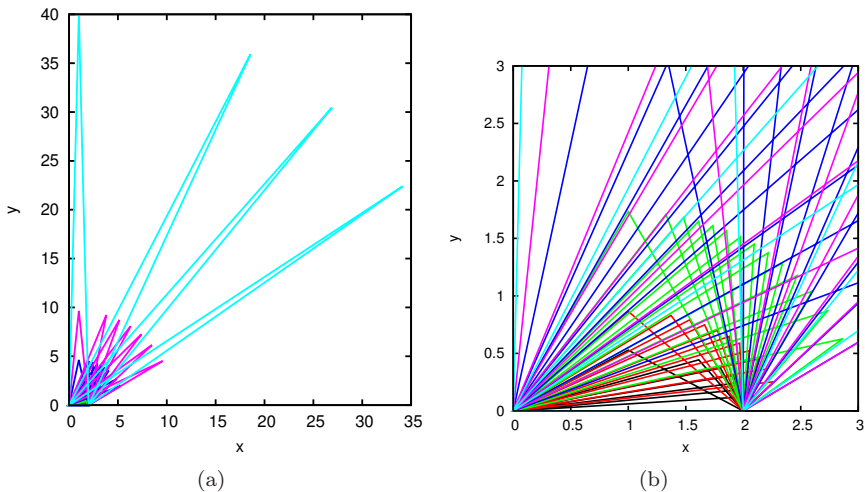


Figure 3.3: Triangle shapes used for the stability analysis: global view (a) and zoom (b).

same polynomial space  $\mathcal{P}_p(T)$ . This means that the stability bound depends only on the order  $p$  of the polynomial approximation. In Sec. 3.3, results are presented for order  $p$  from 1 to 10, as most practical simulations are performed within this range.

The choice of the numerical flux  $\widehat{f}_h$  strongly influences the stability of the method. The Lax-Friedrichs flux and the upwind flux, described in Sec. 2.1.1, are studied in this work because they are the most commonly used with linear equations. In this work, the constant in the dissipative term of the Lax-Friedrichs flux is taken as the advection velocity  $\|\mathbf{a}\|$ , following Eq. (2.4). For non-linear equations, popular choices are the Lax-Friedrichs flux again, the Godunov flux [32] and the Engquist-Osher [44] (or Osher-Salomon [110]) flux. The Godunov flux reduces to the upwind flux in the linear case, so does the Engquist-Osher flux in regions where the sign of the characteristic velocity is constant [44, 110].

## Time Discretization

Numerous RK schemes can be chosen in the framework of the method of lines. The schemes used in this chapter are summarized in Table 3.1, and the coefficients  $\gamma_k$  of their amplification factor  $R(z)$ , that determines their stability properties, are listed in Appendix A. The choice of a particular scheme generally results from a trade-off between accuracy and stability, thus it depends on the application targeted. In this chapter, the focus is on two types of RK schemes.

In a first step, we study a group of RK schemes commonly used with, or specifically designed for linear wave propagation problems, for which the DG method is increasingly popular. All of them are fourth-order accurate for linear equations. They are all designed with five or more stages, so that the coefficients for higher stages, that are not used to fulfill the order conditions, provide extra degrees of freedom for optimization. Carpenter and Kennedy [25] were among the first to propose a  $2N$ -storage scheme, that they optimized with respect to stability. Allampalli et al. [5], Mead and Renaut [104] also presented schemes with optimal stability region. Hu et al. [71] devised RK schemes optimized with respect to dissipation and dispersion, for which Stanescu and Habashi [127] gave a  $2N$ -storage implementation. A similar methodology was followed by Berland et al. [15]. Finally, Calvo et al. [24], as well as Tselios and Simos [139], optimized their scheme with respect to both stability and accuracy. It is to be noted that the schemes proposed by Berland et al. [15] and Calvo et al. [24] are almost the same, although they were obtained through different methods. Absolute stability regions of all these schemes are shown in Fig. 3.4.

They were all optimized with respect to finite-difference semi-discrete operators, except those of Mead and Renaut [104] who used pseudo-spectral operators. As high-order finite-difference methods are usually based on central schemes, they are non-diffusive, thus the eigenvalue spectra of the corresponding operators lie on the imaginary axis. This explains why the stability region of RK schemes optimized for stability are larger along the imaginary axis, but not necessarily along the real axis. As seen from the stability plot in Fig. 2.2, the extent of the RK stability region along the real axis is more relevant for RKDG stability, but to our knowledge, no RK method has been specifically designed for DG space operators yet. This is addressed in Chap. 5.

In a second step, optimal strong-stability-preserving (SSP) RK schemes, that are used with non-linear applications [53, 124], are studied. To our knowledge, non-linear stability of RKDG methods has only been demonstrated with SSP schemes [32]. The optimal three-stage third-order scheme is classical [53]. For non-linear fourth-order accuracy, a minimum of five stages is required, and the optimal scheme used here is obtained through a numerical optimization procedure [124]. Absolute stability regions of the SSP RK schemes studied in this work are shown in Fig. 3.5.

Finally, simple low-storage RK schemes [74] with  $p + 1$  stages are used for comparison purpose. They yield a formally  $(p + 1)$ -order RKDG method up to fourth order. Their stability regions are plotted in Fig. 3.6. One can note that the 3-stage and 4-stage schemes are equivalent to the (3,3)-SSP and “standard” fourth-order RK schemes respectively, as all  $s$ -stage,  $s^{\text{th}}$ -order RK schemes have the same stability region.

## 3.3 Results

### 3.3.1 Advection Velocity and Numerical Flux

Before studying the CFL conditions, it is interesting to qualitatively assess the influence of the advection velocity on stability. It can be seen from Eqs. (2.7), (2.4) and (2.5) that  $\mathbf{L}$  is proportional to the advection velocity  $\|\mathbf{a}\|$ , so that we set  $\|\mathbf{a}\| = 1$ , and study only the effect of the advection direction  $\theta$  with  $\mathbf{a} = (\cos \theta, \sin \theta)$ . Additionally, it can be deduced from symmetry considerations that the problem is invariant with respect to the sign of  $\mathbf{a}$  (i.e. the results are  $\pi$ -periodic in  $\theta$ ). In this section, results obtained with Jameson RK are presented, but the same behavior is found with other RK schemes.

Fig. 3.7 shows the mesh pattern and maximum time step  $\Delta t^*$  in function of the advection direction  $\theta$  for an equilateral triangle (which is the triangle shape of

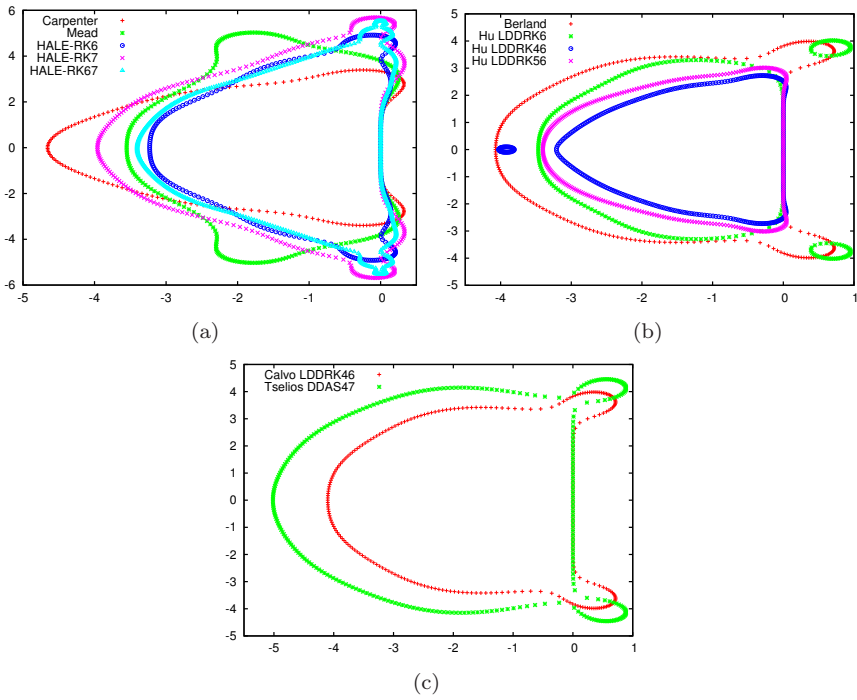


Figure 3.4: Absolute stability regions of RK schemes for linear wave propagation problems, optimized with respect to stability (a), to accuracy (b), and to both stability and accuracy (c).

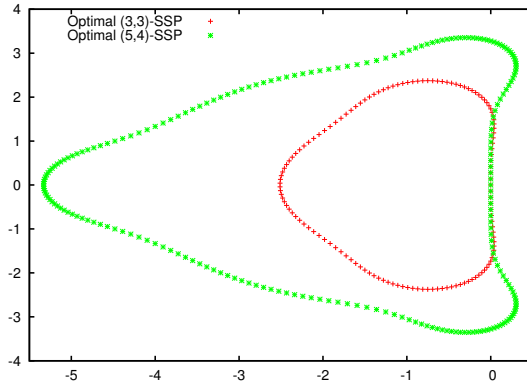
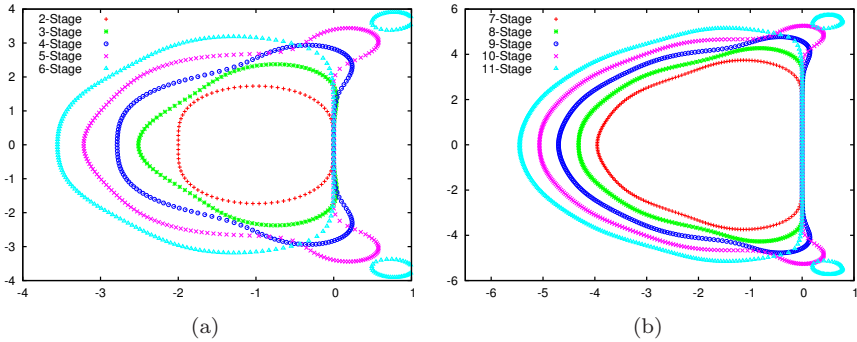


Figure 3.5: Absolute stability regions of SSP RK schemes.

Name	Order	Stages	Storage
Carpenter [25]	4	5	2N
Mead RKC [104]	4	6	5N
HALE-RK6 [5]	4	6	2N
HALE-RK7 [5]	4	7	2N
HALE-RK67 [5]	4	6+7	2N
Hu LDDRK6 [71]	4	6	3N (2N [127])
Hu LDDRK46 [71]	4	4+6	3N
Hu LDDRK56 [71]	4	5+6	3N (2N [127])
Berland [15]	4	6	2N
Calvo LDDRK46 [24]	4	6	2N
Tselios DDAS47 [139]	4	7	2N
Optimal (3,3)-SSP [53]	3	3	3N
Optimal (5,4)-SSP [124]	4	5	5N
Jameson [74]	Variable	$p+1$	2N

Table 3.1: Main characteristics of RK schemes used in this chapter.

Figure 3.6: Absolute stability regions of Jameson  $(p+1)$ -stage RK schemes, 2 to 6 stages (a), and 7 to 11 stages (b).

highest quality,  $\gamma = 1$ ). One can see that the time step is almost constant for the Lax-Friedrichs flux, whereas the dependence on  $\theta$  is stronger but moderate for the upwind flux. The same plots are presented in Fig. 3.8 for a triangle of lower quality. The time step variation in function of  $\theta$  remains moderate with the Lax-Friedrichs flux, but with upwind flux the time step becomes much larger in the advection direction parallel to the longest triangle sides. We verify that this behavior is qualitatively the same for higher order  $p$ .

In practical simulations, the governing system of multidimensional hyperbolic equations often has characteristics that do not degenerate into lines. Instead, there is an infinite set of characteristic directions forming a Monge cone. Thus, a unique advection direction cannot be identified for each characteristic variable, and all advection directions have to be considered. This is the case, for instance, with the acoustic modes featured by the Euler equations in fluid dynamics. Thus, only the minimum value  $\widehat{\Delta t}$  of the time step with respect to  $\theta$  is considered for the assessment of the CFL conditions in Sec. 3.3.2:

$$\widehat{\Delta t} = \min_{\theta} (\Delta t^*)$$

which is the value that ensures stability for all advection directions. For this purpose,  $\theta$  sweeps the range  $[0, 180^\circ]$  with a step of  $4^\circ$ , and a stability analysis is carried out for each value of  $\mathbf{a}$ .

By comparing Fig. 3.7 and 3.8, one can observe that the time step  $\Delta t^*$  is significantly greater with the upwind flux than with the Lax-Friedrichs flux for all advection directions in the case of the equilateral triangle, whereas the minimum value,  $\widehat{\Delta t}$ , seems to be almost equal with both types of numerical fluxes in the case of the stretched triangle. We verify that the upwind flux yields a greater or equal time step in all cases. The maximum and minimum relative difference in  $\widehat{\Delta t}$  of the set of triangles studied are defined as:

$$\Delta_{max} = \max_{\gamma} \left( \frac{\widehat{\Delta t}_{Upwind} - \widehat{\Delta t}_{LF}}{\widehat{\Delta t}_{LF}} \right)$$

$$\Delta_{min} = \min_{\gamma} \left( \frac{\widehat{\Delta t}_{Upwind} - \widehat{\Delta t}_{LF}}{\widehat{\Delta t}_{LF}} \right)$$

where  $\max_{\gamma}$  and  $\min_{\gamma}$  denote respectively the maximum and minimum of a quantity with respect to the element shape, that is, the maximum and minimum value in the set of triangles studied. The quantities  $\Delta_{max}$  and  $\Delta_{min}$  are plotted for all RK schemes and order  $p$  from 1 to 10 in Fig. 3.9. As a general trend, the differences  $\Delta_{max}$  and  $\Delta_{min}$  between both types of flux grow with increasing order  $p$ , that is, the advantage of the upwind flux over the Lax-Friedrichs flux is

greater at higher order  $p$ . The maximum difference  $\Delta_{max}$ , that varies between 25% and 60%, is always obtained with the equilateral triangle (i.e. the best quality element). The minimum difference  $\Delta_{min}$ , increasing from 0% at  $p = 1$  to 33% at  $p = 10$  for most RK schemes, is given by high-aspect-ratio triangles. The optimal (4,5)-SSP RK, and to a lesser extent the Carpenter and Hu LDDRK46 RK, seem to give less advantage to the upwind flux than the other RK schemes studied in this work. They yield a particularly small minimum difference in  $\widehat{\Delta t}$  at low order  $p$ , which occur on highly stretched triangles. This is important in view of practical simulations, when the upwind flux requires additional computational effort per time step, because of the characteristic decomposition of the governing system of equations that it involves. Then the upwind flux may not be competitive with the Lax-Friedrichs flux in terms of computational efficiency, especially at low order  $p$  with low-quality grids, when using these less advantageous RK schemes.

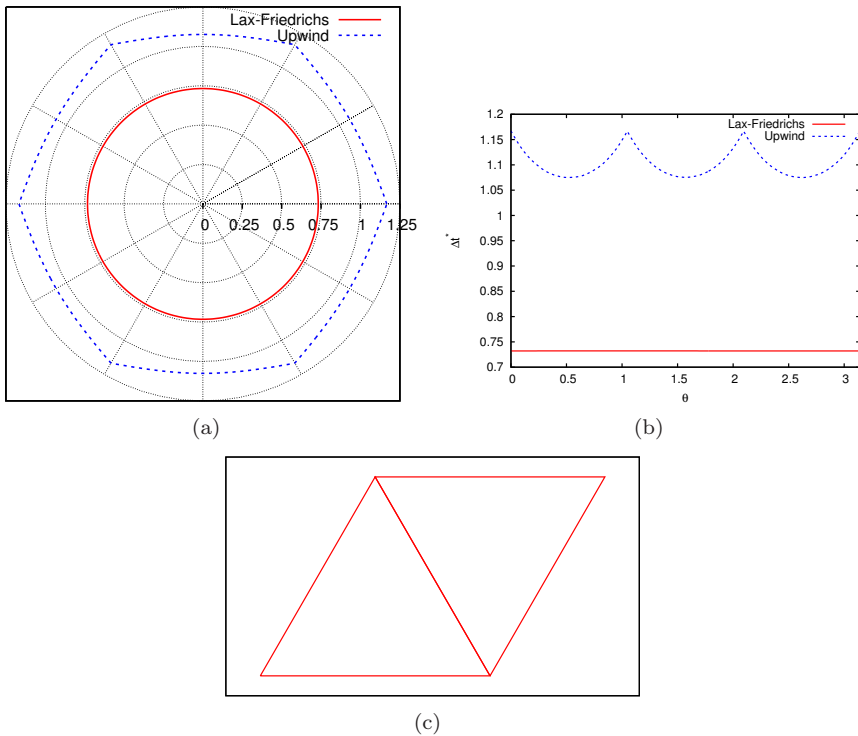


Figure 3.7: Maximum time step  $\Delta t^*$  in function of the advection direction  $\theta$  with the Jameson RK for an equilateral triangle at  $p = 1$ : polar (a) and Cartesian (b) plots, corresponding mesh pattern (c).

### 3.3.2 CFL Conditions

From  $\Delta t^*$ , the maximum Courant number  $\nu^*$  can now be calculated:

$$\nu^*(\mathbf{a}) = \|\mathbf{a}\| \frac{\Delta t^*}{h}$$

and the minimum value  $\widehat{\nu}$  over all advection directions is considered, as explained in Sec. 3.3.1:

$$\widehat{\nu} = \|\mathbf{a}\| \frac{\widehat{\Delta t}}{h}$$

Various geometrical parameters can be chosen as element size  $h$ . Although different parameters can be interlinked by geometrical relations in the triangle,

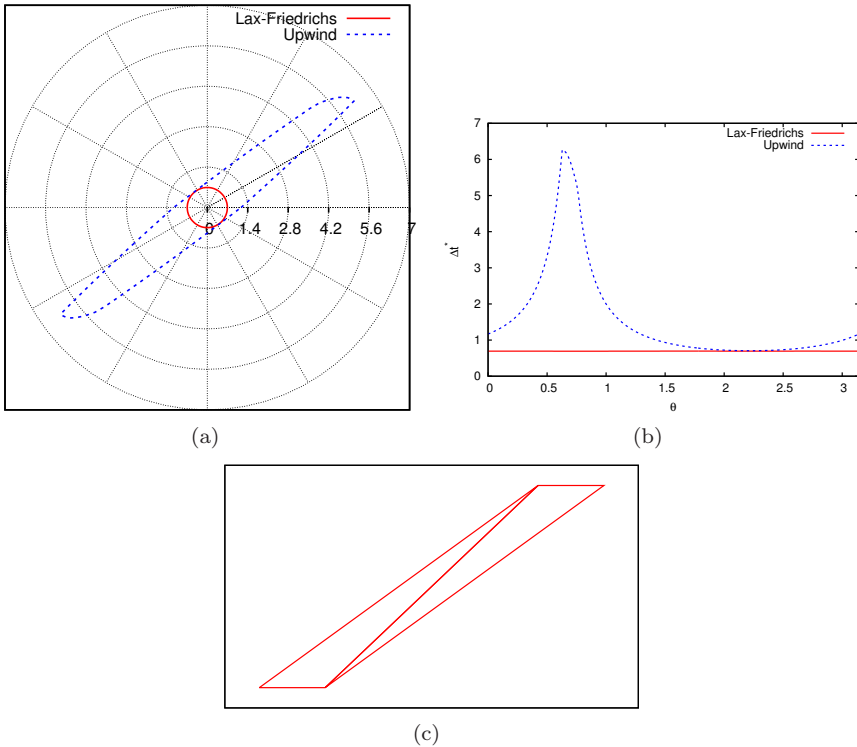


Figure 3.8: Maximum time step  $\Delta t^*$  in function of the advection direction  $\theta$  with the Jameson RK for a triangle of higher aspect ratio at  $p = 1$ : polar (a) and Cartesian (b) plots, corresponding mesh pattern (c).

they do not depend on the element shape in the same manner, so that the influence of the element shape on the maximum Courant number depends on the parameter chosen as size measure  $h$ . In this work, five different element size measures  $h$  are studied: the shortest edge in the triangle ( $\nu_l^*$ ), the side length of the equilateral triangle with equal area ( $\nu_e^*$ ), the radius of the circumscribed circle ( $\nu_c^*$ ), the radius of the inscribed circle ( $\nu_r^*$ ) and the shortest height in the triangle ( $\nu_h^*$ ). Courant numbers based on the radius of the inscribed circle are very commonly used in finite volume and finite element methods. Obviously, the ideal CFL condition would yield the same maximum Courant number whatever the shape of the element. However, none of the five element size measures manages to reflect perfectly the influence of element shape on the stability bound, and there is dispersion among the 52 values of  $\hat{\nu}$ , corresponding to the 52 triangles studied, for a given size measure.

We denote by  $\min_\gamma(\hat{\nu})$  and  $\max_\gamma(\hat{\nu})$  respectively, the minimum and maximum of  $\hat{\nu}$  with respect to the element shape, that is, the minimum and maximum values of  $\hat{\nu}$  in the set of triangles studied. The value  $\min_\gamma(\hat{\nu})$ , which ensures stability for any element shape, is the safest choice for use in practical simulations, but one may want to use higher values in special cases, as explained in Sec. 3.3.2. In Appendix B, values of  $\min_\gamma(\hat{\nu})$  and  $\max_\gamma(\hat{\nu})$  are provided for  $\hat{\nu}$  based on the most interesting element size measures, with the two kind of numerical fluxes and order  $p$  ranging from 1 to 10, for all the RK schemes described in Sec. 3.2.2. As the evolution of the Courant number with respect to  $p$  seems to be more complex than the simple  $1/(2p+1)$  dependence, we assess

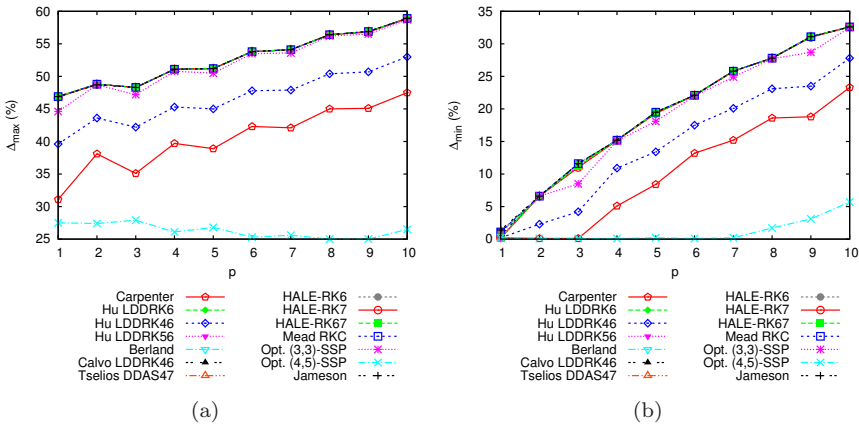


Figure 3.9: Relative maximum (a) and minimum (b) difference in  $\hat{\Delta t}$  between upwind and Lax-Friedrichs fluxes in the set of triangles studied.

logarithmic relations, and curves of the form:

$$\ln(\cdot) = \alpha_0 + \alpha_1 \ln(p) + \alpha_2 [\ln(p)]^2 \quad (3.2)$$

are found to fit the data for  $\min_\gamma(\hat{\nu})$  and  $\max_\gamma(\hat{\nu})$  as a function of  $p$ , with a maximum error of approximately 1%. The values of the coefficients  $\alpha_0$ ,  $\alpha_1$  and  $\alpha_2$  are also given in Appendix B. To characterize the dependence of the CFL conditions on the element shape, the deviation of  $\hat{\nu}$  is computed with respect to the minimum value in the set of triangles studied:

$$D = \frac{\max_\gamma(\hat{\nu}) - \min_\gamma(\hat{\nu})}{\min_\gamma(\hat{\nu})}$$

### Element Size Measures

Fig. 3.10 shows the value of  $\hat{\nu}$  based on each of the five element size measures, for all triangles, at order  $p = 1$ , with the Jameson RK scheme. One can see that  $\hat{\nu}_l$ ,  $\hat{\nu}_e$  and  $\hat{\nu}_c$ , based respectively on the shortest side length, the side length of the equilateral triangle with equal area and the radius of the circumscribed circle, exhibit large relative deviations with respect to their minimum value. This is due to the fact that these measures do not take low values for “flat”, high-aspect-ratio triangles (under the condition that the three side length are have the same order of magnitude for  $\hat{\nu}_l$ ), whereas such ill-conditioned elements yield small  $\Delta t^*$ . As they fail to correctly characterize such “pathological” cases, the results obtained with the set of triangles described in Sec. 3.2.1 cannot be generalized, and they are not appropriate for use with arbitrary unstructured grids. Obviously, the argument stated above being based on geometry, the same behaviour is observed at higher polynomial order  $p$  and with other RK schemes.

On the contrary,  $\hat{\nu}_r$  and  $\hat{\nu}_h$  exhibit less relative variation with the element shape, for both types of numerical fluxes. Therefore, only the results for  $\hat{\nu}_r$  and  $\hat{\nu}_h$  are presented in Appendix B. As seen in Fig. 3.10,  $\hat{\nu}_r$  increases with  $\gamma$  (more for the upwind flux than for the Lax-Friedrichs flux), whereas  $\hat{\nu}_h$  decreases (Lax-Friedrichs flux) or remains almost constant (upwind flux). We verify that the same behaviour is obtained for all RK schemes and all orders  $p$  studied in this work. These remarks can be exploited to fine-tune the value of  $\nu^*$  set in practical simulations. In some applications, the global time step is more likely to be limited by small or medium-size low-quality elements (for instance the elements used to mesh the boundary layer in CFD) than by small, high-quality elements: then minimum values of  $\hat{\nu}_r$  are optimal, whereas with the Lax-Friedrichs flux, higher values of  $\hat{\nu}_h$ , close to  $\max_\gamma(\hat{\nu}_h)$ , are appropriate. If, on the other side, a grid has uniformly good quality, then minimum values

of  $\hat{\nu}_r$  are sub-optimal, whereas minima of  $\hat{\nu}_h$  suit the Lax-Friedrichs flux. Fig. 3.11 shows the deviation  $D$  in  $\hat{\nu}_r$  and  $\hat{\nu}_h$  with the Lax-Friedrichs flux.  $D$  varies between 7% and 31% for  $\hat{\nu}_r$ , depending on the order  $p$  and the RK scheme used, whereas the deviation is generally higher (between 20% and 42%) for  $\hat{\nu}_h$ . However, one can see that the CFL condition based on the inner radius is more accurate only up to order  $p = 6$ , the shortest height becoming a generally better size measure for higher order  $p$ . The same quantities are plotted in Fig. 3.12 for the upwind flux. Surprisingly, the commonly-used inner radius yields a relatively inaccurate CFL condition (52% to 63% deviation), whereas the shortest height measure is very reliable (4% to 13% deviation).

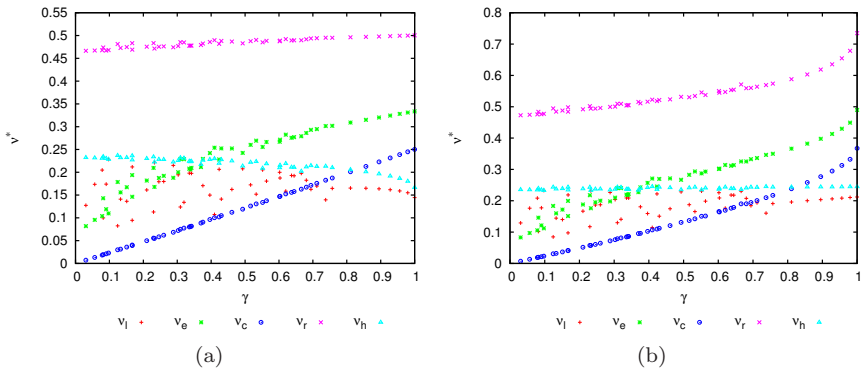


Figure 3.10: Minimum value  $\hat{\nu}$  over all advection directions of the maximum Courant number  $\nu^*$ , in function of the mesh quality measure  $\gamma$ , at order  $p = 1$ , with the Lax-Friedrichs flux (a) and the upwind flux (b), for Jameson RK scheme.

## Runge-Kutta Schemes

As seen in Fig. 3.11 and 3.12, the CFL conditions have similar accuracy with most RK schemes, for a given type of numerical flux, a given element size measure and a given order  $p$ . Nevertheless, one can note that the shortest height measure is more appropriate for the optimal (4,5)-SSP RK scheme whatever the order  $p$ , for the Lax-Friedrichs flux. Also, the CFL conditions seem to be generally slightly less accurate with the optimal (4,5)-SSP and the Carpenter RK schemes than with other RK schemes for the upwind flux.

A general comparison the computational efficiency based on  $\min_{\gamma}(\hat{\nu})$  is difficult, as this minimum value is obtained with different triangle shapes depending on the numerical flux, the element size measure and sometimes even on the order  $p$ . Thus, the exact answer to the question of which RK scheme minimizes the

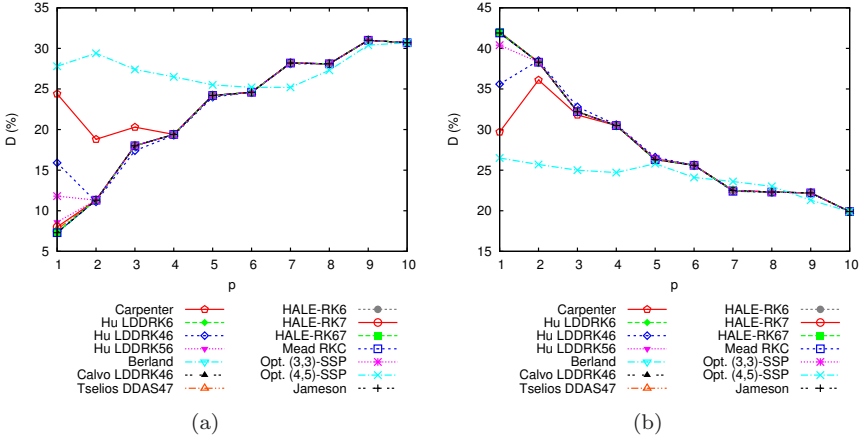


Figure 3.11: Deviation  $D$ , among all element shapes studied, of  $\hat{\nu}$  based on the inner radius (a) and the shortest height (b), in function of the order  $p$ , with the Lax-Friedrichs flux, for all RK schemes.

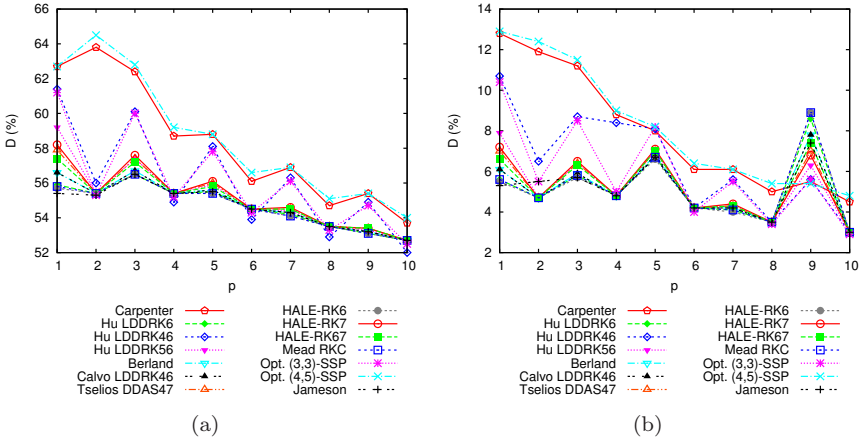


Figure 3.12: Deviation  $D$ , among all element shapes studied, of  $\hat{\nu}$  based on the inner radius (a) and the shortest height (b), in function of the order  $p$ , with the upwind flux, for all RK schemes.

computation time for a practical simulation is grid-specific. However, trends can be observed in the results reported in Appendix B. As the computational effort of a RK scheme in one time step is proportional to its number of stages, the Courant number per stage is taken a measure of the efficiency. It is assumed here that the accuracy of the scheme can be disregarded, but a more comprehensive study of the computational efficiency of RKDG methods can be found in Chap. 5. Fig. 3.13 and 3.14 show the minimum value of the maximum Courant numbers  $\hat{\nu}_r$  and  $\hat{\nu}_h$  per stage with the Lax-Friedrichs flux and the upwind flux respectively. In all cases, it can be seen that the Carpenter RK and the optimal SSP RK schemes are most efficient, which seems logical as they are all optimized for stability. The Hu LDDRK, Berland RK, Calvo RK and Tselios RK schemes, designed (at least partially) for high accuracy, are computationally less efficient. The presence of the HALE RK and Mead RKC schemes among the least efficient, although they are optimized for stability, demonstrates that optimizing a RK scheme with respect to Finite Difference or Pseudo-Spectral spatial operators does not necessarily yield the expected results with the DG method, as explained in Sec. 3.2.2. Finally, the Jameson scheme is relatively efficient for order  $p \leq 2$ , but it becomes less interesting for higher order. In particular, for  $p > 3$ , its number of stages increases without necessarily providing higher order, and the free coefficients are not optimized for anything.

The values of  $\min_\gamma(\hat{\nu}_r)$  given in Tables B.1 and B.7, as well as Fig. 3.13 and 3.14, are barely higher with the upwind flux than with the Lax-Friedrichs flux for moderate order  $p$ . This is because the minima of  $\hat{\nu}$  based on the inner radius are obtained on bad-quality elements, where the upwind flux is less advantageous, as explained in Sec. 3.3.1.

### 3.4 Examples

In order to illustrate the application of the results obtained in Sec. 3.3, we compute the maximum time step  $\Delta t^*$  allowed for stability with two different triangular grids, that are more representative of practical problems than the structured grids described in Sec. 2.2. The exact  $\Delta t^*$  is obtained by considering periodic boundary conditions and assembling directly the semi-discrete operator  $\mathbf{L}$  for the whole grid. The minimum value over all advection directions is then compared to the CFL conditions based on the inner radius and on the shortest height. As the advection velocity is uniform over the whole computational domain, the most restrictive value of  $\Delta t^*$  computed by the CFL conditions is obtained for the smallest element in the grid. We show results obtained with both minimum values  $\min_\gamma \hat{\nu}$  (Tables B.1, B.4, B.7 and B.10)

and maximum values  $\max_\gamma \hat{\nu}$  (Tables B.2, B.5, B.8 and B.11) of  $\hat{\nu}$  given in Appendix B.

The first grid, shown in Fig. 3.15, is unstructured and contains 334 triangular elements. Its quality can be considered as uniformly good, with  $\gamma$  ranging from 0.78 to 1. The results of time step calculations at order  $p = 4$  are given in Tables 3.2 for the Lax-Friedrichs flux and Table 3.3 for the upwind flux. With the Lax-Friedrichs flux, the maximum values of the Courant number  $\hat{\nu}_r$  in the CFL condition based on the inner radius provide large time steps that do not exceed the real stability limit, as expected from the discussion on good-quality grids in Sec. 3.3.2. On the other hand, the time steps obtained

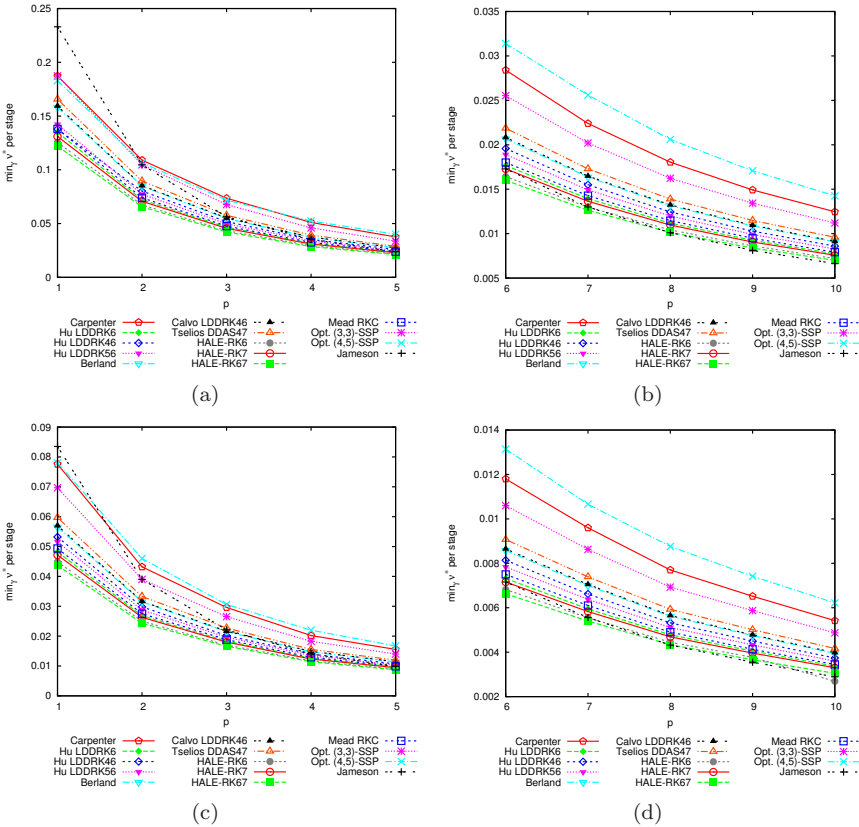


Figure 3.13: Minimum value  $\min_\gamma (\hat{\nu})$  of  $\hat{\nu}$  per stage, based on the inner radius (a) and (b), and based on the shortest height (c) and (d), in function of the order  $p$ , with the Lax-Friedrichs flux, for all RK schemes.

by using maximum values of  $\hat{\nu}_h$  for the CFL condition based on the shortest height exceed the stability limit with most of the RK schemes, as then  $\hat{\nu}_h$  is globally decreasing with  $\gamma$ . With the upwind flux, both elements size measures give better results for high values of the Courant number  $\hat{\nu}$ , in accordance with the observations in Sec. 3.3.2.

The second grid, shown in Fig. 3.16, is made up of a structured part and an unstructured part, like those commonly used to resolve boundary layers in CFD or CAA applications. It contains 164 triangles of heterogeneous quality ( $0.13 < \gamma < 1$ ), the worst elements being located in the structured part. The results of time step calculations at order  $p = 5$  are given in Tables 3.4 and 3.5.

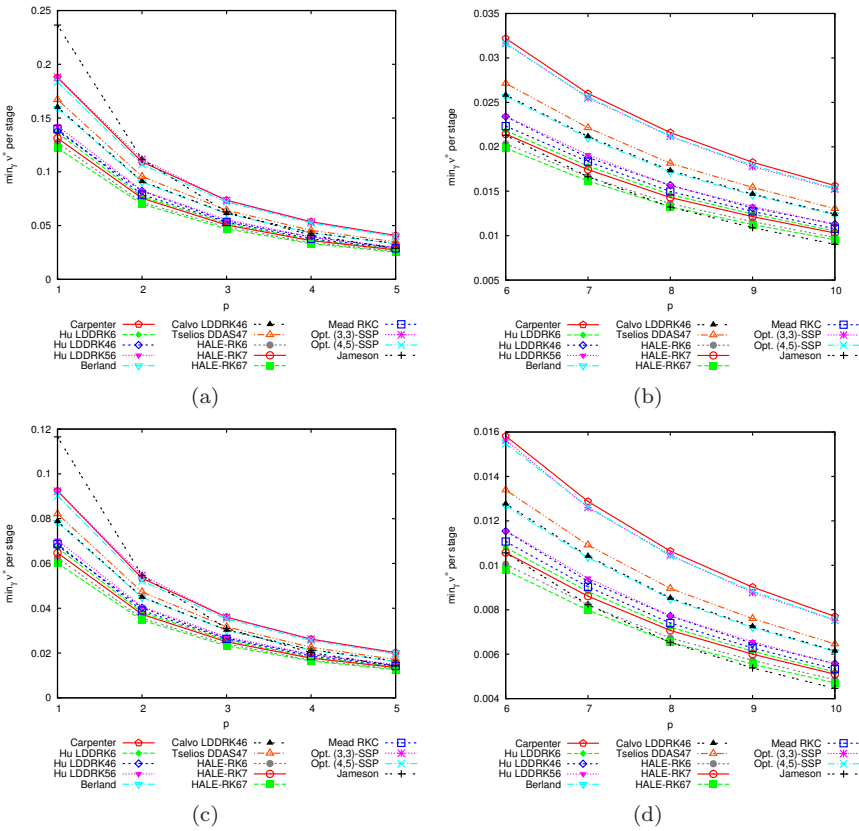


Figure 3.14: Minimum value  $\min_{\gamma}(\hat{\nu})$  of  $\hat{\nu}$  per stage based on the inner radius (a) and (b), and based on the shortest height (c) and (d), in function of the order  $p$ , with the upwind flux, for all RK schemes.

For the Lax-Friedrichs flux, the minimum value of  $\hat{\nu}_r$  and maximum value of  $\hat{\nu}_h$  yield accurate results, as they are suited to the high-aspect-ratio elements of the structured zone that restrict the time step on this grid. The minimum value of  $\hat{\nu}_h$  performs worse, and the maximum value of  $\hat{\nu}_r$  leads to a violation of the exact stability restriction, in accordance with the conclusions of Sec 3.3.2. For the upwind flux, only the maximum value of  $\hat{\nu}_r$  yields reasonably good accuracy, whereas it should give overestimated time steps, according to the discussion in Sec. 3.3.2.

In these two examples, the relative accuracy of different CFL conditions behaves in accordance with the qualitative observations of Sec. 3.3.2 with respect to the type of flux, the kind of grid, and the range of Courant number used. However, the general level of accuracy can be considered as disappointing in view of the results of Sec. 3.3.2 (time steps of less than half of the optimal time step with the hybrid grid and the upwind flux, for instance). The main reason for this lack of accuracy is not a misprediction in the influence of the element shape on the time step restriction. It is due to the fact that local criteria, such as the CFL conditions, can only provide bounds for stability, and the global stability condition may be less restrictive. This is even more the case when other types of boundary conditions than periodicity are imposed, because they generally add constraints to the solution, which may eliminate some of the unstable modes. Nevertheless, the accuracy of CFL conditions is found to be mainly independent of the RK scheme used, and the upwind flux yields greater time steps than the Lax-Friedrichs flux, as in Sec. 3.3.

## 3.5 Conclusion

In this chapter, the time step restrictions that arise from RKDG discretizations of the scalar advection equation on triangular grids have been studied. Two kinds of numerical fluxes, namely the Lax-Friedrichs flux and the upwind flux, as well as a set of RK schemes targetting both linear wave propagation and non-linear applications, have been considered. The stability analysis techniques presented in Sec. 2.2.3 have been applied to derive the linear stability conditions that restrict the time step. The use of structured grids made up of congruent elements, as introduced in Sec. 2.2.1, is particularly appropriate to investigate the influence of triangle shape on the time step limitations. We have focused on the most restrictive condition over all advection directions, which is relevant for generalizing the results to the systems of hyperbolic equations used in practical simulations.

It has been confirmed that the upwind flux generally allows larger time steps

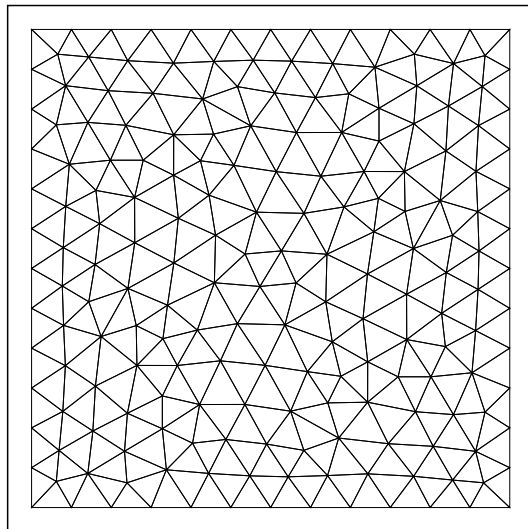


Figure 3.15: Unstructured grid.

	Exact	$\widehat{\nu}_r$		$\widehat{\nu}_h$	
		Min.	Max.	Min.	Max.
Carpenter	6.80	4.66 (31.4%)	5.56 (18.2%)	5.21 (23.3%)	6.81 (-0.3%)
Hu LDDRK6	5.06	3.47 (31.4%)	4.15 (18.0%)	3.90 (22.9%)	5.09 (-0.5%)
Hu LDDRK46	4.68	3.22 (31.3%)	3.84 (18.0%)	3.61 (22.9%)	4.71 (-0.6%)
Hu LDDRK56	4.97	3.40 (31.5%)	4.06 (18.3%)	3.83 (22.9%)	5.00 (-0.6%)
Berland	5.94	4.08 (31.4%)	4.86 (18.2%)	4.58 (23.0%)	5.99 (-0.7%)
Calvo	5.99	4.11 (31.3%)	4.90 (18.1%)	4.62 (22.9%)	6.04 (-0.9%)
Tselios	7.32	5.03 (31.3%)	6.00 (18.1%)	5.63 (23.2%)	7.38 (-0.8%)
HALE-RK6	4.71	3.24 (31.3%)	3.86 (18.2%)	3.63 (22.9%)	4.74 (-0.5%)
HALE-RK7	5.78	3.97 (31.4%)	4.74 (18.1%)	4.45 (22.9%)	5.83 (-0.9%)
HALE-RK67	4.97	3.40 (31.6%)	4.08 (17.9%)	3.83 (22.9%)	5.00 (-0.6%)
Mead RKC	5.19	3.57 (31.2%)	4.24 (18.2%)	4.00 (22.9%)	5.21 (-0.5%)
Opt. (3,3)-SSP	3.67	2.52 (31.2%)	3.00 (18.2%)	2.83 (22.9%)	3.69 (-0.6%)
Opt. (4,5)-SSP	7.78	4.79 (38.4%)	6.05 (22.1%)	5.68 (27.0%)	7.12 (8.4%)
Jameson	4.70	3.22 (31.5%)	3.84 (18.2%)	3.62 (22.9%)	4.72 (-0.6%)

Table 3.2: Maximum time step  $\Delta t^* \times 100$  for the unstructured grid shown in Fig. 3.15, at order  $p = 4$ , with the Lax-Friedrichs flux: exact value calculated from the global semi-discrete operator, estimations obtained by minimum and maximum values of  $\widehat{\nu}$  for CFL conditions based on the inner radius ( $\widehat{\nu}_r$ ) and on the shortest height ( $\widehat{\nu}_h$ ). The relative error with respect to the exact value is indicated in parenthesis, with a negative number if the exact value is exceeded.

	Exact	$\widehat{\nu}_r$		$\widehat{\nu}_h$	
		Min.	Max.	Min.	Max.
Carpenter	10.3	4.90 (52.3%)	7.77 (24.4%)	6.76 (34.2%)	7.38 (28.2%)
Hu LDDRK6	8.36	4.02 (51.9%)	6.25 (25.2%)	5.63 (32.7%)	5.88 (29.6%)
Hu LDDRK46	7.42	3.60 (51.5%)	5.58 (24.9%)	4.98 (32.9%)	5.42 (27.0%)
Hu LDDRK56	8.21	3.95 (51.9%)	6.14 (25.1%)	5.52 (32.7%)	5.78 (29.6%)
Berland	9.82	4.74 (51.8%)	7.35 (25.2%)	6.61 (32.7%)	6.92 (29.6%)
Calvo	9.89	4.77 (51.7%)	7.41 (25.1%)	6.66 (32.7%)	6.97 (29.5%)
Tselios	12.1	5.83 (51.8%)	9.07 (25.1%)	8.16 (32.6%)	8.52 (29.6%)
HALE-RK6	7.79	3.75 (51.9%)	5.83 (25.1%)	5.21 (33.1%)	5.47 (29.8%)
HALE-RK7	9.55	4.61 (51.8%)	7.15 (25.2%)	6.40 (33.0%)	6.71 (29.8%)
HALE-RK67	8.21	3.95 (51.9%)	6.14 (25.2%)	5.52 (32.7%)	5.78 (29.6%)
Mead RKC	8.57	4.13 (51.8%)	6.42 (25.1%)	5.78 (32.5%)	6.04 (29.5%)
Opt. (3,3)-SSP	6.05	2.93 (51.6%)	4.54 (25.0%)	4.07 (32.8%)	4.27 (29.4%)
Opt. (4,5)-SSP	10.1	4.79 (52.4%)	7.63 (24.2%)	6.61 (34.3%)	7.23 (28.2%)
Jameson	7.76	3.75 (51.7%)	5.82 (25.1%)	5.21 (32.8%)	5.47 (29.5%)

Table 3.3: Maximum time step  $\Delta t^* \times 100$  for the unstructured grid shown in Fig. 3.15, at order  $p = 4$ , with the upwind flux: exact value calculated from the global semi-discrete operator, estimations obtained by minimum and maximum values of  $\widehat{\nu}$  for CFL conditions based on the inner radius ( $\widehat{\nu}_r$ ) and on the shortest height ( $\widehat{\nu}_h$ ). The relative error with respect to the exact value is indicated in parenthesis, with a negative number if the exact value is exceeded.

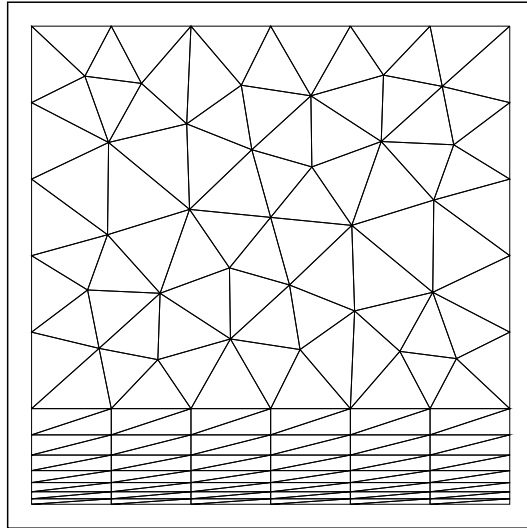


Figure 3.16: Hybrid grid.

	Exact	$\widehat{\nu}_r$		$\widehat{\nu}_h$	
		Min.	Max.	Min.	Max.
Carpenter	1.14	1.03 (9.7%)	1.28 (-11.9%)	0.883 (22.8%)	1.12 (2.4%)
Hu LDDRK6	0.851	0.769 (9.7%)	0.956 (-12.3%)	0.657 (22.8%)	0.831 (2.4%)
Hu LDDRK46	0.804	0.714 (11.2%)	0.884 (-10.0%)	0.607 (24.5%)	0.769 (4.3%)
Hu LDDRK56	0.835	0.753 (9.9%)	0.934 (-11.8%)	0.645 (22.8%)	0.815 (2.5%)
Berland	1.000	0.901 (9.9%)	1.12 (-12.1%)	0.772 (22.8%)	0.975 (2.5%)
Calvo	1.01	0.906 (9.9%)	1.13 (-11.9%)	0.777 (22.8%)	0.982 (2.5%)
Tselios	1.23	1.11 (9.9%)	1.38 (-11.9%)	0.951 (22.8%)	1.20 (2.3%)
HALE-RK6	0.793	0.714 (9.9%)	0.890 (-12.3%)	0.612 (22.8%)	0.773 (2.5%)
HALE-RK7	0.972	0.879 (9.6%)	1.09 (-11.9%)	0.750 (22.8%)	0.949 (2.4%)
HALE-RK67	0.836	0.753 (9.9%)	0.939 (-12.4%)	0.646 (22.7%)	0.815 (2.5%)
Mead RKC	0.872	0.786 (9.9%)	0.978 (-12.1%)	0.673 (22.8%)	0.850 (2.5%)
Opt. (3,3)-SSP	0.617	0.555 (10.1%)	0.692 (-12.2%)	0.477 (22.7%)	0.601 (2.5%)
Opt. (4,5)-SSP	1.31	1.10 (16.1%)	1.38 (-5.3%)	0.948 (27.6%)	1.19 (9.0%)
Jameson	0.873	0.786 (10.0%)	0.978 (-12.1%)	0.674 (22.7%)	0.851 (2.5%)

Table 3.4: Maximum time step  $\Delta t^* \times 1000$  for the hybrid grid shown in Fig. 3.16, at order  $p = 5$ , with the Lax-Friedrichs flux: exact value calculated from the global semi-discrete operator, estimations obtained by minimum and maximum values of  $\widehat{\nu}$  for CFL conditions based on the inner radius ( $\widehat{\nu}_r$ ) and on the shortest height ( $\widehat{\nu}_h$ ). The relative error with respect to the exact value is indicated in parenthesis, with a negative number if the exact value is exceeded.

	Exact	$\widehat{\nu}_r$		$\widehat{\nu}_h$	
		Min.	Max.	Min.	Max.
Carpenter	2.62	1.12 (57.2%)	1.78 (32.0%)	1.15 (56.2%)	1.24 (52.7%)
Hu LDDRK6	2.06	0.928 (55.0%)	1.44 (30.0%)	0.946 (54.1%)	1.01 (51.1%)
Hu LDDRK46	1.84	0.808 (56.1%)	1.28 (30.4%)	0.825 (55.1%)	0.892 (51.5%)
Hu LDDRK56	2.02	0.906 (55.1%)	1.42 (29.9%)	0.926 (54.2%)	0.991 (51.0%)
Berland	2.42	1.09 (55.1%)	1.69 (30.1%)	1.11 (54.1%)	1.18 (51.3%)
Calvo	2.44	1.10 (54.9%)	1.71 (29.9%)	1.12 (54.2%)	1.19 (51.1%)
Tselios	2.98	1.34 (55.0%)	2.09 (29.9%)	1.36 (54.3%)	1.46 (50.8%)
HALE-RK6	1.92	0.862 (55.1%)	1.35 (30.0%)	0.882 (54.1%)	0.941 (51.0%)
HALE-RK7	2.35	1.05 (55.1%)	1.65 (29.9%)	1.08 (54.2%)	1.16 (50.7%)
HALE-RK67	2.02	0.906 (55.2%)	1.42 (29.9%)	0.927 (54.1%)	0.992 (50.9%)
Mead RKC	2.11	0.950 (55.0%)	1.48 (30.1%)	0.970 (54.1%)	1.03 (51.0%)
Opt. (3,3)-SSP	1.48	0.659 (55.5%)	1.04 (29.6%)	0.672 (54.7%)	0.727 (50.9%)
Opt. (4,5)-SSP	2.58	1.10 (57.4%)	1.75 (32.2%)	1.12 (56.7%)	1.20 (53.3%)
Jameson	2.11	0.950 (55.1%)	1.48 (30.1%)	0.970 (54.1%)	1.03 (51.1%)

Table 3.5: Maximum time step  $\Delta t^* \times 1000$  for the hybrid grid shown in Fig. 3.16, at order  $p = 5$ , with the upwind flux: exact value calculated from the global semi-discrete operator, estimations obtained by minimum and maximum values of  $\widehat{\nu}$  for CFL conditions based on the inner radius ( $\widehat{\nu}_r$ ) and on the shortest height ( $\widehat{\nu}_h$ ). The relative error with respect to the exact value is indicated in parenthesis, with a negative number if the exact value is exceeded.

than the Lax-Friedrichs flux. CFL conditions, based on various element size measures, have been derived. Only two of them, based respectively on the inner radius and on the shortest height, have been found to be appropriate for time step calculation in practical simulations, although they are not totally independent of the element shape. The corresponding values of the Courant number, as well as their general behaviour with respect to the element shape, are reported. We have verified that this general behaviour is not strongly affected by the choice of the RK scheme. A general picture of the relative merits of the RK schemes in terms of maximum Courant number per stage has been deduced from the results. The application of these results to two examples, involving respectively an unstructured grid and a hybrid grid, has confirmed these conclusions. However, it has showed that the global stability condition may be much less restrictive than the one given by local criteria such as the CFL conditions.

Most of RK schemes studied in this chapter were optimized for use with finite difference or pseudo-spectral space discretization methods. One can wonder whether a significant gain in computational efficiency could be obtained with a RK scheme specially designed for DG spatial operators. It is also important to note that the aspects of computational efficiency that are addressed in this chapter are solely related to the stability restrictions. They do not deal with accuracy, which is another important criterion for the choice of a time integration method, particularly when using high-order space discretizations. These topics are addressed in Chap. 5.

# Chapter 4

## Alternatives to CFL Conditions

In this chapter, alternative methods are studied to determine the stability limit of RKDG methods, with the objective of obtaining better estimates of the maximum time step  $\widehat{\Delta t}$  than with the CFL conditions derived in Chap. 3. Two techniques for straight elements are first described, that are based respectively on the simplification of the stability analysis procedure introduced in Sec. 2.2 and on the properties of the semi-discrete operator  $\mathbf{L}$  under the mapping  $\mathcal{M}^T$ . They are applied to the two grids presented in Sec. 3.4, and their performance is compared to the CFL conditions. Then, the effect of element curvature on the maximum time step  $\widehat{\Delta t}$ , that the CFL conditions fail to take into account, is investigated. Although the qualitative results show that the element curvature has a strong effect on the conditioning of the semi-discrete operator  $\mathbf{L}$ , we cannot isolate a geometrical parameter that correctly characterizes the stability restriction, and no simple method applicable to practical simulations is derived.

### 4.1 Introduction

The results reported in Chap. 3 show that the CFL conditions for the RKDG method may provide an inexact estimation of the maximum time step  $\widehat{\Delta t}$  that can be set in a simulation, for two main reasons. First, the stability limit is estimated successively for each element in the grid, and only the most

restrictive element is considered to set the global time step, whereas the global stability condition may be much less strict. Second, the CFL conditions cannot reflect exactly the influence of the element shape, because the geometry of the element is only taken into account through the use of a element size measure  $h$ . In Chap. 3, the effect of the element shape is studied only for straight-edge triangles. However, the problem is even more acute for curved element, such as those involved in the advanced boundary treatments presented in Chap. 7.

In order to overcome these difficulties, the exact stability limit for a given simulation could be determined by assembling the semi-discrete operator  $\mathbf{L}$  for the whole grid and computing its eigenvalues, possibly for many advection directions. As explained in Sec. 2.2.1, this procedure is computationally far too expensive. Even assuming that the time step can be estimated from quantities obtained for a lower computational cost, like the spectral radius of  $\mathbf{L}$  approximated by iterative techniques, the global assembly of  $\mathbf{L}$  is still required. This operation necessitates data structures and algorithms to manipulate large sparse matrices and link them to the grid topology, which is commonly found in solvers with implicit time integration, but not in RKDG codes that are designed to work element-by-element. Thus, the effort of implementing such a procedure in a RKDG solver only to improve the estimation of  $\widehat{\Delta t}$  is prohibitive.

Therefore, local methods for the determination of the maximum time step  $\widehat{\Delta t}$ , that are intended to better take into account the element shape than the CFL conditions, are investigated in this chapter.

## 4.2 Straight Elements

As a more accurate alternative to CFL conditions, the determination of time step during the initialization of a simulation could be performed by considering each element in the grid, and executing stability analyses for the corresponding periodic pattern with varying advection direction, as described in Sec. 2.2.3. Unfortunately, this technique is computationally far too costly for practical applications, so that possible simplifications in the procedure are sought.

### 4.2.1 Maximum Dissipation Method

In this section, we take the perspective of Chap. 3, and examine more closely the properties of the eigenvalue spectrum of  $\mathbf{L}(\mathbf{k})$  obtained for the set of 52 triangles described in Sec. 3.2.1 with varying advection direction  $\theta$ . From the resulting observations, a method consisting of 3 steps is derived.

### Estimation of $\widehat{\Delta t}$ from the Maximum Amount of Dissipation

The stability analysis technique presented in Sec. 2.2.3 involves a time-consuming non-linear search to find the maximum time step  $\Delta t^*$  for which all values  $\lambda_m \cdot \Delta t$  remain within the RK stability region  $S = \{z : |R(z)| \leq 1\}$ . However, we notice that the eigenvalue corresponding to the most unstable mode (i.e. the eigenvalue  $\lambda_m$  for which  $R(\lambda_m \Delta t^*) = 1$ ) is generally the purely (or almost purely) real one that is most negative. Graphically, it means that the eigenvalue  $\lambda_m$  that leaves the stability region first when increasing the time step is located furthest on the negative real axis (see Fig. 2.2). As the real part of  $\lambda_m \cdot \Delta t$  corresponds to dissipation and its imaginary part to dispersion, the most unstable mode is the one that is most dissipative, without being dispersive. This behaviour calls for an estimation of the maximum time step  $\Delta t^*$  as:

$$\Delta t^* \approx \frac{-\inf \Re(S)}{-\min \Re(\lambda_m)} = \frac{-\inf \Re(S)}{\delta} \quad (4.1)$$

where  $\delta = -\min \Re(\lambda_m)$  represents the *maximum amount of dissipation*. Note that the most negative eigenvalue located on the real axis is also the largest one in magnitude, so that  $\delta$  is equal to the largest spectral radius of  $\mathbf{L}(\mathbf{k})$ . Obviously, the estimation of the minimum value  $\widehat{\Delta t}$  of  $\Delta t^*$  over all advection directions  $\theta$  is obtained for  $\delta = \max_{\theta} \delta$ .

We verify the accuracy of the estimation of  $\widehat{\Delta t}$  in Eq. (4.1) for all RK schemes studied in Chap. 3. The mean and maximum error in  $\widehat{\Delta t}$  for the Carpenter, Hu LDDRK46, (3,3)-SSP and (5,4)-SSP schemes is shown in Tab. 4.1, 4.2, 4.3 and 4.4 respectively. For all the other RK schemes, the maximum error in  $\widehat{\Delta t}$  at order  $p > 2$  does not exceed 1% with the Lax-Friedrichs flux and 2% with the upwind flux. Overall, the estimation is very accurate with the Lax-Friedrichs flux, and less with the upwind flux. The predictions for the (5,4)-SSP scheme, in particular, are likely to be less interesting than the CFL conditions assessed in Sec. 3.3.2.

It is to be noted that when Eq. (4.1) is not exact (i.e. when the most unstable modes are not the most dissipative), the maximum time step  $\Delta t^*$  is overestimated. The stability plot in Fig. 4.1 illustrates this situation. Thus, using Eq. (4.1) in the cases where the error is greater than a few percents may lead to instability.

### Extrapolation from Order $p = 2$

Although the costly non-linear search can be avoided by estimating  $\widehat{\Delta t}$  from the maximum amount of dissipation  $\delta$ , the determination of  $\widehat{\Delta t}$  is still expensive

$p$	Lax-Friedrichs Flux		Upwind Flux	
	Mean Err. (%)	Max. Err. (%)	Mean Err. (%)	Max. Err. (%)
1	10.8	16.2	14.5	16.1
2	2.5	6.8	10.8	15.1
3	1.2	2.1	12.0	14.4
4	0.0	0.0	9.1	11.5
5	0.0	0.0	10.3	11.1
6	0.0	0.0	8.3	10.0
7	0.0	0.1	9.6	10.2
8	0.0	0.0	8.0	9.3
9	0.0	0.0	9.2	12.3
10	0.0	0.0	7.7	8.9

Table 4.1: Error in the estimation of  $\widehat{\Delta t}$  from the maximum amount of dissipation  $\delta$ , in percent, with the Carpenter RK scheme.

$p$	Lax-Friedrichs Flux		Upwind Flux	
	Mean Err. (%)	Max. Err. (%)	Mean Err. (%)	Max. Err. (%)
1	5.8	8.8	7.7	8.7
2	0.0	0.1	4.0	5.6
3	0.0	0.5	6.3	6.9
4	0.0	0.1	3.8	4.5
5	0.0	0.2	5.5	6.0
6	0.1	0.5	3.8	4.0
7	0.0	0.1	5.0	5.6
8	0.1	0.8	3.7	3.9
9	0.1	0.8	4.8	7.9
10	0.1	1.0	3.7	3.9

Table 4.2: Error in the estimation of  $\widehat{\Delta t}$  from the maximum amount of dissipation  $\delta$ , in percent, with the Hu LDDRK46 scheme.

$p$	Lax-Friedrichs Flux		Upwind Flux	
	Mean Err. (%)	Max. Err. (%)	Mean Err. (%)	Max. Err. (%)
1	2.0	4.3	3.2	4.2
2	0.0	0.0	0.1	0.8
3	0.0	0.0	2.0	2.6
4	0.0	0.0	0.1	0.2
5	0.0	0.0	1.3	1.9
6	0.0	0.0	0.1	0.1
7	0.0	0.0	1.0	1.4
8	0.0	0.0	0.0	0.1
9	0.0	0.0	0.8	3.6
10	0.0	0.0	0.0	0.1

Table 4.3: Error in the estimation of  $\widehat{\Delta t}$  from the maximum amount of dissipation  $\delta$ , in percent, with the (3,3)-SSP RK scheme.

$p$	Lax-Friedrichs Flux		Upwind Flux	
	Mean Err. (%)	Max. Err. (%)	Mean Err. (%)	Max. Err. (%)
1	29.4	36.1	34.1	36.0
2	19.1	25.2	29.7	34.9
3	17.7	19.7	31.1	34.1
4	10.3	11.9	27.6	30.7
5	9.0	10.2	28.9	30.3
6	4.0	5.6	26.6	28.7
7	3.1	5.2	27.9	28.7
8	0.4	1.8	26.1	27.8
9	0.2	1.5	27.4	31.0
10	0.0	0.0	25.7	27.3

Table 4.4: Error in the estimation of  $\widehat{\Delta t}$  from the maximum amount of dissipation  $\delta$ , in percent, with the (5,4)-SSP RK scheme.

at high order, because the computational cost of the eigenvalue problem is proportional to the cube of the number of unknowns, that in turn grows quadratically with the order  $p$ . Thus, the eigenvalue spectra obtained in Chap. 3 is examined with the hope to find scaling laws for  $\delta$  with respect to  $p$ .

Fig. 4.2 shows the value of the maximum amount of dissipation  $\delta$  at order  $p = 5$  for all triangle shapes against the corresponding value of  $\delta$  at order  $p = 2$ , with the Lax-Friedrichs flux, for the horizontal advection  $\mathbf{a} = (1, 0)$ . The scaling of  $\delta$  when varying the element shape is well described by a linear fit. However, this linear law depends on the advection direction  $\theta$ , as made obvious in Fig. 4.3. In the case of the upwind flux, a proportionality relation appears to be accurately satisfied, the proportionality constant being independent of the advection direction  $\theta$ , as illustrated in Fig. 4.4. We verify the accuracy of the linear laws for both types of numerical fluxes in all advection directions, the results are reported in Tab. 4.5. Overall, the linear fits are found to be accurate for most elements, with a low mean error, whereas only a few elements deviate with a maximum error of 5% to 15% for orders  $p \geq 3$ .

Now, for reasons mentioned in Sec. 3.2.1,  $\delta$  is proportional to the inverse of a scale size, whereas its dependence on the order  $p$  is measured for the set of 52 elements with one fixed edge length  $l_1 = \Delta x$ . The scale factor can be taken into account for an arbitrary triangle by defining a *scaled* maximum amount of

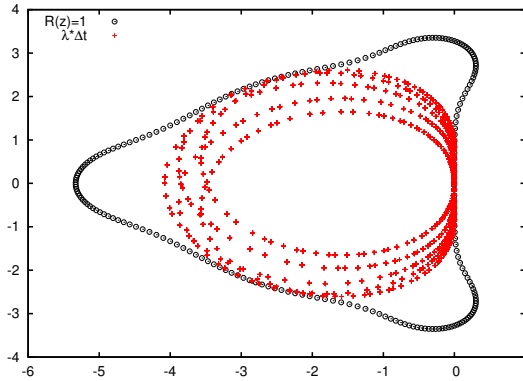


Figure 4.1: Stability plot for an equilateral triangle under horizontal advection, with the upwind flux and the (5,4)-SSP RK scheme, at order  $p = 4$  ( $\Delta t = \Delta t^*$ ): the first eigenvalues leaving the stability region are not located on the real axis.

dissipation  $\bar{\delta}$ :

$$\bar{\delta} = \frac{l_1}{\Delta x} \delta$$

In the general case, the linear fit for  $\bar{\delta}$  can be expressed as:

$$\bar{\delta} = \alpha \bar{\delta}_{p=2} + \beta$$

where the coefficients  $\alpha$  and  $\beta$  generally depend on both  $p$  and  $\theta$ . For the Lax-Friedrichs flux,  $\alpha$  and  $\beta$  do depend on  $\theta$ , whereas  $\alpha$  is independent of  $\theta$  and  $\beta = 0$  for the upwind flux. For a given element, the maximum amount of dissipation  $\delta$  can then be computed at any order  $p$  from the maximum amount of dissipation  $\delta_{p=2}$  at order  $p = 2$  through the relation:

$$\delta = \alpha \delta_{p=2} + \beta \frac{\Delta x}{l_1} \quad (4.2)$$

provided that the values of  $\alpha$  and  $\beta$  are tabulated for each value of  $p$  and, if applicable, for each value of  $\theta$ .

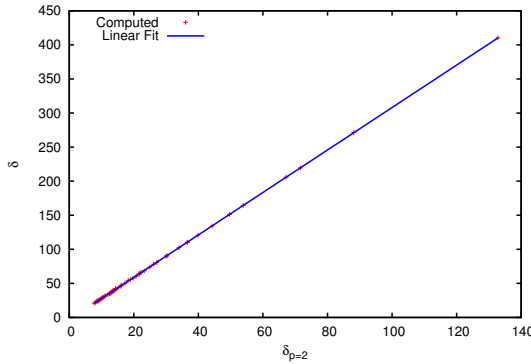


Figure 4.2: Maximum amount of dissipation  $\delta$  at order  $p = 5$  as a function of  $\delta$  at order  $p = 2$ , for the Lax-Friedrichs flux, with horizontal advection.

### Maximum Amount of Dissipation $\delta$ at Order $p = 2$

The maximum amount of dissipation  $\delta$  at order  $p = 2$  can be computed by the procedure described in Sec. 2.2.1. This process is still computationally intensive, as a whole range of modes  $\mathbf{k} = (k_x, k_y)$  has to be considered: the semi-discrete space operator  $\mathbf{L}(\mathbf{k})$  must be built and its eigenvalues computed for each value of  $\mathbf{k}$ .

However, the eigenvalue spectra of  $\mathbf{L}$  computed in Chap. 3 show that for even values of the order  $p$ , the maximum dissipation is obtained for  $\mathbf{k} = (0, 0)$ . We verify this for all element shapes and all advection directions in the database, at order  $p \in \{2, 4, 6, 8, 10\}$ , with both types of numerical fluxes.

Taking into account this observation, the computational effort for one element and one advection direction is reduced to one eigenvalue problem on the operator  $\mathbf{L}_{p=2}(\mathbf{0})$  (i.e. a  $12 \times 12$  matrix), which is relatively affordable. The analytical expression of  $\mathbf{L}_{p=2}(\mathbf{0})$  in function of the coordinates of the triangle vertices can be obtained by means of a Computer Algebra System and plugged into any RKDG solver.

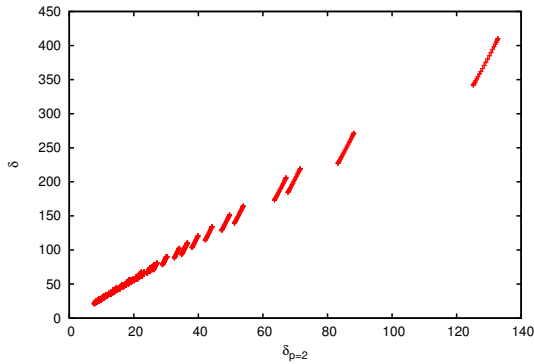


Figure 4.3: Maximum amount of dissipation  $\delta$  at order  $p = 5$  as a function of  $\delta$  at order  $p = 2$ , for the Lax-Friedrichs flux, with all advection directions.

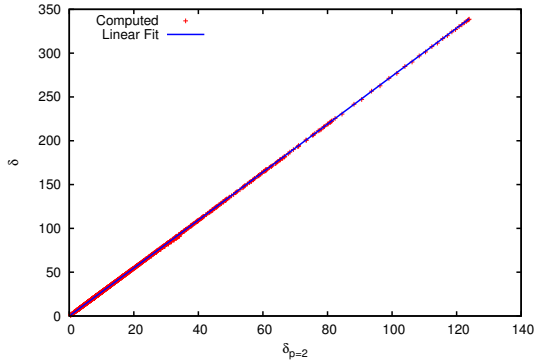


Figure 4.4: Maximum amount of dissipation  $\delta$  at order  $p = 5$  as a function of  $\delta$  at order  $p = 2$ , for the upwind flux, with all advection directions.

## Full Procedure

To summarize, the full procedure to calculate the maximum time step for an arbitrary triangular grid is described by the following pseudo-code:

```

for each element  $T$  in the grid do
  for each value of  $\theta$  do
    Compute  $\delta_{p=2}$  for  $\mathbf{k} = (0, 0)$ 
    Compute  $\delta$  from  $\delta_{p=2}$  with Formula (4.2).
    Compute  $\Delta t^*$  from  $\delta$  with Formula (4.1)
  end for
  Retain  $\widehat{\Delta t} = \min_{\theta} \Delta t^*$ 
end for
Retain  $\min_T \widehat{\Delta t}$ 

```

The accuracy of the estimation of  $\widehat{\Delta t}$  by the full procedure with the Carpenter RK scheme for the set of 52 triangles is reported in Tab. 4.6. The error with the Lax-Friedrichs flux, that is mainly due the extrapolation of  $\delta$ , is about 2% in average for order  $p \geq 2$ . The error with the upwind flux is higher (about 10% in average), and dominated by the overestimation of  $\Delta t^*$  from  $\delta$ , which makes this prediction less reliable, because it may exceed the exact stability limit.

This procedure can even be safely optimized by pre-selecting the elements  $T$  to be analyzed with a geometric criterion based on the CFL condition, instead of applying it to every element in the computational domain. A further

$p$	Lax-Friedrichs Flux		Upwind Flux	
	Mean Err. (%)	Max. Err. (%)	Mean Err. (%)	Max. Err. (%)
1	0.4	3.4	0.3	25.3
2	-	-	-	-
3	0.9	4.8	0.3	11.6
4	0.9	6.0	0.1	0.2
5	1.4	9.0	0.2	7.9
6	1.4	9.6	0.2	0.4
7	1.8	11.7	0.3	4.3
8	1.8	12.2	0.4	0.8
9	2.2	14.2	0.6	7.2
10	2.1	14.2	0.6	1.2

Table 4.5: Error in the approximation of the maximum amount of dissipation  $\delta$  at arbitrary order  $p$  from  $\delta$  at  $p = 2$  by linear fit, in percent, for all advection directions.

improvement could be to take advantage of the observations in Sec. 3.3.1 about the influence of the advection direction on  $\Delta t^*$  to further reduce the range of  $\theta$  to be swept over.

## 4.2.2 Mapping Method

Another time step determination method can be derived directly from considerations on the mapping  $\mathcal{M}^T$  used to perform the integration of the DG equations, as proposed by Hindenlang [61]. Recalling Eq. (2.8) and choosing the upwind flux of Eq. (2.5), one can write:

$$\mathbf{M}^T \frac{\partial \mathbf{q}^T}{\partial t} - \sum_{r=1}^d \mathbf{K}_r^T a_r \mathbf{q} + \sum_{i=1}^b \mathbf{M}^{\partial T_i} (\mathbf{a} \cdot \mathbf{n}^{\partial T_i}) \mathbf{q}^\pm = \mathbf{0} \quad (4.3)$$

with

$$\mathbf{q}^\pm = \begin{cases} \mathbf{q}^T, & \mathbf{a} \cdot \mathbf{n}^{\partial T_i} \geq 0 \\ \mathbf{q}^{T_i^+}, & \mathbf{a} \cdot \mathbf{n}^{\partial T_i} < 0 \end{cases}$$

Using the element mapping  $\mathcal{M}^T$  and the reference element coordinates  $\boldsymbol{\xi}$  instead of the local mapping  $\mathcal{M}^{\partial T_i}$  and the local parametrization  $\bar{\boldsymbol{\xi}}^i$ , all face integral terms in Eq. (2.13) can be expressed with the element Jacobian  $J^T$  instead of the face Jacobians  $J^{\partial T_i}$ . With straight elements,  $J^T$  is constant,

$p$	Lax-Friedrichs Flux		Upwind Flux	
	Mean Err. (%)	Max. Err. (%)	Mean Err. (%)	Max. Err. (%)
1	10.3	15.6	15.5	18.0
2	2.5	6.8	10.8	15.1
3	2.1	6.4	12.5	15.8
4	1.2	3.8	9.1	11.8
5	1.9	5.9	10.5	11.9
6	1.8	5.6	8.3	10.0
7	2.3	7.2	9.7	10.5
8	2.2	7.0	7.9	9.0
9	2.7	8.2	9.2	9.7
10	2.4	8.2	7.7	8.9

Table 4.6: Error in the estimation of  $\widehat{\Delta t}$  with the maximum dissipation method, in percent, for the Carpenter RK scheme.

and the quadrature-free form of Eq. (4.3) yields:

$$|J^T| \mathbf{M}^R \frac{\partial \mathbf{q}^T}{\partial t} - \sum_{r=1}^d \sum_{s=1}^d (J^T)_{sr}^{-1} |J^T| a_r \mathbf{K}_s^R \mathbf{q} + \sum_{i=1}^b |J^T| \mathbf{M}^{\partial R_i} (\mathbf{a} \cdot \mathbf{n}^{\partial T_i}) \mathbf{q}^\pm = \mathbf{0}$$

where the face matrix is expressed as:

$$\mathbf{M}_{kj}^{\partial R_i} = \int_{\partial R_i} \varphi_k \varphi_j d\xi$$

The normal  $\mathbf{n}^{\partial R_i}$  to  $\partial R_i$  can be introduced in the face integral term through the relation  $\mathbf{n}^{\partial T_i} = (J^T)^{-1} \mathbf{n}^{\partial R_i}$ , and  $|J^T|$  can be dropped:

$$\mathbf{M}^R \frac{\partial \mathbf{q}^T}{\partial t} - \sum_{r=1}^d \sum_{s=1}^d (J^T)_{sr}^{-1} a_r \mathbf{K}_s^R \mathbf{q} + \sum_{i=1}^b \mathbf{M}^{\partial R_i} \left[ (J^T)^{-1} \mathbf{a} \cdot \mathbf{n}^{\partial R_i} \right] \mathbf{q}^\pm = \mathbf{0}$$

Using the image  $\bar{\mathbf{a}}^T = (J^T)^{-1} \mathbf{a}$  of  $\mathbf{a}$  in the reference space, this can be rewritten as:

$$\mathbf{M}^R \frac{\partial \mathbf{q}^T}{\partial t} - \sum_{s=1}^d \mathbf{K}_s^R \bar{a}_s^T \mathbf{q} + \sum_{i=1}^b \mathbf{M}^{\partial R_i} (\bar{\mathbf{a}}^T \cdot \mathbf{n}^{\partial R_i}) \mathbf{q}^\pm = \mathbf{0} \quad (4.4)$$

Comparing Eq. (4.3) and Eq. (4.4), it becomes clear that the operator  $\mathbf{L}(\mathbf{k})$  obtained by applying the analysis described in Sec. 2.2.1 to an element  $T$  with an advection  $\mathbf{a}$  is the same as the one obtained by applying the analysis to the reference element  $R$  with the advection  $\bar{\mathbf{a}}^T$ . The maximum time steps are thus equal:

$$\Delta t^*(\mathbf{a}) = \overline{\Delta t}^*(\bar{\mathbf{a}}^T)$$

This observation, combined with the fact that  $\Delta t^*$  is inversely proportional to  $\|\mathbf{a}\|$ , is exploited in an efficient method for the determination of  $\widehat{\Delta t}$ . Supposing that the value of the maximum time step  $\overline{\Delta t}^*$  is tabulated for the reference element  $R$  as a function of the advection direction  $\bar{\theta}$  with  $\bar{\mathbf{a}}^T = (\cos \bar{\theta}, \sin \bar{\theta})$ , then  $\Delta t^*$  can be computed as:

$$\Delta t^*(\theta) = \|J^T \bar{\mathbf{a}}^T\| \overline{\Delta t}^*(\bar{\theta}) \quad (4.5)$$

where  $\theta$  is the advection direction corresponding to  $\mathbf{a} = J^T \bar{\mathbf{a}}^T$ . Thus,  $\widehat{\Delta t}$  can be calculated as:

$$\widehat{\Delta t} = \min_{\bar{\theta}} \|J^T \bar{\mathbf{a}}^T\| \overline{\Delta t}^*(\bar{\theta})$$

This technique is much faster than the maximum diffusion method presented in Sec 4.2.1, because it only involves a matrix-vector product of dimension 2 per advection direction, instead of an eigenvalue problem of dimension 12. Up to the accuracy of the sampling in  $\bar{\theta}$ , it gives the exact  $\widehat{\Delta t}$  for a given element.

The derivation of Eq. (4.4) requires the numerical flux to be proportional to  $\mathbf{a} \cdot \mathbf{n}$ , so that the method is strictly valid for the upwind flux, but not for the Lax-Friedrichs flux. However, one can wonder in which measure the estimation of Eq. (4.5) is approximate with the Lax-Friedrichs flux, as it could prove useful if it was accurate enough, even without being exact. Fig. 4.5 and Fig. 4.6 show a comparison of the exact and estimated values of  $\Delta t^*$  as a function of the advection direction  $\theta$  at  $p = 4$  for two element shapes respectively. The variation of  $\Delta t^*$  with  $\theta$  is overestimated, above all with the high-aspect-ratio triangle. Most importantly, the minimum value  $\widehat{\Delta t}$  of  $\Delta t^*$  over all advection directions is underestimated. The error in the estimation of  $\widehat{\Delta t}$  with the set of 52 triangles described in Chap. 3 is reported in Tab. 4.7. It is comprised between 34% and 39% for all values of the order  $p$ , so that it is not competitive with respect to the best CFL conditions derived in Sec. 3.3.2.

$p$	Mean Err. (%)	Max. Err. (%)
1	34.5	46.9
2	38.2	49.9
3	37.5	50.2
4	37.9	50.9
5	36.9	49.7
6	36.9	49.8
7	36.2	49.0
8	36.2	49.1
9	35.8	48.5
10	35.8	48.7

Table 4.7: Error in the estimation of  $\widehat{\Delta t}$  with the Lax-Friedrichs flux, in percent, for the set of triangles described in Sec. 3.2.1.

### 4.2.3 Examples

In order to illustrate the relative performance of the different methods, the maximum time step  $\widehat{\Delta t}$  is computed with the Carpenter RK scheme on the two triangular grids described in Sec. 3.4, shown respectively in Fig. 3.15 and 3.16. The reference value is the exact  $\widehat{\Delta t}$ , obtained by direct assembly the semi-discrete operator  $\mathbf{L}$  for the whole grid. The CFL conditions based on the inner

radius ( $\widehat{\nu}_r$ ) and on the shortest height ( $\widehat{\nu}_h$ ) are compared to the maximum dissipation and the mapping methods.

For both grids, all methods predict a significantly lower  $\widehat{\Delta t}$  than the exact one because of their local (element-by-element) character: as mentioned in Sec. 3.4, local criteria yield more restrictive stability limits than the exact global condition, which explains why even the mapping method with the upwind flux provides suboptimal values of  $\widehat{\Delta t}$ . With the Lax-Friedrichs flux, the mapping method is unsurprisingly much less accurate than the other methods. The maximum dissipation method, however, yield slightly better results than the most accurate CFL condition. With the upwind flux, both alternative methods perform better than the CFL conditions. The fact that the maximum dissipation method provides a higher accuracy is to be taken with care, because

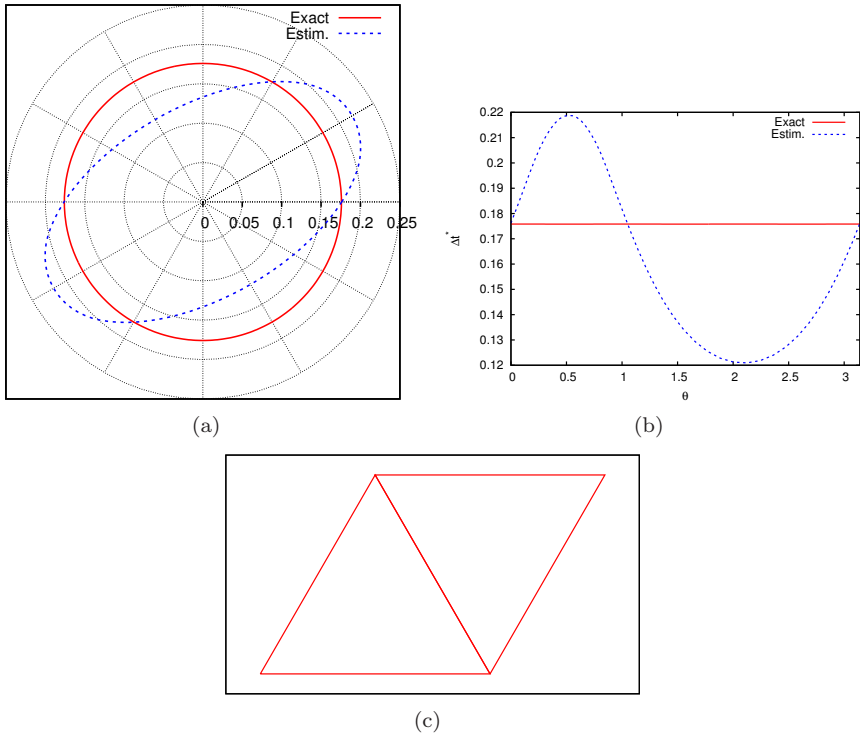


Figure 4.5: Exact and estimated maximum time step  $\Delta t^*$  in function of the advection direction  $\theta$  with the Lax-Friedrichs flux and the Carpenter RK for an equilateral triangle at  $p = 4$ : polar (a) and Cartesian (b) plots, corresponding mesh pattern (c).

it comes from the overestimation of  $\widehat{\Delta t}$  for each element taken separately, which compensates the global under-prediction.

Overall, for the upwind flux, the mapping method gives the exact local  $\widehat{\Delta t}$  (up to the accuracy of the sampling in  $\theta$ ), on top of being very fast and easy to implement, so that it may be advantageous with respect to the CFL conditions. For the Lax-Friedrichs flux, the slight gain in accuracy brought by the maximum dissipation method compared to the CFL conditions is counterbalanced by its computational cost and by its complexity. It may be interesting only in simulation of long periods of time, in which case a small increase in the time step compensates for the slower initialization phase and justifies the implementation effort.

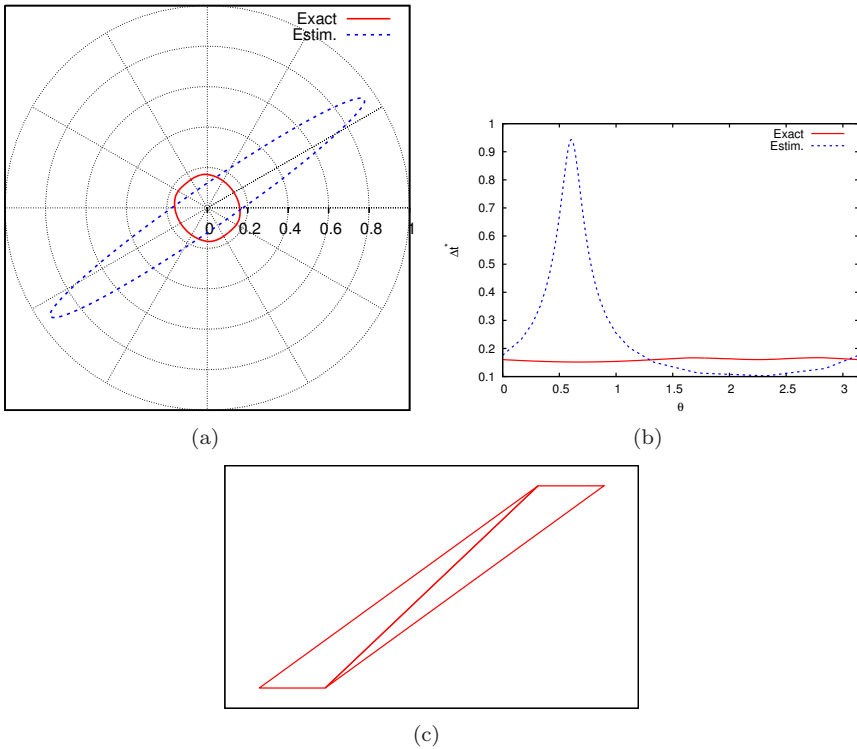


Figure 4.6: Exact and estimated maximum time step  $\Delta t^*$  in function of the advection direction  $\theta$  with the Lax-Friedrichs flux and the Carpenter RK for a triangle of higher aspect ratio at  $p = 4$ : polar (a) and Cartesian (b) plots, corresponding mesh pattern (c).

## 4.3 Curved Elements

The results obtained in Chap. 3 and Sec. 4.2 are restricted to triangles with straight edges. However, curved elements are also used in practice, for instance with the advanced boundary treatments presented in Chap. 7. Although the proportion of curved elements in the whole computational domain is usually small, these elements are among the smallest and the worst conditioned, because they lie in the vicinity of wall boundaries. Thus, they may influence the global time step, and it is important to characterize the influence of the curvature on the stability of RKDG methods.

### 4.3.1 Study of the Stability with Curved Elements

The stability of the RKDG method with curved elements is studied by means of the von Neumann-type analysis technique described in Sec. 2.2, in the same manner as with straight elements. As in Chap. 3, the analysis is carried out on grids made up of periodic patterns. However, the elements used here are of second geometric order, so that the mapping  $\mathcal{M}^T$  is quadratic, and the Jacobian  $J^T$  is linear, as mentioned in Sec. 2.1.1. The mappings are defined through control points on the edges of the element, as commonly done in classical FEM. The corresponding mesh patterns are shown in Fig. 4.7. A

	Lax-Friedrichs	Upwind
Exact	6.796	10.27
CFL - $\hat{\nu}_r$	4.663 (31.4%)	4.901 (52.3%)
CFL - $\hat{\nu}_h$	5.214 (23.3%)	6.763 (34.2%)
Maximum Dissipation Method	5.366 (21.0%)	7.887 (23.2%)
Mapping Method	3.713 (45.4%)	7.311 (28.8%)

Table 4.8: Maximum time step ( $\times 100$ ) for the unstructured grid of Fig. 3.15, at order  $p = 4$ .

	Lax-Friedrichs	Upwind
Exact	8.627	20.44
CFL - $\hat{\nu}_r$	7.801 (9.6%)	8.845 (56.7%)
CFL - $\hat{\nu}_h$	6.696 (22.4%)	8.977 (56.1%)
Maximum Dissipation Method	7.855 (8.9%)	9.876 (51.7%)
Mapping Method	4.342 (49.7%)	9.895 (51.6%)

Table 4.9: Maximum time step ( $\times 10^4$ ) for the hybrid grid of Fig. 3.16, at order  $p = 6$ .

semi-discrete operator  $\mathbf{L}(k)$  depending on the wavenumber  $k$  is formulated, based on a harmonic wave assumption. The maximum allowable time step  $\Delta t^*$  is found through a bisection method that evaluates the stability condition  $|R(\lambda_m \cdot \Delta t)| \leq 1$  for all eigenvalues  $\lambda_m(k)$  of  $\mathbf{L}(k)$ ,  $R(z)$  being the amplification factor of the RK scheme. To our knowledge, there is no report of such method being applied to curved elements in the literature.

In one spatial dimension, the element cannot be geometrically curved, but the use of a quadratic mapping mimics the effect of element curvature. This curvature is quantified by the non-dimensional parameter  $\chi$ , that is defined as the distance between the control point and the center of the segment, divided by the half-length of the segment (see Fig. 4.7). The value  $\chi = 0$  corresponds to a linear mapping  $\mathcal{M}^T$  (i.e. no curvature). The maximum curvature is reached for  $\chi = 0.5$ , at which point the Jacobian determinant changes sign over the segment, so that the numerical method becomes invalid.

In 2D, two parameters  $\chi_T$  and  $\chi_N$  (see Fig. 4.7(b)), non-dimensionalized with the edge half-length, are used to quantify the displacement of the control point of each edge from its center in the tangential and normal directions respectively (see Fig. 4.7). The maximum curvature that can be reached without affecting the bijective character of  $\mathcal{M}^T$  depends on the shape of the corresponding straight-edge triangle. Note that in the case of curved elements in 2D, the two elements of the grid pattern are not congruent, so that the stability limit obtained from the analysis may be considered as over-restrictive if the element shape of interest is the “largest” of both.

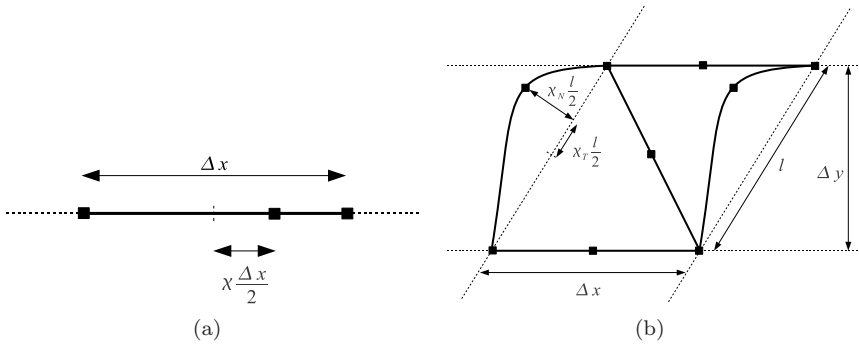


Figure 4.7: Mesh patterns used for the stability analysis with curved elements in 1D (a) and 2D (b).

### 4.3.2 Qualitative Assessment of the Curvature Effect in 2D

Fig. 4.8 shows the result of the progressive deformation of an edge of an equilateral triangle in the normal direction up to  $\chi_N = 0.8$ , with the Lax-Friedrichs flux and the Standard RK4 scheme, the advection being horizontal. The eigenvalue spectrum  $\lambda_m$  of the semi-discrete operator  $\mathbf{L}(\mathbf{k})$  stretches along the real axis, which explains the drop of the maximum time step  $\Delta t^*$ . The plot of the normalized maximum time step  $\Delta t^*/\Delta t^*_{\chi_N=0}$  in Fig 4.8(c) shows that the decrease of  $\Delta t^*$  is proportionally steeper at higher order  $p$ . Even for a moderate curvature of  $\chi_N = 0.4$ , for instance, the maximum time step  $\Delta t^*$  is 20% to 30% smaller than with the straight-edge element.

The effect of a tangential deformation when the normal deformation fixed at  $\chi_N = 0.4$  is shown in Fig. 4.9. Although the drop in  $\Delta t^*$  seems to be limited at low order  $p$ , it is much sharper at higher order. The fact that the maximum time step  $\Delta t^*$  undergoes a dramatic variation, whereas the global shape of the element looks relatively unaffected, explains why the CFL conditions that used for straight-edge elements, based on the inner radius and the minimum height, are inappropriate for curved elements.

These observations suggest that the influence of the element curvature on the time step is governed by localized geometrical properties of the triangle. We verify that the qualitative behaviour described above is the same irrespective of the type of numerical flux, the RK scheme, as well as the advection direction and the shape of the straight-edge triangle that is deformed.

### 4.3.3 Influence of the Curvature in 1D

In the hope of discovering a possible relation between the maximum time step  $\Delta t^*$  and a geometrical parameter characterizing the element curvature, the simpler case of one spatial dimension is considered, which avoids the complications linked to the straight-edge element shape, the advection direction and the type of numerical flux. As in the 2D configuration, the starting point is the linear element and a progressive deformation is applied by moving the control point away from the center of the element.

For geometrically linear 1D elements, it can be deduced from Eq. (2.8) and (2.12) that the maximum time step  $\Delta t^*$  is proportional to  $|J^T|$ . As in curved 2D element,  $\Delta t^*$  apparently decreases when  $|J^T|$  locally tends to zero, it seems sensible to test the dependence of  $\Delta t^*$  on  $\min_{\xi} |J^T|$ . Fig. 4.10 shows the evolution of the normalized maximum time step  $\Delta t^*/\Delta t^*_{\chi=0}$  as a function of the normalized minimum Jacobian determinant  $\min_{\xi} |J^T|/|J^T|_{\chi=0}$ . Not only

the dependence of  $\Delta t^*/\Delta t_{\chi=0}^*$  on  $\min_{\xi} |J^T|/|J^T|_{\chi=0}$  is non-linear, but it also varies with the order  $p$ . This is due to the fact that the Jacobian terms cannot be taken out of the integrals in Eq. 2.11, so that the influence of the element geometry on the conditioning of the semi-discrete operator  $\mathbf{L}$  cannot be decoupled from the polynomial basis  $\mathcal{B}_p^T$ . Thus, the effect of curvature cannot be fully taken into account by a purely geometrical parameter only.

Then, we consider the dependence of  $\Delta t^*$  on the minimum distance  $\Delta x_N$  in the physical space between the Lagrange-Gauss-Lobatto nodes on which the base interpolating polynomials  $\varphi^T$  are defined. This parameter depends both on the polynomial basis  $\mathcal{B}_p^T$  and on  $|J^T|$ . Moreover, it is closely related to the conditioning of the semi-discrete operator  $\mathbf{L}$ , as when two nodes  $i$  and  $j$  come close to each other, the corresponding basis functions  $\varphi_i^T$  and  $\varphi_j^T$  tend to become equal, and the mass matrix  $\mathbf{M}^T$  tends to become singular.

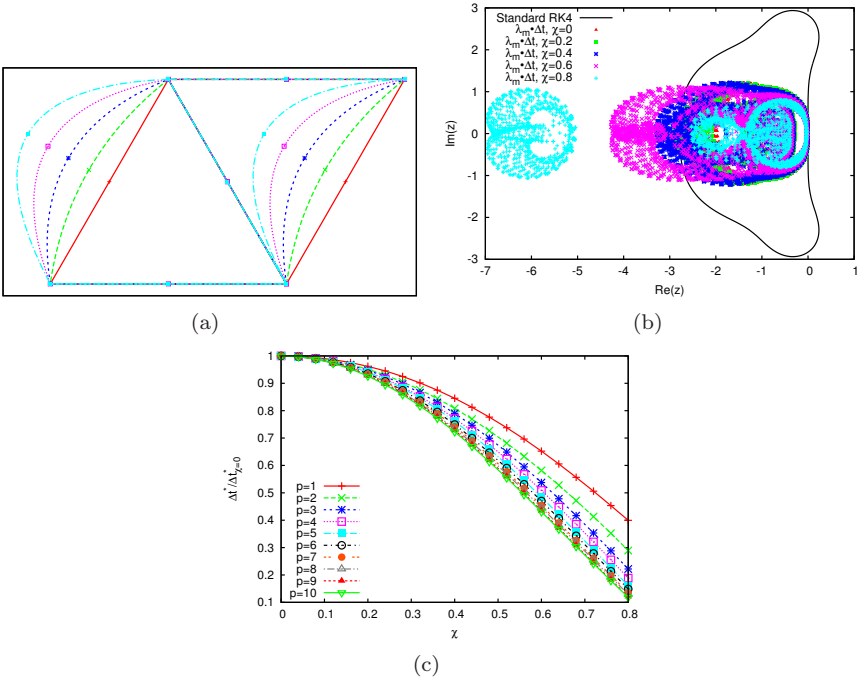


Figure 4.8: Deformation of equilateral elements in the direction normal to an edge, with the Lax-Friedrichs flux, the Standard RK4 scheme and an horizontal advection: mesh pattern (a), corresponding stability plot (b) at order  $p = 1$ , and evolution of the normalized maximum time step  $\Delta t^*/\Delta t_{\chi_N=0}^*$  for order  $p$  from 1 to 10 (c).

Fig. 4.11 shows the normalized maximum time step  $\Delta t^*/\Delta t_{\chi=0}^*$  as a function of the normalized minimum node distance  $\Delta x_N/\Delta x_{N,\chi=0}$ . The dependence of  $\Delta t^*/\Delta t_{\chi=0}^*$  on  $\Delta x_N/\Delta x_{N,\chi=0}$  is non-linear, and varies with the order  $p$ . In the extreme case of  $p = 1$ ,  $\Delta x_N$  remains constant under deformation (because the only two nodes are end points of the segment), whereas  $\Delta t^*$  decreases. Therefore, the minimum node distance  $\Delta x_N$  cannot be used to evaluate the influence of curvature on the maximum time step  $\Delta t^*$ .

Finally, the applicability of the maximum dissipation method presented in Sec. 4.2.1 to curved elements is investigated. For this purpose, the validity of the extrapolation of the maximum amount of dissipation  $\delta$  from order  $p = 2$  is tested for geometrically quadratic elements. The maximum amount of dissipation  $\delta$  at order  $p$  from 1 to 10 is plotted in Fig. 4.12 against  $\delta$  at order 2 for a curvature  $\chi$  varying from 0 to 0.49. The relation is obviously non-linear

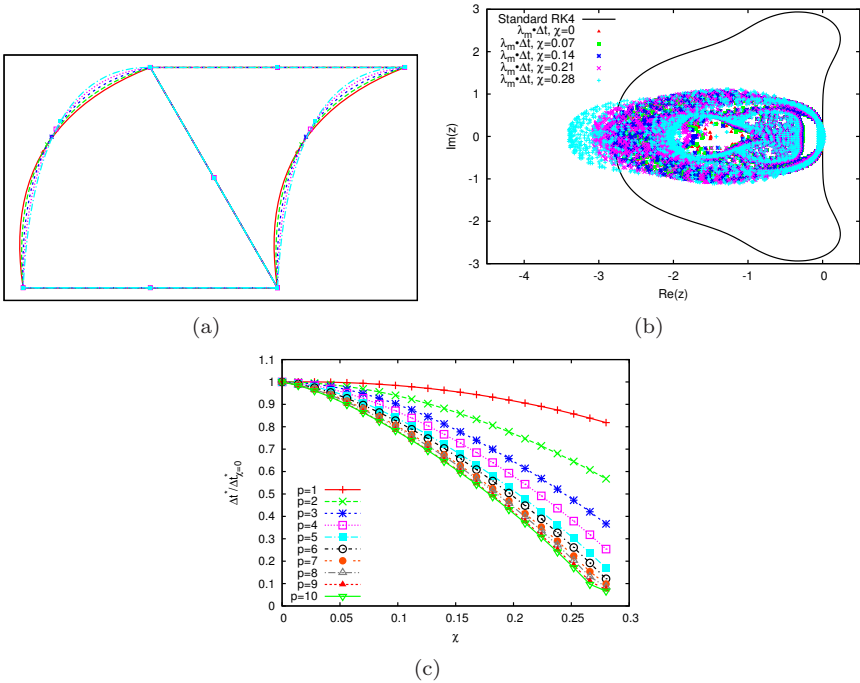


Figure 4.9: Deformation of equilateral elements in the direction tangential to an edge, the normal deformation being fixed at  $\chi_N = 0.4$ , with the Lax-Friedrichs flux, the Standard RK4 scheme and an horizontal advection: mesh pattern (a), corresponding stability plot (b) at order  $p = 1$ , and evolution of the normalized maximum time step  $\Delta t^*/\Delta t_{\chi_N=0}^*$  for order  $p$  from 1 to 10 (c).

(except of course for  $p = 2$ ), so that the maximum time step  $\Delta t^*$  cannot be estimated through the procedure presented in Sec. 4.2.1.

Overall, it seems difficult to find a geometrical quantity that characterizes the influence of the element curvature on the stability of RKDG methods. Moreover, the observations used in Sec. 4.2 to derive alternative estimation methods for the maximum time step do not apply to elements of geometrical order 2. One is thus bound to the full analysis of Sec. 2.2, that is inapplicable in practical simulations, to determine the stability limits of the RKDG method with curved elements.

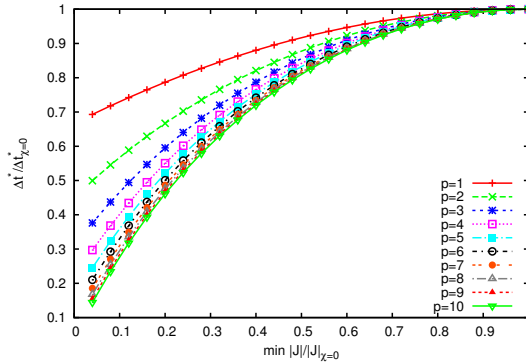


Figure 4.10: Normalized maximum time step  $\Delta t^*/\Delta t^*_{\chi=0}$  as a function of the normalized minimum Jacobian determinant  $\min_{\xi} |J^T|/|J^T|_{\chi=0}$  for order  $p$  from 1 to 10 in 1D.

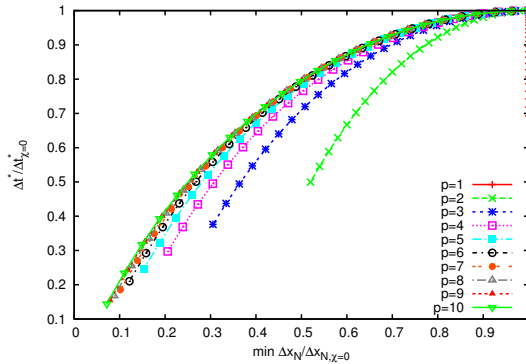


Figure 4.11: Normalized maximum time step  $\Delta t^*/\Delta t^*_{\chi=0}$  as a function of the normalized minimum node distance  $\Delta x_N/\Delta x_{N,\chi=0}$  for order  $p$  from 1 to 10 in 1D.

## 4.4 Conclusion

In this chapter, we have investigated alternative methods to the CFL conditions for the determination of the maximum time step  $\widehat{\Delta t}$  that can be set in a RKDG simulation.

In the case of straight elements, two methods have been derived. The first one is based on a number of assumptions on the behaviour of the maximum amount of dissipation  $\delta$ . These assumptions, that are found to be valid (exactly or approximately) for the structured grids based on set of triangles described in Chap. 3, reduce the stability analysis to a 3-step procedure that is computationally affordable. The second method relies on the equivalence of the time step for each element between the physical space and the reference space through the mapping  $\mathcal{M}^T$ , when the upwind flux is used. Both techniques have been applied to the two examples introduced in Sec. 3.4. With the upwind flux, it was found that the mapping method is beneficial, because it is reliable, accurate, computationally inexpensive and simple to implement. For the Lax-Friedrichs flux, the slight increase in performance brought by the maximum dissipation method compared to appropriate CFL conditions is balanced by its complexity and its computational cost.

With curved elements however, the influence of the element curvature on the conditioning of the semi-discrete operator  $\mathbf{L}$  cannot be decoupled from the polynomial basis  $\mathcal{B}_p^T$ , and it is not possible to isolate a geometrical parameter that properly characterizes the stability restriction. Also, the basic assumptions leading to the two alternative methods with straight elements do not apply to

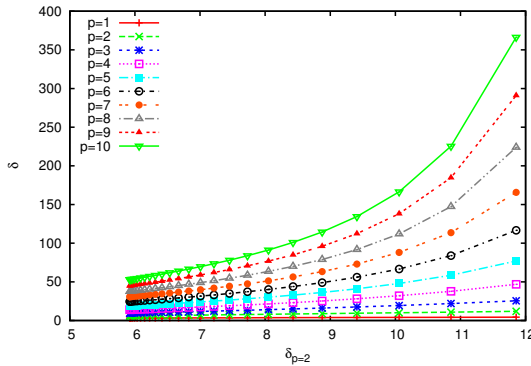


Figure 4.12: Maximum amount of dissipation  $\delta$  at order  $p$  from 1 to 10, as a function of the maximum amount of dissipation  $\delta$  at order  $p = 2$ , in 1D.

elements of higher geometric order. Thus, there has been no success in deriving a simple method that could be used to determine of the maximum time step  $\widehat{\Delta t}$  in practical simulations with curved elements.

## Chapter 5

# Optimized Runge-Kutta Schemes for Wave Propagation Problems

In this chapter, the focus is on the time integration part of the numerical method. The analysis techniques described in Chap. 2 are used to assess the performance of the fully discrete scheme, which is employed in an optimization procedure. Two scenarios, deriving from a global view on computational efficiency, are considered. In the first one, a cost metric involving both stability and accuracy is defined, following the considerations in Ref. [17, 114]. In the second one, stability is favored over accuracy. RK schemes of order  $q$  of 3 and 4 are examined, with a number of stages  $s$  up to  $q + 4$ . One scheme is selected as the best in the first scenario, whereas two are retained in the second one. The  $2N$ -storage coefficients are given for these three RK schemes, and their performance is extensively verified.

### 5.1 Context

In response to the computational challenges raised by CAA and wave propagation problems in general, several authors have devised specially adapted RK schemes. Some of them are presented in Chap. 3. The key idea is to

find the RK coefficients that yield the largest stability limit (thus allowing the largest time steps), the highest accuracy (often expressed in terms of dissipation and dispersion), or a combination of both objectives. Moreover, low-storage formulations [23, 146] reduce the memory requirements of the numerical method.

Carpenter and Kennedy [25] were among the first to propose a  $2N$ -storage scheme, that they optimized with respect to stability. Allampalli et al. [5], Mead and Renault [104] also presented schemes with optimal stability region. Hu et al. [71] devised RK schemes optimized with respect to dissipation and dispersion, for which Stanescu and Habashi [127] gave a  $2N$ -storage implementation. A similar methodology was followed by Berland et al. [15]. Calvo et al. [24], as well as Tselios and Simos [139], optimized their scheme with respect to both stability and accuracy. Finally, Pirozzoli [114] and Bernardini and Pirozzoli [17] introduced a general framework for performance analysis, and derived families of schemes optimized for “temporal resolving efficiency”.

All of these RK integrators were optimized with respect to finite difference methods, except those of Mead and Renault [104] who used pseudo-spectral methods, and those of Bernardini and Pirozzoli [17] that are based on exact spatial discretization. As explained in Sec. 3.2.2, these types of space operators and DG have very different spectral footprints, so that one can expect the RK schemes listed above to be sub-optimal when combined with DG. To our knowledge, no RK method has been specifically designed for DG space operators yet. The work described in this chapter aims at filling this gap, providing RK schemes that maximize the computational efficiency of the RKDG method for linear wave propagation problems.

## 5.2 Computational Efficiency

In order to characterize the performance of the RKDG method for practical problems, it is assumed that general indicators can be derived from the stability and accuracy properties of the 1D numerical method, as described in Sec. 2.2. However, the generalization to multiple spatial dimensions is not straightforward, as seen in Chap. 3.

### 5.2.1 Definition of the Problem

At first sight, it may seem that the issue of computational efficiency is only linked to the maximum time step  $\Delta t^*$  (i.e. to the maximum Courant number  $\nu^*$ )

allowed by the CFL Condition (2.25), because larger  $\Delta t$  imply fewer temporal iterations to reach a given simulated time. However, the perspective can be broadened by considering that the end user has control over the meshing of the computational domain, and that he can exert this control, along with the choice of the scheme, to find the most efficient way to solve the computational problem.

For a wave propagation problem, the question can be described in the following terms: which is the least computationally intensive combination of mesh and numerical method that guarantees the solution to meet a given accuracy requirement over a given frequency range? On one side, one may want to use a numerical scheme that favors stability over accuracy, so that the large number of small elements needed to reach the required accuracy is compensated by the higher Courant number. On the other side, one can use a method that gives priority to accuracy rather than stability, in which case the fewer, larger elements counteract the lower Courant number. Thus, appropriate measures need to be derived in order to quantify the effect of both the mesh and the numerical method on the computational cost and the accuracy.

## 5.2.2 Cost Measure

Following Ref. [17, 114], a cost measure is defined that takes into account the trade-off between stability and accuracy, with the objective to compare and optimize RK schemes. Consider a problem involving a simulated time period of  $T$  and a computational domain of characteristic length  $L$  in  $d$  spatial dimensions. Then the computation time is proportional to the number of stages  $s$  of the RK scheme, to the number  $T/\Delta t$  of time iterations, and to the number of elements in the domain, that varies like  $(L/\Delta x)^d$ :

$$\text{Cost} \propto s \frac{T}{\Delta t} \left( \frac{L}{\Delta x} \right)^d$$

For a given wavenumber  $k$ , this expression can be normalized by dividing by the number of time periods  $Tka/2\pi$  and by the number of wavelengths contained in the domain  $(Lk/2\pi)^d$ :

$$\text{Normalized Cost} \propto s \frac{2\pi}{ka\Delta t} \left( \frac{2\pi}{k\Delta x} \right)^d = s \frac{\Delta x}{a\Delta t} \left( \frac{2\pi}{k\Delta x} \right)^{d+1}$$

Thus, dropping the constant, the normalized cost  $\kappa$  is defined as:

$$\kappa(\nu, k\Delta x) = \frac{s}{\nu (k\Delta x)^{d+1}} \quad (5.1)$$

As explained in Ref. [17], the quantity  $\kappa$  is used to determine in which conditions  $(k\Delta x, \nu)$  a given numerical scheme is most efficient. It is also well-suited to measure the relative computation time of fully discrete schemes based on the same spatial method and different RK time integrators. However, it cannot be used to compare numerical methods based on different spatial schemes (i.e. different orders  $p$  of the DG polynomial approximation), because it does not take into account the difference in cost when evaluating different spatial operators for the same number of elements. The derivation of a cost measure that enables the direct comparison between different orders  $p$  is not necessary for optimizing the RK schemes, therefore it is not addressed in this work.

### 5.2.3 Error Measure

The error  $E_{total}$  derived in Sec. 2.2.2 provides a measure of the dissipation and dispersion introduced by the scheme in one time iteration. However, we need a definition of the error that is independent of the discretization, in order to compare different working conditions  $(k\Delta x, \nu)$  and different RK integrators. Thus, the error introduced by the scheme during the travel of a wave over one wavelength (i.e. during one time period) is computed with:

$$E_{mag} = \left| 10 \log_{10} \left( |E_{total}|^{\frac{2\pi}{\omega\Delta t}} \right) \right|$$

for the dissipation error expressed in dB per wavelength, and:

$$E_{phase} = \frac{2\pi}{\omega\Delta t} \arg(E_{total})$$

for the dispersion error expressed in radians per wavelength.

From Eq. (2.22) and (2.9), one can see that  $\mathbf{L}$  is proportional to  $a$  and  $\Delta x^{-1}$  for fixed  $k\Delta x$ , so that  $\lambda_m \Delta t$  depends only on  $k\Delta x$  and  $\nu$ . As  $\omega\Delta t = k\Delta x \cdot \nu$ , Eq. (2.23) shows that  $E_{total}$ , and thus  $E_{mag}$  and  $E_{phase}$ , depend only on  $k\Delta x$  and  $\nu$ .

## 5.3 Optimized RK Schemes

### 5.3.1 Optimization Objectives

Given the problem posed in Sec. 5.2.1, we look for RK schemes providing the minimal computational cost  $\kappa_{opt}$  for a given error tolerance, as well as the conditions  $(k\Delta x, \nu)_{opt}$  for which this minimal cost is reached. With this, a given physical problem can be solved in the most efficient way by:

- Meshing the computational domain so that the maximum wavenumber of interest  $k_{max}$  satisfies  $k_{max}\Delta x = (k\Delta x)_{opt}$  everywhere. This way, the error tolerance is reached for  $k_{max}$ , and lower wavenumbers are resolved more accurately, as the error increases monotonically with  $k$ .
- Running the simulation with the time step determined by  $\nu_{opt}$ .

In other words, the optimization of the RK scheme affects both the resolution ability (corresponding to  $k\Delta x$ , that could also be expressed in terms of degrees of freedom per wavelength) and the stability limit (corresponding to  $\nu$ ) of the full RKDG scheme, so that a particular combination  $(k\Delta x, \nu)_{opt}$  of  $k\Delta x$  and  $\nu$  minimizes the computational cost  $\kappa$ . In this way, the user obtains the fastest possible simulation that solves his physical problem with a given error tolerance, if he chooses the mesh  $\Delta x$  and time step  $\Delta t$  that match  $(k\Delta x, \nu)_{opt}$ .

As, to our knowledge, dissipation is usually more problematic than dispersion in wave propagation problems of engineering and scientific interest solved with RKDG methods, we seek to optimize RK schemes for a given dissipation requirement.  $E_{mag} = 0.01$  dB per wavelength is chosen as the typical dissipation level required for a practical wave propagation application. For instance, in an acoustic problem, this would correspond to an attenuation of 1 dB in sound intensity at a distance of 5 m from the source for a wave of 3400 Hz. The cost  $\kappa$  is computed for two spatial dimensions ( $d = 2$ ).

This procedure assumes that the user has complete control over the element size, as mentioned in Sec. 5.2.1. However, this is not true for all problems: it can happen that geometrical features of the computational domain constrain the element size locally or globally, to the point that  $(k\Delta x)_{opt}$  corresponds to a much higher frequency than needed. The scheme is then unnecessarily accurate. In this scenario, it is more efficient to use a scheme that favours stability over accuracy, and RK schemes with the highest maximal Courant number per stage  $\nu^*/s$  are sought.

### 5.3.2 Existing RK Schemes

It is interesting to evaluate the performance of RK schemes found in literature with respect to the objectives defined in Sec. 5.3.1, before deriving new ones. Relevant schemes, along with their main characteristics, are listed in Table 5.1. The coefficients  $\gamma_k$  of their amplification factor  $R(z)$  are given in Appendix A.

In the scenario assuming free element size, the performance of RK schemes can be illustrated by plotting the iso-lines of  $E_{mag}$  and  $\kappa$  in the parameter space  $(k\Delta x, \nu)$  [17]. For a given error level, the optimal working conditions

$(k\Delta x, \nu)_{opt}$  are found at the point where the iso- $E_{mag}$  line intersects the “right-most” iso- $\kappa$  line. Such plots are shown for the standard fourth-order RK scheme at  $p = 5$  and for the Carpenter RK scheme at  $p = 10$  in Fig. 5.1. One can see that for error levels of  $E_{mag} = 0.01$  dB per wavelength and greater, the minimal cost is obtained at  $\nu_{opt} = \nu^*$ , because the iso- $E_{mag}$  lines are almost vertical (constant  $k\Delta x$ ). This is due to the fact that the error from the spatial scheme is dominant in this range of accuracy, even at maximal Courant number  $\nu^*$  and high order  $p$ , as illustrated in Fig. 5.2. We verify that  $\nu_{opt} = \nu^*$  for order  $p$  ranging from 1 to 10, and for all RK schemes listed in Table 5.1, except the third-order (3,3)-SSP scheme. Therefore, in Sec. 5.3.3 the new RK schemes are optimized for the minimal cost  $\kappa_{opt}^*$  at maximum Courant number  $\nu^*$ :

$$\kappa_{opt}^* = \min_{k\Delta x} \kappa(k\Delta x, \nu^*)$$

instead of searching for the minimal cost over both  $k\Delta x$  and  $\nu$ , so that the optimization procedure becomes computationally affordable. The efficiency of the different RK schemes from literature is compared for  $p = 1$ ,  $p = 5$  and  $p = 10$  in Fig. 5.3. For high accuracy requirements ( $E_{mag} \leq 0.005$  dB per wavelength), the Tselios DDAS47 and Calvo LDDRK46 schemes are most efficient, whereas the Carpenter and (5,4)-SSP schemes yield a lower cost at lower accuracy ( $E_{mag} \geq 0.01$  dB per wavelength). Both third-order schemes are particularly inefficient at moderate to high accuracy.

Regarding the scenario in which elements are constrained to a small size, the performance of the different RK schemes from literature in terms of maximal Courant number per stage  $\nu^*/s$  is compared in Fig. 5.4. The Carpenter and both SSP schemes yield the best results, whereas the Bernardini ORK37-3

Name	Order	Stages	Storage
Bernardini ORK37-3 [17]	3	7	2N
Calvo LDDRK46 [24]	4	6	2N
Carpenter [25]	4	5	2N
HALE-RK7 [5]	4	7	2N
HALE-RK67 [5]	4	6+7	2N
Hu LDDRK6 [71]	4	6	3N (2N [127])
Hu LDDRK56 [71]	4	5+6	3N (2N [127])
Mead RKC [104]	4	6	5N
Optimal (3,3)-SSP [53]	3	3	3N
Optimal (5,4)-SSP [124]	4	5	5N
Tselios DDAS47 [139]	4	7	2N
Standard	4	4	4N (2N [74])

Table 5.1: RK schemes from literature.



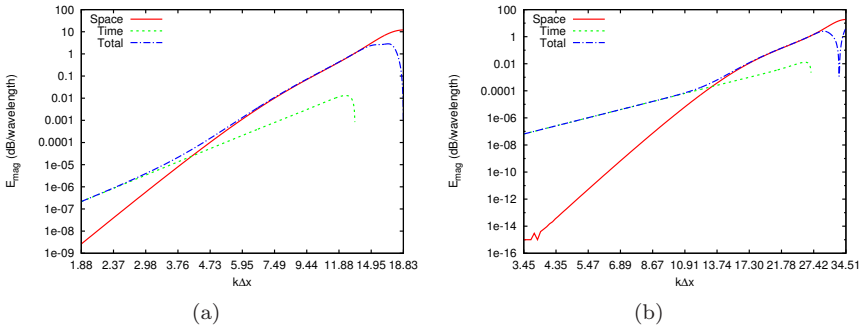


Figure 5.2: Error due to the spatial scheme, the temporal scheme and the fully discrete scheme at  $\nu = \nu^*$  as a function of  $k\Delta x$ : standard fourth-order RK scheme at  $p = 5$  (a) and Carpenter RK scheme at  $p = 10$  (b).

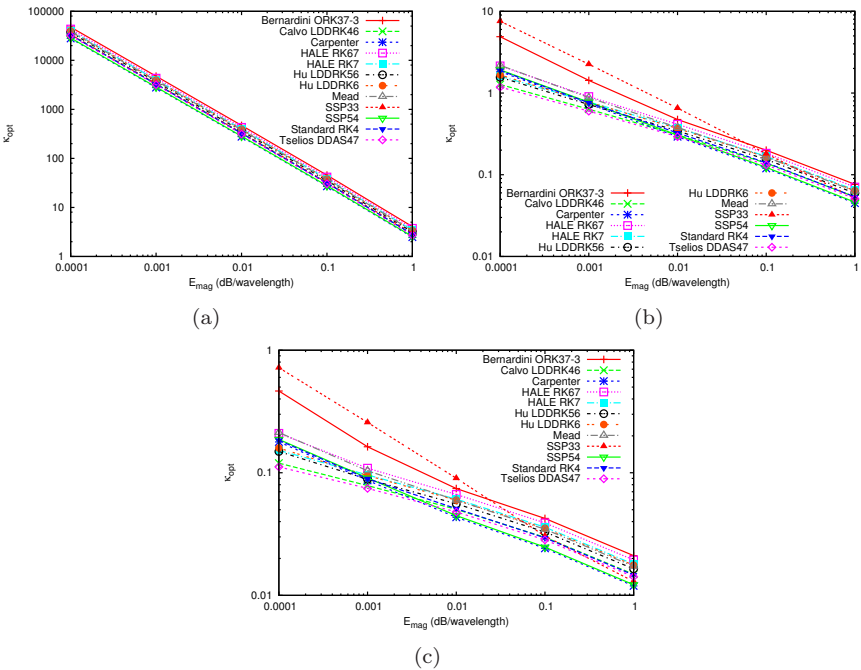


Figure 5.3: Minimal cost  $\kappa_{opt}$  at  $p = 1$  (a),  $p = 5$  (b) and  $p = 10$  (c), as a function of the dissipation error  $E_{mag}$  with all RK schemes listed in Table 5.1.

$a_{ij}$ ,  $b_i$  and  $c_i$  satisfying the definition of  $R(z)$  and the non-linear order conditions is searched for. In this work, only schemes with  $s \leq q + 4$  are investigated, because the cost of the optimization procedure becomes prohibitive for a higher number of free parameters.

The scope of this study is also limited to third- and fourth-order schemes. Indeed, the non-linear order conditions for  $q > 4$  impose  $s > q$ , with constraints on  $\{\gamma_k, k = q + 1 \dots s\}$  [22]. The optimization procedure is then more complicated and costly, because the parameters  $\gamma_k$  cannot be optimized independently of the RK coefficients. Moreover, the reduced freedom for the additional coefficients is less likely to compensate with accuracy and stability the increased computation time implied by additional stages.

Unfortunately, the optimization problem consisting in finding the free parameters  $\{\gamma_k, k = q + 1 \dots s\}$  that result in the minimal cost or in the maximal stability is strongly non-linear, and it is difficult to find a global optimum. In practice, a sufficiently large region in the space of parameters  $\{\gamma_k, k = q + 1 \dots s\}$  is sampled, the objective function is evaluated for each of the sampled points, and the best few points are used as initial guesses for a sequential quadratic programming routine.

### “Free Element Size” Scenario

We first consider the “free element size” scenario, and search for the parameters  $\gamma_k$  that yield the lowest cost  $\kappa_{opt}^*$  for an error of  $E_{mag} = 0.01$  dB per wavelength (typical dissipation requirement), with each  $s$ -stage scheme of order  $q$ . In practice, the evaluation of  $\kappa_{opt}^*$  for given parameters  $\gamma_k$  is performed by first

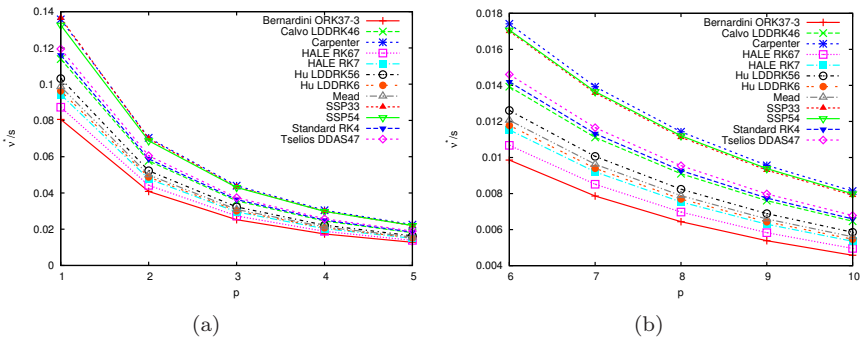


Figure 5.4: Maximal Courant number per stage  $v^*/s$  for  $p = 1 \dots 5$  (a) and for  $p = 6 \dots 10$  (b) with all RK schemes listed in Table 5.1.

determining the maximum time step  $\Delta t^*$  by the bisection method described in Sec. 2.2.3, then using Eq. (2.23) with  $\Delta t = \Delta t^*$  to find the value  $k = k_{opt}$  yielding  $E_{mag} = 0.01$  dB per wavelength, and finally calculating  $\kappa_{opt}^*$  from  $\nu^*$  and  $(k\Delta x)_{opt}$  with Eq. (5.1). As the DG operator depends on the order  $p$  of the polynomial approximation, the optimization is performed for each value of  $p$  ranging from 1 to 10 individually. The resulting RK schemes are referred to with the generic nomenclature  $RKFsqPp$ .

For each pair  $(s, q)$ , we notice that the parameters  $\gamma_k$  for schemes  $RKFsqP2$  to  $RKFsqP10$  are very similar,  $RKFsqP1$  being the only scheme deviating. For the sake of presenting RK schemes that are useful over a large range of orders  $p$ , and considering that the DG method is of limited interest at order  $p = 1$ , the  $RKFsq$  schemes are derived by optimizing the parameters  $\gamma_k$  for the minimal mean relative cost over the range  $p = 2 \dots 10$ , using the objective function:

$$\text{Obj}_{RKFsq} = \frac{1}{9} \sum_{p=2}^{10} \left( \frac{\kappa_{opt,RKFsq}^*}{\kappa_{opt,RKFsqPp}^*} - 1 \right)$$

Table 5.2 shows that the  $RKFsq$  schemes are close to the optimal  $RKFsqPp$  schemes for order  $p$  between 2 and 10, with a mean difference of 3% at most. The absolute performance of these schemes in terms of  $\kappa_{opt}^*$  is summarized in Table 5.3. The  $RKF84$  scheme is the most efficient for all values of the order  $p$ , and is selected as the scheme of choice in this scenario. Practical information needed to use this scheme, like the working conditions and corresponding performance for different dissipation error requirements, is given in Appendix C.1.

$p \setminus sq$	43	53	63	73	54	64	74	84
1	7.8	0.7	13.0	25.6	0.6	6.0	9.2	8.2
2	0.0	0.4	2.4	2.6	0.4	2.5	2.4	2.4
3	0.0	0.0	0.1	3.1	0.0	0.0	0.9	3.1
4	0.0	0.4	1.0	4.0	0.3	0.8	0.6	3.4
5	0.0	0.5	1.1	2.6	0.4	0.9	0.3	2.9
6	0.0	0.2	0.6	1.2	0.2	0.5	0.2	2.8
7	0.0	0.1	0.2	0.4	0.0	0.1	0.1	2.7
8	0.0	0.0	0.1	0.2	0.0	0.0	0.0	2.7
9	0.0	0.2	0.4	0.5	0.2	0.4	0.2	2.5
10	0.0	0.4	1.0	0.8	0.5	1.1	0.4	1.8
Mean	0.0	0.2	0.8	1.7	0.2	0.7	0.6	2.7

Table 5.2: Relative difference in  $\kappa_{opt}^*$  (%) between  $RKFsq$  and  $RKFsqPp$  schemes for all values of the order  $p$ , and mean over the range  $p = 2 \dots 10$ .

### “Constrained Element Size” Scenario

In the “constrained element size” scenario, the parameters  $\gamma_k$  that yield the largest maximal Courant number per stage  $\nu^*/s$  are searched for. As in the “free element size” scenario, optimal  $s$ -stage RK schemes of order  $q$ , called  $\text{RKC}_{sq}Pp$ , are first derived for each value of  $p$  individually. Then, considering that these schemes are very similar for all values of the order ( $p = 1 \dots 10$ ), the  $\text{RKC}_{sq}$  schemes that are optimal in average over the range of order  $p = 1 \dots 10$  are obtained by minimizing the objective function:

$$\text{Obj}_{\text{RKC}_{sq}} = \frac{1}{10} \sum_{p=1}^{10} \left( 1 - \frac{\nu_{\text{RKC}_{sq}}^*}{\nu_{\text{RKC}_{sq}Pp}^*} \right)$$

One can see in Table 5.4 that the  $\text{RKC}_{sq}$  schemes perform nearly optimally over the whole range of order  $p$ , the mean difference with  $\text{RKC}_{sq}Pp$  schemes being 2% at most. The maximum Courant number per stage  $\nu^*/s$  is summarized in Table 5.5. Here, third order schemes are generally more efficient than fourth-order schemes, above all for lower order  $p$ . However, as shown in Sec. 5.3.3, third-order schemes achieve this high stability limit at the expense of much lower accuracy, thus they become computationally interesting only for very small element sizes. Therefore, both  $\text{RKC}73$  and  $\text{RKC}84$  are selected as schemes of interest in this scenario. Practical information on these schemes is reported in Appendices C.2 and C.3.

$p \setminus sq$	43	53	63	73	54	64	74	84
1	32370	27750	27110	26580	27770	27170	26480	25140
2	920.3	786.7	750.4	719.7	787.1	751.2	718.2	690.9
3	178.2	154.7	143.1	132.5	154.6	143	132.8	129.1
4	65.53	57.34	52.27	47.48	57.31	52.19	47.71	46.62
5	32.45	28.41	25.82	23.32	28.4	25.77	23.45	22.89
6	19.03	16.6	15.13	13.7	16.59	15.11	13.75	13.4
7	12.45	10.79	9.896	9.000	10.79	9.889	9.023	8.772
8	8.785	7.562	6.983	6.396	7.562	6.982	6.391	6.194
9	6.551	5.604	5.208	4.808	5.606	5.209	4.797	4.622
10	5.094	4.333	4.049	3.764	4.336	4.052	3.75	3.596

Table 5.3: Cost  $\kappa_{opt}^* \times 100$  of  $\text{RKF}_{sq}$  schemes for all values of the order  $p$ .

### Performance of Optimized Schemes

Considering the “free element size” scenario, Fig. 5.5 shows the minimal cost  $\kappa_{opt}$  and minimal cost at maximum Courant number  $\kappa_{opt}^*$  for the optimized schemes. For the RKF84 scheme, the minimal cost is obtained at maximum Courant number in almost all the range of accuracy considered, which justifies a posteriori the idea of optimizing the scheme for  $\kappa_{opt}^*$  instead of  $\kappa_{opt}$ . For the RKC73 however,  $\kappa_{opt}$  is lower than  $\kappa_{opt}^*$  in most of the accuracy range considered. This is due to the inaccuracy of the RKC73 scheme that overwhelms the error due to the spatial discretization, as explained in Sec. 5.3.2. Fig. 5.6 compares the three optimized schemes with the Carpenter and Tselios

$p \setminus sq$	43	53	63	73	54	64	74	84
1	0.0	-2.9	-3.8	-4.3	-0.3	-2.3	-3.9	-3.2
2	0.0	-2.1	-3.2	-4.2	-0.1	-1.7	-3.3	-3.1
3	0.0	-1.5	-2.2	-2.8	0.0	-1.1	-2.3	-1.8
4	0.0	-1.0	-1.3	-1.5	0.0	-0.8	-1.5	-0.5
5	0.0	-0.7	-0.6	-0.4	0.0	-0.5	-0.9	-0.6
6	0.0	-0.4	0.0	-0.5	0.0	-0.3	-0.4	-1.3
7	0.0	-0.2	-0.5	-1.0	0.0	-0.2	0.0	-1.6
8	0.0	0.0	-1.0	-1.4	0.0	-0.1	-0.5	-2.1
9	0.0	-0.3	-1.3	-1.7	0.0	-0.4	-0.8	-2.5
10	0.0	-0.6	-1.6	-2.2	0.0	-0.6	-1.2	-2.6
Mean	0.0	-1.0	-1.6	-2.0	-0.1	-0.8	-1.5	-1.9

Table 5.4: Relative difference in  $\nu^*/s$  (%) between RKC $sq$  and RKC $sqPp$  schemes for all values of the order  $p$ , and mean over the range  $p = 1 \dots 10$ .

$p \setminus sq$	43	53	63	73	54	64	74	84
1	15.23	16.31	17.17	17.82	13.58	14.33	14.94	15.71
2	7.898	8.479	8.886	9.152	7.042	7.447	7.73	8.077
3	4.949	5.362	5.658	5.855	4.401	4.713	4.923	5.165
4	3.436	3.75	3.984	4.149	3.047	3.296	3.466	3.659
5	2.545	2.794	2.985	3.125	2.252	2.454	2.596	2.721
6	1.972	2.174	2.334	2.43	1.742	1.908	2.028	2.104
7	1.579	1.747	1.864	1.944	1.393	1.532	1.635	1.683
8	1.297	1.44	1.527	1.595	1.142	1.261	1.34	1.381
9	1.087	1.203	1.278	1.335	0.9564	1.054	1.12	1.156
10	0.9258	1.023	1.087	1.135	0.8139	0.8958	0.9527	0.984

Table 5.5: Maximum Courant number per stage  $\nu^*/s \times 100$  of RKC $sq$  schemes for all values of the order  $p$ .

DDAS47 schemes in terms of  $\kappa_{opt}$ , and shows that the RKC73 becomes less interesting with higher accuracy requirement. The RKF84 scheme is the most efficient in a broad range of error level, although it was optimized specifically for  $E_{mag} = 0.01$  dB per wavelength. The RKC84 scheme lies in between and is globally as effective as the Carpenter scheme. Table 5.6 shows that the RKF84 scheme outperforms the RKC84, Carpenter and Tselios DDAS47 schemes by 22% to 29% for an error of  $E_{mag} = 0.01$  dB per wavelength, while the RKC73 is about twice as expensive computationally.

In the scenario assuming a constrained, small element size, Fig. 5.7 shows the maximal Courant number per stage  $\nu^*/s$  for the optimized and Carpenter RK schemes. The RKC73 is clearly the most efficient scheme, while the RKC84, RKF84 and Carpenter schemes are respectively about 13%, 17% and 27% less efficient, as reported in Table 5.7. Fig. 5.8 compares the stability region of these RK schemes with that of the standard RK4 scheme. The stability region of optimized schemes is much more extended along the real axis, as expected from the observations in Sec. 5.3.2.

In summary, the best scheme from literature is about 22% less efficient than the RKF84 scheme for  $E_{mag} = 0.01$  dB per wavelength in the “free element size” scenario, and about 27% and 16% less efficient than the RKC73 and RKC84 schemes respectively in the “constrained element size” scenario. Yet, in order to make the most of the optimized RK schemes, it is necessary to know where the border between both scenarios lies, that is, which of the three schemes is the most efficient for a given element size constraint  $k\Delta x \leq (k\Delta x)_{max}$ . Obviously, for  $(k\Delta x)_{max} \geq (k\Delta x)_{opt,RKF84}$ , the constraint is not restrictive, so that the most efficient scheme is the RKF84 used in optimal working conditions, as in the “free element size” scenario. For  $(k\Delta x)_{max} < (k\Delta x)_{opt,RKF84}$ , i.e. in over-accurate conditions, the most efficient scheme is the one that allows the largest Courant number per stage  $\nu/s$  while fulfilling the accuracy requirement. The choice of the most efficient scheme in function of  $(k\Delta x)_{max}$  can be made by means of Fig. C.1. For low accuracy requirements, the RKC73 scheme is the best over a large range of  $(k\Delta x)_{max}$ . For higher accuracy requirements, the RKC73 scheme becomes useful only for the most restrictive element size constraints, and the choice of the RKC84 scheme is justified for a large range of higher values of  $(k\Delta x)_{max}$ . When very high accuracy is required, there is even a significant range of constraints for which the RKF84 scheme is the most efficient, although it was not optimized to work in over-accurate conditions.

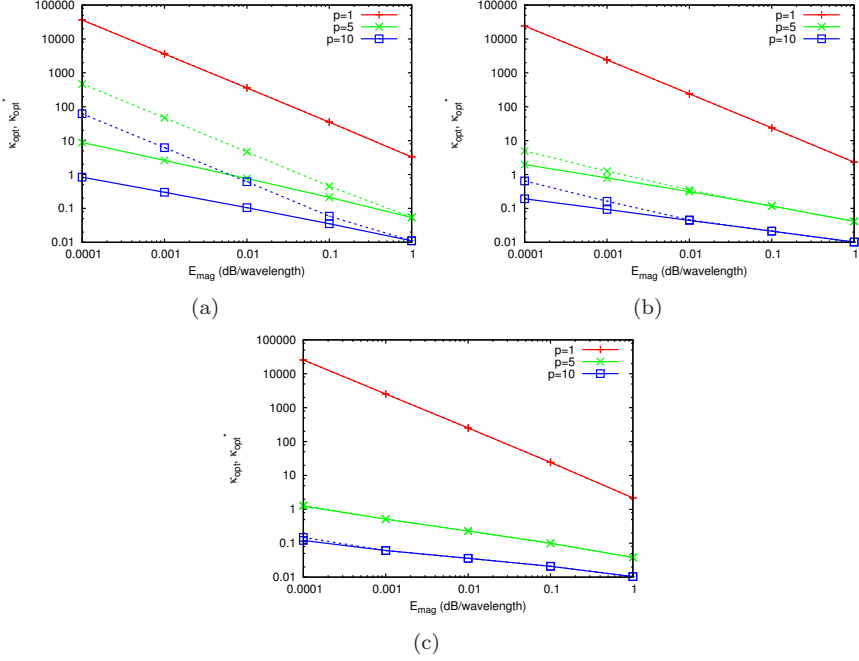


Figure 5.5: Minimal cost  $\kappa_{opt}$  (solid line) and minimal cost at maximum Courant number  $\kappa_{opt}^*$  (dotted line) for  $p = 1$ ,  $p = 5$  and  $p = 10$ , with the RKC73 (a), RKC84 (b) and RKF84 (c) schemes, as a function of the dissipation error  $E_{mag}$ .

$p$	Carpenter	Tselios DDAS47	RKC73	RKC84
1	10.2	25.0	42.3	-4.5
2	14.1	26.4	166.5	7.8
3	21.8	26.8	216.0	26.6
4	26.2	27.0	230.6	34.4
5	27.7	28.0	232.3	36.5
6	27.0	29.1	227.6	35.6
7	25.4	30.3	219.9	33.2
8	23.6	31.4	211.1	30.1
9	22.0	32.4	201.6	26.7
10	20.5	33.3	192.0	23.1
Mean	21.9	29.0	194.0	25.0

Table 5.6: Relative difference in  $\kappa_{opt}$  (%) of optimized RKC, Carpenter and Tselios DDAS47 RK schemes with respect to the RKF84 scheme at  $E_{mag} = 0.01$ : values for order  $p$  from 1 to 10, and mean over the range  $p = 1 \dots 10$ .

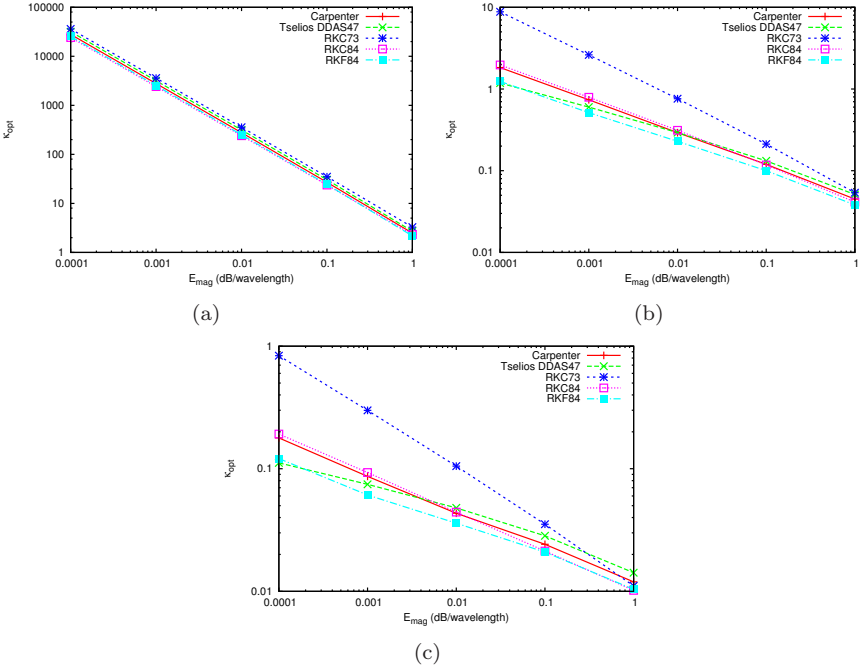


Figure 5.6: Minimal cost  $\kappa_{opt}$  at  $p = 1$  (a),  $p = 5$  (b) and  $p = 10$  (c), as a function of the dissipation error  $E_{mag}$  with optimized RK schemes, as well as Carpenter and Tselios DDAS47 schemes.

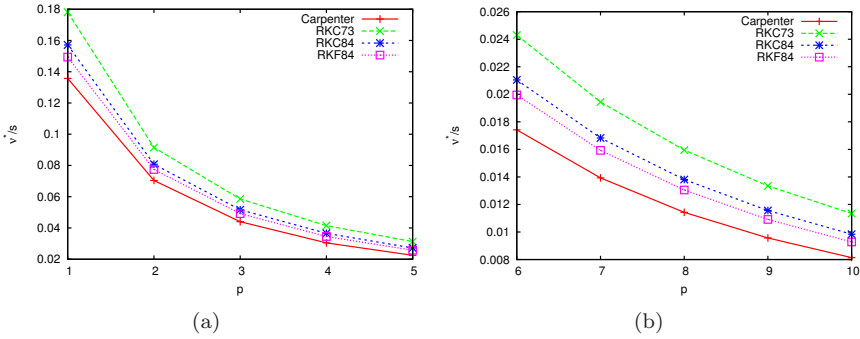


Figure 5.7: Maximal Courant number per stage  $\nu^*/s$  for  $p = 1 \dots 5$  (a) and for  $p = 6 \dots 10$  (b) with the optimized and Carpenter RK schemes.

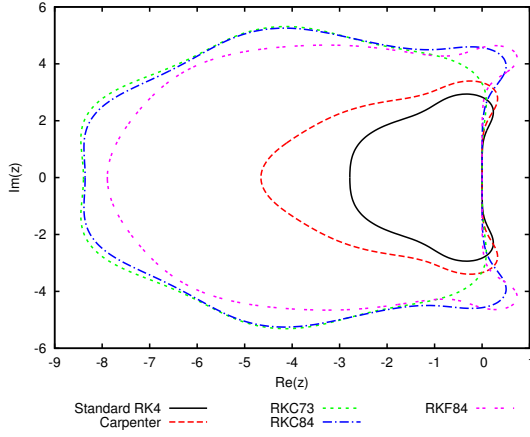


Figure 5.8: Stability regions for the Standard RK4 scheme, for the Carpenter scheme and for the optimized RK schemes.

$p$	Carpenter	RKC84	RKF84
1	-23.8	-11.8	-16.2
2	-23.1	-11.7	-15.4
3	-24.8	-11.8	-15.9
4	-26.6	-11.8	-16.8
5	-27.9	-13.0	-17.6
6	-28.3	-13.4	-17.9
7	-28.3	-13.4	-18.1
8	-28.4	-13.4	-18.2
9	-28.3	-13.4	-18.3
10	-28.3	-13.3	-18.2
Mean	-26.8	-12.7	-17.2

Table 5.7: Relative difference in  $\nu^*/s$  (%) of RKF84, RKC84 and Carpenter RK schemes with respect to the RKC73 scheme for order  $p$  from 1 to 10, and mean over the range  $p = 1 \dots 10$ .

## Low-Storage Coefficients

The results obtained in this section show that with proper optimization, adding stages can improve the efficiency of RK schemes in terms of computational time. However, the classical RK formulation of Eq. (2.14) can lead to large memory consumption due to the  $sN$  storage requirement, as mentioned in Sec. 2.1.2. Therefore, the coefficients of the RKF84, RKC73 and RKC84 schemes are sought in the  $2N$ -storage formulation of Williamson [146]:

$$d\mathbf{q}^{(i)} = A_i d\mathbf{q}^{(i-1)} + \Delta t \mathbf{L} \left( t_n + c_i \Delta t, \mathbf{q}^{(i-1)} \right)$$

$$\mathbf{q}^{(i)} = \mathbf{q}^{(i-1)} + B_i d\mathbf{q}^{(i)}, \quad i = 1 \dots s$$

with  $A_1 = 0$ , as explicit, self-starting schemes are considered. The link between the  $2N$ -storage coefficients  $A_i$  and  $B_i$  and the classical coefficients  $a_{ij}$ ,  $b_i$  and  $c_i$  is given by the recurrence relation [146]:

$$\begin{aligned} B_i &= a_{i+1,i}, & i &= 1 \dots s-1 \\ B_s &= b_s \\ A_i &= \frac{b_{i-1} - B_{i-1}}{b_i}, & i &= 2 \dots s, b_j \neq 0 \\ A_i &= \frac{a_{i+1,i-1} - c_i}{B_i}, & i &= 2 \dots s, b_j = 0 \end{aligned} \quad (5.2)$$

Eq. (5.2) is used in a numerical procedure to solve the system in Eq. (2.17), along with the non-linear order conditions in Eq. (2.15) and (2.16), directly for  $A_i$  and  $B_i$ . The system is under-determined, and a solution with increasing  $c_i$  is chosen. The coefficients for the RKF84, RKC73 and RKC84 schemes are given in Tables C.1, C.7 and C.13 respectively.

## 5.4 Examples

### 5.4.1 2D Advection Test

The first application of the optimized RK schemes consists in a 2D advection case, in which a square domain of side length 10 with periodic boundary conditions is discretized with structured triangular meshes, as illustrated in Fig. 5.9. An initial harmonic wave of wavelength 2 is convected in the  $y$ -direction during time 100 at a velocity of 1, so that at the final time, the exact

solution is equal to the initial solution. The numerical solution can then be compared to the exact solution by computing the  $L_2$  error:

$$\text{Err} = \frac{\|\mathbf{q}_{end} - \mathbf{q}_{init}\|_2}{N}$$

where  $\mathbf{q}$  is the vector of all unknowns, as in Eq. (2.10), and  $N$  is the number of unknowns. The order of the DG polynomial basis is set to  $p = 6$ , and simulations are carried out at maximum Courant number with grid resolutions from  $3 \times 3$  elements to  $10 \times 10$  elements, corresponding to  $3.14 \leq k\Delta x \leq 10.5$ . A comparison of the efficiency (in terms of  $L_2$  error and CPU time) between the schemes derived in Sec. 5.3.3 and three other  $2N$ -storage RK integrators is shown in Fig. 5.10. The RKC73 scheme is interesting only for very low accuracy. For moderate accuracy, the RKC84 scheme is the most efficient one, and the RKF84 scheme dominates for higher accuracy, in accordance with the results of Sec. 5.3.3.

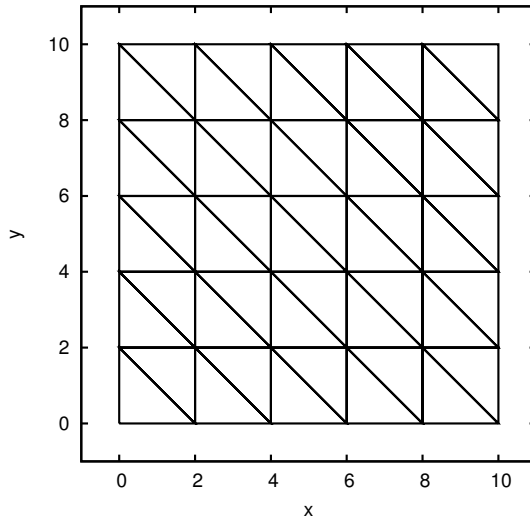


Figure 5.9: Example of a mesh used for the 2D advection test.

## 5.4.2 Acoustic Properties of an Elliptical Muffler

The second example, taken from Part III, is an acoustic problem featuring an elliptical muffler with square inlet and outlet ducts. The Euler equations linearized about a quiescent mean flow, equivalent to the acoustic wave equation (see Chap. 6), are used to compute the transmission loss. The case, as well as

the methodology to compute the transmission loss, are described in detail in Sec. 7.3.4.

Considering a maximum frequency of  $f_{max} = 3000$  Hz, waves travel at most over about 220 wavelengths until the final simulation time is reached. For an accuracy of 1 dB in transmission loss, that corresponds to a maximum attenuation of 0.5 dB in wave amplitude at final time, the requirement on the dissipation error is then approximately  $E_{mag} = 0.002$  dB per wavelength.

When meshing the computational domain, the size of the elements is severely constrained by the confined nature of the problem, and by the necessity of correctly representing the curved boundaries. Two different unstructured, tetrahedral meshes are used. The first one, named Grid 1 in Sec. 7.3.4, is made as coarse as possible (199 elements) by using curved tetrahedra to model the elliptic chamber (see Chap. 7). The order of the DG polynomial basis is set to  $p = 5$  for computations with this grid. The second mesh, called Grid 4 in Sec. 7.3.4, is only made up of straight elements, so that it has to be finer (1322 elements) to correctly represent the curved geometry, and a polynomial order of  $p = 4$  is sufficient.

Using the inradius of the tetrahedron as element size, we estimate  $(k\Delta x)_{max} = 0.25$  and  $(k\Delta x)_{max} = 0.16$  for the smallest elements of grids 1 and 4 respectively. Based on these values, Fig. C.1(d) suggests that the RKC73 and RKC84 schemes are more efficient than the RKF84 scheme. For the largest elements of grids 1 and 4,  $(k\Delta x)_{max} = 1$  and  $(k\Delta x)_{max} = 0.75$  respectively, and Table C.11 show that the RKC73 and RKC84 schemes could be accurate enough in the whole domain at maximum Courant number.

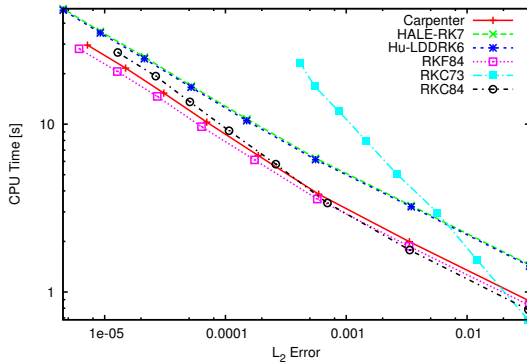


Figure 5.10: Comparison of the CPU time as a function of the  $L_2$  error between the optimized RK schemes and three other RK integrators for the 2D advection test.

Simulations are performed with the three optimized schemes, as well as four other RK schemes using Williamson's 2N-storage formulation (namely, the Carpenter, HALE-RK7, Hu LDDRK6 and (3,3)-SSP schemes). The results in terms of transmission loss, shown in Fig. 5.11, are practically equal for all RK schemes on the same grid. Tables 5.8 and 5.9 contain the maximum time step, determined by trial-and-error, and the corresponding CPU time, for each grid respectively. With the fine grid 4, the RKC73 is clearly the fastest scheme, and the RKC84, RKF84 and Carpenter schemes are respectively 10%, 15% and 24% slower. With the coarse grid 1, the RKC84 scheme is the fastest, while the RKF84 and Carpenter schemes are almost as efficient (+4% and +6% CPU time respectively). The surprisingly low performance of the RKC73 scheme with grid 1 (+12% CPU time with respect to the RKC84 scheme) could be explained by the fact that the element curvature affects the spectral footprint of the DG space operator, which would not fit the stability region of this particular RK scheme as well as with straight elements. This effect is more thoroughly investigated in Chap. 4.

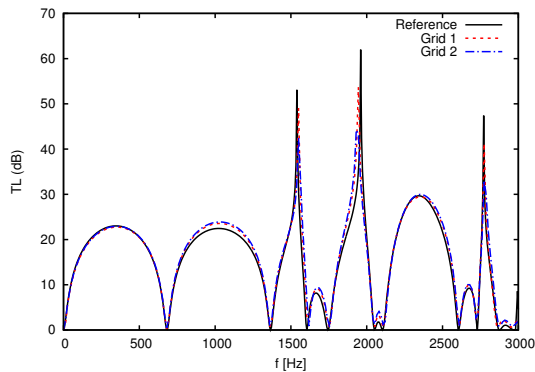


Figure 5.11: Transmission loss obtained from the reference solution and from the simulations for the muffler case. As the results for the different RK schemes tested are undistinguishable, they are all represented by the same dashed line.

## 5.5 Conclusion

In this chapter, the performance of methods of lines combining DG spatial schemes with explicit RK time integrators has been studied, in order to derive optimal RK methods. The issue of computational efficiency has been tackled from the point of view of the user, who aims to use the combination of mesh and numerical method that solves in the shortest time a given physical problem with

a given accuracy requirement. Classical 1D stability and accuracy analysis has been applied to define objective error and computational cost measures, that make it possible to compare and optimize fully discrete RKDG schemes based on different RK integrators for DG spatial schemes of same polynomial order  $p$ .

Two scenarios have been considered. In the first one, the user has total control over the element size, so that the computation cost depends on both accuracy and stability limit. In the second one, the element size is constrained by the geometry of the computational domain, so that the scheme is assumed to work in over-accurate conditions, and the efficiency depends only on stability. In each case, relevant RK schemes from literature have been assessed. Then optimal RK schemes of order  $q$  from 3 to 4 and number of stages  $s$  up to  $q+4$  have been derived, and the performance of the best ones has been thoroughly analyzed.

In the first scenario, it was found that the error is dominated by the DG spatial scheme for most of the RK schemes in literature, even at maximum Courant

RK Scheme	$\Delta t$	CPU Time
Carpenter	0.00124	41 min 28 s (+6%)
HALE-RK7	0.00106	1 h 7 min 43 s (+73%)
Hu LDDRK6	0.00092	1 h 6 min 53 s (+71%)
(3,3)-SSP	0.00067	45 min 59 s (+17%)
RKF84	0.00202	40 min 39 s (+4%)
RKC73	0.00165	43 min 47 s (+12%)
RKC84	0.0021	39 min 8 s

Table 5.8: Time step and CPU time for the 3D muffler case with the optimized and other 2N-storage RK schemes on grid 1. The relative difference in CPU time with respect to the best RK scheme (RKC84) is shown in brackets.

RK Scheme	$\Delta t$	CPU Time
Carpenter	0.00105	3 h 5 min 15 s (+24%)
HALE-RK7	0.000897	5 h 3 min 49 s (+103%)
Hu LDDRK6	0.000786	4 h 56 min 34 s (+98%)
(3,3)-SSP	0.00057	3 h 24 min 49 s (+37%)
RKF84	0.00179	2 h 52 min 36 s (+15%)
RKC73	0.00181	2 h 29 min 47 s
RKC84	0.00189	2 h 44 min 52 s (+10%)

Table 5.9: Time step and CPU time for the 3D muffler case with the optimized and other 2N-storage RK schemes on grid 4. The relative difference in CPU time with respect to the best RK scheme (RKC73) is shown in brackets.

number. Therefore, the new RK schemes have been obtained by minimizing the cost at maximum Courant number, which makes the optimization procedure computationally affordable. The new 8-stage, fourth-order scheme, called RKF84, has been selected as the most efficient. It brings a mean improvement in computational cost of about 22% over the best scheme from literature, for a dissipation error requirement of 0.01 dB per wavelength. In the second scenario, it was found that the 7-stage, third-order scheme, called RKC73, is most efficient, with a mean improvement of 27% over literature. However, it achieves a high stability limit at the expense of a great accuracy loss, which limits its interest to very small element size restrictions. Therefore, we have also retained the 8-stage, fourth-order RKC84 scheme, that is less efficient for small element size restrictions, but is accurate enough to be beneficial with larger element size.

Finally, the coefficients for a 2N-storage implementation of the RKF84, RKC73 and RKC84 schemes have been provided, as well as the information needed by users to correctly employ them. Their benefits have been demonstrated in two examples involving respectively a 2D advection test and the acoustic characterization of an elliptical muffler. However, extrapolating the theoretical performance of these RK schemes in 1D to arbitrary, multi-dimensional problems is not straightforward, above all when curved meshes are involved.

Although the new RK schemes devised in this chapter have a beneficial impact on the performance of RKDG methods on their own, they could also be combined with other techniques such as implicit-explicit (IMEX) time integration, local timestepping, or non-uniform polynomial order over the computational domain, in order to further increase the computational efficiency.

## **Part III**

# **RKDG Methods for Aeroacoustics**



## Chapter 6

# RKDG Methods Applied to Aeroacoustics

This chapter presents the application of the numerical method described in Chap. 2 to linear aeroacoustics. We first introduce the continuous equations governing the physical phenomena to be modeled, namely the Linearized Euler Equations (LEE) and the Linearized Navier-Stokes Equations (LNSE). The decomposition of these hyperbolic equations into characteristic variables, which plays a role in the numerical method, is also explained. Then, the specifics of the RKDG method applied to the LEE and LNSE are discussed, with the formulation of the discrete problem along with the corresponding boundary conditions. Practical difficulties related to the issue of high-order interpolation, that impact the fidelity and the stability of the simulations, are also considered. Finally, we describe how the numerical method is implemented and how the different aspects of the code are verified.

### 6.1 Linear Equations in Aeroacoustics

This section deals with the derivation of the equations that govern linear aeroacoustic phenomena. In the literature, the main interest for linear aeroacoustics is the propagation of sound in non-uniform flows, including effects like convected propagation and refraction. However, the governing equations presented here also model the evolution of other kind of perturbations than

acoustic waves, as explained in Sec. 6.1.2. Thus, they can be used to study phenomena of linear sound generation resulting from the interaction of these different modes, as in Chap. 8, in addition to the mere acoustic propagation.

## 6.1.1 Linearized Euler and Navier-Stokes Equations

### Linearization of the Navier-Stokes Equations

The most general case, a flow not subject to body forces nor external heat source is governed by the Navier-Stokes equations:

$$\frac{\partial \rho}{\partial t} + \nabla \cdot (\rho \mathbf{u}) = 0 \quad (6.1)$$

$$\frac{\partial(\rho \mathbf{u})}{\partial t} + \nabla \cdot (\rho \mathbf{u} \otimes \mathbf{u}) + \nabla p - \nabla \cdot \boldsymbol{\tau} = 0 \quad (6.2)$$

$$\frac{\partial(\rho e)}{\partial t} + \nabla \cdot [(\rho e + p) \mathbf{u}] - \nabla \cdot (\boldsymbol{\tau} \cdot \mathbf{u}) = 0 \quad (6.3)$$

where  $\rho$  is the density,  $\mathbf{u}$  is the velocity vector,  $p$  is the pressure,  $e$  is the specific energy, and  $\boldsymbol{\tau}$  is the viscous stress tensor expressed as:

$$\boldsymbol{\tau} = \mu \left[ \nabla \otimes \mathbf{u} + (\nabla \otimes \mathbf{u})^T \right] + \lambda (\nabla \cdot \mathbf{u}) \mathbf{I} \quad (6.4)$$

with the dynamic viscosity  $\mu$  and the coefficient  $\lambda$  being linked by Stokes' hypothesis  $2\mu + 3\lambda = 0$ . Decomposing the total energy  $e$  into internal and kinetic energy, and using the ideal gas law as equation of state, yields:

$$\rho e = \frac{p}{\gamma - 1} + \frac{1}{2} \rho \mathbf{u} \cdot \mathbf{u}$$

where  $\gamma$  is the ratio of specific heats. The energy equation can then be replaced with a pressure equation through the combination (6.3) -  $\mathbf{u} \cdot$  (6.2) +  $1/2 (\mathbf{u} \cdot \mathbf{u})$  (6.1):

$$\frac{\partial p}{\partial t} + \gamma p \nabla \cdot \mathbf{u} + \mathbf{u} \cdot \nabla p - (\gamma - 1) \boldsymbol{\tau} : (\nabla \otimes \mathbf{u}) = 0 \quad (6.5)$$

While the Navier-Stokes equations (6.1), (6.2) and (6.5) model all possible phenomena encountered in aerodynamics, their numerical treatment is computationally very intensive, mainly because of the non-linear terms. As explained in Chap. 1, the small amplitude of acoustic perturbations can be exploited to

derive a linearized version of the governing equations, that is computationally less demanding.

It is assumed that each variable ( $\rho$ ,  $\mathbf{u}$  and  $p$ ) can be decomposed into the sum of a time-averaged quantity and a smaller unsteady quantity [37]:  $(\cdot) = (\cdot)_0 + (\cdot)'$ . The linearization can be performed in different ways, that come down to equivalent formulations at first order [20].

### The Linearized Euler Equations

In most problems of sound propagation, the viscous effects can be neglected. In this case, the Navier-Stokes equations are reduced to the Euler equations, and their linearization yields the LEE. In this work, we use the conservative form of the LEE [20], that is the most relevant for discretization by the DG method. Using Cartesian coordinates and dropping the prime for the perturbation variables, they can be expressed as:

$$\frac{\partial \rho}{\partial t} + \frac{\partial}{\partial x_r} (\rho_0 u_r + \rho u_{0r}) = S_{dens} \quad (6.6)$$

$$\frac{\partial(\rho_0 u_s)}{\partial t} + \frac{\partial}{\partial x_r} (\rho_0 u_s u_{0r} + p) + (\rho_0 u_r + \rho u_{0r}) \frac{\partial u_{0s}}{\partial x_r} = S_{mom,s} \quad (6.7)$$

$$\frac{\partial p}{\partial t} + \frac{\partial}{\partial x_r} (\gamma p_0 u_r + p u_{0r}) + (\gamma - 1) \left( p \frac{\partial u_{0r}}{\partial x_r} - u_r \frac{\partial p_0}{\partial x_r} \right) = S_{press} \quad (6.8)$$

where  $s = 1 \dots 3$  for the momentum equations (6.7), and Einstein's summation convention is used over the index  $r$ . The system is excited by the source terms  $S$  in the right-hand side. In case the LEE are used to model the propagation of the sound generated by non-linear phenomena, the sources  $S$  are calculated as an approximation of the non-linear terms of the full Navier-Stokes equations. The LEE can be reformulated in matrix notation:

$$\frac{\partial \mathbf{q}}{\partial t} + \frac{\partial \mathbf{A}_r \mathbf{q}}{\partial x_r} + \mathbf{C} \mathbf{q} = \mathbf{S} \quad (6.9)$$

with

$$\mathbf{q} = \begin{bmatrix} \rho \\ \rho_0 u_1 \\ \rho_0 u_2 \\ \rho_0 u_3 \\ p \end{bmatrix}$$

$$\mathbf{A}_r = \begin{bmatrix} u_{0r} & \delta_{1r} & \delta_{2r} & \delta_{3r} & 0 \\ 0 & u_{0r} & 0 & 0 & \delta_{1r} \\ 0 & 0 & u_{0r} & 0 & \delta_{2r} \\ 0 & 0 & 0 & u_{0r} & \delta_{3r} \\ 0 & c_0^2 \delta_{1r} & c_0^2 \delta_{2r} & c_0^2 \delta_{3r} & u_{0r} \end{bmatrix}$$

$$\mathbf{C} = \begin{bmatrix} 0 & 0 & 0 & 0 & 0 \\ u_{0r} \frac{\partial u_{01}}{\partial x_r} & \frac{\partial u_{01}}{\partial x_1} & \frac{\partial u_{01}}{\partial x_2} & \frac{\partial u_{01}}{\partial x_3} & 0 \\ u_{0r} \frac{\partial u_{02}}{\partial x_r} & \frac{\partial u_{02}}{\partial x_1} & \frac{\partial u_{02}}{\partial x_2} & \frac{\partial u_{02}}{\partial x_3} & 0 \\ u_{0r} \frac{\partial u_{03}}{\partial x_r} & \frac{\partial u_{03}}{\partial x_1} & \frac{\partial u_{03}}{\partial x_2} & \frac{\partial u_{03}}{\partial x_3} & 0 \\ 0 & \frac{(1-\gamma)}{\rho_0} \frac{\partial p_0}{\partial x_1} & \frac{(1-\gamma)}{\rho_0} \frac{\partial p_0}{\partial x_2} & \frac{(1-\gamma)}{\rho_0} \frac{\partial p_0}{\partial x_3} & (\gamma - 1) \frac{\partial u_{0r}}{\partial x_r} \end{bmatrix}$$

$$\mathbf{S} = \begin{bmatrix} S_{dens} \\ S_{mom,1} \\ S_{mom,2} \\ S_{mom,3} \\ S_{press} \end{bmatrix}$$

where the sound velocity  $c_0$  can be calculated as  $c_0^2 = \gamma p_0 / \rho_0$ . The matrices  $\mathbf{A}_r$  are the flux Jacobians, and the term  $\mathbf{Cq}$  accounts for the non-uniform mean flow effects.

## The Linearized Navier-Stokes Equations

In some cases studied in this work, namely those presented in Chap. 8 where the dissipation of vortices is a significant aspect of the physical phenomena to be simulated, it is necessary to model the viscous effects. However, the dissipative effects in these cases are still small enough for the process to be considered as isentropic, so that the perturbation approximately verifies the relation:

$$\frac{\partial p}{\partial \rho} = c_0^2 = \frac{\gamma p_0}{\rho_0}$$

With this assumption, the energy equation (6.8) becomes redundant, and can be removed from the system, yielding:

$$\frac{\partial \rho}{\partial t} + \frac{\partial}{\partial x_r} (\rho_0 u_r + \rho u_{0r}) = S_{dens} \quad (6.10)$$

$$\frac{\partial(\rho_0 u_s)}{\partial t} + \frac{\partial}{\partial x_r} (\rho_0 u_s u_{0r} + c_0^2 \rho + \tau_{sr}) + (\rho_0 u_r + \rho u_{0r}) \frac{\partial u_{0s}}{\partial x_r} = S_{mom,s} \quad (6.11)$$

The isentropic assumption thus lowers the computational cost by reducing the number of variables and equations. Above all, it removes the complex terms deriving from the linearization of the viscous part in the energy equation, which are difficult to implement. On the contrary, the viscous stress term in Eq. (6.2) is a linear function of the velocity  $\mathbf{u}$ , so that it does not induce any non-uniform mean flow term outside the flux, and the perturbation  $\boldsymbol{\tau}$  is expressed as in Eq. (6.4). The matrix formulation yields:

$$\mathbf{q} = \begin{bmatrix} \rho \\ \rho_0 u_1 \\ \rho_0 u_2 \\ \rho_0 u_3 \end{bmatrix}$$

$$\mathbf{A}_r = \begin{bmatrix} u_{0r} & \delta_{1r} & \delta_{2r} & \delta_{3r} \\ c_0^2 \delta_{1r} & u_{0r} & 0 & 0 \\ c_0^2 \delta_{2r} & 0 & u_{0r} & 0 \\ c_0^2 \delta_{3r} & 0 & 0 & u_{0r} \end{bmatrix}$$

$$\mathbf{C} = \begin{bmatrix} 0 & 0 & 0 & 0 \\ u_{0r} \frac{\partial u_{01}}{\partial x_r} & \frac{\partial u_{01}}{\partial x_1} & \frac{\partial u_{01}}{\partial x_2} & \frac{\partial u_{01}}{\partial x_3} \\ u_{0r} \frac{\partial u_{02}}{\partial x_r} & \frac{\partial u_{02}}{\partial x_1} & \frac{\partial u_{02}}{\partial x_2} & \frac{\partial u_{02}}{\partial x_3} \\ u_{0r} \frac{\partial u_{03}}{\partial x_r} & \frac{\partial u_{03}}{\partial x_1} & \frac{\partial u_{03}}{\partial x_2} & \frac{\partial u_{03}}{\partial x_3} \end{bmatrix}$$

$$\mathbf{S} = \begin{bmatrix} S_{dens} \\ S_{mom,1} \\ S_{mom,2} \\ S_{mom,3} \end{bmatrix}$$

## 6.1.2 Modes of Fluctuation and Characteristics

Although the LEE are commonly used to model acoustic phenomena in non-uniform flows, they support other modes of fluctuation than the mere sound

propagation. Chu and Kovásznyai [29] showed that the Navier-Stokes equations perturbed about a uniform mean flow support three modes, namely the acoustic mode, the vorticity mode and the entropy mode.

Whereas these three modes can easily be put in evidence with one spatial dimension through a characteristic decomposition of the equations, the multi-dimensional case is less obvious, because the flux Jacobian matrices  $\mathbf{A}_r$  cannot be diagonalized with the same eigenvectors. This results in an infinite set of characteristics forming a Monge cone, which is materialized by the fact that an isotropic acoustic perturbation propagates in all directions simultaneously.

In order to bring the characteristic form of the LEE to light, the homogeneous 2D version of Eq. (6.9) is projected on an arbitrary direction  $\mathbf{n} = (n_1, n_2)$ , assuming a uniform mean flow. Performing an eigendecomposition of the projected flux Jacobian leads to:

$$\mathbf{A}_n = \mathbf{A}_1 n_1 + \mathbf{A}_2 n_2 = \begin{bmatrix} u_{0n} & n_1 & n_2 & 0 \\ 0 & u_{0n} & 0 & n_1 \\ 0 & 0 & u_{0n} & n_2 \\ 0 & c_0^2 n_1 & c_0^2 n_2 & u_{0n} \end{bmatrix} = \mathbf{L}\mathbf{\Lambda}\mathbf{L}^{-1}$$

where  $u_{0n} = \mathbf{u}_0 \cdot \mathbf{n} = u_{01}n_1 + u_{02}n_2$ , and:

$$\mathbf{L} = \begin{bmatrix} 1 & 0 & \frac{1}{2c_0} & \frac{1}{2c_0} \\ 0 & n_2 & \frac{n_1}{2} & -\frac{n_1}{2} \\ 0 & -n_1 & \frac{n_2}{2} & -\frac{n_2}{2} \\ 0 & 0 & \frac{c_0}{2} & \frac{c_0}{2} \end{bmatrix}$$

$$\mathbf{\Lambda} = \begin{bmatrix} u_{0n} & 0 & 0 & 0 \\ 0 & u_{0n} & 0 & 0 \\ 0 & 0 & u_{0n} + c_0 & 0 \\ 0 & 0 & 0 & u_{0n} - c_0 \end{bmatrix}$$

Left-multiplying Eq. (6.9) by  $\mathbf{L}^{-1}$ , the LEE can then be reformulated in a system of advection equations by [62, 137]:

$$\frac{\partial w_1}{\partial t} + \mathbf{u} \cdot \nabla w_1 = 0 \quad (6.12)$$

$$\frac{\partial w_2}{\partial t} + \mathbf{u} \cdot \nabla w_2 = \frac{c_0}{2} (\mathbf{t} \cdot \nabla) (w_3 + w_4) \quad (6.13)$$

$$\frac{\partial w_3}{\partial t} + (\mathbf{u} + c_0 \mathbf{n}) \cdot \nabla w_3 = c_0 (\mathbf{t} \cdot \nabla) w_2 \quad (6.14)$$

$$\frac{\partial w_4}{\partial t} + (\mathbf{u} - c_0 \mathbf{n}) \cdot \nabla w_4 = c_0 (\mathbf{t} \cdot \nabla) w_2 \quad (6.15)$$

where  $\mathbf{t} = (-n_2, n_1)$  and the characteristic variables can be calculated as:

$$\begin{bmatrix} w_1 \\ w_2 \\ w_3 \\ w_4 \end{bmatrix} = \mathbf{L}^{-1} \mathbf{q} = \begin{bmatrix} \rho - \frac{p}{c_0^2} \\ n_2 \rho_0 u_1 - n_1 \rho_0 u_2 \\ n_1 \rho_0 u_1 + n_2 \rho_0 u_2 + \frac{p}{c_0} \\ -n_1 \rho_0 u_1 - n_2 \rho_0 u_2 + \frac{p}{c_0} \end{bmatrix}$$

In the system of Eq. (6.12)-(6.15), the coupling introduced by the right hand side is due to the variation of the variables  $w_2$ ,  $w_3$  and  $w_4$  in the direction  $\mathbf{t}$  normal to  $\mathbf{n}$ . Equations (6.12) and (6.13) govern the entropy and vorticity modes, represented respectively by the characteristic variables  $w_1$  and  $w_2$ : they are simply convected by the mean flow with characteristic velocity  $\mathbf{u}_0$ . Equations (6.14) and (6.15) describe the propagation of the two acoustic modes corresponding to the variables  $w_3$  and  $w_4$ .

The characteristic decomposition for the plain LNSE is the same, as it is performed only on the hyperbolic part of the equation. However, the isentropic assumption suppresses the entropy mode, so that the decomposition matrices become:

$$\mathbf{L} = \begin{bmatrix} 0 & \frac{1}{2c_0} & \frac{1}{2c_0} \\ n_2 & \frac{n_1}{2} & -\frac{n_1}{2} \\ -n_1 & \frac{n_2}{2} & -\frac{n_2}{2} \end{bmatrix}$$

$$\mathbf{\Lambda} = \begin{bmatrix} u_{0n} & 0 & 0 \\ 0 & u_{0n} + c_0 & 0 \\ 0 & 0 & u_{0n} - c_0 \end{bmatrix}$$

and the characteristic variables are:

$$\begin{bmatrix} w_1 \\ w_2 \\ w_3 \end{bmatrix} = \begin{bmatrix} n_2 \rho_0 u_1 - n_1 \rho_0 u_2 \\ c_0 \rho + n_1 \rho_0 u_1 + n_2 \rho_0 u_2 \\ c_0 \rho - n_1 \rho_0 u_1 - n_2 \rho_0 u_2 \end{bmatrix}$$

leaving only the vorticity mode and the two acoustic modes.

In the case of a non-uniform flow, the presence of the term  $\mathbf{C}\mathbf{q}$  induces a coupling between the entropy, vorticity and acoustic modes, in which the energy is not conserved. This effect is sometimes modeled on purpose, like in the cases studied in Chap. 8. However, it can lead in sheared flows to the unbounded growth of the vorticity mode, that pollutes the solution when the goal is to simulate only the acoustic propagation.

## 6.2 DG Method for Linear Aeroacoustic Equations

### 6.2.1 Discretization

#### LEE

Following the work of Reymen [122], the numerical method described in Chap. 2 is applied to the LEE, in order to come up with the semi-discrete formulation:

$$\mathbf{M}^T \frac{\partial \mathbf{q}^T}{\partial t} - \sum_{r=1}^d \mathbf{K}_r^T \mathbf{A}_r^T \mathbf{q}^T + \sum_{i=1}^b \mathbf{M}^{\partial T_i} \widehat{\mathbf{f}}^{\partial T_i} + \mathbf{M}^T \mathbf{C}^T \mathbf{q}^T = \mathbf{M}^T \mathbf{S}^T \quad (6.16)$$

where  $\mathbf{q}^T$ ,  $\widehat{\mathbf{f}}^{\partial T_i}$  and  $\mathbf{S}^T$  are matrices in which each column corresponds to a variable.

The definition of the numerical fluxes has to be adapted to the LEE, that can be seen as a system of advection equations deriving from the characteristic decomposition along the normal  $\mathbf{n}$  to the face  $\partial T_i$ , as described in Sec. 6.1.2. The local Lax-Friedrichs flux is calculated by replacing the advection velocity  $\|\mathbf{a}\|$  in Eq. (2.4) with the largest characteristic velocity found in the diagonal of  $\mathbf{\Lambda}$ . The upwind flux defined in Eq. (2.5) is adapted by performing the upwinding on each characteristic variable independently, yielding:

$$\widehat{\mathbf{f}} = \mathbf{L} \left( \mathbf{\Lambda}_+ \mathbf{L}^{-1} \mathbf{q}^T + \mathbf{\Lambda}_- \mathbf{L}^{-1} \mathbf{q}^{T'} \right)$$

where  $T'$  is the element sharing the face  $\partial T_i$  with  $T$ , and  $\mathbf{\Lambda}_+$  and  $\mathbf{\Lambda}_-$  are respectively the positive and negative parts of  $\mathbf{\Lambda}$ .

## LNSE

The application of the DG method to the LNSE is more complex, because of the second derivatives of the velocity contained in the viscous terms. Unfortunately, the treatment of these terms consisting in applying twice the DG derivation operator leads to an unstable formulation [60, Chap. 7]. Therefore, we resort to the so-called “BR1” mixed finite element formulation [6, 13], that was originally developed by Bassi and Rebay [11]. In this method, the gradients of the velocity  $\mathbf{q}$  are treated as independent variables, and extra equations are added to the system in order to solve for them:

$$\mathbf{w}^s - \frac{\partial \mathbf{q}}{\partial x_s} = \mathbf{0} \tag{6.17}$$

$$\frac{\partial \mathbf{q}}{\partial t} + \frac{\partial \mathbf{A}_r \mathbf{q}}{\partial x_r} + \frac{\partial \mathbf{f}_r^v}{\partial x_r} + \mathbf{C} \mathbf{q} = \mathbf{S} \tag{6.18}$$

where  $\mathbf{f}^v = \mathbf{f}^v(\mathbf{w}^1, \mathbf{w}^2, \mathbf{w}^3)$  is the viscous flux vector, and Eq. (6.17) gives the derivative  $\mathbf{w}^s$  of the variables  $\mathbf{q}$  in the direction  $x_s$ , with  $s = 1 \dots 3$ .

Both equations are discretized with the DG method, using the same polynomial space  $\mathcal{P}_p(T)$  for the sake of simplicity, although  $\mathbf{w}^s$  is of lower degree. Equation (6.17) is solved for  $\mathbf{w}^s$  first, using central numerical fluxes. Then, Eq. (6.18) is solved in the same way as the LEE in Eq. (6.16), with the extra viscous term. The viscous flux contribution is integrated by parts just like its convective counterpart, but the central flux is chosen over the Lax-Friedrichs or upwind fluxes to calculate the element boundary part, because the diffusive nature of this term does not exhibit any preferred direction.

This formulation is known to be unstable when the convective term is negligible with respect to the viscous term. The more sophisticated “BR2” formulation has better stability properties [6, 13], but its use of complex lift operators makes it computationally more costly in an explicit RKDG framework, in addition to being more difficult to implement. Another issue is the significant adverse effect of diffusion on the conditional stability of the method: the so-called viscous CFL condition, that depends on the square of the element size  $h$ , can severely restrict the maximum time step  $\Delta t^*$ . In this work however, the LNSE is employed in cases dominated by the convection effects (see Chap. 8), so that the “BR1” formulation is sufficient, and the stability and accuracy properties of the scheme are similar to description in Part II, just like with the LEE.

## 6.2.2 Boundary Conditions

As mentioned in Chap. 2, the boundary conditions are prescribed in a weak manner through the specification of the numerical flux at boundary faces. In this work, two main kinds of boundaries are considered: rigid walls (i.e. walls with infinite acoustic resistance and no reactance) and non-reflecting boundaries, that enable the modeling of infinite physical domains by finite computational domains.

### Rigid Wall Boundary Conditions

Rigid wall boundaries are modeled by *slip* condition that imposes a zero normal velocity perturbation:

$$\mathbf{u} \cdot \mathbf{n} = 0$$

where  $\mathbf{n}$  is the normal to the boundary. The precise boundary treatment, in particular the definition of  $\mathbf{n}$  and its implications for acoustic problems, are the subject of Chap. 7.

With the LEE, the boundary condition is imposed only by specifying the numerical flux as

$$\widehat{\mathbf{f}} = \mathbf{A}_r n_r \mathbf{q}_{BC} \quad (6.19)$$

where  $\mathbf{q}_{BC}^T$  is the vector of variables on the boundary, where the velocity perturbation  $\mathbf{u}$  is replaced with its tangential component  $\mathbf{u} - (\mathbf{u} \cdot \mathbf{n}) \mathbf{n}$ .

With the LNSE, the prescription of the viscous part of the numerical flux is necessary, on top of Eq. (6.19), to complete the boundary condition for Eq. (6.18):

$$\widehat{\mathbf{f}}^v = \mathbf{f}_r^v n_r \quad (6.20)$$

where the viscous flux vector  $\mathbf{f}^v$  on the boundary is not modified, as there is no condition imposed on the velocity gradients  $\mathbf{w}$ . In the auxiliary equation (6.17), the numerical flux is simply taken as  $\mathbf{q}$ .

### Non-Reflecting Boundary Conditions

Non-reflecting boundary conditions are necessary to simulate acoustic problems in infinite domains by limiting the computational domain to the region

of interest. Many kinds of non-reflecting boundary conditions have been developed for different applications. A review can be found in Ref. [34].

In this work, the classical characteristic boundary conditions are considered, because they are efficient, easy to use and simple to implement. The characteristic decomposition of the LEE presented in Sec. 6.1.2 is performed along the boundary normal  $\mathbf{n}$ , so that the incoming waves (corresponding to negative eigenvalues in  $\Lambda$ ) can be controlled, and the numerical flux is expressed as:

$$\hat{\mathbf{f}} = \mathbf{L} (\Lambda_+ \mathbf{L}^{-1} \mathbf{q}^T + \Lambda_- \mathbf{L}^{-1} \mathbf{q}_{BC}) \quad (6.21)$$

where  $\mathbf{q}_{BC}$  can be used to introduce an excitation in the domain. If the boundary is meant to be passively absorbing, then  $\mathbf{q}_{BC} = \mathbf{0}$ , and only the outgoing characteristics contribute to the numerical flux.

For the LNSE, the viscous effects are assumed to be small compared to the convective effects, so that the quality of the non-reflective boundary condition formulated in Eq. (6.21) remains unaffected. As in the case of walls, there is no specific condition on the velocity gradients, so that the viscous part of the numerical flux is given by Eq. (6.20). Similarly, the numerical flux in the auxiliary equation (6.17) is  $\mathbf{q}$ .

The characteristic non-reflective boundary condition given by Eq. (6.21) actually results from the approximation that the outgoing wavefronts are locally parallel to the boundary, i.e. the right-hand side of Eq. (6.12)-(6.15) is neglected. If the waves reach the boundary with a significant tangential incidence, acoustic reflections may occur. This is often the case when vorticity is convected through the boundary.

### 6.2.3 High-Order Interpolation

As mentioned in Chap. 2, the numerical scheme considered in this work is a nodal version of the DG method, which means that the basis functions  $\varphi^T$  are basis Lagrange polynomials. In practice, some operations can then be efficiently performed by working directly on the unknowns, which implies a transparent interpolation. This is the case, for instance, of the multiplication of two fields in an element  $T$ , or the restriction of a field in  $T$  to the element boundary  $\partial T$ . However, the numerical method is preferably used with high order  $p$  of the polynomial approximation, for reasons of computational efficiency. The well-known problems associated to high-order interpolation (Runge's phenomenon, aliasing) may then alter the fidelity and the stability of the numerical method [60, Chap. 5]. These difficulties occur mainly in the specification of the mean flow, and in the computation of the fluxes.

## Mean Flow Specification

In some of the problems that studied in this work, the mean flow about which the Euler and Navier-Stokes equations are linearized is not uniform. It is either obtained from an incompressible CFD simulation (i.e. available as a set of points and variable values corresponding to the vertices of the CFD mesh), or calculated from an analytical solution. Following the principles of the numerical method introduced in Chap. 2, each mean flow variable (density, velocity components, pressure) is approximated in an element  $T$  with a function  $q^T \in \mathcal{P}_p(T)$ , that is defined by its components  $q_j^T$  in the basis  $\mathcal{B}_p^T$ . Each component  $q_j^T$  represents the value of  $q^T$  at the node  $j$  associated with the basis Lagrange polynomial  $\varphi_j^T$ .

In order to illustrate the implications of this approximation for the mean flow, we consider the case of the function  $q(y) = 0.1 \cdot [\tanh(3y) + 2]$ , that could represent the velocity in a mixing layer with hyperbolic tangent profile between two flows of non-dimensional velocity 0.1 and 0.3. This function is approximated at order  $p = 7$  on a square domain of size  $20 \times 20$ , with a mesh of 42 triangles. The mesh and the analytical solution  $q(y)$  are shown in Fig. 6.1.

An obvious way of obtaining the mean flow data is thus to calculate  $q_j^T$  as  $q_j^T = q(y_j^T)$ , where  $y_j^T$  is the  $y$  coordinate of node  $j$  in element  $T$ . This results in unwanted “wiggles” in the mixing layer zone, which can be seen in Fig 6.2. Thus, the direct computation of  $q_j^T$  (by a closed expression or by interpolation from CFD data) is to be avoided if some features of the mean flow are not totally resolved: it may cause spurious spatial oscillations of  $q^T$  at high order  $p$ , due to Runge’s phenomenon.

In order to alleviate this problem, a least-square approach is used that fits the approximation  $q^T$  to the ideal solution. The function  $q(y)$  (or, in the general case, the CFD data) is first sampled on a dense cloud of points in each element  $T$ . The nodal set corresponding to the Lagrange polynomial basis  $\mathcal{B}_p^T$  of order  $p + 4$  is usually used for this purpose. Then, a least-square technique is used to find the polynomial  $q^T$  that best approximates the sampled values. To do so, the least-square system can simply be solved in each element  $T$  individually. This reduces the spurious oscillations in the vicinity of under-resolved mean flow features, but it may result in discontinuities between elements, as shown for the example case in Fig. 6.3. Therefore, a global procedure is preferred, in which some degrees of freedom are removed by imposing the continuity of the approximation between the elements, and the least-square system is solved simultaneously for all elements in the domain. As shown in Fig. 6.4, this technique reduces the spurious oscillations, while maintaining a continuous approximation over the whole domain.

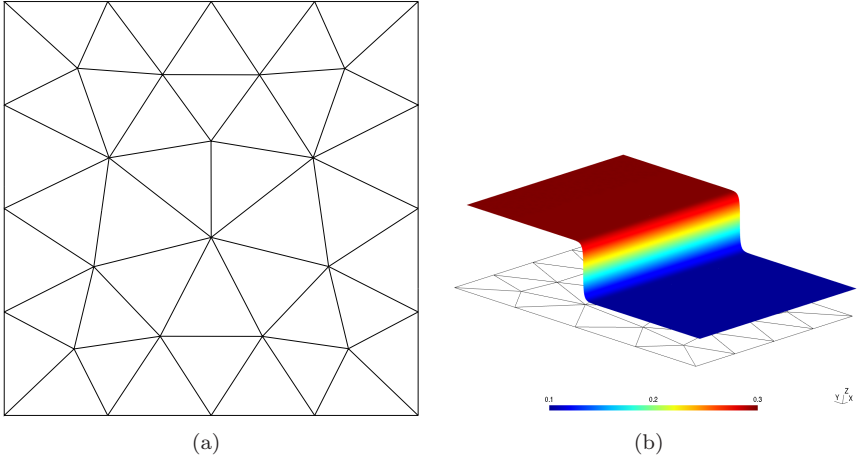


Figure 6.1: Example case of mean flow specification: mesh (a) and analytical solution (b).

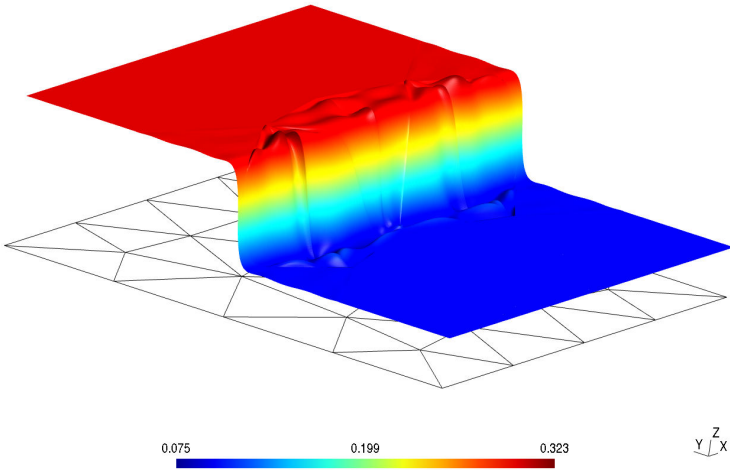


Figure 6.2: Example case of mean flow specification: direct interpolation.

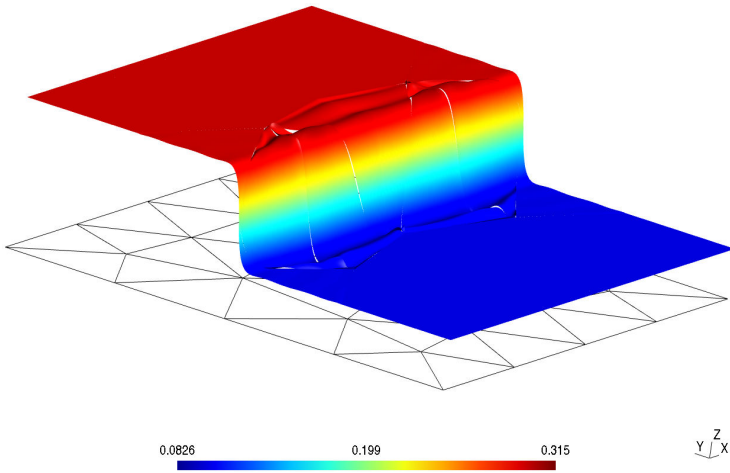


Figure 6.3: Example case of mean flow specification: local least-square procedure.

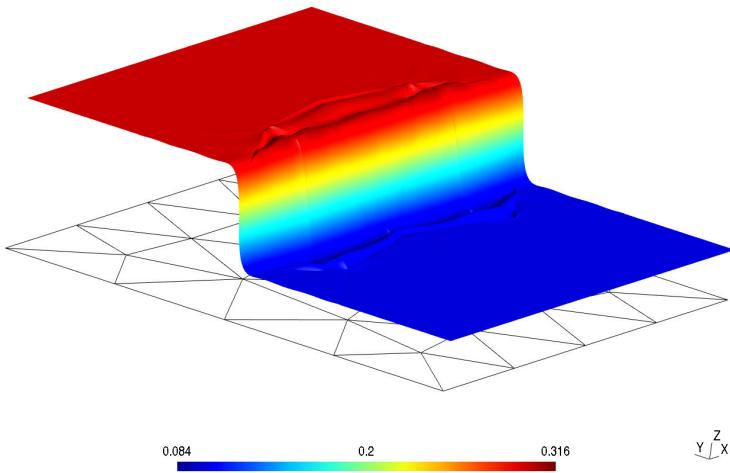


Figure 6.4: Example case of mean flow specification: global least-square procedure with imposed continuity between elements.

## Flux Computation

The non-uniformity of the mean flow may also cause problems related to high-order interpolation in the computation of the fluxes  $\mathbf{A}_r^T \mathbf{q}^T$  and, to a lesser extent, in the computation of the mean flow gradient term  $\mathbf{C}^T \mathbf{q}^T$ . Indeed, the mean flow (thus the flux Jacobians  $\mathbf{A}_r^T$ ) and the vector of variables  $\mathbf{q}^T$  are both defined in  $\mathcal{P}_p(T)$ . The product  $\mathbf{A}_r^T \mathbf{q}^T$  should then be represented exactly by polynomials of degree  $2p$ . However, it is defined in  $\mathcal{P}_p(T)$  in this work, so that the matrices  $\mathbf{K}_r^T$  and  $\mathbf{M}^T$  corresponding to the basis  $\mathcal{B}_p^T$  can be used.

The representation of  $\mathbf{A}_r^T \mathbf{q}^T$  in  $\mathcal{P}_p(T)$  is then obtained very easily by calculating the product at each node  $j$ :  $(\mathbf{A}_r^T \mathbf{q}^T)_j = \mathbf{A}_{r,j}^T \mathbf{q}_j^T$ . This implies an interpolation of a polynomial of degree  $2p$  by a polynomial of degree  $p$ , which is prone to the so-called *aliasing* phenomenon: the modes of order higher than  $p$  are transformed into spurious contributions to modes of order lower than  $p$  by the interpolation. This effect, that is described at length in Ref. [60, Chap. 5], is a major cause of instability in the numerical method.

A natural remedy to this problem is to compute the fluxes  $\mathbf{A}_r^T \mathbf{q}^T$ , as well as the mean flow term  $\mathbf{C}^T \mathbf{q}^T$ , by projection rather than by interpolation. This can be carried out in the reference space, introducing the projection matrix  $\mathbf{P}^{p,q}$  from a base  $\mathcal{B}_q = \{\varphi_j^q, j = 1 \dots N_q\}$  of  $\mathcal{P}_q(T)$  to a base  $\mathcal{B}_p = \{\varphi_k^p, k = 1 \dots N_p\}$  of  $\mathcal{P}_p(T)$ :

$$\mathbf{P}_{kj}^{p,q} = \int_R \varphi_k^p \varphi_j^q d\xi$$

The fluxes  $\mathbf{A}_r^T \mathbf{q}^T$  in  $\mathcal{P}_p(T)$  can then be computed as  $\mathbf{A}_r^T \mathbf{q}^T = \mathbf{P}^{p,2p} (\mathbf{A}_r^T \mathbf{q}^T)^{2p}$ , where the fluxes  $(\mathbf{A}_r^T \mathbf{q}^T)^{2p}$  in  $\mathcal{P}_{2p}(T)$  are obtained by interpolation at order  $2p$ :

$$(\mathbf{A}_r^T \mathbf{q}^T)^{2p}_j = (\mathbf{P}^{2p,p} \mathbf{A}_r^T)_j (\mathbf{P}^{2p,p} \mathbf{q}^T)_j$$

This interpolation is not subject to aliasing, as  $\mathbf{P}^{2p,p} \mathbf{A}_r^T$  and  $\mathbf{P}^{2p,p} \mathbf{q}^T$  contain only modes of order lower or equal to  $p$ , although they are defined on  $\mathcal{B}_{2p}^T$ .

However, this stabilization method is computationally very expensive: it adds three multiplications by matrices of size  $N_{2p} \times N_p$  or  $N_p \times N_{2p}$ , and the flux is computed for  $N_{2p}$  unknowns, while  $N_p$  grows like  $p^2$  in 2D and  $p^3$  in 3D. Therefore, the more pragmatic filtering approach described in Ref. [60, Chap. 5] is preferred. It consists in applying to each mode of the solution a filter of the form:

$$\sigma(n) = \begin{cases} 1, & n \leq n_{CO} \\ \exp \left[ -\alpha \left( \frac{n-n_{CO}}{p-n_{CO}} \right)^s \right], & n > n_{CO} \end{cases}$$

where  $n$  is the degree of the polynomial,  $n_{CO}$  is the cut-off degree of the filter,  $s$  is the order of the filter (that must be even), and  $\alpha = 36$  is a constant. The filter is defined in the modal approach, that is, it acts on each component of the underlying polynomial basis that is orthogonal in the reference element. In the nodal setting used in this work, it results in a  $N_p \times N_p$  matrix by which the solution is multiplied at each stage of the RK scheme. This technique amounts to damping the higher-order modes in a controlled manner, for a reasonable direct computation cost (one  $N_p \times N_p$  matrix multiplication). By adjusting the filter parameters  $n_{CO}$  and  $s$ , the user can add just the right amount of dissipation to avoid the aliasing instability, so that the accuracy is not too degraded. Typical values of the parameters are  $n_{CO} = 0$  and  $s = 16$ , for which an example of the filter function  $\sigma(n)$  is drawn in Fig. 6.5.

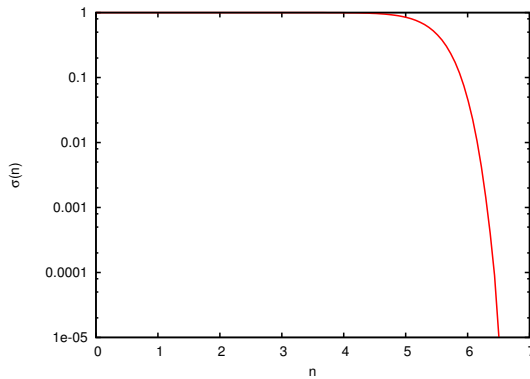


Figure 6.5: Filter function  $\sigma(n)$  with parameters  $n_{CO} = 0$  and  $s = 16$ , for order  $p = 7$ .

## 6.3 Implementation and Verification

### 6.3.1 Implementation

The method described in Sec. 6.2.1 and in Chap. 2 is implemented in a numerical code, that is able to solve the LEE or LNSE with non-uniform mean flow. It runs on triangular meshes in 2D and tetrahedral meshes in 3D, with possibly curved elements. It is an extension of the code written by Reymen [122], that was restricted to straight tetrahedral elements, with limited non-uniform mean flow capabilities. The implementation follows the work of Hesthaven and Warburton [58, 60], in particular for the definition and manipulation of the Lagrange polynomial basis along with the underlying

modal basis. Besides the handling of the grid data structure and the RKDG procedure, the code is supplemented with algorithms to generate output at regular intervals of time. The first type of output is the value of the solution, obtained directly from the polynomial approximation, on a user-specified set of points. The second type of output is the solution in the whole computational domain for visualization. Both pre- and post-processing are performed through the Gmsh software [51], that particularly suits DG methods because of its ability to generate high-order grids and to visualize high-order solutions.

The C++ programming language is chosen for the implementation, because it is available on most computing platforms, and because its object-oriented character facilitates the design and the maintenance of a large numerical code. As seen in Sec. 6.2.1, most basic operations are of matrix-vector and matrix-matrix type. For efficiency reasons, these calculations are carried out by BLAS routines [19] from external libraries (for instance ATLAS [145]).

### 6.3.2 Grid Convergence

In order to verify the correct implementation of the numerical scheme, a grid convergence study is performed for the free-field propagation of a Gaussian pressure pulse with the 2D LEE. An analytical solution is available for this problem, that provides accurate data for comparison with the present numerical results [131].

The computational domain consists of a square of non-dimensional size  $200 \times 200$ , centered at the origin. The initial conditions are:

$$\begin{aligned} p|_{t=0} &= \rho|_{t=0} = e^{-(\ln 2) \frac{x^2+y^2}{5^2}} \\ u_1|_{t=0} &= u_2|_{t=0} = 0 \end{aligned} \tag{6.22}$$

The mean flow velocity is set to zero, with a sound speed of  $c_0 = 1$ , and the Gaussian pressure pulse is left propagating until a non-dimensional time of  $t = 20$ . This ensures that the wave front remains inside the domain, to prevent the solution from being polluted by any spurious reflection at boundaries. Several grids with increasing refinement are used, their characteristics being summarized in Table 6.1. The order  $p$  of the polynomial approximation varies from 1 to 6. For all grids and all values of the order  $p$ , the error in  $L_2$  norm with respect to the analytical solution at the final time is measured.

Fig. 6.6 shows the error as a function of the square root of the number of elements, that can be considered as inversely proportional to the element size. The scheme exhibits the correct convergence behaviour, and the theoretical

order of accuracy  $p + 1$  featured of the DG method is reached as long as the number of elements is sufficiently high.

Fig. 6.7 shows the duration of the computations in CPU time as a function of the error. While the advantage of increasing the order  $p$  is unclear for very low accuracy, computations at higher order  $p$  are clearly more efficient when the pulse is accurately resolved. For instance, the computation with Grid 2 at order  $p = 5$  yields as accurate results as the computation with Grid 5 at order  $p = 1$ , but is 15 times faster.

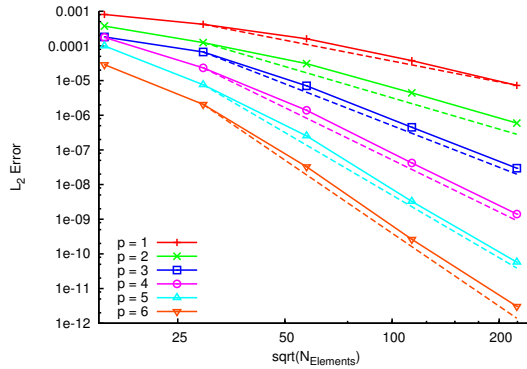


Figure 6.6: Grid convergence study: error in  $L_2$  norm as a function of the square root of the number of elements. The dashed lines correspond to the theoretical order of accuracy  $p + 1$ .

### 6.3.3 Boundary Conditions

In order to verify the correct behaviour of the non-reflective boundary conditions introduced in Sec. 6.2.2, a test problem similar to the one described in Sec. 6.3.2 is used. The initial Gaussian pressure pulse defined in Eq. (6.22) is left propagating until non-dimensional time  $t = 300$  in a square domain of non-dimensional size  $100 \times 100$ , where non-reflecting boundary conditions are imposed at each side. The mean flow is uniform, with a non-dimensional horizontal velocity of  $u_{01} = 0.5$  and a sound speed of  $c_0 = 1$ . Thus, the pulse

Grid Nr.	1	2	3	4	5
Vertices	122	435	1654	6455	25519
Elements	242	868	3306	12908	50236

Table 6.1: Characteristics of the grids used for the grid convergence study.

front reaches first the right boundary at  $t \approx 33$ , and it completely leaves the domain through the upper left corner at  $t \approx 109$ , as can be seen from the numerical solution shown in Fig. 6.8. A sufficiently fine grid of 800 triangular elements is used, while the order of the polynomial approximation is set to  $p = 6$ . The  $L_2$  norm of the pressure is computed on a set of  $100 \times 100$  points evenly distributed in the domain:

$$L_p = \sqrt{\sum_{i=1}^{10000} p_i^2}$$

where  $p_i$  is the value of pressure at point  $i$ .

The measured quantity  $L_p$ , normalized by its initial value  $L_p(t=0)$ , is compared in Fig. 6.9 to the reference value obtained from the analytical solution [131]. For time  $t > 109$ , the residual pressure is higher in the numerical results than in the reference solution. This is due to the reflections that occur when the pulse front reaches the boundary with oblique incidence, as shown in Fig. 6.8. However, both curves remain almost superimposed for  $t < 109$ , indicating that the amplitude of the reflections at boundaries is small compared to the amplitude of the incident front.

The implementation of the more simple rigid wall boundary condition is verified extensively in the test problems presented in Chap. 7.

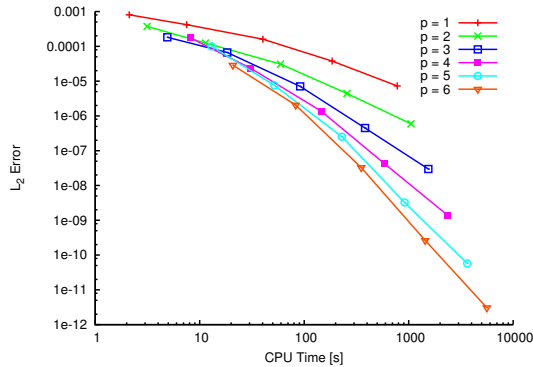


Figure 6.7: Grid convergence study: error in  $L_2$  norm against the CPU time.

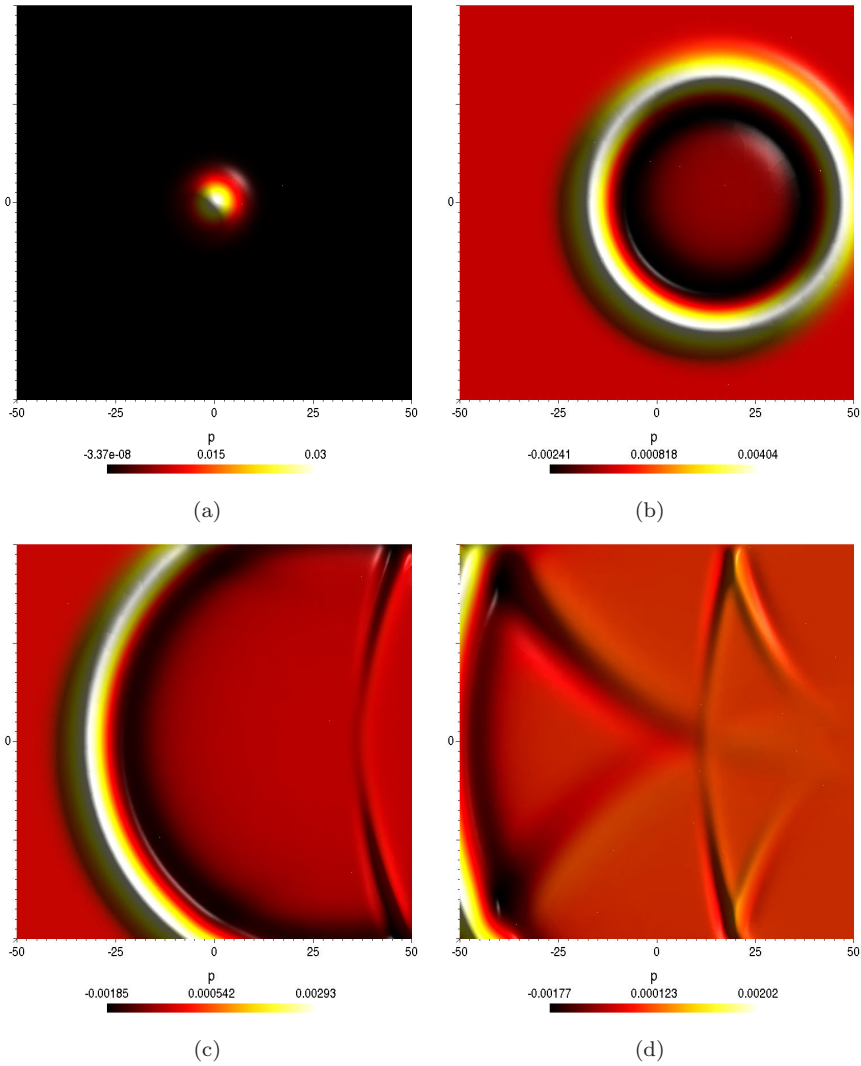


Figure 6.8: Verification of the non-reflecting boundary conditions: pressure perturbation field (numerical solution) at  $t = 0$  (a),  $t = 30$  (b),  $t = 60$  (c) and  $t = 110$  (d).

### 6.3.4 Non-Uniform Flow

Finally, a general verification of the code is performed with a problem involving a non-uniform mean flow. The test consists in simulating the 2D sound radiation of a monopole located in a boundary layer [14, 128]. It corresponds to Case D of Ref. [128], where the free-stream Mach number is  $M_\infty = 0.3$ , the acoustic wavelength (at  $M = 0$ ) is equal to the boundary layer thickness, and the Reynolds number (based on the free-stream velocity and the acoustic wavelength at  $M = 0$ ) is  $Re = 3.75 \cdot 10^3$ . The directivity of the sound radiation computed with the LEE and the isentropic LNSE is compared to reference data obtained from a DNS computation [128].

The case is set up in a semi-circular domain of radius 23, centered at  $(x_1, x_2) = (7, 0)$ , as can be seen in Fig 6.10. A rigid wall boundary condition is imposed on the lower flat boundary, and the other boundaries are non-reflective. The mean flow density and pressure are  $\rho = 1$  and  $p = 1/\gamma$  respectively, so that the sound speed is uniformly  $c_0 = 1$ . The mean flow velocity is given by the Polhausen profile for a flat plate boundary layer of thickness 1 [14]:

$$u_{01} = \begin{cases} M_\infty (2y - 2y^3 + y^4), & 0 \leq y < 1 \\ M_\infty, & y \geq 1 \end{cases}$$

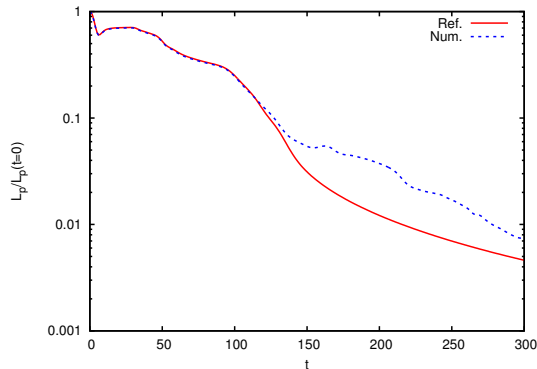


Figure 6.9: Verification of the non-reflecting boundary conditions: normalized  $L_2$  norm of the pressure  $L_p/L_p(t=0)$  as a function of the time  $t$ , for the numerical and reference solutions.

For the LNSE, the viscosity coefficient is set to  $\mu = 8 \cdot 10^{-5}$ . The acoustic monopole is modeled by a source term of the form:

$$\mathbf{S} = \begin{bmatrix} 1 \\ 0 \\ 0 \\ 1 \end{bmatrix} e^{-(\ln 2) \frac{x^2+y^2}{0.1^2}} \sin(2\pi t)$$

for the LEE (the pressure source term is removed for the isentropic LNSE). The simulation is run until non-dimensional time  $t = 30$ . A grid of 3366 triangular elements is used, while the order of the polynomial approximation is set to  $p = 7$ .

The pressure perturbation field at  $t = 30$  is shown in Fig. 6.10: the solution features channeled waves within the downstream boundary layer, free-field radiation in an angle range of  $[7^\circ, 160^\circ]$  around the source, and a shadow zone upstream.

The RMS pressure is measured on a circle of radius 15, centered on the monopole. As the monopole is modeled differently in the reference DNS and in the present simulations, the results are normalized with respect to the maximum RMS pressure in the direct radiation zone [14]. The directivity plot in Fig. 6.11 compares the reference data with the results from the LEE and LNSE simulations. There is a discrepancy between the results obtained here and the DNS data for the channeled waves and the very low angle radiation (below  $10^\circ$ ), which is likely to be due to the difference in boundary layer profile [14]. However, the radiation directivity at higher angle is well predicted. In the downstream region, the results with the LNSE are slightly closer to the reference data than with the LEE. In addition to a weak viscous effect, this may be explained by the isentropic assumption: the significant size of the monopole source model in the sheared flow may interact with the entropic mode of the LEE, which is probably not the case in the reference DNS simulation where the source is much more localized. The peak angle ( $130^\circ$  and  $129^\circ$  for the LEE and LNSE results respectively against  $129^\circ$  for the reference data), as well as the critical angle (beyond which there is no radiation), are well predicted in both cases. Overall, given the modelization differences between the present simulations and the DNS (governing equations, boundary layer profile, monopole), the agreement can be considered as satisfactory.

## 6.4 Conclusion

In this chapter, we have explained how the RKDG method can be used to tackle aeroacoustics problems that involve linear sound generation and acoustic

propagation in non-uniform flows. First, two sets of governing equations have been derived by linearization of the Navier-Stokes equations: the LEE, that exclude viscous effects, and the LNSE, that is simplified with the assumption of isentropic flow. Several modes of fluctuation supported by these systems have been put in evidence through a characteristic decomposition: the acoustic mode, the vorticity mode and, in the absence of isentropic assumption, the entropy mode. Then, the application of the RKDG method to the governing equations has been described, detailing the basic discretization and two types of boundary conditions (rigid wall and non-reflecting boundary condition). In practical cases, problems can arise because of the high-order interpolation that is implied by the nodal approach, and remedies to these difficulties have been presented. Finally, we have shortly explained how the method is implemented. The numerical behaviour of the code has been assessed through a grid convergence study, and the correctness of the boundary and mean flow treatments has been verified.

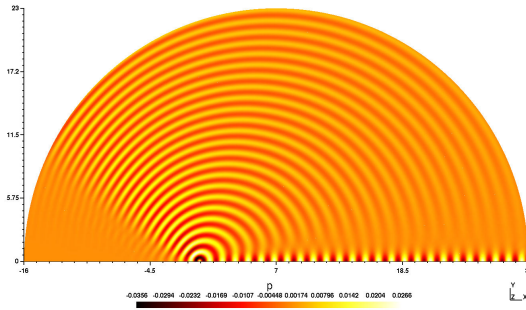


Figure 6.10: Case of a monopole in a boundary layer: pressure perturbation field at  $t = 30$ .

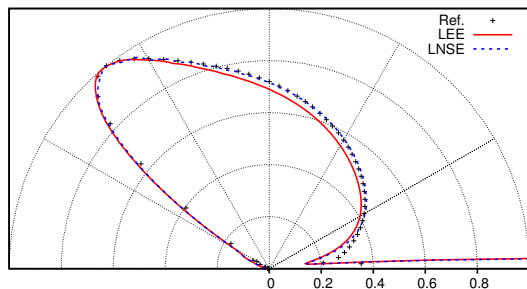


Figure 6.11: Directivity plot for the case of a monopole in a boundary layer: normalized RMS pressure for the reference, LEE and LNSE solutions.

Although the accuracy of the basic scheme and the non-reflecting boundary conditions has been tested in this chapter, the influence of the wall boundary condition has not been thoroughly addressed. This is the subject of Chap. 7. The developments presented in both chapters pave the way for the application of the method to a practical case, which is reported in Chap 8.

## Chapter 7

# Curved Boundary Treatments for Aeroacoustic Propagation

This chapter deals with the impact of the discretization of curved wall boundaries on the accuracy of the DG method presented in Chap. 6, in the context of acoustic propagation. In addition to the classical linear treatment of wall boundaries, two treatments involving a second-order representation of the geometry are introduced. The simulation of acoustic scattering problems confirms that the linear treatment can limit the accuracy at high order  $p$ , and demonstrates how the boundary treatment involving curved elements overcomes this restriction while avoiding unnecessary grid refinement. The benefits of higher-order treatments are also assessed for more realistic geometries, namely a high-lift airfoil and an elliptical muffler.

### 7.1 Introduction

As mentioned in Chap. 1, the question of the accuracy of the DG spatial scheme for wave propagation problems has been thoroughly addressed in the literature, by means of theory and numerical experiments [4, 55, 70, 72]. In this work, a technique for the analysis of the accuracy is presented in Chap. 2 and applied in Chap. 5 to assess the relative computational efficiency of RKDG schemes. The convergence rate of our implementation for linear aeroacoustics is verified

in Chap. 6. All these studies deal with the DG scheme in itself, and exclude purposely the issue of the error that is due to the boundary conditions.

The performance of the non-reflective boundary condition that are used in this work for aeroacoustic applications is evaluated in Chap. 6. However, the rigid wall treatment poses different issues. When the wall to be modeled is flat, the boundary condition does not introduce any error in the simulation. This is not the case with curved geometries: the grid is classically composed of straight-sided elements, resulting in a piecewise linear approximation of the curved boundary. If the spatial discretization scheme is accurate enough, the error due to the approximate modelization of the wall may dominate.

In the framework of the non-linear Euler equations, the necessity of a higher-order treatment of curved wall boundaries was put in evidence by Bassi and Rebay [12], and is now generally accepted [88]. Ref. [12] and [88] suggest that the accuracy mainly depends on the correct representation of the normals to the geometry, when dealing with 2D Euler flows. However, this might not be the case with acoustic propagation problems. Concerning the LEE, Atkins reported the use of higher-order geometry description and its benefits on problems of acoustic scattering [8].

In this chapter, the impact of boundary treatments for curved walls is investigated. Academic problems of acoustic scattering in 2D and 3D are used to show how the linear treatment of wall boundaries limits the accuracy. The improvement brought by two different boundary treatments based on a higher-order geometry representation is evaluated for these problems. The benefits of higher-order boundary treatments are also applied to more realistic geometries, with the computation of sound scattering by a high-lift airfoil and the analysis of transmission loss in an elliptical muffler. In all test cases presented in this chapter, the LEE are used with quiescent mean flow, so that results are restricted to pure acoustics, in order to isolate the accuracy and stability issues raised by boundary treatments.

## 7.2 Higher-Order Wall Boundary Treatments

In this section, two wall boundary treatments based on a second-order representation of the geometry are introduced, in addition to the classical linear one. The higher-order geometrical modelization implies not only a different numerical treatment of the boundary in the DG space discretization, but also specific capabilities for the meshing software.

## 7.2.1 Wall Treatments

As explained in Chap. 6, the wall boundary conditions are prescribed in a weak manner by specifying the numerical flux at boundary faces. The numerical flux at a face  $\partial T_i$  is computed from the fluxes through Eq. (6.19), imposing the slip boundary condition:

$$\mathbf{u} \cdot \bar{\mathbf{n}} = 0$$

where  $\bar{\mathbf{n}}$  is either the normal  $\mathbf{n}$  to  $\partial T_i$ , or the local normal  $\mathbf{n}_{\mathbf{g}}$  to the quadratically-represented geometry. In this work, three different wall boundary treatments, illustrated in Fig. 7.1, are considered:

1.  $\partial T_i$  is a straight edge and  $\bar{\mathbf{n}} = \mathbf{n}$ . In this case the treatment of wall boundaries is fully linear, and the quadrature-free DGM is used, as described in Chap. 2.
2.  $\partial T_i$  is a straight edge and  $\bar{\mathbf{n}} = \mathbf{n}_{\mathbf{g}}$ . As in the linear case, the quadrature-free DGM is used. This treatment, proposed in Ref. [12] and Ref. [88] as a computationally inexpensive way to improve accuracy, will be hereafter referred to as *mixed*.
3.  $\partial T_i$  is a curved edge (i.e.  $\mathbf{n} = \mathbf{n}_{\mathbf{g}}$ ), in this case  $\bar{\mathbf{n}} = \mathbf{n}_{\mathbf{g}}$  and the treatment is fully quadratic. Integration over the edge  $\partial T_i$  and the adjacent element  $T$  is then performed by quadrature, and additional face matrices  $\mathbf{M}_r^{\partial T_i}$  including the components of  $\mathbf{n}$  are defined, as explained in Chap. 2.

Lined walls are not considered in this work, because the formulation of an impedance boundary condition in time domain raises other issues than the mere boundary treatment: the impedance being formulated in frequency domain, a costly convolution is required to compute the condition on pressure. An innovative solution to this problem is proposed in Ref. [123].

## 7.2.2 Mesh Generation and Robustness

As mentioned in Chap. 6, the software that used for mesh generation is Gmsh [51], which is able to cope with second-order meshes following a process illustrated in Fig. 7.2. First-order grids, made out of straight elements, are generated in a classical manner, as shown in Fig. 7.2(a). From these, second-order grids are then produced by projecting the mid-point of boundary edges on the geometry, resulting in curved elements on the boundary. This second-order information can be used in conjunction with the original first-order grid for the mixed treatment.

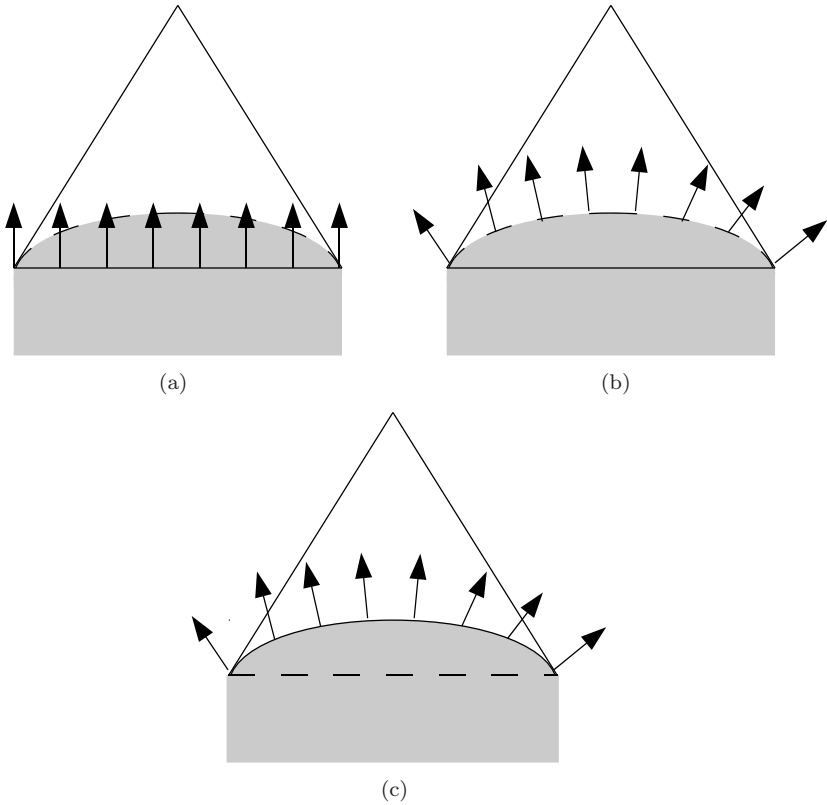


Figure 7.1: Illustration of the linear boundary treatment (a), the mixed boundary treatment (b) and the quadratic boundary treatment (c). The arrows represent the normals  $\bar{n}$  used for prescribing the slip condition, solid lines are the element boundaries on which the flux is integrated.

The projection step is sometimes not sufficient to obtain satisfying second-order meshes. It can result in highly curved elements, that have an impact on the conditioning of the DG spatial operator, as explained extensively in Chap. 4. Time steps must then be decreased to maintain the stability of computations. It can even lead to ill-shaped elements for which the mapping degenerates, as shown in Fig. 7.2(b). The numerical method is unusable with such grids.

Gmsh solves this problem by applying an additional smoothing step that consists in curving edges away from the boundary and involves edge swapping where necessary (see Fig. 7.2(c)). Nevertheless, curved elements remain confined in a region close to the geometry, and the elements in the rest of the computational domain can be considered as straight. As Gmsh outputs second-order information for the whole domain, a criterion based on a “distortion” measure  $\gamma$  is used to discriminate between straight and curved elements:

$$\gamma = \min_T \left( \frac{|J^T|}{|J_0^T|}, \frac{|J_0^T|}{|J^T|} \right)$$

where  $|J_0^T|$  is the Jacobian for the straight element corresponding to a second-order element  $T$ .

## 7.3 Results

The method described in Sec. 7.2 is applied to four test problems, with the objective of assessing the benefits of higher-order boundary treatments. As the interest of the mixed treatment appears to be limited in the two 2D cases presented in Sections 7.3.1 and 7.3.2, it is not retained for evaluation in the 3D problems. In all cases, coarse meshes are used in conjunction with high order, in order to maximize the computational efficiency. A satisfying trade-off between computational cost and accuracy is found at order  $p = 7$  in most simulations, except for the muffler problem in Section 7.3.4 where lower order is needed.

### 7.3.1 Acoustic Scattering by a Cylinder

In order to assess the impact of wall boundary treatments, the problem Nr. 2, Category 1 of the Second CAA Workshop on Benchmark Problems [130] is studied. It consists in the scattering of a Gaussian pressure pulse by a cylinder. An analytical solution is available for this case. In addition to the results presented here, complementary data and a detailed discussion are available in Ref. [138].

The computational domain shown in Fig. 7.3 is a disc with a non-dimensional diameter of 20, containing a cylinder of diameter 1 centered at the origin. The initial conditions consist of a Gaussian pulse located at point  $P(4,0)$ :

$$p|_{t=0} = \rho|_{t=0} = e^{-(\ln 2) \frac{(x-4)^2 + y^2}{0.2^2}}$$

$$u_1|_{t=0} = u_2|_{t=0} = 0$$

The mean flow velocity is set to zero and characteristic-based non-reflecting boundary conditions are imposed in the far-field. The order of the polynomial approximation is set to  $p = 7$ . A set of grids is generated by progressively refining the discretization of the cylinder, while maintaining a constant element size in the far-field. The grid characteristics are summarized in Table 7.1 and

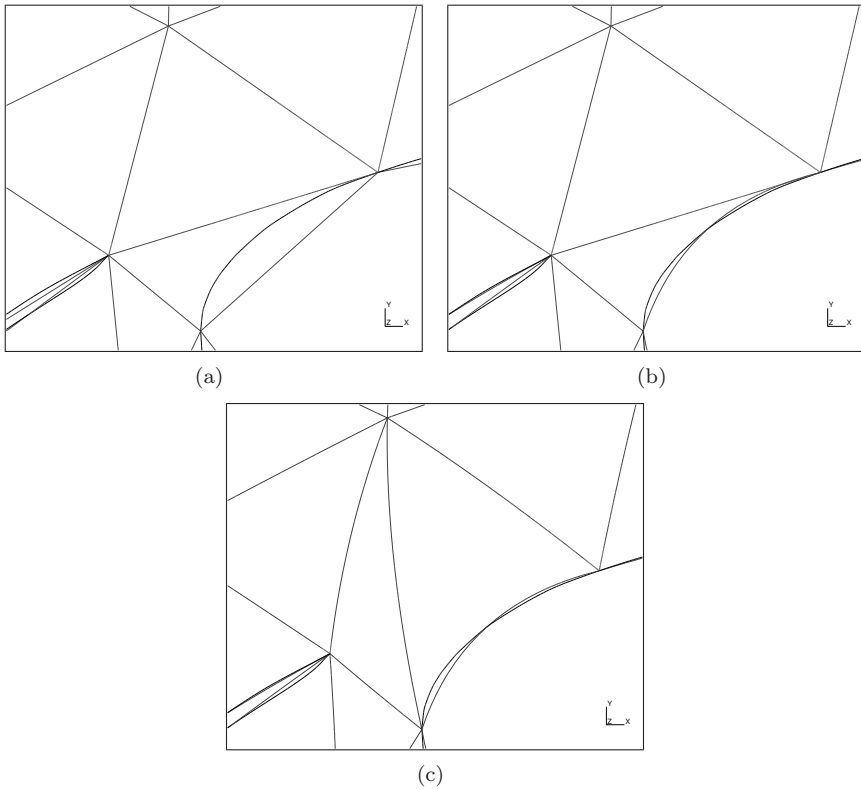


Figure 7.2: Detail of the meshing process close to the leading edge of the high-lift airfoil presented in Sec. 7.3.2: first-order mesh (a), primary second-order mesh (b) and smoothed second-order mesh (c).

the nomenclature of the test cases is explained in Table 7.2. The simulations are run until a non-dimensional time of  $t = 10$ .

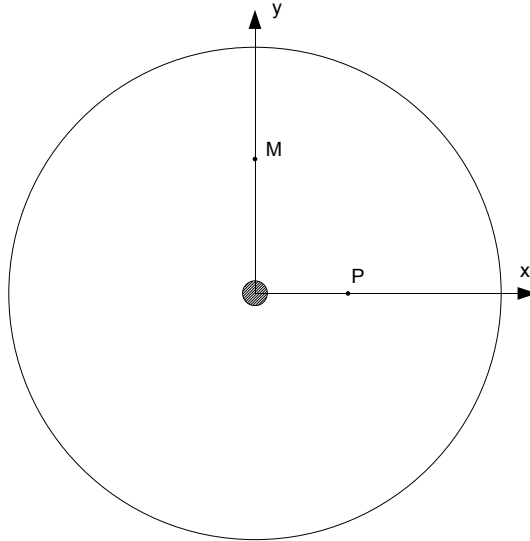


Figure 7.3: Computational domain for the 2D acoustic scattering problem.  $P(4,0)$  is the center of the pulse at initial time,  $M(0,5)$  is the point where the pressure is monitored.

Grid Name	Vertices on the Cylinder	Vertices	Elements
C4	4	924	1738
C8	8	1373	2636
C12	12	1618	3122
C16	16	1877	3636
C18	18	2030	3940
C20	20	2153	4184

Table 7.1: Characteristics of grids used for the 2D acoustic scattering problem.

In order to assess the effect of geometry discretization and wall boundary treatment on the quality of the solution, the pressure is monitored at point  $(0, 5)$  and compared with the analytical solution. The reference solution features a first maximum at about  $t = 6.3$ , corresponding to the direct field, and a second maximum at  $t = 8.2$ , corresponding to the scattered field.

Fig. 7.4 shows the results of computations with the linear boundary treatment on grids C4, C8 and C16. In all cases, the direct pulse is well resolved.

All grids are thus sufficiently refined to eliminate spurious dissipation and dispersion. However, a relatively large error in phase and amplitude appears in the scattered field on grid C4, and the results converge toward the reference data with geometry refinement. At  $p = 7$ , the accuracy is thus limited by the rough modeling of the cylinder.

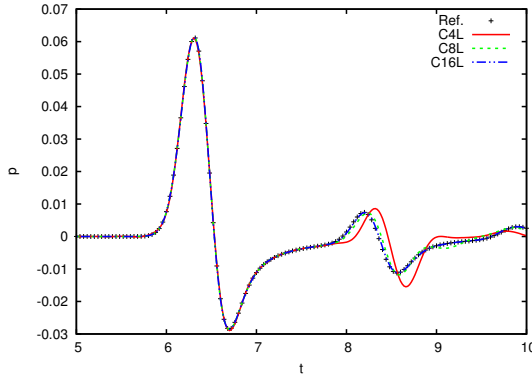


Figure 7.4: Pressure at point (0,5) with linear boundary treatment on grids C4, C8 and C16 for the 2D acoustic scattering problem.

Fig. 7.5 shows the effect of higher-order boundary treatments on the scattered field with the coarsest grid C4. With this mesh, the mixed treatment does not significantly improve the accuracy (although it can prove useful on more refined grids, see Ref. [138]). The full quadratic treatment, on the other hand, yields a significant improvement: as the cylinder geometry is well represented by the quadratic boundary, the phase error is suppressed. This is the reason why the solution for case C4Q is even more accurate than results obtained on refined grids with other boundary treatments, as shown in Table 7.3, that gives

Test Case Name	Grid Name	Bnd. Treatment
C4L	C4	Linear
C4M	C4	Mixed
C4Q	C4	Quadratic
C8L	C8	Linear
C8M	C8	Mixed
C12L	C12	Linear
C16L	C16	Linear
C18L	C18	Linear
C20L	C20	Linear

Table 7.2: Nomenclature of test cases for the 2D acoustic scattering problem.

an overview of the accuracy of various simulations in the scattered field. One can note that 18 linear boundary elements (case C18L) are needed to achieve a similar accuracy as with 4 quadratic boundary elements (case C4Q), i.e. 4.5 times more. This ratio cannot be generalized to other test problems, as it depends on how well the real geometry is approximated by second-order edges.

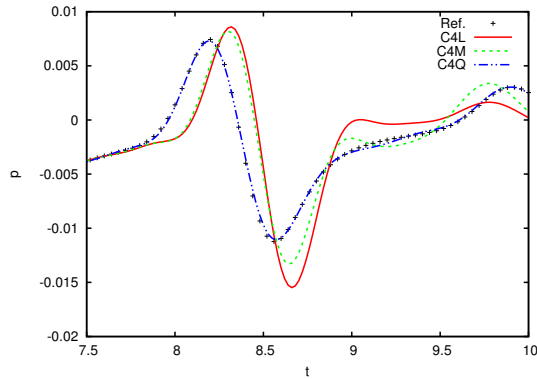


Figure 7.5: Pressure at point (0,5) with different boundary treatments on grid C4 for the 2D acoustic scattering problem.

Case Name	Error
C4L	$2.78 \cdot 10^{-5}$
C4M	$1.83 \cdot 10^{-5}$
<b>C4Q</b>	<b><math>7.73 \cdot 10^{-8}</math></b>
C8L	$2.63 \cdot 10^{-6}$
C8M	$1.46 \cdot 10^{-6}$
C12L	$4.51 \cdot 10^{-7}$
C16L	$1.28 \cdot 10^{-7}$
<b>C18L</b>	<b><math>7.77 \cdot 10^{-8}</math></b>
C20L	$5.04 \cdot 10^{-8}$

Table 7.3:  $L_2$  error in pressure at point (0,5) over the time interval [7.5, 10] for some cases of the 2D acoustic scattering problem.

### 7.3.2 Sound Propagation around a High-Lift Airfoil

The influence of higher-order wall boundary treatments is assessed on the problem of a high-lift airfoil. The geometry is a 3-element airfoil based on the RA16SC1 profile, with the slat and flap deflected by  $30^\circ$  and  $20^\circ$  respectively.

The chord of the main element is 480 mm, and the computational domain is a disc of radius 1000 mm centered on a point P located close to the trailing edge. The acoustic excitation consists of a monopole source placed at point P, with the following source terms:

$$p_s = c_0^2 \rho_s = A \cdot \cos(2\pi f \cdot t) \cdot e^{-(\ln 2) \frac{(x-x_P)^2 + (y-y_P)^2}{b^2}}$$

$$u_{1s} = u_{2s} = 0$$

with

$$c_0 = 340 \text{ m} \cdot \text{s}^{-1}$$

$$b = 3 \text{ mm}$$

$$A = 1 \text{ Pa}$$

$$f = 7816 \text{ Hz}$$

No mean flow is applied and characteristic-based non-reflecting boundary conditions are imposed at the outer limits of the computational domain shown in Fig. 7.6. Four different grids are generated: the element size remains constant in the far-field, while the geometry is increasingly refined, particularly around curved parts of the geometry such as the slat, the leading edge of the main element and the leading edge of the flap (see Fig. 7.7). The grid characteristics are summarized in Table 7.4. Order  $p = 7$  is used for the 6 simulations whose parameters are listed in Table 7.5. The simulations are run until a periodic regime is reached. The results obtained with the finest grid are taken as reference data. Fig. 7.8 shows the corresponding pressure field. The pressure is measured along a circle of radius 750 mm, centered at point P, in order to evaluate the influence of the boundary treatment on sound directivity.

Grid	Vertices	Elements
1	1819	3479
2	2481	4781
3	3397	6585
Ref.	6790	13239

Table 7.4: Characteristics of grids used for the high-lift airfoil case.

The directivity of the sound pressure level for grids 1, 2 and 3 with the linear treatment can be seen in Fig. 7.9. The results obtained on the coarse grid 1 do not match well the reference data, especially in the  $[\pi/2, \pi]$  and  $[-\pi/2, 0]$  quadrants; computations with a refined geometry discretization yield better results.

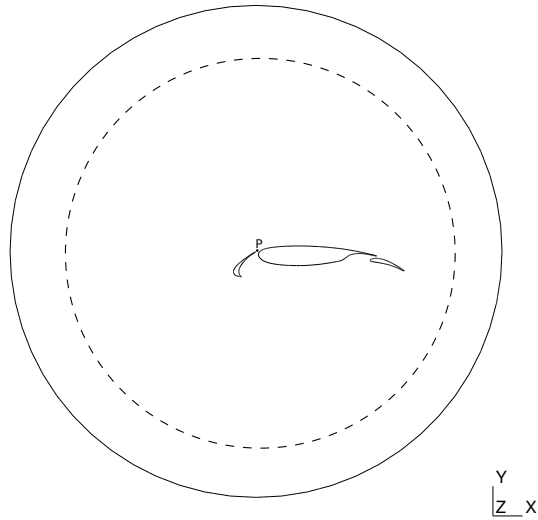


Figure 7.6: Computational domain for the high-lift airfoil problem. Solid lines are the boundaries of the domain, the dashed line represents the surface where the pressure is monitored. Point P is the center of the domain where the acoustic monopole source is located.

Test Case	Grid	Bnd. Treatment
1L	1	Linear
1M	1	Mixed
1Q	1	Quadratic
2L	2	Linear
3L	3	Linear
Ref.	Ref.	Linear

Table 7.5: Computation parameters used for the high-lift airfoil case.

Fig. 7.10 shows the effect of higher-order boundary treatments on the coarsest grid 1. Similarly to the 2D cylinder problem, the mixed treatment does not significantly improve the accuracy, whereas the solution with the quadratic treatment is in excellent agreement with the reference data. Table 7.6 indicates the time step, as well as an estimation of the CPU time and memory requirements, for each computation. It can be noted that the quadratic treatment only has a minor additional computation cost in view of the improvement that it brings in accuracy. Although it achieves a lower accuracy than case 1Q, case 3L has a higher computation cost, due to the higher number of elements involved and the smaller time step, that is linked to the small element size. In grids 1 and 2, the smallest element size is limited by the size of gaps between wing elements, which explains the similar time steps with grids 1 and 2. Without such geometrical constraints, case 1Q would be even more

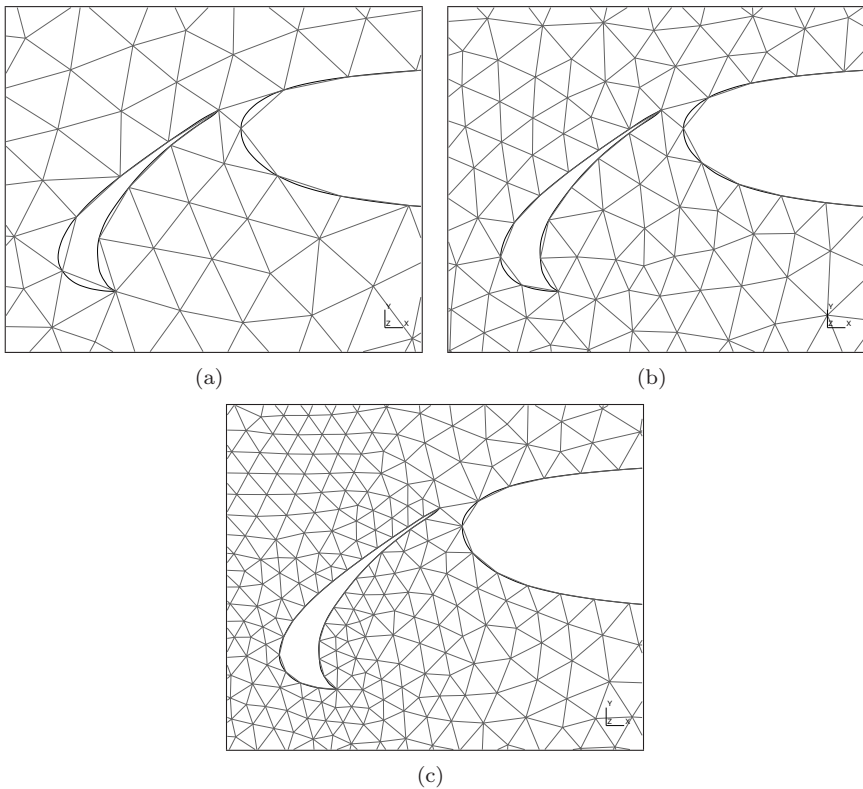


Figure 7.7: Details of grids 1 (a), 2 (b) and 3 (c) close to the slat and the nose of the main element of the high-lift airfoil.

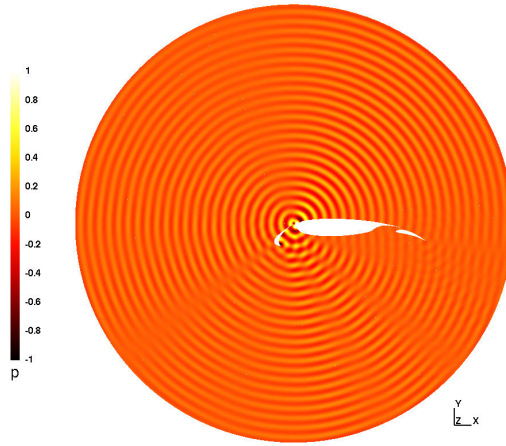


Figure 7.8: Reference pressure field for the high-lift airfoil case.

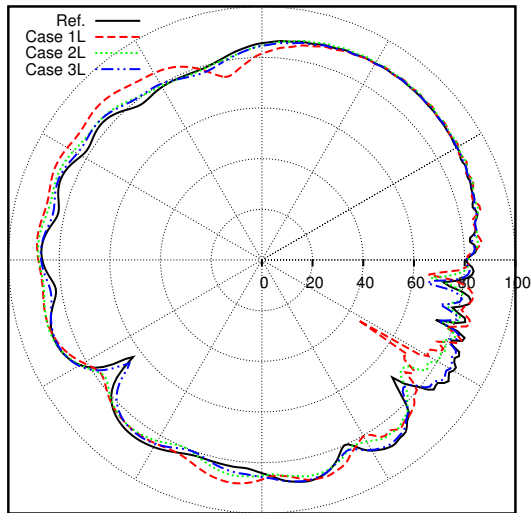


Figure 7.9: Directivity of the sound pressure level (dB) for the high-lift airfoil case: effect of grid refinement.

advantageous in terms of CPU time, because it would allow for a larger time step.

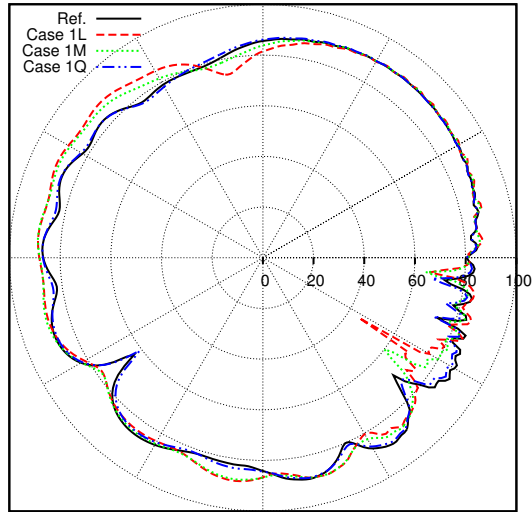


Figure 7.10: Directivity of the sound pressure level (dB) for the high-lift airfoil case: comparison between the linear, mixed and quadratic treatments on the coarsest grid.

Test Case	Time Step	CPU Time	Memory
1L	0.68	26 min	33.5 MB
1M	0.68	25 min	34.2 MB
1Q	0.64	28 min	36.0 MB
2L	0.67	35 min	45.2 MB
3L	0.36	1 h 31 min	61.4 MB

Table 7.6: Time step and approximate computational cost for each computation of the high-lift airfoil case.

### 7.3.3 Acoustic Scattering by a Sphere

In order to verify the validity of curved boundary conditions in 3D, the problem of sound scattering by a sphere is studied. The computational domain is a ball with a non-dimensional diameter of 20, containing a rigid sphere of diameter 2 centered at the origin. A monopole source is located at point  $(2, 0, 0)$ , so that

the source terms are:

$$p_s = \rho_s = \cos(\omega t) \cdot e^{-(\ln 2) \frac{(x-2)^2 + y^2}{b^2}}$$

$$u_{1s} = u_{2s} = 0$$

where

$$\omega = \frac{5}{2}\pi$$

$$b = 0.25$$

The mean flow velocity is set to zero and characteristic-based non-reflecting boundary conditions are imposed in the far-field. The order of the polynomial approximation is set to  $p = 7$ . The characteristics of the different grids used for this problem are summarized in Table 7.7. They feature the same element size in the far-field, but differ in the discretization of the sphere. Table 7.8 explains the naming convention for the different configurations. The simulations are run until a periodic regime is reached. The pressure along the circle  $x^2 + y^2 = 25$  is measured to check the effect of the boundary treatment. The results on the finest grid with the linear boundary treatment are chosen as reference data.

Grid	Faces on the sphere	Vertices	Elements
S8	8	4889	21553
S32	32	4854	21371
S94	94	5020	22272
Ref.	192	5636	25875

Table 7.7: Characteristics of grids used for the 3D acoustic scattering problem.

Test Case	Grid	Bnd. Treatment
S8L	1	Linear
S8Q	1	Quadratic
S32L	2	Linear
S94L	3	Linear
Ref.	Ref.	Linear

Table 7.8: Computation parameters used for the 3D acoustic scattering problem.

Fig. 7.11 shows the effect of grid refinement with the linear treatment. The computation with grids S8 and S32 exhibits a small error, whereas the results obtained with grid S94 are in good agreement with the reference data. Fig. 7.12 shows that the quadratic boundary treatment suppresses the error with the

coarse geometry discretization of grid S8. Table 7.9, that gives the time step and the approximate computational cost for each case, demonstrates that the improvement in accuracy brought by the quadratic boundary treatment comes for lower additional CPU time than with grid refinement. The higher computation time in case S92L is mainly due to a smaller time step, as the number of elements involved is similar to the other cases.

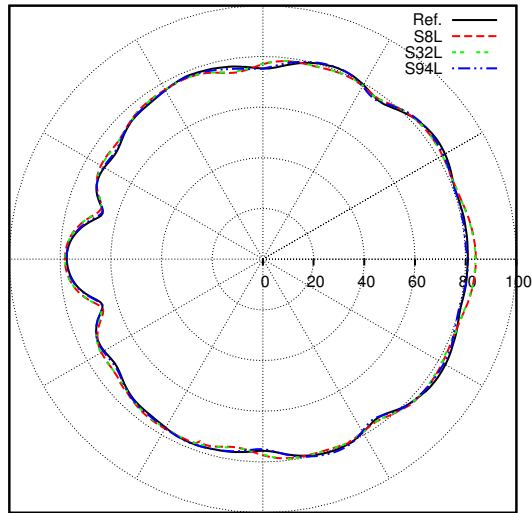


Figure 7.11: Directivity of the sound pressure level (dB) for the 3D scattering problem: effect of grid refinement.

Test Case	Time Step	CPU Time	Memory
S8L	0.015	13 h 25 min	786.4 MB
S8Q	0.015	13 h 29 min	937.0 MB
S32L	0.015	13 h 18 min	779.9 MB
S94L	0.010	20 h 41 min	812.0 MB

Table 7.9: Time step and approximate computational cost for each computation of the 3D scattering problem.

It should be mentioned that for this problem, increasing the frequency of the acoustic source would better illustrate the effect of the geometry discretization on sound scattering. Higher frequencies, however, are not investigated in this work because of the large requirements in computation time.

### 7.3.4 Transmission Loss of a Muffler

The last test problem involves an elliptical muffler with square inlet and outlet ducts, as shown in Fig. 7.13. The chamber has a length of 0.25 m, its elliptical section has a major semi-axis of 0.23/2 m and a minor semi-axis of 0.13/2 m. The reference solution for this configuration is computed by means of a modal expansion [39, 63].

A plane pressure pulse is specified as initial condition in the inlet duct:

$$p|_{t=0} = \rho|_{t=0} = e^{-(\ln 2) \frac{(z+0.21)^2}{0.01^2}} \quad (7.1)$$

$$u_1|_{t=0} = u_2|_{t=0} = 0 \quad (7.2)$$

No mean flow is applied and characteristic-based non-reflecting boundary conditions are applied in the inlet and outlet sections. The different grids, whose characteristics are given in Table 7.10, differ in the refinement of the chamber geometry. Order  $p = 5$  is used in all cases, except for grid 4 that is fine enough to use order  $p = 4$  without significant dissipation nor dispersion over the frequency range considered. An overview of the different configurations is given in Table 7.11.

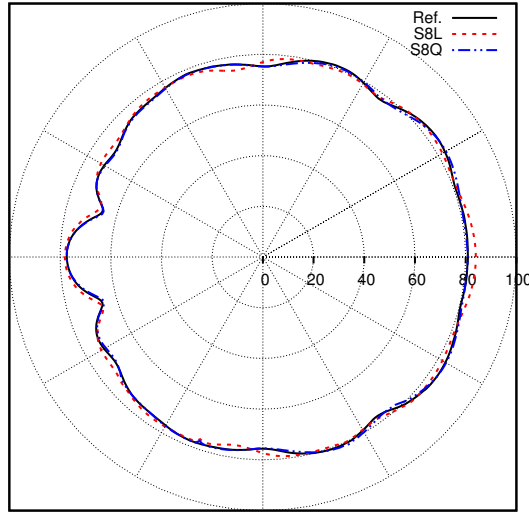


Figure 7.12: Directivity of the sound pressure level (dB) for the 3D scattering problem: effect of the boundary treatment.

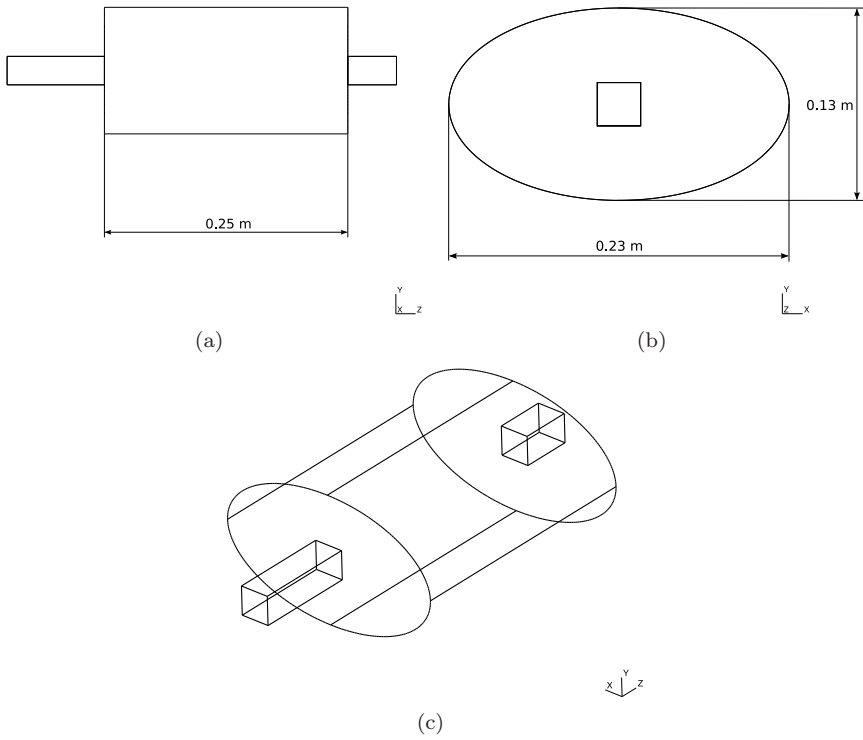


Figure 7.13: Geometry for the muffler problem.

Grid	Vertices	Elements
1	75	199
2	114	325
3	223	698
4	432	1322

Table 7.10: Characteristics of grids used for the muffler problem.

Test Case	Grid	$p$	Bnd. Treatment
1L	1	5	Linear
1Q	1	5	Quadratic
2L	2	5	Linear
3L	3	5	Linear
4L	4	4	Linear

Table 7.11: Computation parameters used for the muffler problem.

The pressure is measured at two points  $P_1$  and  $P_2$  in the inlet duct and two points  $P_3$  and  $P_4$  in the outlet duct until time  $t = 7.35 \cdot 10^{-2} s$ , when most of the acoustic energy introduced by the initial pulse has been propagated out of the system. After translation into the frequency domain by means of Fast Fourier Transforms, these values are used to calculate the amplitude of right-traveling ( $p^+$ ) and left-traveling ( $p^-$ ) waves in the inlet and outlet ducts, assuming 1D propagation (below the cut-off frequency of about 5800 Hz):

$$\begin{bmatrix} p_{Inlet}^+ \\ p_{Inlet}^- \end{bmatrix} = \begin{bmatrix} e^{-ikz_1} & e^{ikz_1} \\ e^{-ikz_2} & e^{ikz_2} \end{bmatrix}^{-1} \cdot \begin{bmatrix} p_1 \\ p_2 \end{bmatrix}$$

$$\begin{bmatrix} p_{Outlet}^+ \\ p_{Outlet}^- \end{bmatrix} = \begin{bmatrix} e^{-ikz_3} & e^{ikz_3} \\ e^{-ikz_4} & e^{ikz_4} \end{bmatrix}^{-1} \cdot \begin{bmatrix} p_3 \\ p_4 \end{bmatrix}$$

The transmission loss of the muffler is then computed as:

$$TL = 20 \cdot \log \left( \frac{p_{Inlet}^+}{p_{Outlet}^+} \right)$$

Fig. 7.14 shows the effect of grid refinement on the computed transmission loss. At lower frequencies, the propagation through the chamber is longitudinal, so that it is not much affected by the discretization of the geometry. Resonances at 680 Hz, 1360 Hz, 2040 Hz and 2720 Hz, corresponding to longitudinal modes, are captured by all grids. The geometry discretization strongly affects the simulation of transversal modes that appear above 1500 Hz, and only the finer grids yield accurate results over the whole frequency range considered.

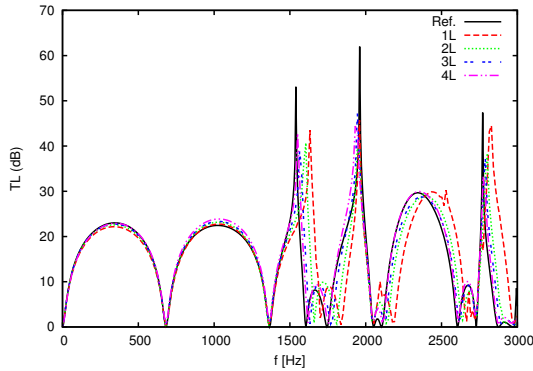


Figure 7.14: Transmission loss for the muffler problem: effect of grid refinement.

The improvement in accuracy obtained by the use of the quadratic treatment on the coarsest grid (case 1Q) is shown in Fig 7.15. The accuracy is comparable

to the one of the linear treatment applied to the finest grid (case 4L), whereas its computational cost is much lower, as shown in Table 7.12. In particular, the CPU time for case 1Q is about 4.4 time lower than for case 4L. As in the high-lift airfoil problem presented in Sec. 7.3.2, the time step of all simulations is constrained by the geometry of the inlet and outlet ducts, where the smallest elements are located. The absence of such geometrical restrictions would make the combination of curved boundary treatments and coarse grids even more advantageous over grid refinement in terms of computation time.

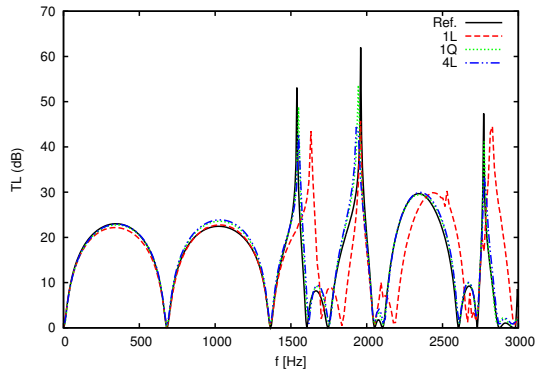


Figure 7.15: Transmission loss for the muffler problem: comparison between linear and quadratic boundary treatment.

Test Case	Time Step	CPU Time	Memory
1L	0.0012	41 min	8.5 MB
1Q	0.0012	42 min	21.0 MB
2L	0.0012	1 h 10 min	10.7 MB
3L	0.0011	2 h 48 min	17.3 MB
4L	0.0010	3 h 06 min	18.7 MB

Table 7.12: Time step and approximate computational cost for each computation of the muffler problem.

## 7.4 Conclusion

In this chapter, wall boundary treatments based on a second-order representation of the geometry have been introduced and studied. The simulation of various 2D and 3D problems of acoustic propagation has demonstrated that the accuracy at high order can be limited by the linear treatment of curved

geometries. The results of 2D cases show that the mixed treatment consisting in prescribing wall boundary conditions with normals to the quadratic geometry, while integrating over elements with straight edges, is of limited interest for aeroacoustic applications. The full quadratic treatment, involving curved elements, proves successful in increasing the accuracy with little additional computation cost for all test cases considered in this work.

The use of meshes featuring curved elements in the vicinity of curved wall boundaries makes it possible to employ a uniform grid density over the whole computational domain, without excessive refinement near the geometry, and is thus necessary to fully benefit from the efficiency of high-order DG methods. However, few methods for curved mesh generation are available today, and they still have to undergo development to reach satisfying standards in terms of robustness and grid quality.



## Chapter 8

# Acoustic Characterization of Orifices Under Grazing Flow

This chapter deals with the prediction of the acoustic behaviour of orifices under grazing flow by numerical means. The RKDG method described in Chap. 6 is used to solve the LNSE, as part of a hybrid approach where the steady, incompressible mean flow is previously obtained from a RANS simulation. A methodology involving a virtual impedance tube and two computations for each case (one with mean flow and one without) make it possible to isolate the contribution of the mean flow to the orifice impedance. The method is verified against theoretical models and experimental data from the literature, and is used to study the influence of orifice geometry variations on the mean flow contribution to the impedance.

## 8.1 Introduction

### 8.1.1 Context

Orifices in the wall of flow ducts, such as the one drawn in Fig. 8.1(a), are a common feature of industrial products. They can be found in sound attenuation devices such as mufflers for HVAC and automotive applications, or lining treatments for jet engines in the aeronautical industry. The presence of

perforations is sometimes dictated by other considerations than acoustic design, as in film cooling techniques for combustion chambers.

From a theoretical point of view, the acoustic behaviour of an orifice in a quiescent medium is relatively well understood. In the frequency range of interest, the wave length of acoustic fluctuations is usually much greater than the size of the opening, so that the waves can be considered as locally plane, with uniform pressure and velocity fluctuations over either side of the opening. It is then convenient to characterize the acoustic behaviour of the orifice through the jump of impedance between both sides. The dominating effect is a purely reactive response, that is induced by the inertia of the volume of fluid in the orifice considered as an incompressible air piston. However, the one-dimensional assumption is invalid in the vicinity of the opening: the variation of velocity at each of the two section discontinuities represents a mass insertion and an additional pressure drop. This can still be included in the one-dimensional model by virtually increasing the height of the fluid slab, that can be represented as a fictitious pipe emerging from the opening, as explained in Fig. 8.1. This *length correction* accounts for the influence of the orifice geometry. The one-dimensional model was first formalized by Rayleigh [120, Chap. XVI] in terms of acoustic conductivity.

In most of the aforementioned applications, the orifices cannot be considered to lie in a quiescent medium. The acoustic waves are fluctuations around a non-uniform flow, that is either grazing (i.e. tangential to the orifice), bias (i.e. flowing through the orifice), or a combination of both. It is a known fact that this mean flow influences significantly the acoustic properties of the orifices. In this chapter, the focus is on the case of orifices under grazing flow.

Such configurations have been the subject of many experimental investigations. Some of the most recent studies can be found in Ref. [41, 52, 80, 82, 92, 101, 112, 136]. The experimental results vary in a large extent, mainly because they address different orifice geometries and flow conditions [82]. Therefore, the resulting empirical models of orifice impedance lack generality [41, 112], particularly in the earlier works that did not consider the boundary layer characteristics [82]. Only a general trend at low Strouhal numbers is shared by all experimental studies: the grazing mean flow increases the orifice resistance and decreases the orifice reactance compared to the no-flow case.

The physical phenomena lying behind the mean flow effects are still not clearly understood [112], and can be interpreted in a number of ways [41]. Most of the theoretical models that have been proposed involve some type of empirical parameter [112], and agree only qualitatively with experimental data [41]. A purely theoretical method has been derived by Howe [64, 65, 66], Howe et al. [67]. It is based on the linear perturbation of an infinitely thin vortex sheet spanning

the aperture, which models the interaction between the acoustic fluctuations and the unstable shear layer that conveys the vortices shed at the upstream edge. This model has been adapted in Ref. [54] to handle different orifice geometries, and in Ref. [75, 113] to take into account the finite thickness of the shear layer. This theory predicts, at least qualitatively, the alternating frequency ranges of sound absorption and sound generation for a number of cases.

Numerical simulation can help understanding the underlying physical phenomena, as it enables the direct visualization and measurement of the small-scale flow features, while being significantly easier and cheaper to set up than experimental studies. It is relatively widespread in the adjacent field of cavity noise [129]. Resonators for lining applications have been investigated through DNS [134, 135], and perforated plates for cooling purpose through LES [43, 106]. The acoustic response of shear layers has been predicted in systems like T-joints [102] and corrugations in ducts [108] by combining incompressible flow simulations with vortex sound theory. A hybrid method combining incompressible CFD computations with frequency-domain linearized simulations has been applied to several configurations in ducts [81]. However, no numerical study focusing on the case of an orifice in grazing flow has been carried out, to our knowledge. The work described in this chapter aims at showing that numerical methods, in particular the RKDG method developed in Chap. 6, can be used to study the acoustic properties of orifices under grazing flow.

## 8.1.2 Impedance and Related Quantities

The acoustic impedance of a medium on a surface of area  $S$  is expressed as:

$$Z = \frac{p}{Su}$$

where  $p$  and  $u$  are the amplitude of the acoustic pressure and velocity fluctuations respectively. The concept of impedance is particularly useful when combined with the plane wave assumption, as in pipe systems operating below their cut-off frequency. In this case, the impedance is used to characterize the system as an acoustic filter [107, Chap. 1]. Small elements of the system, as the orifice pictured in Fig. 8.1(a), can be modeled in a lumped manner by an impedance jump  $\Delta Z = Z^+ - Z^-$ , even if they locally break the one-dimensional assumption.

Rayleigh [120, Chap. XVI] studied the problem of an orifice of thickness  $H$ , as drawn in Fig. 8.1. The assumption of incompressible acoustic flow, justified

by the small size of the opening, allowed him to formulate the conductivity  $K_R$  using the velocity potential. Considering harmonic waves with a time dependence in the form  $e^{i\omega t}$ , the conductivity  $K_R$  can be related to the impedance jump as:

$$\Delta Z = -i\omega\rho_0 \frac{1}{K_R}$$

If the incompressibility assumption holds strictly, the value of  $K_R$  is purely real and:

$$K_R = \frac{S}{l}$$

where  $l = \delta^- + H + \delta^+$  is the *effective length* that represents the physical length  $H$  of the channel augmented with both end corrections  $\delta^-$  and  $\delta^+$ . In the more general case of an element that is both resistive and reactive, the

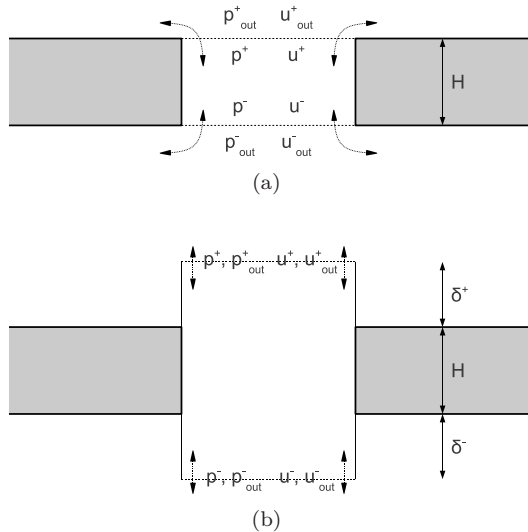


Figure 8.1: Orifice in a plate of thickness  $H$  in free field. Actual orifice (a): the plane-wave acoustic variables are not continuous across the opening at both sides,  $(\cdot)^+ \neq (\cdot)_{out}^+$  and  $(\cdot)^- \neq (\cdot)_{out}^-$ , because the acoustic flow is not one-dimensional in the vicinity of the edges. Model of Rayleigh (b): a fictitious pipe with corrected lengths  $\delta^+$  and  $\delta^-$  accounts for the mass insertion and additional pressure drop, in order to recover the continuity of plane-wave acoustic variables,  $(\cdot)^+ = (\cdot)_{out}^+$  and  $(\cdot)^- = (\cdot)_{out}^-$ .

lumped impedance jump  $\Delta Z$  can be reformulated as:

$$\Delta Z = -\frac{Z_0}{S} (r + ikl) \quad (8.1)$$

where  $r$  is a non-dimensional acoustic resistance,  $k = \omega/c_0$  is the wavenumber, and  $Z_0 = \rho_0 c_0$  is the specific impedance of the medium.

For the orifice drawn in Fig. 8.1(a), the impedance at either side of the element is defined as  $Z^+ = p_{out}^+/Su_{out}^+$  and  $Z^- = p_{out}^-/Su_{out}^-$ , because the plane-wave amplitudes ( $p_{out}, u_{out}$ ) are directly measurable and include the end corrections.

## 8.2 Method

In this work as in most of the studies in the literature, the focus is on orifices in plates that are subject to a grazing mean flow only on one side. This work is also restricted to two-dimensional geometries. Thus, the results should be representative of slit orifices in the high aspect ratio limit. To our knowledge, the most similar geometries that have been investigated in the literature are those of Ref. [52] and, to a lesser extent, Ref. [82]. In this section, the configuration that is most appropriate for the measurement of the impedance is first determined. Then, the cases to be studied are precisely defined, and the numerical methodology is described.

### 8.2.1 Impedance Measurement and Configuration

Considering an orifice through an infinite plate in free field, the most obvious manner to determine the lumped impedance  $\Delta Z$  from a simulation is to measure the quantities ( $p_{out}, u_{out}$ ) at either side of the orifice, and to directly calculate the impedances  $Z^+$  and  $Z^-$ . This is difficult or even impossible to put in practice experimentally, but is easily achieved in a numerical approach. However, it is not clear where the measure points shall be located. If they are placed too close to the orifice, they fall in the region where the acoustic flow is not one-dimensional, and the measured acoustic fluctuations do not represent the plane-wave amplitudes ( $p_{out}, u_{out}$ ). If they are placed too far from the opening, the measured variables do not correspond to the impedance of the orifice only. Moreover, the non-uniform mean flow in the vicinity of the orifice creates vorticity perturbations, that are measured along with the acoustic fluctuations. In the shear layer, the vorticity mode can even dominate. While it is possible to extract the acoustic information from such measurements [37], the splitting procedure is complex.

Therefore, the orifice impedance is measured indirectly by means of an impedance tube in this work, as in several experimental studies [41, 52, 82]. For this purpose, the side of the orifice that is not subject to grazing flow is set at the end of a tube of width  $L_{tu}$  and length  $H_{tu}$ , as shown in Fig. 8.2. A Gaussian plane pulse is introduced in the tube through its open end (i.e. the lower one), and the pressure is measured in two points  $P_1$  and  $P_2$  until all the acoustic energy has been propagated away from the system or dissipated. Care is taken to place  $P_1$  and  $P_2$  far enough from the orifice to avoid any mean flow influence, so that only acoustic fluctuations are measured. After obtaining the pressure fluctuations  $p_1$  and  $p_2$  in the frequency domain through Fast Fourier Transforms, the amplitude of up-traveling ( $p_+$ ) and down-traveling ( $p_-$ ) waves are calculated as:

$$\begin{bmatrix} p_+ \\ p_- \end{bmatrix} = \begin{bmatrix} e^{-\imath ky_1} & e^{\imath ky_1} \\ e^{-\imath ky_2} & e^{\imath ky_2} \end{bmatrix}^{-1} \cdot \begin{bmatrix} p_1 \\ p_2 \end{bmatrix}$$

The reflection coefficient at the orifice is then  $p_-/p_+$ , and the impedance at the opening can be calculated as:

$$Z^- = \frac{Z_0}{S_{tu}} \cdot \frac{p_+ + p_-}{p_+ - p_-} \tag{8.2}$$

where  $S_{tu}$  is the area of the tube cross-section.

In order to isolate the effect of the mean flow on the acoustic properties of the orifice, the lumped impedance jump  $\Delta Z$  is split:

$$\Delta Z = \Delta Z_G + \Delta Z_F$$

where  $\Delta Z_G$  is the no-flow part depending only on the geometry of the orifice, and  $\Delta Z_F$  is the contribution of the mean flow. Now, as the radiation impedance is the same with or without mean flow,  $Z^+ = Z_G^+$ . Recalling Eq. (8.1), one can write:

$$\Delta Z_F = Z_G^- - Z^- = -\frac{Z_0}{S} (r_F + \imath k \delta_F)$$

where  $r_F$  and  $\delta_F$  are the contribution of the mean flow to the non-dimensional resistance and the end correction respectively. This calculation thus requires two simulations for each case: one without mean flow to obtain  $Z_G^-$ , and one with mean flow to obtain  $Z^-$ . Using Eq. (8.2),  $r_F$  and  $\delta_F$  can be expressed directly as:

$$r_F = \frac{S}{S_{tu}} \Re \left( \left[ \frac{p_+ + p_-}{p_+ - p_-} \right] - \left[ \frac{p_+ + p_-}{p_+ - p_-} \right]_G \right)$$

$$\delta_F = \frac{S}{k S_{tu}} \Im \left( \left[ \frac{p_+ + p_-}{p_+ - p_-} \right] - \left[ \frac{p_+ + p_-}{p_+ - p_-} \right]_G \right)$$

In 2D, the ratio of areas reduces to the ratio of dimensions  $S/S_{tu} = L/L_{tu}$ .

Finally, the influence of the mean flow on the acoustic behaviour of the orifice is characterized through the *scaled* non-dimensional quantities  $\tilde{r}_F$  and  $\tilde{\delta}_F$  [52]:

$$\tilde{r}_F = \frac{r_F}{M_\infty}$$

$$\tilde{\delta}_F = \frac{\delta_F}{L}$$

where  $M_\infty = U_\infty/c_0$  is the free-stream Mach number, and  $U_\infty$  is the free-stream mean flow velocity. The use of  $\tilde{r}_F$  and  $\tilde{\delta}_F$  is dictated by the fact that these quantities depend only on the Strouhal number  $St = \omega L/U_\infty$  and on the shear layer parameters, according to the theory of Howe et al. [67].

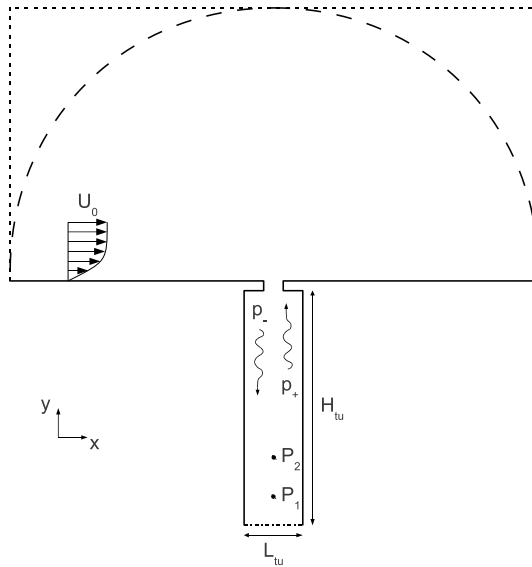


Figure 8.2: Schematic view of the computational domain for the orifice case. Thick solid line: plate, orifice and tube wall boundaries. Dotted line: free-field boundary for the mean flow simulation. Dashed line: free-field boundary for the acoustic simulation. Dashed-dotted line: open end boundary of the tube.

## 8.2.2 Cases

In this work, various orifice and tube geometries are studied. In particular, we consider several tube widths, orifice lengths and plate thicknesses. The effect

of round edges, both upstream and downstream, is also assessed. The relevant geometrical parameters are defined in Fig. 8.3.

The geometries investigated in this work are listed in Table 8.1, along with the corresponding Reynolds number  $Re$  based on the inlet mean flow velocity and the orifice length. In all cases, the kinematic viscosity is  $1.461 \cdot 10^{-5}$ , and the inlet mean flow velocity is set to 5 m/s. This relatively low velocity is intended to avoid non-linear phenomena (see Sec. 8.2.3). The simulations are set up in such way that the boundary layer thickness  $\delta$  is approximately 24 mm at the orifice, which enables a fair comparison with the experimental results of Ref. [52], where  $\delta$  lies between 10.9 mm and 38.4 mm.

Case	$H$	$L$	$R_{up}$	$R_{down}$	$L_{tu}$	$Re$
1	1	7	0	0	14	2396
2	1	7	0	0	21	2396
3	1	7	0	0	28	2396
4	1	14	0	0	28	4791
5	1	21	0	0	28	7187
6	2	7	0	0	14	2396
7	4	7	0	0	14	2396
8	2	7	0.75	0	14	2396
9	2	7	1.5	0	14	2396
10	2	7	0	0.75	14	2396
11	2	7	0	1.5	14	2396

Table 8.1: Characteristics of the orifice cases simulated. All dimensions are expressed in millimeters.

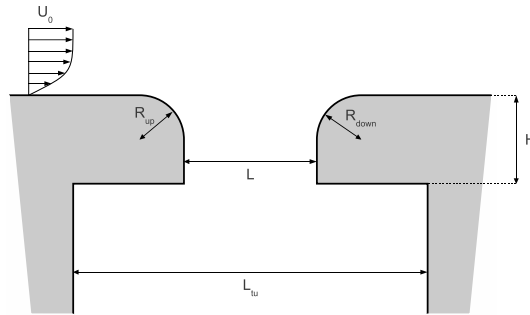


Figure 8.3: Orifice geometry.

## 8.2.3 Numerical Methodology

### Linearity and Hybrid Approach

In a quiescent medium, the acoustic propagation is linear up to relatively high sound pressure levels. However, non-uniform flows can in general be subject to non-linear mechanisms of sound generation or damping. The presence or absence of non-linear phenomena is an important aspect in the choice of the simulation methodology.

The mean flow effect on the acoustic behaviour of orifices in grazing flows seems to be dominated by the shear layer instability [52]. The qualitative success of the linear theory of Howe et al. [67] tends to show that this effect is not non-linear in essence. The experimental study in Ref. [82] indicates that non-linear phenomena are triggered at lower sound amplitude around the instability frequency, but the acoustic response is still linear for low-amplitude excitations. As pointed out in Ref. [64, 113], the non-linear mechanisms result in the saturation of the shear layer oscillations, but do not significantly affect the instability frequency. Finally, Kirkegaard [81] successfully simulated the acoustic behaviour of similar configurations (orifice plates and area expansions in ducts) with a methodology involving linear governing equations.

These considerations support the fact that simulations based on the LEE or the LNSE are appropriate to study the acoustics of orifices under grazing flow. Thus, a hybrid methodology is chosen, in which the mean flow is first obtained from a steady, fully non-linear CFD simulation, and the linear acoustic computation is then performed by means of the numerical method presented in Chap. 6.

### Computational Domain

The computational domain for both simulations is shown in Fig. 8.2. The free-field region, located on the upper side of the plate, is defined by a rectangular boundary in the mean flow simulation and by a semi-circular boundary in the acoustic simulation. It extends from 1.5 m upstream to 1.5 m downstream of the orifice. This large size, compared to a typical orifice length of  $L = 10$  mm, is due to the necessity of attenuating the acoustic waves before they reach the boundaries in the acoustic simulation, in order to reduce the amplitude of spurious reflections.

On the lower side of the plate, only the impedance tube is included in the simulations. Thus, the impedance tube method has the advantage of reducing

the size of the computational domain compared to the determination of  $Z^-$  by direct measurement of  $p$  and  $u$  in free-field, so that the computational cost is lower. The length of the impedance tube is  $H_{tu} = 200$  mm.

### Mean Flow Simulation

The mean flow is obtained from a steady RANS simulation by means of the CFD software OpenFOAM [1]. The SST  $k-\omega$  turbulence model, that is solved all the way down to the wall without any specific wall modeling, is used.

The steady, incompressible flow is solved through the SIMPLE algorithm. The spatial discretization method is a standard FVM in which the convective terms are treated with upwind fluxes, while the diffusive terms are treated with central fluxes.

The upper side of the plate, the orifice and the tube walls that are represented by a no-slip boundary condition. The upper and downstream sides of the free-field region, as well as the tube lower end, are pressure outlets. The upstream side of the free-field region is a velocity inlet, that can be set to any velocity profile. In the present simulations however, the inlet velocity is set to a uniform profile, because the domain is just large enough for the boundary layer to grow and reach the desired thickness (about 24 mm) at the orifice. We use hybrid grids that are structured in the boundary layer and shear layer region, as well as in the orifice, while they are unstructured in the rest of the domain. An example of a grid in the region of the orifice is shown in Fig. 8.4. They contain between 27000 and 53000 cells, depending on the geometry of the orifice, and are built so that the non-dimensional wall distance  $y^+$  of the first cell is everywhere of the order of 1 or lower, in accordance with the requirements of the turbulence model.

The mean flow velocity and pressure around the orifice of Case 1 are plotted in Fig. 8.5. It can be seen that the flow over the orifice is mainly grazing, with a faint stagnation point on the downstream edge and little velocity in the opening. The weak character of the recirculation in the tube suggests that the mean flow effect on the acoustic behaviour should mainly depend on the shear layer over the orifice, and that the tube geometry should have little influence, as expected. The boundary layer parameters, listed in Table 8.2, are verified to be nearly identical for all cases.

Case	$U_\infty$	$\delta$	$\delta^*$	$\theta$	$H$
1	5.047	24.21	4.847	3.205	1.512
2	5.047	24.25	4.845	3.203	1.512
3	5.047	24.32	4.836	3.199	1.511
4	5.047	24.30	4.759	3.160	1.506
5	5.049	24.35	4.705	3.135	1.501
6	5.047	24.19	4.852	3.207	1.513
7	5.047	24.21	4.825	3.195	1.510
8	5.047	24.91	4.688	3.144	1.491
9	5.047	24.86	4.658	3.135	1.486
10	5.047	24.91	4.688	3.144	1.491
11	5.048	24.98	4.727	3.157	1.497

Table 8.2: Boundary layer characteristics at a distance  $L$  upstream from the orifice: free-stream velocity  $U_\infty$ , thickness  $\delta$ , displacement thickness  $\delta^*$ , momentum thickness  $\theta$  and shape factor  $H$ . All dimensions are expressed in millimeters, and the free-stream velocity  $U_\infty$  is expressed in meters per second.

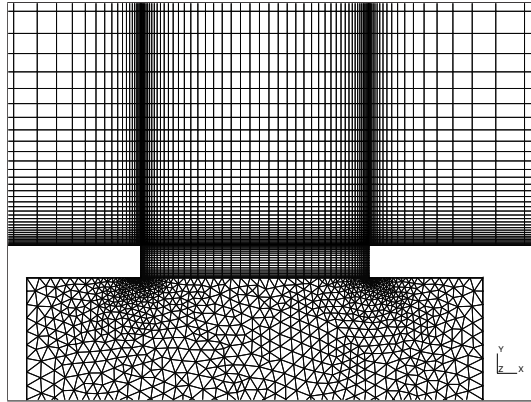


Figure 8.4: Detail of the CFD mesh in the region of the orifice.

## Acoustic Simulation

The acoustic simulation is performed through the numerical method described in Chap. 6. The LNSE are chosen as governing equations. Indeed, preliminary simulations with the LEE result in a very slow damping or even a growth of the shear layer oscillations, depending on the grid. Thus, the damping of the instability with the LEE is only due to numerical dissipation, and not to mean flow effects. This indicates that dissipative effects play a significant role in the evolution of the shear layer instability, so that the viscous terms must be included in the model to correctly predict the orifice impedance.

The wall on the plate upper side, in the orifice and in the tube are modeled with the slip boundary condition described extensively in Chap. 7. The free-field boundary and the open end of the impedance tube are subject to non-reflecting boundary conditions. Unstructured grids refined in the orifice and in the shear layer are used in order to correctly resolve the vortices. On the contrary, the strong grid stretching in the free-field region provides additional numerical dissipation that compensates for the limited performance of the non-reflecting boundary conditions by progressively damping the acoustic (and possibly vortical) disturbances before they reach the boundary. The grids are composed of 680 to 1150 elements, depending on the geometry of the orifice. An example of a grid in the region of the orifice is shown in Fig. 8.6. The order of the polynomial approximation is set to  $p = 4$ . A suitable high-order representation of the mean flow is obtained from the CFD results by using the least-square procedure presented in Sec. 6.2.3.

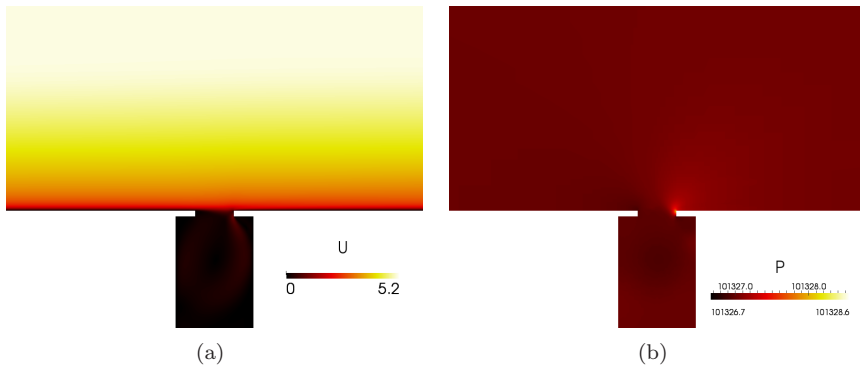


Figure 8.5: Detail of the mean flow around the orifice for Case 1: velocity magnitude (a) and pressure (b).

## 8.3 Results

In this section, the results obtained for the cases described in Sec. 8.2.2 are reported, focusing on the effect of the mean flow on the orifice impedance. The outcome of the acoustic simulations is mainly presented in terms of scaled non-dimensional resistance  $\tilde{r}_F$  and end correction  $\tilde{\delta}_F$ , in order to allow a fair comparison with theoretical and experimental data from the literature, as well as between cases with different geometries.

### 8.3.1 Verification

In order to ensure that the method described in Sec. 8.2 yields realistic results, the impedance calculated from the simulations is compared to theoretical and experimental data from the literature. The coherence of the impedance measurement method is also assessed by varying the tube geometry.

#### Comparison with Experiments

In order to better assess the correctness of the present simulations, the numerical results are first compared to the experimental data of Golliard [52]. The two orifice geometries of Cases 1 and 5, with straight edges and plate thickness  $H = 1$  mm, correspond exactly to those investigated experimentally. However, the boundary layer characteristics are not identical. The comparison in terms of scaled non-dimensional resistance  $\tilde{r}_F$  and end correction  $\tilde{\delta}_F$  is shown

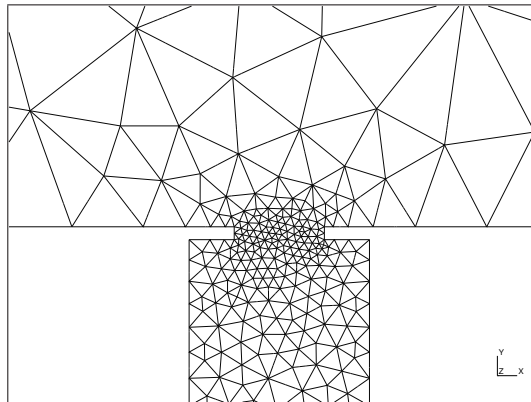


Figure 8.6: Detail of the acoustic mesh in the region of the orifice.

in Fig. 8.7 and 8.8, for orifices of lengths  $L = 7$  mm and  $L = 14$  mm respectively. Experimental results are plotted for four different boundary layers, of which the parameters are listed in Table 8.3. The qualitative behaviour of the numerical and experimental curves is the same, even if the higher-frequency peak of  $\tilde{r}_F$  and  $\tilde{\delta}_F$  in the  $L = 14$  mm case is not well predicted by the simulations. Bearing in mind that the experimental data shown in Fig. 8.7 and 8.7 represent averages of several runs, and that the results between runs vary in amplitude [52], the agreement with the numerical predictions can be considered as satisfying.

Name	$U_\infty$	$\delta$	$\theta$	$H$
B	39.9	10.9	1.1	1.28
C	39.4	16.3	1.9	1.38
E	38.4	32.0	4.0	1.38
F	39.8	38.4	4.0	1.38

Table 8.3: Experimental boundary layer characteristics, measured 28 cm upstream from the orifice [52]: free-stream velocity  $U_\infty$ , thickness  $\delta$ , momentum thickness  $\theta$  and shape factor  $H$ . All dimensions are expressed in millimeters, and the free-stream velocity  $U_\infty$  is expressed in meters per second.

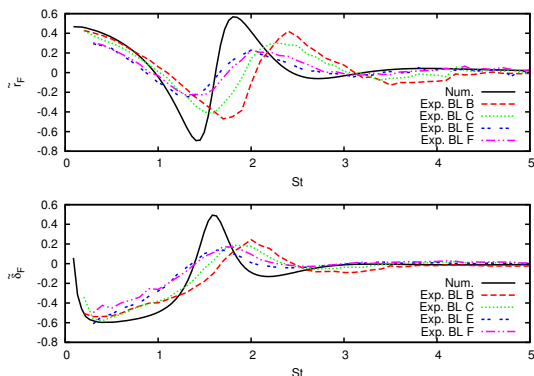


Figure 8.7: Scaled non-dimensional resistance  $\tilde{r}_F$  and end correction  $\tilde{\delta}_F$  for an orifice of length  $L = 7$  mm: comparison between the simulation and experimental results [52].

### Comparison with Theory

In a second step, the impedance results are compared with the theory of Howe et al. [67]. For a rectangular orifice subject to grazing flows of velocity  $U_+$  and

$U_-$  on the upper and lower side respectively, the Rayleigh conductivity can be expressed as:

$$K_R = \frac{\pi b}{2 [F(\sigma_1, \sigma_2) + \Psi]} \tag{8.3}$$

where  $b$  is the spanwise dimension of the orifice, and:

$$\sigma_1 = \frac{\omega L}{2} \frac{1 + \iota}{U_+ + \iota U_-}$$

$$\sigma_2 = \frac{\omega L}{2} \frac{1 - \iota}{U_+ - \iota U_-}$$

$$F = \frac{-\sigma_1 J_0(\sigma_2) [J_0(\sigma_1) - 2W(\sigma_1)] + \sigma_2 J_0(\sigma_1) [J_0(\sigma_2) - 2W(\sigma_2)]}{\sigma_1 W(\sigma_2) [J_0(\sigma_1) - 2W(\sigma_1)] - \sigma_2 W(\sigma_1) [J_0(\sigma_2) - 2W(\sigma_2)]}$$

with  $W(x) = ix[J_0(x) - \iota J_1(x)]$ ,  $J_0$  and  $J_1$  being Bessel functions. In this case, the velocities are set  $U_+ = U_\infty$ ,  $U_- = 0$ , and the function  $\Psi$  accounting for the acoustic environment of the orifice is [52]:

$$\Psi = \frac{1}{2} \left( -\gamma_E + \ln \frac{16}{\pi} + \ln \frac{Ltu}{L} + \ln \frac{1}{kL} \right)$$

where  $\gamma_E$  is Euler’s constant. As a 2D problem is considered, the resistance  $r$  and the end correction  $\delta$  are calculated from the conductivity per unit span  $K_R/b$ . Note that the function  $\Psi$  only accounts for the reactance of the orifice

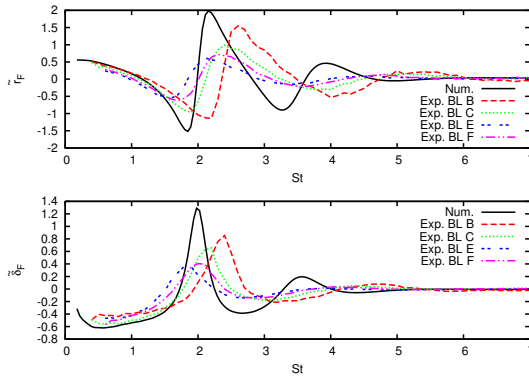


Figure 8.8: Scaled non-dimensional resistance  $\tilde{r}_F$  and end correction  $\tilde{\delta}_F$  for an orifice of length  $L = 14$  mm: comparison between the simulation and experimental results [52].

and its environment, and does not include the resistive part. Neglecting the acoustic boundary layers in the orifice, the geometry-related resistance is only caused by radiation. In a 2D space, the impedance of an acoustically compact ( $kL \ll 1$ ) plane radiator in a baffle wall can be calculated as [105, Chap. F.20]:

$$Z_{rad} = \frac{Z_0}{S} \frac{kL}{2}$$

The numerical, experimental and theoretical results are compared for Cases 1 and 4, for which the plate thickness is  $H = 1$  mm and the edges are straight. The numerical and theoretical impedances  $Z^-$  measured without mean flow are plotted in Fig. 8.9 in terms of scaled non-dimensional resistance and effective length. The numerical and theoretical predictions are in good agreement. In the high frequency range, the computed non-dimensional resistance  $\Re(Z^-) S/Z_0$  for the longer orifice deviates slightly from theory, which can be explained by the breakdown of the acoustic compactness assumption: at  $f = 3000$  Hz,  $kL = 0.39$ . The numerical impedance curves for both cases feature weak oscillations in the low frequency range, which may be due to the limited performance of the non-reflecting boundary conditions in the far field.

The numerical, experimental (with boundary layer E [52]), and theoretical results for the cases with mean flow are shown in Fig. 8.10 and 8.11. The theory of Howe et al. [67] predicts that the scaled non-dimensional resistance  $\tilde{r}_F$  and end correction  $\tilde{\delta}_F$  should be independent of the orifice geometry. This is not the case in the present simulations, nor in the experiments. The qualitative behaviour of the numerical and experimental results is similar, whereas have the theoretical results differ fundamentally. This is due to the crude approximations on which the theory relies (infinitely thin vortex sheet, zero plate thickness).

## Impedance Measurement Method

Finally, the reliability of the impedance measurement method is verified by performing simulations with different tube widths, while the orifice geometry is fixed (straight edges with  $L = 7$  mm and  $H = 1$  mm). The results of Cases 1, 2 and 3 are plotted in Fig. 8.12. The three tube widths yield very similar impedance curves, except in the very low Strouhal number range. However, they exhibit the expected behaviour in the low frequency limit, with a positive scaled resistance  $\tilde{r}_F$  corresponding to an increased absorption of sound, and a negative scaled end correction  $\tilde{\delta}_F$  that can be interpreted as the added mass of the end correction being “blown away” [52].

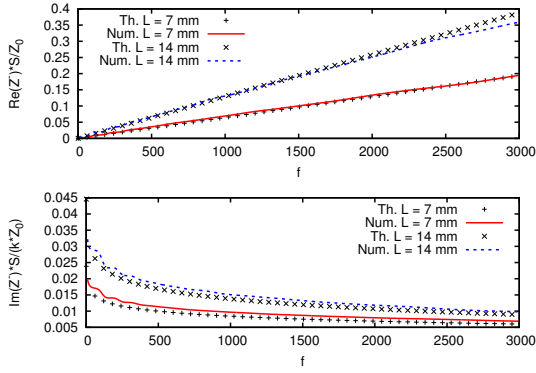


Figure 8.9: Scaled non-dimensional resistance  $\Re(Z^-)S/Z_0$  and effective length  $\Im(Z^-)S/kZ_0$  without flow for orifices of lengths  $L = 7$  mm and  $L = 14$  mm: comparison between the simulation and the theory [52, 67, 105].

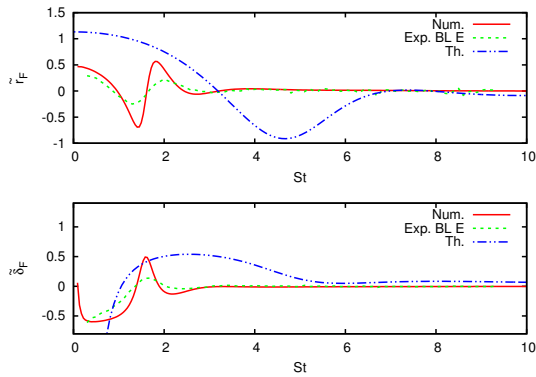


Figure 8.10: Scaled non-dimensional resistance  $\tilde{r}_F$  and end correction  $\tilde{\delta}_F$  for an orifice of lengths  $L = 7$  mm: comparison between the numerical, experimental [52] and theoretical [52, 67] results.

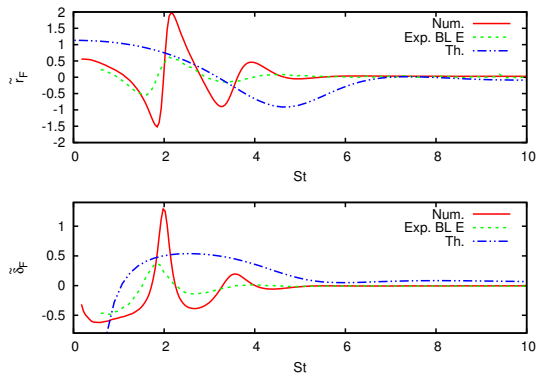


Figure 8.11: Scaled non-dimensional resistance  $\tilde{r}_F$  and end correction  $\tilde{\delta}_F$  for an orifice of lengths  $L = 14$  mm: comparison between the numerical, experimental [52] and theoretical [52, 67] results.

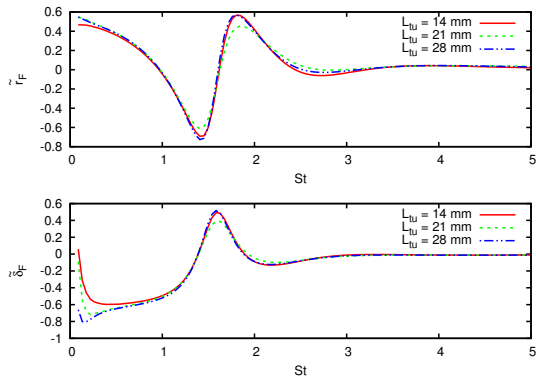


Figure 8.12: Scaled non-dimensional resistance  $\tilde{r}_F$  and end correction  $\tilde{\delta}_F$ : comparison between simulations with different tube widths.

### 8.3.2 Geometry Variations

After having verified the numerical methodology, the interaction of the geometry and the mean flow effects is investigated by examining the influence of geometry variations on the scaled non-dimensional resistance  $\tilde{r}_F$  and end correction  $\tilde{\delta}_F$ .

#### Orifice Length

First, a variation in orifice length is considered. Fig. 8.13 shows the results obtained with Cases 1, 4 and 5, corresponding to orifices of thickness  $H = 1$  mm with straight edges. As the orifice is enlarged, the number of oscillations increase, reaching higher Strouhal numbers, and their amplitude grows. This effect has also been observed in experimental studies [52, 82]. The Strouhal number shift is due to the fact that the upper frequency limit for instabilities of a shear layer depends only on its momentum thickness and exterior velocity. The boundary layers being identical in all three cases, the shear layers are unstable in the same frequency range that corresponds to higher Strouhal numbers for longer orifices, as can be seen in Fig. 8.14. Longer orifices enable lower-frequency oscillation modes of the vortex sheet in addition to those of higher-frequency, which explains the increased number of oscillations.

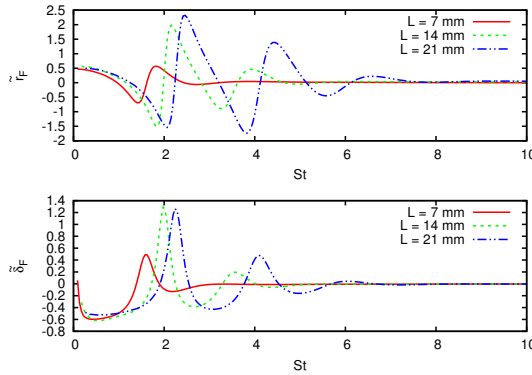


Figure 8.13: Scaled non-dimensional resistance  $\tilde{r}_F$  and end correction  $\tilde{\delta}_F$ : comparison between simulations with different orifice lengths  $L$ .

**Plate Thickness**

Fig. 8.15 shows the results of Cases 1, 6 and 7, that correspond to orifices of length  $L = 7$  mm with straight edges and varying plate thickness  $H$ . Although the effect of plate thickness on the frequency of the shear layer instability is unclear, the amplitude of the oscillations in scaled non-dimensional resistance  $\tilde{r}_F$  and end correction  $\tilde{\delta}_F$  seem to slightly decrease with increasing thickness.

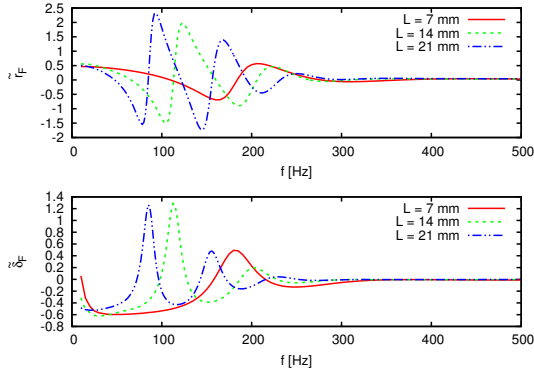


Figure 8.14: Scaled non-dimensional resistance  $\tilde{r}_F$  and end correction  $\tilde{\delta}_F$  as functions of the frequency  $f$ : comparison between simulations with different orifice lengths  $L$ .

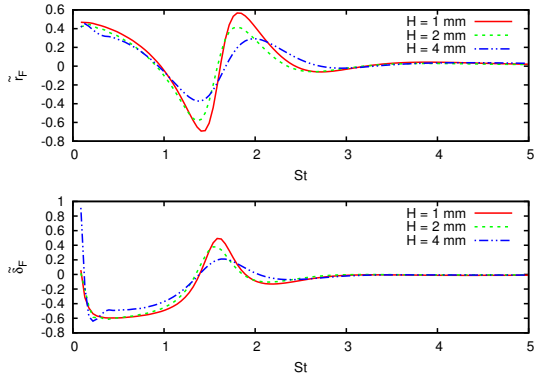


Figure 8.15: Scaled non-dimensional resistance  $\tilde{r}_F$  and end correction  $\tilde{\delta}_F$ : comparison between simulations with different plate thicknesses  $H$ .

## Edge Rounding

Finally, the effect of edge rounding is evaluated by considering Cases 6, 8, 9 10 and 11, that correspond to orifices of length  $L = 7$  mm and a plate thickness of  $H = 2$  mm. As can be seen in Fig. 8.16, the influence of edge rounding on the amplitude of the oscillations is not obvious. However, the frequency of the shear layer instability seems to be slightly decreased by rounding the upstream edge. The  $\tilde{r}_F$  and  $\tilde{\delta}_F$  curves are less affected by rounding the downstream edge. This seems logical, as the vortices that result from the shear layer instability are shed from the upstream edge.

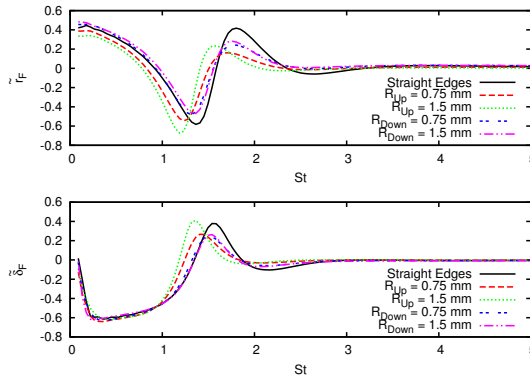


Figure 8.16: Scaled non-dimensional resistance  $\tilde{r}_F$  and end correction  $\tilde{\delta}_F$ : comparison between simulations with different edges.

## 8.4 Conclusion

In this chapter, a numerical methodology for the prediction of the acoustic properties of orifices under grazing flow has been presented. This hybrid approach consists of two steps. First, the steady, incompressible mean flow is simulated through a RANS solver. Then, the RKDG method described in Chap. 6 is used to solve the LNSE. The orifice is characterized acoustically by its impedance, expressed in terms of non-dimensional resistance and end correction, which is indirectly measured by means of a virtual impedance tube. The effect of the mean flow on the acoustic behaviour of the orifice is isolated by subtracting the results of a simulation without mean flow from the results of a simulation with mean flow for the same orifice geometry.

The method compares well with the theory for no-flow cases, but a large discrepancy is observed in presence of a mean flow, which is due to the fundamental shortcomings of the theoretical model. The agreement with experimental data, measured for the same orifice geometries but under different boundary layers, is much better. The method has also been used to study the interaction between the orifice geometry and the mean flow effect. The consequence of increasing the orifice length correspond to experimental observations from the literature. However, the influence of varying plate thickness and rounded orifice edges on the mean flow effect seems to be limited.

The LNSE simulations have proved successful in predicting the behaviour of the instable shear layer that dominates the mean flow effect on the orifice impedance. However, these results are only representative of low amplitude excitations, whereas the higher noise level encountered in realistic applications may trigger nonlinear saturation phenomena. Moreover, these results have been obtained for a relatively low free-stream velocity. As the viscous effects seem to play an important role in the shear layer, the linear simulations may overestimate strength of the instability for higher free-stream velocities, due to the lack of turbulent dissipation. Nevertheless, these limitations may affect only the amplitude of the oscillations in the part of the impedance related to the mean-flow, so that the prediction of the instability frequencies should remain accurate.

## **Part IV**

# **Conclusion**



# Chapter 9

## Conclusion

### 9.1 Summary and Achievements

In Chap. 1, we have explained the context of our research work, and justified the choice of a RKDG numerical method to study linear aeroacoustic problems. From a discussion on the shortcomings of the RKDG method, four research goals have been defined.

#### 9.1.1 Method Description

Before reporting the research work, Chap. 2 has allowed us to formalize the RKDG method as a method of line associating the DG space discretization with RK time integration schemes. For this purpose, we have focused on the scalar advection equation, that is a simple model of the hyperbolic conservation laws governing linear aeroacoustics. The DG spatial scheme has been derived for triangular grids, considering two types of numerical fluxes, namely the Lax-Friedrichs flux and the upwind flux. We have described efficient implementation techniques that are based on nodal interpolation, and on a mapping of each element in the computational domain onto a unique reference element. These techniques enable a quadrature-free evaluation of the local mass, stiffness and face matrices, in case of straight elements. Then, the theory of RK schemes has been introduced for time integration. The second part of that chapter

is dedicated to the presentation of a technique for the stability and accuracy analysis of the numerical schemes. This technique, that exploits the periodicity of structured grid composed of congruent elements, is an essential part of the investigations related in Part II.

In Chap. 6, the equations that govern linear aeroacoustics problems have been introduced. Two systems of equations have been derived by linearization of the Navier-Stokes equations: the viscosity-free LEE, and the LNSE simplified by an isentropy assumption. The modes of fluctuation of these equations, obtained by characteristic decomposition, have been put in evidence. Then, the application of the RKDG method to the LEE and the LNSE has been described, including the basic discretization and two types of boundary conditions, namely the rigid wall and non-reflecting boundary conditions. We have also explained how the problems related to the interpolative nature of the spatial discretization can be circumvented. We have shown that the implementation verifies the theoretical grid convergence rate, and that the non-reflecting boundary conditions work correctly. Finally, both the LEE and the LNSE have shown good agreement with DNS data from the literature for a validation case involving a monopole in a boundary layer.

### 9.1.2 RKDG Stability Restrictions

The first research goal defined in Chap. 1 deals with the general understanding of the stability restrictions of RKDG methods, and the means to accurately determine the maximum allowable time step in practical simulations using unstructured grids. These issues have been addressed in Chap. 3 and 4.

In Chap. 3, the influence of the element shape on the CFL conditions has been investigated with several variants of the RKDG methods, including various RK schemes from the literature, and both types of numerical fluxes. First, the superior time stepping capabilities of the upwind flux compared to the Lax-Friedrichs flux have been confirmed. Then, we have identified two element size measures that are suited to CFL conditions for triangular grids, and the values of the corresponding maximum Courant number have been reported in Appendix B. We have shown that the qualitative influence of the element shape on the CFL condition is not strongly affected by the choice of the RK scheme, and we have given a general view of the relative performance of RK schemes in terms of maximum time step. Finally, two examples have confirmed these results, although they have proved that the CFL conditions can be significantly too restrictive compared to the global stability restrictions.

In Chap. 4, we have tried to go beyond the CFL conditions, that take into account the element shape only through one size parameter. Two methods

have been derived for the determination of the maximum time step with unstructured grids composed of straight triangular elements. The first one is a 3-step procedure based on a various assumptions related to the most dissipative mode of the discrete operator. It is only slightly superior to the CFL conditions, so that its benefit is questionable, in view of its complexity. The second method is based on the equivalence of the semi-discrete equations between the computational space and the reference space. It works only for the upwind flux, but can be considered as a superior alternative to the CFL conditions. Also, the impact of the element curvature on the stability restrictions has been investigated. It was found that the element curvature influences adversely the maximum allowable time step through the conditioning of the semi-discrete operator, but this effect could not be isolated and properly quantified.

Overall, the results obtained in these two chapters contribute to the comprehension of the stability restrictions on the time step of RKDG methods. The values of the maximum Courant number provided in Appendix B for use with the CFL conditions, as well as the advanced time step determination method for the upwind flux, can help users to set time step values closer to optimal, in order to reduce the computation time. Only the correct evaluation of the maximum time step with curved elements remains out of reach.

### 9.1.3 Optimized RK Schemes

The second research goal defined in Chap. 1 is to improve the computational efficiency of RKDG methods by deriving specially designed RK schemes. This is the subject of Chap. 5, in which the computational efficiency has been defined from the point of view of the user, as the computation time required to solve a problem with a given accuracy using the optimal combination of mesh and numerical method. This has allowed us to define objective measures of the error and the computation cost, which have been used in optimization procedures. Two main scenarios have been considered. In the first one, the user has total control over the element size, and the optimization with respect to both accuracy and stability of the scheme has resulted in a new 8-stage, fourth-order scheme called RKF84. The second scenario, in which the schemes are forced to work in over-accurate conditions by an element size constraint, has produced two new schemes. The 7-stage, third-order RKC73 scheme is most efficient, but has a limited applicability due to its inaccuracy. The 8-stage, fourth-order RKC84 is slightly less efficient, but works for larger element size restrictions. The performance of all three new schemes has been thoroughly analyzed, compared to RK schemes from the literature, and verified on theoretical and practical test cases.

The new RKF84, RKC73 and RKC84 schemes contribute to the improvement of the efficiency of RKDG methods by 16% to 27%, depending on the scenario. Appendix C compiles the low-storage coefficients for these schemes, as well as all the information required to use them optimally, so that the efficiency improvements are immediately accessible to the research and engineering community.

### 9.1.4 Curved Wall Treatments for Aeroacoustics

The third research goal defined in Chap. 1 is to introduce advanced treatments for curved wall boundaries in aeroacoustic problems. Chap. 7 has clearly shown that the accuracy at high order can be limited by the classical, linear modeling of curved walls, through the results of various 2D and 3D cases of acoustic propagation. In order to overcome this restriction, wall boundary treatments based on a second-order representation of the geometry have been presented. The results of 2D cases show that a mixed treatment, involving the quadratic representation of the boundary for the slip velocity condition and the linear representation for the discretization scheme, is of limited interest for aeroacoustic applications. However, the full quadratic treatment, that is based on curved elements, shows a significant accuracy improvement with little computational overhead for all test cases.

The boundary treatments presented in Chap. 7 thus contribute to make the efficiency of high-order DG simulations accessible, by enabling the use of a uniform grid density without excessive refinement near curved geometry features. However, they rely on the high-order capabilities of mesh generation software, that is under development.

### 9.1.5 Application to a Linear Aeroacoustics Case

Finally, the fourth research goal defined in Chap. 1 deals with the application of the RKDG method to a linear aeroacoustic problem of scientific interest. In Chap. 7, the acoustic behaviour of orifices under grazing flow has been studied by means of a hybrid methodology, in which the steady, incompressible mean flow is first obtained from a RANS calculation, before solving the LNSE with the RKDG method described in Chap. 6. The orifice impedance has been measured through a virtual impedance tube, and the part due to the mean flow has been isolated by subtracting the results of simulations without mean flow to the results of simulations with mean flow. The mean flow contribution to the orifice impedance has been compared with experimental data and with

a theoretical model, before carrying out a short study of the impact of various orifice geometries.

This work contributes to the knowledge of the acoustic behaviour of orifices under grazing flow, by proposing the first numerical model of such configurations that succeeds to reproduce the experimental observations, at least qualitatively. Although some questions about the validity range of this model remain open, it represents the most interesting alternative to experiments, as theoretical models fail to provide satisfying results for these cases. Moreover, it demonstrates the capabilities of the RKDG method in a challenging multi-scale problem, where short vorticity fluctuations produced by the shear layer instability need to be resolved, in addition to the longer acoustic waves.

## 9.2 Perspectives for Future Research

The research work presented in this thesis contributes to the improvement of the computational efficiency of the RKDG method for linear aeroacoustic problems, both by ameliorating the numerical method (new RK schemes, curved wall boundary treatments) and by providing information that allows the user to fully exploit the capabilities of the method (study of the CFL conditions). However, there may still be significant potential for improvement. Also, the method could be applied to a broader range of cases.

### 9.2.1 General Computation Strategy

In this thesis, we have assumed that the order  $p$  of the polynomial approximation is uniform over the whole computational domain. However, this may not be the most interesting situation from the point of view of the computational efficiency. Indeed, the accuracy requirement is often not uniform, which is usually addressed by refining the grid, as in Chap. 8: this is the so-called  $h$ -refinement approach. If the size of the largest elements is constrained, the scheme is locally over-accurate, which is inefficient. However, non-uniform accuracy can also be obtained by using approximations of different orders  $p$  in different elements. This approach, called  $p$ -refinement, is probably less flexible than the  $h$ -refinement, because in practice only a limited set of values of  $p$  are implemented in RKDG codes, and because the interpolation at the boundary shared by elements with different approximation orders has a non-negligible computation cost. However, both approaches can be combined in  $hp$ -refinement methods, that are a subject of intensive research in the field of DGM. This

approach can also be used for the opposite problem, namely to obtain near-uniform accuracy when the size of the smallest elements is constrained [27].

An adjacent topic is the question of the element type. The work described in this thesis is restricted to simplicial elements, i.e. triangles and tetrahedra. A recent study [147] suggests that quadrilateral meshes yield a better computational efficiency than triangular meshes. In Ref. [147], the lower number of elements and edges in quadrilateral meshes, as well as the richer polynomial basis, are credited for this superior efficiency. It can also be noted that the ratio of the number of DoF's representing the solution on the edges of an element to the total number of DoF's in the element is lower for quadrilaterals than for triangles. These arguments extend to hexahedral meshes against tetrahedral meshes in 3D. Therefore, it may be valuable to investigate a hybrid RKDG method that would associate the usual simplicial elements in the vicinity of complex wall boundaries to large tensor elements in the far-field, possibly in a non-conforming grid. To our knowledge, the RKDG method has not been used in this manner, at least for aeroacoustic propagation.

At the implementation level, an obvious improvement to our realization of the RKDG method for linear aeroacoustics is the parallelization: as mentioned in Chap. 1, parallel RKDG implementations show very good performance, due to the compact nature of the scheme. A related subject is that of Graphics Processing Units (GPU's), that deliver outstanding numerical performance. The adaptation of RKDG algorithms to such kind of hardware, involving parallelization and vectorization techniques, is becoming a popular research topic.

Finally, the accuracy of our implementation could benefit from improvements in the mitigation of the high-order interpolation issues mentioned in Chap. 6 (mean flow pre-processing and filtering). Such improvements would reduce the resolution requirements in regions of highly non-uniform mean flow, and thus reduce the computation cost.

## 9.2.2 Time Discretization

The stability restrictions, that severely limit the efficiency of RKDG methods, have been thoroughly studied in Part. II. An original attempt at relaxing the stability condition for structured meshes has recently been made [143], but its extension to unstructured grids is not obvious. The only way to obtain a significant improvement in the maximum time step is to deeply modify the discretization technique. Implicit-Explicit (IMEX) time integration and local time stepping are receiving increased attention and could make use of the optimized RK schemes that have been derived in Chap. 5, but they are complex

to implement. It may be worth exploring a space-time DG discretization, because such method has the potential to bring the high-order and flexible nature of DG to the time dimension.

### 9.2.3 Applications

Finally, our RKDG method for linear aeroacoustics could be used to study a broader range of problems. In the aeroacoustic literature, cases potentially subject to linear sound generation and scattering such as those of Chap. 8 are extensively documented, due to their practical importance. For instance, the tendency of slits, corrugations or side branches in duct systems to whistle under certain flow conditions is of strong industrial relevance. Applying the hybrid approach described in Chap. 8 to these problems, that are rarely tackled numerically, would be a methodological innovation that could bring valuable knowledge.

Also, some aeroacoustic propagation problems have important industrial implications. This is the case of the fan noise propagation in turbofan nacelles, and its near-field radiation [7]. Such problem could be efficiently simulated through an axisymmetric version of our RKDG method, including advanced impedance boundary conditions [123] to predict the effect of inlet lining.



## **Part V**

# **Appendix**



# Appendix A

## Runge-Kutta Amplification Factor Coefficients

### A.1 Jameson and Standard RK Schemes

The Jameson schemes are  $s$ -stage RK schemes that are  $s$ -order accurate for linear, homogeneous and autonomous systems, so that the coefficients  $\gamma_k$  of their amplification factor  $R(z)$  are entirely determined by Eq. (2.18):

$$\gamma_k = \frac{1}{k!}, \quad k = 1 \dots s$$

as explained in Sec. 2.1.2. The standard four-stage, fourth order RK scheme belongs to this family.

### A.2 Third-Order RK Schemes

The first four coefficients  $\gamma_k$  of third-order RK schemes are constrained by the linear order conditions of Eq. (2.18):

$$\gamma_0 = 1 \quad \gamma_1 = 1 \quad \gamma_2 = \frac{1}{2} \quad \gamma_3 = \frac{1}{6}$$

This is sufficient to determine all the coefficients of  $R(z)$  for the optimal (3,3)-SSP scheme. The additional coefficients  $\gamma_k$  of other stage-exceeding-order RK schemes used in this work are listed in Table A.1.

	RKC73 (Chap. 5)	Bernardini ORK37-3 [17]
$\gamma_4 \cdot 10^{-2}$	3.6519899181265	4.07702666666667
$\gamma_5 \cdot 10^{-3}$	5.10443948218378	8.24394333333333
$\gamma_6 \cdot 10^{-4}$	4.14954258898683	10.6568888888889
$\gamma_7 \cdot 10^{-5}$	1.49868460648008	23.0382698412698

Table A.1: Additional coefficients  $\gamma_k$  of the amplification factor  $R(z)$  for optimized third-order RK schemes used in this work.

### A.3 One-Step Fourth-Order RK Schemes

The first five coefficients  $\gamma_k$  of fourth-order RK schemes are constrained by the linear order conditions of Eq. (2.18):

$$\gamma_0 = 1 \quad \gamma_1 = 1 \quad \gamma_2 = \frac{1}{2} \quad \gamma_3 = \frac{1}{6} \quad \gamma_4 = \frac{1}{24}$$

This is sufficient to determine all the coefficients of  $R(z)$  for the standard four-stage, fourth-order scheme. The additional coefficients  $\gamma_k$  of optimized one-step, fourth-order RK schemes used in this work are listed in Table A.2.

### A.4 Two-Step Fourth-Order RK Schemes

The total amplification factor  $R(z)$  of a two-step RK scheme is the product of the amplification factors of the two one-step schemes that are applied successively. The amplification factors of both one-step RK schemes are subject to the linear order conditions of Eq. (2.18), so that the first five coefficients of  $R(z)$  are:

$$\gamma_0 = 1 \quad \gamma_1 = 2 \quad \gamma_2 = 2 \quad \gamma_3 = \frac{4}{3} \quad \gamma_4 = \frac{2}{3}$$

The additional coefficients  $\gamma_k$  of optimized two-step, fourth-order RK schemes used in this work are listed in Table A.3.

Name	$\gamma_5 \cdot 10^{-3}$	$\gamma_6 \cdot 10^{-4}$	$\gamma_7 \cdot 10^{-5}$	$\gamma_8 \cdot 10^{-6}$
Carpenter [25]	5.00000000000147			
Hu LDDRK6 [71]	7.81005	13.2141		
Berland [15]	7.856772044	9.59998595		
Calvo LDDRK46 [24]	7.85333	9.4889		
Tselios DDAS47 [139]	8.0898413573674	11.4500144821215	9.33161720160216	
HALE-RK6 [5]	05.56351	9.2671		
HALE-RK7 [5]	7.70233	8.7053	10.7	
Mead RKC [104]	5.676975	6.42853125		
Optimal (5,4)-SSP [124]	4.47771830307601			
RKC84 (Chap. 5)	7.63396514532222	9.5588281554956	7.24046178276778	2.48648556949577
RKF84 (Chap. 5)	8.02921837189987	11.0873426499598	9.46273413180222	3.68184991253961

Table A.2: Additional coefficients  $\gamma_k$  of the amplification factor  $R(z)$  for optimized one-step, fourth-order RK schemes used in this work.

Name	Hu LDDRK46 [71]	Hu LDDRK56 [71]	HALE-RK67 [5]
$\gamma_5 \cdot 10^{-1}$	2.662098	2.657206	2.6331853
$\gamma_6 \cdot 10^{-2}$	8.851789444444444	8.802423444444444	8.455754444444444
$\gamma_7 \cdot 10^{-2}$	2.485743888888889	2.460837888888889	2.246872388888889
$\gamma_8 \cdot 10^{-3}$	5.869569444444444	5.785806111111111	4.979151111111111
$\gamma_9 \cdot 10^{-3}$	1.152683333333333	1.131556666666667	0.91703375
$\gamma_{10} \cdot 10^{-4}$	1.1931875	1.62856432716667	1.376736989346
$\gamma_{11} \cdot 10^{-5}$		1.0323105495	1.72810749678
$\gamma_{12} \cdot 10^{-6}$			1.4464698912
$\gamma_{13} \cdot 10^{-7}$			1.1630304

Table A.3: Additional coefficients  $\gamma_k$  of the amplification factor  $R(z)$  for optimized two-step, fourth-order RK schemes used in this work.

## **Appendix B**

# **Maximum Courant Number Results for Triangular Grids**

### **B.1 Results for the Lax-Friedrichs Flux**

$p$	1	2	3	4	5	6	7	8	9	10
Carpenter	0.936	0.545	0.368	0.255	0.188	0.142	0.112	0.0902	0.0746	0.0623
Hu LDDRK6	0.809	0.433	0.280	0.190	0.140	0.106	0.0836	0.0671	0.0555	0.0464
Hu LDDRK46	0.689	0.401	0.259	0.176	0.130	0.0979	0.0775	0.0622	0.0514	0.0430
Hu LDDRK56	0.783	0.425	0.274	0.186	0.137	0.104	0.0821	0.0659	0.0545	0.0455
Berland	0.949	0.509	0.328	0.223	0.164	0.124	0.0982	0.0789	0.0652	0.0545
Calvo LDDRK46	0.956	0.512	0.331	0.225	0.165	0.125	0.0989	0.0794	0.0657	0.0548
Tselios DDAS47	1.16	0.627	0.404	0.275	0.202	0.153	0.121	0.0972	0.0804	0.0671
HALE-RK6	0.753	0.404	0.260	0.177	0.130	0.0985	0.0779	0.0625	0.0517	0.0432
HALE-RK7	0.917	0.495	0.319	0.217	0.160	0.121	0.0955	0.0767	0.0634	0.0530
HALE-RK67	0.793	0.426	0.274	0.186	0.137	0.104	0.0821	0.0659	0.0545	0.0455
Mead RKC	0.828	0.444	0.286	0.195	0.143	0.108	0.0857	0.0688	0.0569	0.0475
Opt. (3,3)-SSP	0.562	0.314	0.203	0.138	0.101	0.0766	0.0606	0.0487	0.0403	0.0336
Opt. (4,5)-SSP	0.915	0.533	0.359	0.262	0.200	0.157	0.128	0.103	0.0854	0.0713
Jameson	0.466	0.314	0.225	0.176	0.143	0.121	0.104	0.0910	0.0812	0.0729

Table B.1: Minimum value  $\min_{\gamma}(\hat{\nu}_r)$  of  $\hat{\nu}_r$  based on the inner radius, with the Lax-Friedrichs flux.

$p$	1	2	3	4	5	6	7	8	9	10
Carpenter	1.16	0.648	0.443	0.304	0.233	0.177	0.144	0.116	0.0977	0.0814
Hu LDDRK6	0.867	0.483	0.330	0.227	0.174	0.132	0.107	0.0860	0.0728	0.0606
Hu LDDRK46	0.798	0.446	0.304	0.210	0.161	0.122	0.0993	0.0797	0.0674	0.0562
Hu LDDRK56	0.851	0.474	0.324	0.222	0.170	0.129	0.105	0.0844	0.0714	0.0595
Berland	1.02	0.567	0.387	0.266	0.204	0.155	0.126	0.101	0.0855	0.0712
Calvo LDDRK46	1.03	0.571	0.390	0.268	0.205	0.156	0.127	0.102	0.0861	0.0717
Tselios DDAS47	1.25	0.698	0.477	0.328	0.251	0.191	0.155	0.125	0.105	0.0877
HALE-RK6	0.808	0.449	0.307	0.211	0.162	0.123	0.0999	0.0801	0.0678	0.0565
HALE-RK7	0.990	0.551	0.377	0.259	0.198	0.150	0.122	0.0983	0.0831	0.0692
HALE-RK67	0.851	0.474	0.324	0.223	0.171	0.129	0.105	0.0845	0.0715	0.0595
Mead RKC	0.888	0.494	0.338	0.232	0.178	0.135	0.110	0.0881	0.0745	0.0621
Opt. (3,3)-SSP	0.628	0.350	0.239	0.164	0.126	0.0954	0.0777	0.0624	0.0527	0.0439
Opt. (4,5)-SSP	1.17	0.689	0.458	0.331	0.251	0.197	0.160	0.132	0.111	0.0932
Jameson	0.500	0.350	0.265	0.210	0.178	0.150	0.133	0.117	0.106	0.0953

Table B.2: Maximum value  $\max_{\gamma}(\hat{\nu}_r)$  of  $\hat{\nu}_r$  based on the inner radius, with the Lax-Friedrichs flux.

	$\min_\gamma(\hat{\nu}_r)$		$\max_\gamma(\hat{\nu}_r)$	
	$\alpha_0$	$\alpha_1$	$\alpha_0$	$\alpha_1$
Carpenter	-0.0679	-0.576	-0.262	-0.213
Hu LDDRK6	-0.213	-0.739	-0.219	-0.213
Hu LDDRK46	-0.365	-0.636	-0.251	-0.213
Hu LDDRK56	-0.243	-0.723	-0.224	-0.213
Berland	-0.0519	-0.739	-0.219	-0.213
Calvo LDDRK46	-0.0450	-0.739	-0.219	-0.213
Tselios DDAS47	0.153	-0.733	-0.221	-0.213
HALE-RK6	-0.284	-0.739	-0.219	-0.213
HALE-RK7	-0.0857	-0.730	-0.222	-0.213
HALE-RK67	-0.232	-0.737	-0.220	-0.213
Mead RKC	-0.189	-0.739	-0.219	-0.213
Opt. (3,3)-SSP	-0.572	-0.688	-0.235	-0.213
Opt. (4,5)-SSP	-0.0983	-0.592	-0.219	-0.202
Jameson	-0.752	-0.544	-0.118	-0.111

Table B.3: Fit coefficients for the minimum value  $\min_\gamma(\hat{\nu}_r)$  and maximum value  $\max_\gamma(\hat{\nu}_r)$  of  $\hat{\nu}_r$  based on the inner radius, with the Lax-Friedrichs flux, as a function of  $p$ . The fit equation is  $\ln(\cdot) = \alpha_0 + \alpha_1 \ln(p) + \alpha_2 [\ln(p)]^2$ .

$p$	1	2	3	4	5	6	7	8	9	10
Carpenter	0.388	0.216	0.148	0.101	0.0778	0.0590	0.0480	0.0385	0.0326	0.0271
Hu LDDRK6	0.289	0.161	0.110	0.0756	0.0579	0.0439	0.0357	0.0287	0.0243	0.0202
Hu LDDRK46	0.266	0.149	0.101	0.0700	0.0535	0.0407	0.0331	0.0266	0.0225	0.0187
Hu LDDRK56	0.284	0.158	0.108	0.0742	0.0568	0.0431	0.0351	0.0281	0.0238	0.0198
Berland	0.339	0.189	0.129	0.0887	0.0680	0.0515	0.0420	0.0337	0.0285	0.0237
Calvo LDDRK46	0.342	0.190	0.130	0.0894	0.0685	0.0519	0.0423	0.0339	0.0287	0.0239
Tselios DDAS47	0.418	0.233	0.159	0.109	0.0838	0.0635	0.0517	0.0415	0.0351	0.0292
HALE-RK6	0.269	0.150	0.102	0.0704	0.0539	0.0409	0.0333	0.0267	0.0226	0.0188
HALE-RK7	0.330	0.184	0.126	0.0863	0.0661	0.0501	0.0408	0.0328	0.0277	0.0231
HALE-RK67	0.284	0.158	0.108	0.0742	0.0569	0.0431	0.0351	0.0282	0.0238	0.0198
Mead RK	0.296	0.165	0.113	0.0774	0.0593	0.0450	0.0366	0.0294	0.0248	0.0207
Opt. (3,3)-SSP	0.209	0.117	0.0796	0.0548	0.0420	0.0318	0.0259	0.0208	0.0176	0.0146
Opt. (4,5)-SSP	0.390	0.230	0.153	0.110	0.0835	0.0657	0.0533	0.0438	0.0371	0.0311
Jameson	0.167	0.117	0.0883	0.0701	0.0594	0.0501	0.0445	0.0389	0.0355	0.0318

Table B.4: Minimum value  $\min_{\gamma}(\hat{\nu}_h)$  of  $\hat{\nu}_h$  based on the shortest height, with the Lax-Friedrichs flux.

$p$	1	2	3	4	5	6	7	8	9	10
Carpenter	0.503	0.294	0.195	0.132	0.0983	0.0740	0.0588	0.0471	0.0398	0.0325
Hu LDDRK6	0.410	0.222	0.145	0.0986	0.0732	0.0551	0.0438	0.0351	0.0296	0.0242
Hu LDDRK46	0.361	0.206	0.135	0.0913	0.0678	0.0511	0.0405	0.0325	0.0275	0.0224
Hu LDDRK56	0.403	0.218	0.143	0.0968	0.0718	0.0541	0.0430	0.0344	0.0291	0.0238
Berland	0.482	0.261	0.171	0.116	0.0859	0.0647	0.0514	0.0412	0.0348	0.0284
Calvo LDDRK46	0.485	0.263	0.172	0.117	0.0865	0.0652	0.0518	0.0415	0.0351	0.0286
Tselios DDAS47	0.594	0.322	0.210	0.143	0.106	0.0798	0.0633	0.0507	0.0429	0.0351
HALE-RK6	0.382	0.207	0.135	0.0918	0.0681	0.0513	0.0408	0.0327	0.0276	0.0226
HALE-RK7	0.469	0.254	0.166	0.113	0.0836	0.0630	0.0500	0.0401	0.0339	0.0277
HALE-RK67	0.403	0.218	0.143	0.0968	0.0718	0.0541	0.0430	0.0344	0.0291	0.0238
Mead RKC	0.420	0.228	0.149	0.101	0.0749	0.0565	0.0448	0.0359	0.0304	0.0248
Opt. (3,3)-SSP	0.294	0.161	0.105	0.0715	0.0530	0.0399	0.0317	0.0254	0.0215	0.0176
Opt. (4,5)-SSP	0.493	0.289	0.191	0.138	0.105	0.0815	0.0659	0.0539	0.0450	0.0373
Jameson	0.237	0.161	0.117	0.0915	0.0750	0.0629	0.0545	0.0475	0.0434	0.0381

Table B.5: Maximum value  $\max_{\gamma}(\hat{\nu}_h)$  of  $\hat{\nu}_h$  based on the shortest height, with the Lax-Friedrichs flux.

	$\min_{\gamma}(\widehat{\nu}_h)$		$\max_{\gamma}(\widehat{\nu}_h)$	
	$\alpha_0$	$\alpha_1$	$\alpha_0$	$\alpha_1$
Carpenter	-0.952	-0.662	-0.682	-0.610
Hu LDDRK6	-1.25	-0.662	-0.891	-0.718
Hu LDDRK46	-1.33	-0.658	-1.02	-0.653
Hu LDDRK56	-1.26	-0.662	-0.910	-0.718
Berland	-1.09	-0.662	-0.731	-0.718
Calvo LDDRK46	-1.08	-0.662	-0.724	-0.718
Tselios DDAS47	-0.877	-0.662	-0.522	-0.718
HALE-RK6	-1.32	-0.662	-0.962	-0.718
HALE-RK7	-1.11	-0.662	-0.758	-0.718
HALE-RK67	-1.26	-0.662	-0.910	-0.718
Mead RKC	-1.22	-0.662	-0.867	-0.718
Opt. (3,3)-SSP	-1.57	-0.662	-1.22	-0.704
Opt. (4,5)-SSP	-0.941	-0.631	-0.710	-0.616
Jameson	-1.79	-0.467	-1.43	-0.523

Table B.6: Fit coefficients for the minimum value  $\min_{\gamma}(\widehat{\nu}_h)$  and maximum value  $\max_{\gamma}(\widehat{\nu}_h)$  of  $\widehat{\nu}_h$  based on the shortest height, with the Lax-Friedrichs flux, as a function of  $p$ . The fit equation is  $\ln(\cdot) = \alpha_0 + \alpha_1 \ln(p) + \alpha_2 [\ln(p)]^2$ .

## **B.2 Results for the Upwind Flux**

$p$	1	2	3	4	5	6	7	8	9	10
Carpenter	0.938	0.546	0.368	0.268	0.204	0.161	0.130	0.108	0.0913	0.0782
Hu LDDRK6	0.817	0.462	0.312	0.220	0.169	0.131	0.107	0.0877	0.0746	0.0631
Hu LDDRK46	0.690	0.411	0.270	0.197	0.147	0.117	0.0939	0.0784	0.0656	0.0565
Hu LDDRK56	0.785	0.454	0.305	0.216	0.165	0.129	0.105	0.0860	0.0731	0.0619
Berland	0.955	0.543	0.367	0.259	0.198	0.154	0.126	0.103	0.0875	0.0741
Calvo LDDRK46	0.961	0.547	0.369	0.261	0.200	0.155	0.127	0.104	0.0881	0.0746
Tselios DDAS47	1.17	0.669	0.450	0.319	0.244	0.190	0.155	0.127	0.108	0.0913
HALE-RK6	0.762	0.430	0.291	0.205	0.157	0.122	0.0999	0.0816	0.0695	0.0588
HALE-RK7	0.919	0.528	0.354	0.252	0.192	0.150	0.122	0.100	0.0850	0.0721
HALE-RK67	0.794	0.454	0.305	0.216	0.165	0.129	0.105	0.0861	0.0731	0.0620
Mead RKC	0.838	0.473	0.320	0.226	0.173	0.134	0.110	0.0898	0.0764	0.0647
Opt. (3,3)-SSP	0.564	0.335	0.220	0.160	0.120	0.0950	0.0765	0.0635	0.0533	0.0457
Opt. (4,5)-SSP	0.917	0.534	0.360	0.262	0.200	0.158	0.128	0.106	0.0896	0.0766
Jameson	0.473	0.335	0.251	0.205	0.173	0.149	0.133	0.119	0.109	0.0992

Table B.7: Minimum value  $\min_{\gamma}(\hat{\nu}_r)$  of  $\hat{\nu}_r$  based on the inner radius, with the upwind flux.

$p$	1	2	3	4	5	6	7	8	9	10
Carpenter	1.53	0.895	0.598	0.425	0.324	0.252	0.205	0.168	0.142	0.120
Hu LDDRK6	1.27	0.718	0.489	0.342	0.263	0.202	0.165	0.135	0.114	0.0964
Hu LDDRK46	1.11	0.640	0.432	0.305	0.233	0.180	0.147	0.120	0.102	0.0859
Hu LDDRK56	1.25	0.705	0.480	0.336	0.258	0.199	0.162	0.132	0.112	0.0946
Berland	1.50	0.843	0.574	0.402	0.308	0.238	0.194	0.158	0.134	0.113
Calvo LDDRK46	1.51	0.849	0.578	0.405	0.311	0.239	0.195	0.159	0.135	0.114
Tselios DDAS47	1.84	1.04	0.708	0.496	0.380	0.293	0.239	0.195	0.165	0.139
HALE-RK6	1.19	0.669	0.456	0.319	0.245	0.189	0.154	0.125	0.106	0.0897
HALE-RK7	1.45	0.820	0.559	0.391	0.300	0.231	0.189	0.154	0.130	0.110
HALE-RK67	1.25	0.705	0.480	0.336	0.258	0.199	0.162	0.132	0.112	0.0946
Mead RKC	1.30	0.736	0.501	0.351	0.269	0.207	0.169	0.138	0.117	0.0987
Opt. (3,3)-SSP	0.909	0.520	0.352	0.248	0.190	0.146	0.119	0.0974	0.0825	0.0698
Opt. (4,5)-SSP	1.49	0.878	0.586	0.417	0.318	0.247	0.201	0.164	0.139	0.118
Jameson	0.735	0.520	0.393	0.318	0.269	0.231	0.206	0.182	0.167	0.151

Table B.8: Maximum value  $\max_{\gamma}(\hat{\nu}_r)$  of  $\hat{\nu}_r$  based on the inner radius, with the upwind flux.

	$\min_{\gamma}(\hat{\nu}_r)$			$\max_{\gamma}(\hat{\nu}_r)$		
	$\alpha_0$	$\alpha_1$	$\alpha_2$	$\alpha_0$	$\alpha_1$	$\alpha_2$
Carpenter	-0.0653	-0.641	-0.190	0.425	-0.638	-0.204
Hu LDDRK6	-0.203	-0.680	-0.187	0.240	-0.669	-0.196
Hu LDDRK46	-0.365	-0.640	-0.197	0.108	-0.654	-0.200
Hu LDDRK56	-0.240	-0.659	-0.194	0.220	-0.669	-0.196
Berland	-0.0463	-0.676	-0.189	0.400	-0.669	-0.196
Calvo LDDRK46	-0.0396	-0.675	-0.189	0.407	-0.669	-0.196
Tselios DDAS47	0.155	-0.669	-0.191	0.609	-0.669	-0.196
HALE-RK6	-0.273	-0.681	-0.187	0.168	-0.669	-0.196
HALE-RK7	-0.0832	-0.667	-0.191	0.372	-0.669	-0.196
HALE-RK67	-0.230	-0.672	-0.190	0.221	-0.669	-0.196
Mead RKC	-0.178	-0.681	-0.187	0.264	-0.669	-0.196
Opt. (3,3)-SSP	-0.568	-0.642	-0.197	-0.0964	-0.656	-0.199
Opt. (4,5)-SSP	-0.0883	-0.642	-0.189	0.403	-0.635	-0.204
Jameson	-0.739	-0.490	-0.0849	-0.300	-0.475	-0.0943

Table B.9: Fit coefficients for the minimum value  $\min_{\gamma}(\hat{\nu}_r)$  and maximum value  $\max_{\gamma}(\hat{\nu}_r)$  of  $\hat{\nu}_r$  based on the inner radius, with the upwind flux, as a function of  $p$ . The fit equation is  $\ln(\cdot) = \alpha_0 + \alpha_1 \ln(p) + \alpha_2 [\ln(p)]^2$ .

$p$	1	2	3	4	5	6	7	8	9	10
Carpenter	0.462	0.267	0.180	0.131	0.101	0.0791	0.0644	0.0532	0.0451	0.0385
Hu LDDRK6	0.402	0.229	0.154	0.109	0.0834	0.0648	0.0529	0.0433	0.0368	0.0312
Hu LDDRK46	0.340	0.201	0.133	0.0965	0.0727	0.0577	0.0464	0.0386	0.0324	0.0279
Hu LDDRK56	0.387	0.224	0.150	0.107	0.0816	0.0636	0.0518	0.0425	0.0361	0.0306
Berland	0.470	0.269	0.181	0.128	0.0979	0.0761	0.0621	0.0509	0.0432	0.0367
Calvo LDDRK46	0.473	0.270	0.182	0.129	0.0985	0.0766	0.0625	0.0512	0.0435	0.0369
Tselios DDAS47	0.575	0.331	0.222	0.158	0.120	0.0937	0.0764	0.0627	0.0532	0.0452
HALE-RK6	0.375	0.213	0.144	0.101	0.0777	0.0603	0.0493	0.0404	0.0343	0.0291
HALE-RK7	0.453	0.261	0.175	0.124	0.0949	0.0740	0.0603	0.0495	0.0420	0.0357
HALE-RK67	0.391	0.225	0.151	0.107	0.0817	0.0636	0.0519	0.0425	0.0361	0.0306
Mead RKC	0.412	0.234	0.158	0.112	0.0855	0.0664	0.0542	0.0444	0.0377	0.0320
Opt. (3,3)-SSP	0.277	0.164	0.108	0.0788	0.0592	0.0469	0.0378	0.0314	0.0263	0.0226
Opt. (4,5)-SSP	0.451	0.261	0.176	0.128	0.0983	0.0774	0.0632	0.0521	0.0442	0.0377
Jameson	0.233	0.164	0.124	0.101	0.0855	0.0739	0.0658	0.0588	0.0538	0.0491

Table B.10: Minimum value  $\min_{\gamma}(\hat{\nu}_h)$  of  $\hat{\nu}_h$  based on the shortest height, with the upwind flux.

$p$	1	2	3	4	5	6	7	8	9	10
Carpenter	0.520	0.299	0.201	0.143	0.109	0.0839	0.0683	0.0559	0.0475	0.0402
Hu LDDRK6	0.425	0.239	0.163	0.114	0.0890	0.0675	0.0551	0.0449	0.0400	0.0321
Hu LDDRK46	0.376	0.214	0.145	0.105	0.0786	0.0601	0.0490	0.0400	0.0342	0.0287
Hu LDDRK56	0.417	0.235	0.160	0.112	0.0873	0.0662	0.0541	0.0440	0.0384	0.0315
Berland	0.499	0.281	0.191	0.134	0.104	0.0793	0.0647	0.0527	0.0466	0.0377
Calvo LDDRK46	0.502	0.283	0.193	0.135	0.105	0.0798	0.0651	0.0530	0.0469	0.0380
Tselios DDAS47	0.615	0.346	0.236	0.165	0.129	0.0977	0.0797	0.0649	0.0569	0.0465
HALE-RK6	0.396	0.223	0.152	0.106	0.0829	0.0629	0.0513	0.0418	0.0374	0.0299
HALE-RK7	0.485	0.273	0.186	0.130	0.102	0.0771	0.0629	0.0512	0.0448	0.0367
HALE-RK67	0.417	0.235	0.160	0.112	0.0874	0.0663	0.0541	0.0440	0.0388	0.0316
Mead RKC	0.435	0.245	0.167	0.117	0.0912	0.0691	0.0564	0.0460	0.0411	0.0329
Opt. (3,3)-SSP	0.306	0.173	0.118	0.0827	0.0641	0.0488	0.0398	0.0325	0.0278	0.0233
Opt. (4,5)-SSP	0.509	0.293	0.197	0.140	0.106	0.0823	0.0670	0.0550	0.0466	0.0395
Jameson	0.245	0.173	0.131	0.106	0.0912	0.0770	0.0685	0.0608	0.0578	0.0505

Table B.11: Maximum value  $\max_{\gamma}(\hat{\nu}_h)$  of  $\hat{\nu}_h$  based on the shortest height, with the upwind flux.

	$\min_\gamma(\widehat{\nu}_h)$		$\max_\gamma(\widehat{\nu}_h)$	
	$\alpha_0$	$\alpha_1$	$\alpha_0$	$\alpha_1$
Carpenter	-0.776	-0.649	-0.186	-0.197
Hu LDDRK6	-0.911	-0.677	-0.188	-0.189
Hu LDDRK46	-1.08	-0.643	-0.195	-0.203
Hu LDDRK56	-0.948	-0.655	-0.195	-0.193
Berland	-0.754	-0.673	-0.190	-0.191
Calvo LDDRK46	-0.747	-0.672	-0.190	-0.191
Tselios DDAS47	-0.553	-0.666	-0.191	-0.192
HALE-RK6	-0.981	-0.678	-0.188	-0.189
HALE-RK7	-0.791	-0.664	-0.192	-0.193
HALE-RK67	-0.938	-0.669	-0.191	-0.192
Mead RKC	-0.886	-0.678	-0.188	-0.189
Opt. (3,3)-SSP	-1.28	-0.641	-0.197	-0.196
Opt. (4,5)-SSP	-0.798	-0.652	-0.184	-0.196
Jameson	-1.45	-0.488	-0.0846	-0.0901

Table B.12: Fit coefficients for the minimum value  $\min_\gamma(\widehat{\nu}_h)$  and maximum value  $\max_\gamma(\widehat{\nu}_h)$  of  $\widehat{\nu}_h$  based on the shortest height, with the upwind flux, as a function of  $p$ . The fit equation is  $\ln(\cdot) = \alpha_0 + \alpha_1 \ln(p) + \alpha_2 [\ln(p)]^2$ .

## **Appendix C**

# **Useful Data on the Optimized RK Schemes**

### **C.1 RKF84 Scheme**

Stage	$A_i$	$B_i$	$c_i$	$\gamma_k$
1	0	0.08037936882736950	0	1
2	-0.5534431294501569	0.5388497458569843	0.08037936882736950	1/2
3	0.01065987570203490	0.01974974409031960	0.3210064250338430	1/6
4	-0.5515812888932000	0.09911841297339970	0.3408501826604660	1/24
5	-1.885790377558741	0.7466920411064123	0.3850364824285470	$8.02921837189987 \cdot 10^{-3}$
6	-5.701295742793264	1.679584245618894	0.5040052477534100	$1.10873426499598 \cdot 10^{-3}$
7	2.113903965664793	0.2433728067008188	0.6578977561168540	$9.46273413180222 \cdot 10^{-5}$
8	-0.5339578826675280	0.1422730459001373	0.9484087623348481	$3.68184991253961 \cdot 10^{-6}$

Table C.1: 2N-storage coefficients and coefficients  $\gamma_k$  of the polynomial  $R(z)$  for the RKF84 scheme.

$p$	Optimal Working Conditions			Maximum Courant Number				
	$(k\Delta x)_{opt}$	$\nu_{opt}$	$\kappa_{opt}$	$E_{phase}$	$(k\Delta x)_{opt}^*$	$\nu^*$	$\kappa_{opt}^*$	$E_{phase}$
1	1.45	1.19	2.17	0.0439	1.45	1.19	2.17	0.0439
2	3.42	0.619	0.323	0.0618	3.42	0.619	0.323	0.0618
3	5.56	0.394	0.118	0.0925	5.56	0.394	0.118	0.0925
4	7.78	0.276	0.0614	0.135	7.78	0.276	0.0614	0.135
5	10.1	0.206	0.0381	0.181	10.1	0.206	0.0381	0.181
6	12.4	0.16	0.0265	0.227	12.4	0.16	0.0265	0.227
7	14.7	0.127	0.0197	0.272	14.7	0.127	0.0197	0.272
8	17.1	0.104	0.0154	0.313	17.1	0.104	0.0154	0.313
9	19.4	0.0873	0.0125	0.352	19.4	0.0873	0.0125	0.352
10	21.8	0.0742	0.0104	0.389	21.8	0.0742	0.0104	0.389

Table C.2: Working conditions  $(k\Delta x, \nu)$  (both optimal and at maximum Courant number), as well as corresponding cost  $\kappa$  and dispersion error  $E_{phase}$ , for a dissipation error of  $E_{mag} = 1$  dB per wavelength, with the RKF84 scheme.

$p$	Optimal Working Conditions			Maximum Courant Number				
	$(k\Delta x)_{opt}$	$\nu_{opt}$	$\kappa_{opt}$	$E_{phase}$	$(k\Delta x)_{opt}^*$	$\nu^*$	$\kappa_{opt}^*$	$E_{phase}$
1	0.65	1.19	24.3	0.00303	0.65	1.19	24.3	0.00303
2	2.01	0.619	1.59	0.00276	2.01	0.619	1.59	0.00276
3	3.64	0.394	0.42	0.00154	3.64	0.394	0.42	0.00154
4	5.42	0.276	0.182	0.00221	5.42	0.276	0.182	0.00221
5	7.29	0.206	0.1	0.00448	7.29	0.206	0.1	0.00448
6	9.23	0.16	0.0637	0.00787	9.23	0.16	0.0637	0.00787
7	11.2	0.127	0.0446	0.0116	11.2	0.127	0.0446	0.0116
8	13.2	0.104	0.0332	0.0151	13.2	0.104	0.0332	0.0151
9	15.2	0.0873	0.0259	0.0185	15.2	0.0873	0.0259	0.0185
10	17.3	0.0742	0.0209	0.0215	17.3	0.0742	0.0209	0.0215

Table C-3: Working conditions  $(k\Delta x, \nu)$  (both optimal and at maximum Courant number), as well as corresponding cost  $\kappa$  and dispersion error  $E_{phase}$ , for a dissipation error of  $E_{mag} = 0.1$  dB per wavelength, with the RKF84 scheme.

$p$	Optimal Working Conditions			Maximum Courant Number				
	$(k\Delta x)_{opt}$	$\nu_{opt}$	$\kappa_{opt}$	$E_{phase}$	$(k\Delta x)_{opt}^*$	$\nu^*$	$\kappa_{opt}^*$	$E_{phase}$
1	0.299	1.19	251	0.00015	0.299	1.19	251	0.00015
2	1.23	0.619	6.91	0.000191	1.23	0.619	6.91	0.000191
3	2.51	0.394	1.29	0.00124	2.51	0.394	1.29	0.00124
4	3.96	0.276	0.466	0.00212	3.96	0.276	0.466	0.00212
5	5.54	0.206	0.229	0.00256	5.54	0.206	0.229	0.00256
6	7.2	0.16	0.134	0.00254	7.2	0.16	0.134	0.00254
7	8.95	0.127	0.0877	0.00225	8.95	0.127	0.0877	0.00225
8	10.7	0.104	0.0619	0.00185	10.7	0.104	0.0619	0.00185
9	12.6	0.0873	0.0462	0.0014	12.6	0.0873	0.0462	0.0014
10	14.4	0.0742	0.036	0.000952	14.4	0.0742	0.036	0.000952

Table C.4: Working conditions  $(k\Delta x, \nu)$  (both optimal and at maximum Courant number), as well as corresponding cost  $\kappa$  and dispersion error  $E_{phase}$ , for a dissipation error of  $E_{mag} = 0.01$  dB per wavelength, with the RKF84 scheme.

$p$	Optimal Working Conditions				Maximum Courant Number			
	$(k\Delta x)_{opt}$	$\nu_{opt}$	$\kappa_{opt}$	$E_{phase}$	$(k\Delta x)_{opt}^*$	$\nu^*$	$\kappa_{opt}^*$	$E_{phase}$
1	0.138	1.19	$2.53 \cdot 10^3$	$7.04 \cdot 10^{-6}$	0.138	1.19	$2.53 \cdot 10^3$	$7.04 \cdot 10^{-6}$
2	0.769	0.619	28.4	$6.99 \cdot 10^{-5}$	0.769	0.619	28.4	$6.99 \cdot 10^{-5}$
3	1.76	0.394	3.74	0.000408	1.76	0.394	3.74	0.000408
4	2.93	0.276	1.15	0.000813	2.93	0.276	1.15	0.000813
5	4.23	0.206	0.514	0.00111	4.23	0.206	0.514	0.00111
6	5.63	0.16	0.281	0.00127	5.63	0.16	0.281	0.00127
7	7.14	0.127	0.173	0.00133	7.14	0.127	0.173	0.00133
8	8.72	0.104	0.115	0.00134	8.72	0.104	0.115	0.00134
9	10.4	0.0873	0.082	0.0013	10.4	0.0873	0.082	0.0013
10	12.1	0.0742	0.061	0.00123	12.1	0.0742	0.061	0.00123

Table C.5: Working conditions  $(k\Delta x, \nu)$  (both optimal and at maximum Courant number), as well as corresponding cost  $\kappa$  and dispersion error  $E_{phase}$ , for a dissipation error of  $E_{mag} = 0.001$  dB per wavelength, with the RKF84 scheme.

$p$	Optimal Working Conditions				Maximum Courant Number			
	$(k\Delta x)_{opt}$	$\nu_{opt}$	$\kappa_{opt}$	$E_{phase}$	$(k\Delta x)_{opt}^*$	$\nu^*$	$\kappa_{opt}^*$	$E_{phase}$
1	0.0641	1.19	$2.54 \cdot 10^4$	$3.28 \cdot 10^{-7}$	0.0641	1.19	$2.54 \cdot 10^4$	$3.28 \cdot 10^{-7}$
2	0.483	0.619	115	$1.35 \cdot 10^{-5}$	0.483	0.619	115	$1.35 \cdot 10^{-5}$
3	1.24	0.394	10.7	0.000107	1.24	0.394	10.7	0.000107
4	2.17	0.266	2.95	0.000213	2.14	0.276	2.96	0.000237
5	3.31	0.177	1.24	0.000231	3.09	0.206	1.32	0.000323
6	4.58	0.13	0.639	0.000244	4.1	0.16	0.727	0.000362
7	5.94	0.101	0.377	0.000255	5.19	0.127	0.448	0.000379
8	7.37	0.0822	0.243	0.000261	6.37	0.104	0.296	0.000387
9	8.84	0.0692	0.167	0.000271	7.64	0.0873	0.206	0.00039
10	10.4	0.0593	0.121	0.000276	8.99	0.0742	0.148	0.000392

Table C.6: Working conditions  $(k\Delta x, \nu)$  (both optimal and at maximum Courant number), as well as corresponding cost  $\kappa$  and dispersion error  $E_{phase}$ , for a dissipation error of  $E_{mag} = 0.0001$  dB per wavelength, with the RKF84 scheme.

## **C.2 RKC73 Scheme**

Stage	$A_i$	$B_i$	$c_i$	$\gamma_k$
1	0	0.01197052673097840	0	1
2	-0.8083163874983830	0.8886897793820711	0.01197052673097840	1/2
3	-1.503407858773331	0.4578382089261419	0.1823177940361990	1/6
4	-1.053064525050744	0.5790045253338471	0.5082168062551849	0.0365198991812650
5	-1.463149119280508	0.3160214638138484	0.6532031220148590	5.10443948218378 · 10 <sup>-3</sup>
6	-0.6592881281087830	0.2483525368264122	0.8534401385678250	4.14954258898683 · 10 <sup>-4</sup>
7	-1.667891931891068	0.06771230959408840	0.9980466084623790	1.49868460648008e · 10 <sup>-5</sup>

Table C.7: 2N-storage coefficients and coefficients  $\gamma_k$  of the polynomial  $R(z)$  for the RKC73 scheme.

$p$	Optimal Working Conditions			Maximum Courant Number				
	$(k\Delta x)_{opt}$	$\nu_{opt}$	$\kappa_{opt}$	$E_{phase}$	$(k\Delta x)_{opt}^*$	$\nu^*$	$\kappa_{opt}^*$	$E_{phase}$
1	1.25	1.08	3.28	0.0756	1.19	1.25	3.34	0.0857
2	2.98	0.501	0.527	0.118	2.69	0.641	0.558	0.14
3	4.87	0.324	0.188	0.145	4.41	0.41	0.199	0.166
4	6.83	0.239	0.0922	0.164	6.3	0.29	0.0962	0.179
5	8.82	0.189	0.0538	0.178	8.34	0.219	0.0552	0.186
6	10.8	0.157	0.035	0.19	10.5	0.17	0.0352	0.192
7	12.9	0.134	0.0244	0.2	12.8	0.136	0.0244	0.2
8	15.2	0.112	0.018	0.21	15.2	0.112	0.018	0.21
9	17.5	0.0934	0.0139	0.224	17.5	0.0934	0.0139	0.224
10	20	0.0794	0.0111	0.241	20	0.0794	0.0111	0.241

Table C.8: Working conditions  $(k\Delta x, \nu)$  (both optimal and at maximum Courant number), as well as corresponding cost  $\kappa$  and dispersion error  $E_{phase}$ , for a dissipation error of  $E_{mag} = 1$  dB per wavelength, with the RK73 scheme.

$p$	Optimal Working Conditions			Maximum Courant Number				
	$(k\Delta x)_{opt}$	$\nu_{opt}$	$\kappa_{opt}$	$E_{phase}$	$(k\Delta x)_{opt}^*$	$\nu^*$	$\kappa_{opt}^*$	$E_{phase}$
1	0.566	1.1	35	0.00396	0.54	1.25	35.6	0.00424
2	1.78	0.385	3.23	0.0066	1.34	0.641	4.53	0.00726
3	3.27	0.22	0.911	0.00823	2.19	0.41	1.63	0.00792
4	4.89	0.152	0.394	0.00929	3.11	0.29	0.799	0.00806
5	6.6	0.115	0.212	0.0101	4.14	0.219	0.45	0.00809
6	8.37	0.0921	0.13	0.0107	5.33	0.17	0.271	0.0081
7	10.2	0.0768	0.0866	0.0111	6.67	0.136	0.173	0.0081
8	12	0.0658	0.0616	0.0114	8.13	0.112	0.117	0.0081
9	13.9	0.0573	0.0458	0.0118	9.71	0.0934	0.0818	0.00811
10	15.7	0.0509	0.0353	0.012	11.4	0.0794	0.0591	0.00811

Table C.9: Working conditions  $(k\Delta x, \nu)$  (both optimal and at maximum Courant number), as well as corresponding cost  $\kappa$  and dispersion error  $E_{phase}$ , for a dissipation error of  $E_{mag} = 0.1$  dB per wavelength, with the RKC73 scheme.

$p$	Optimal Working Conditions			Maximum Courant Number				
	$(k\Delta x)_{opt}$	$\nu_{opt}$	$\kappa_{opt}$	$E_{phase}$	$(k\Delta x)_{opt}^*$	$\nu^*$	$\kappa_{opt}^*$	$E_{phase}$
1	0.261	1.11	358	0.000188	0.249	1.25	363	0.000199
2	1.09	0.29	18.4	0.000364	0.64	0.641	41.6	0.000351
3	2.26	0.148	4.08	0.00048	1.01	0.41	16.4	0.000359
4	3.62	0.0954	1.54	0.000556	1.43	0.29	8.2	0.00036
5	5.1	0.0693	0.76	0.000609	1.9	0.219	4.66	0.00036
6	6.66	0.054	0.439	0.000644	2.45	0.17	2.81	0.00036
7	8.28	0.0439	0.281	0.000674	3.06	0.136	1.8	0.00036
8	9.93	0.0371	0.193	0.000691	3.72	0.112	1.21	0.00036
9	11.6	0.0319	0.139	0.000706	4.45	0.0934	0.849	0.00036
10	13.4	0.028	0.105	0.000718	5.24	0.0794	0.614	0.00036

Table C.10: Working conditions  $(k\Delta x, \nu)$  (both optimal and at maximum Courant number), as well as corresponding cost  $\kappa$  and dispersion error  $E_{phase}$ , for a dissipation error of  $E_{mag} = 0.01$  dB per wavelength, with the RKC73 scheme.

$p$	Optimal Working Conditions				Maximum Courant Number			
	$(k\Delta x)_{opt}$	$\nu_{opt}$	$\kappa_{opt}$	$E_{phase}$	$(k\Delta x)_{opt}^*$	$\nu^*$	$\kappa_{opt}^*$	$E_{phase}$
1	0.121	1.09	$3.6 \cdot 10^3$	$8.71 \cdot 10^{-6}$	0.115	1.25	$3.65 \cdot 10^3$	$9.28 \cdot 10^{-6}$
2	0.684	0.216	102	$2.06 \cdot 10^{-5}$	0.3	0.641	406	$1.65 \cdot 10^{-5}$
3	1.6	0.097	17.5	$2.97 \cdot 10^{-5}$	0.47	0.41	165	$1.65 \cdot 10^{-5}$
4	2.74	0.0589	5.78	$3.55 \cdot 10^{-5}$	0.663	0.29	82.7	$1.65 \cdot 10^{-5}$
5	4.03	0.0409	2.61	$3.98 \cdot 10^{-5}$	0.88	0.219	47	$1.65 \cdot 10^{-5}$
6	5.42	0.031	1.42	$4.24 \cdot 10^{-5}$	1.13	0.17	28.4	$1.65 \cdot 10^{-5}$
7	6.88	0.0247	0.869	$4.45 \cdot 10^{-5}$	1.41	0.136	18.2	$1.65 \cdot 10^{-5}$
8	8.41	0.0204	0.577	$4.64 \cdot 10^{-5}$	1.72	0.112	12.2	$1.65 \cdot 10^{-5}$
9	9.98	0.0173	0.406	$4.74 \cdot 10^{-5}$	2.06	0.0934	8.56	$1.65 \cdot 10^{-5}$
10	11.6	0.0151	0.299	$4.81 \cdot 10^{-5}$	2.42	0.0794	6.19	$1.65 \cdot 10^{-5}$

Table C.11: Working conditions  $(k\Delta x, \nu)$  (both optimal and at maximum Courant number), as well as corresponding cost  $\kappa$  and dispersion error  $E_{phase}$ , for a dissipation error of  $E_{mag} = 0.001$  dB per wavelength, with the RKC73 scheme.

$p$	Optimal Working Conditions			Maximum Courant Number				
	$(k\Delta x)_{opt}$	$\nu_{opt}$	$\kappa_{opt}$	$E_{phase}$	$(k\Delta x)_{opt}^*$	$\nu^*$	$\kappa_{opt}^*$	$E_{phase}$
1	0.0555	1.13	$3.61 \cdot 10^4$	$4.11 \cdot 10^{-7}$	0.0535	1.25	$3.67 \cdot 10^4$	$4.32 \cdot 10^{-7}$
2	0.43	0.159	554	$1.2 \cdot 10^{-6}$	0.139	0.641	$4.05 \cdot 10^3$	$7.66 \cdot 10^{-7}$
3	1.14	0.0636	74	$1.9 \cdot 10^{-6}$	0.218	0.41	$1.65 \cdot 10^3$	$7.67 \cdot 10^{-7}$
4	2.1	0.0357	21.2	$2.42 \cdot 10^{-6}$	0.307	0.29	829	$7.67 \cdot 10^{-7}$
5	3.22	0.0239	8.8	$2.77 \cdot 10^{-6}$	0.408	0.219	471	$7.67 \cdot 10^{-7}$
6	4.46	0.0175	4.51	$3.02 \cdot 10^{-6}$	0.525	0.17	284	$7.67 \cdot 10^{-7}$
7	5.79	0.0137	2.64	$3.2 \cdot 10^{-6}$	0.656	0.136	182	$7.67 \cdot 10^{-7}$
8	7.19	0.0111	1.69	$3.35 \cdot 10^{-6}$	0.8	0.112	123	$7.67 \cdot 10^{-7}$
9	8.64	0.00935	1.16	$3.4 \cdot 10^{-6}$	0.956	0.0934	85.8	$7.67 \cdot 10^{-7}$
10	10.2	0.00799	0.836	$3.53 \cdot 10^{-6}$	1.12	0.0794	62	$7.67 \cdot 10^{-7}$

Table C.12: Working conditions  $(k\Delta x, \nu)$  (both optimal and at maximum Courant number), as well as corresponding cost  $\kappa$  and dispersion error  $E_{phase}$ , for a dissipation error of  $E_{mag} = 0.0001$  dB per wavelength, with the RKC73 scheme.

## C.3 RKC84 Scheme

Stage	$A_i$	$B_i$	$c_i$	$\gamma_k$
1	0	0.2165936736758085	0	1
2	-0.7212962482279240	0.1773950826411583	0.2165936736758085	1/2
3	-0.01077336571612980	0.01802538611623290	0.2660343487538170	1/6
4	-0.5162584698930970	0.08473476372541490	0.2840056122522720	1/24
5	-1.730100286632201	0.8129106974622483	0.3251266843788570	$7.63396514532222 \cdot 10^{-3}$
6	-5.200129304403076	1.903416030422760	0.4555149599187530	$9.55882815549560 \cdot 10^{-4}$
7	0.7837058945416420	0.1314841743399048	0.7713219317101170	$7.24046178276778 \cdot 10^{-5}$
8	-0.5445836094332190	0.2082583170674149	0.9199028964538660	$2.48648556949577 \cdot 10^{-6}$

Table C.13: 2N-storage coefficients and coefficients  $\gamma_k$  of the polynomial  $R(z)$  for the RKC84 scheme.

$p$	Optimal Working Conditions			Maximum Courant Number				
	$(k\Delta x)_{opt}$	$\nu_{opt}$	$\kappa_{opt}$	$E_{phase}$	$(k\Delta x)_{opt}^*$	$\nu^*$	$\kappa_{opt}^*$	$E_{phase}$
1	1.4	1.26	2.31	0.0181	1.4	1.26	2.31	0.0181
2	3.21	0.646	0.374	0.0141	3.21	0.646	0.374	0.0141
3	5.21	0.413	0.137	0.025	5.21	0.413	0.137	0.025
4	7.35	0.293	0.0689	0.0489	7.35	0.293	0.0689	0.0489
5	9.61	0.218	0.0414	0.088	9.61	0.218	0.0414	0.088
6	12	0.168	0.0278	0.134	12	0.168	0.0278	0.134
7	14.3	0.135	0.0202	0.181	14.3	0.135	0.0202	0.181
8	16.7	0.11	0.0155	0.228	16.7	0.11	0.0155	0.228
9	19.1	0.0925	0.0124	0.274	19.1	0.0925	0.0124	0.274
10	21.5	0.0787	0.0102	0.317	21.5	0.0787	0.0102	0.317

Table C.14: Working conditions  $(k\Delta x, \nu)$  (both optimal and at maximum Courant number), as well as corresponding cost  $\kappa$  and dispersion error  $E_{phase}$ , for a dissipation error of  $E_{mag} = 1$  dB per wavelength, with the RKC84 scheme.

$p$	Optimal Working Conditions			Maximum Courant Number				
	$(k\Delta x)_{opt}$	$\nu_{opt}$	$\kappa_{opt}$	$E_{phase}$	$(k\Delta x)_{opt}^*$	$\nu^*$	$\kappa_{opt}^*$	$E_{phase}$
1	0.645	1.26	23.7	0.00181	0.645	1.26	23.7	0.00181
2	1.92	0.646	1.75	0.00341	1.92	0.646	1.75	0.00341
3	3.4	0.411	0.494	0.0083	3.4	0.413	0.494	0.00855
4	5.08	0.282	0.217	0.00866	5.01	0.293	0.217	0.011
5	6.84	0.213	0.118	0.00889	6.78	0.218	0.118	0.0104
6	8.68	0.168	0.0726	0.00809	8.68	0.168	0.0726	0.00809
7	10.7	0.135	0.0491	0.00489	10.7	0.135	0.0491	0.00489
8	12.7	0.11	0.0354	0.00117	12.7	0.11	0.0354	0.00117
9	14.8	0.0925	0.0269	0.00278	14.8	0.0925	0.0269	0.00278
10	16.8	0.0787	0.0213	0.00677	16.8	0.0787	0.0213	0.00677

Table C.15: Working conditions  $(k\Delta x, \nu)$  (both optimal and at maximum Courant number), as well as corresponding cost  $\kappa$  and dispersion error  $E_{phase}$ , for a dissipation error of  $E_{mag} = 0.1$  dB per wavelength, with the RK84 scheme.

$p$	Optimal Working Conditions				Maximum Courant Number			
	$(k\Delta x)_{opt}$	$\nu_{opt}$	$\kappa_{opt}$	$E_{phase}$	$(k\Delta x)_{opt}^*$	$\nu^*$	$\kappa_{opt}^*$	$E_{phase}$
1	0.298	1.26	240	$9.39 \cdot 10^{-5}$	0.298	1.26	240	$9.39 \cdot 10^{-5}$
2	1.18	0.646	7.45	0.00107	1.18	0.646	7.45	0.00107
3	2.35	0.378	1.63	0.00216	2.27	0.413	1.66	0.00288
4	3.74	0.243	0.627	0.00235	3.43	0.293	0.677	0.00396
5	5.26	0.176	0.312	0.0025	4.72	0.218	0.349	0.00441
6	6.85	0.137	0.182	0.00261	6.15	0.168	0.204	0.00457
7	8.5	0.111	0.117	0.00269	7.71	0.135	0.129	0.00461
8	10.2	0.0938	0.0806	0.00278	9.39	0.11	0.0875	0.00456
9	11.9	0.0807	0.0586	0.00284	11.2	0.0925	0.0621	0.00444
10	13.7	0.0708	0.0443	0.00291	13	0.0787	0.0459	0.00425

Table C.16: Working conditions  $(k\Delta x, \nu)$  (both optimal and at maximum Courant number), as well as corresponding cost  $\kappa$  and dispersion error  $E_{phase}$ , for a dissipation error of  $E_{mag} = 0.01$  dB per wavelength, with the RKC84 scheme.

$p$	Optimal Working Conditions				Maximum Courant Number			
	$(k\Delta x)_{opt}$	$\nu_{opt}$	$\kappa_{opt}$	$E_{phase}$	$(k\Delta x)_{opt}^*$	$\nu^*$	$\kappa_{opt}^*$	$E_{phase}$
1	0.138	1.26	$2.41 \cdot 10^3$	$4.46 \cdot 10^{-6}$	0.138	1.26	$2.41 \cdot 10^3$	$4.46 \cdot 10^{-6}$
2	0.741	0.646	30.5	0.000203	0.741	0.646	30.5	0.000203
3	1.66	0.339	5.18	0.000401	1.51	0.413	5.62	0.000637
4	2.83	0.204	1.73	0.00044	2.26	0.293	2.36	0.000819
5	4.15	0.141	0.793	0.000467	3.08	0.218	1.26	0.000861
6	5.57	0.107	0.434	0.000489	3.99	0.168	0.746	0.000872
7	7.06	0.0853	0.267	0.000513	5	0.135	0.476	0.000876
8	8.61	0.0704	0.178	0.000527	6.09	0.11	0.32	0.000877
9	10.2	0.0599	0.126	0.000546	7.28	0.0925	0.224	0.000878
10	11.8	0.052	0.0932	0.000558	8.55	0.0787	0.162	0.000878

Table C.17: Working conditions  $(k\Delta x, \nu)$  (both optimal and at maximum Courant number), as well as corresponding cost  $\kappa$  and dispersion error  $E_{phase}$ , for a dissipation error of  $E_{mag} = 0.001$  dB per wavelength, with the RKC84 scheme.

$p$	Optimal Working Conditions				Maximum Courant Number			
	$(k\Delta x)_{opt}$	$\nu_{opt}$	$\kappa_{opt}$	$E_{phase}$	$(k\Delta x)_{opt}^*$	$\nu^*$	$\kappa_{opt}^*$	$E_{phase}$
1	0.0641	1.26	$2.42 \cdot 10^4$	$2.08 \cdot 10^{-7}$	0.0641	1.26	$2.42 \cdot 10^4$	$2.08 \cdot 10^{-7}$
2	0.466	0.646	122	$3.44 \cdot 10^{-5}$	0.466	0.646	122	$3.44 \cdot 10^{-5}$
3	1.18	0.3	16.1	$6.68 \cdot 10^{-5}$	0.989	0.413	20	0.000121
4	2.16	0.169	4.69	$7.47 \cdot 10^{-5}$	1.45	0.293	9.04	0.000139
5	3.31	0.112	1.97	$7.92 \cdot 10^{-5}$	1.95	0.218	4.96	0.000141
6	4.58	0.0821	1.01	$8.35 \cdot 10^{-5}$	2.52	0.168	2.96	0.000141
7	5.93	0.0641	0.598	$8.73 \cdot 10^{-5}$	3.15	0.135	1.9	0.000141
8	7.35	0.0522	0.385	$9.05 \cdot 10^{-5}$	3.84	0.11	1.28	0.000141
9	8.84	0.0437	0.265	$9.24 \cdot 10^{-5}$	4.59	0.0925	0.894	0.000141
10	10.3	0.0376	0.192	$9.56 \cdot 10^{-5}$	5.39	0.0787	0.648	0.000141

Table C.18: Working conditions  $(k\Delta x, \nu)$  (both optimal and at maximum Courant number), as well as corresponding cost  $\kappa$  and dispersion error  $E_{phase}$ , for a dissipation error of  $E_{mag} = 0.0001$  dB per wavelength, with the RKC84 scheme.

## **C.4 Element Size Constraint**

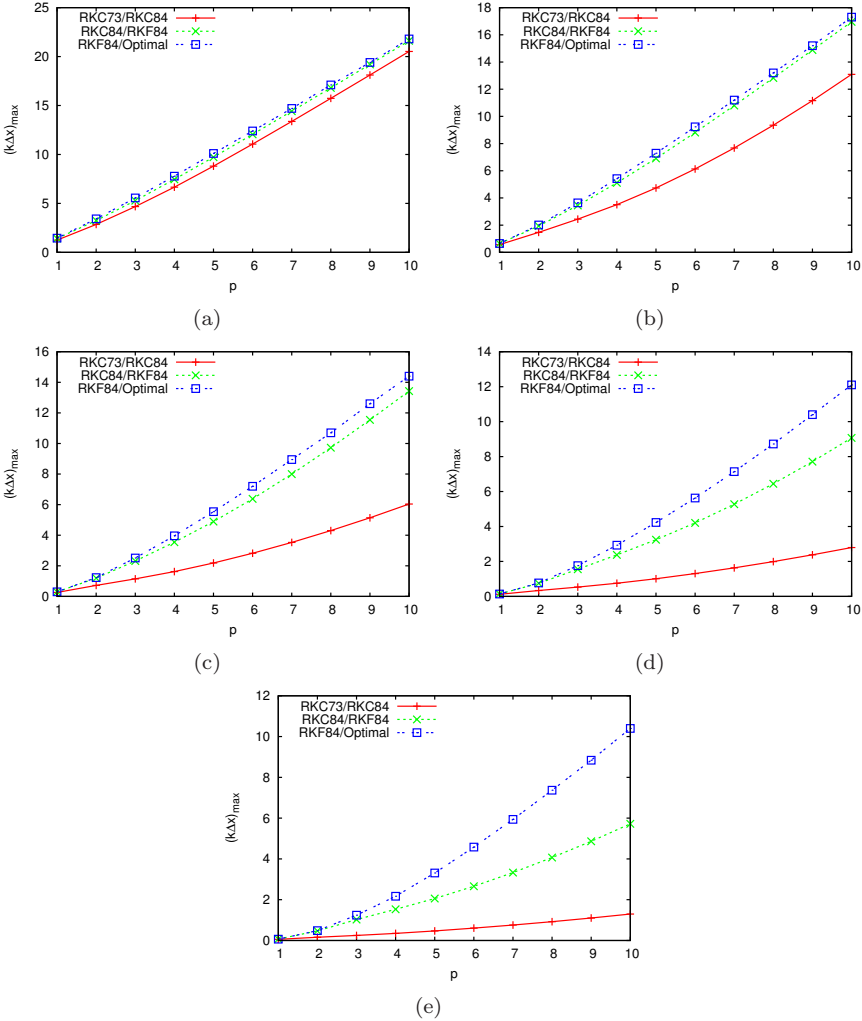


Figure C.1: Choice of the most efficient optimized RK scheme in function of the element size constraint  $(k\Delta x)_{max}$ , for order  $p$  from 1 to 10, with dissipation error requirements of  $E_{mag} = 1$  (a),  $E_{mag} = 0.1$  (b),  $E_{mag} = 0.01$  (c),  $E_{mag} = 0.001$  (d) and  $E_{mag} = 0.0001$  (e). In the area above the dash-spaced line (points  $\square$ ), the constraint is not restrictive, so that the RKF84 scheme used in optimal working conditions is the most efficient. Between the dashed line (points  $\times$ ) and dash-spaced line (points  $\square$ ), the RKF84 scheme is still the most efficient, because it allows for the largest Courant number per stage  $\nu/s$ , even though it is too accurate. Between the solid line (points  $+$ ) and the dashed line (points  $\times$ ), the RKC84 scheme is the one yielding the largest  $\nu/s$  while fulfilling the accuracy requirement. Below the solid line (points  $+$ ), the RKC73 scheme is the most efficient.



# Bibliography

- [1] <http://www.openfoam.org/>. Visited on 21 Nov. 2011. Cited on page(s) 160
- [2] R. Abedi, B. Petracovici, and R. B. Haber. A space-time discontinuous Galerkin method for linearized elastodynamics with element-wise momentum balance. *Comput. Methods Appl. Mech. Eng.*, 195(25-28): 3247–3273, 2006. doi: 10.1016/j.cma.2005.06.013. Cited on page(s) 12
- [3] M. Ainsworth. Dispersive and dissipative behaviour of high order discontinuous Galerkin finite element methods. *J. Comput. Phys.*, 198(1):106–130, 2004. doi: 10.1016/j.jcp.2004.01.004. Cited on page(s) 30
- [4] M. Ainsworth, P. Monk, and W. Muniz. Dispersive and dissipative properties of discontinuous Galerkin finite element methods for the second-order wave equation. *J. Sci. Comput.*, 27:5–40, 2006. doi: 10.1007/s10915-005-9044-x. Cited on page(s) 11, 129
- [5] V. Allampalli, R. Hixon, M. Nallasamy, and S. D. Sawyer. High-accuracy large-step explicit Runge-Kutta (HALE-RK) schemes for computational aeroacoustics. *J. Comput. Phys.*, 228(10):3837–3850, 2009. doi: 10.1016/j.jcp.2009.02.015. Cited on page(s) 40, 43, 82, 86, 187, 188
- [6] D. N. Arnold, F. Brezzi, B. Cockburn, and L. D. Marini. Unified analysis of discontinuous Galerkin methods for elliptic problems. *SIAM J. Numer. Anal.*, 39:1749–1779, May 2001. doi: 10.1137/S0036142901384162. Cited on page(s) 21, 113
- [7] R. J. Astley, R. Sugimoto, and P. Mustafi. Computational aero-acoustics for fan duct propagation and radiation. current status and application to turbofan liner optimisation. *J. Sound Vibrat.*, 330(16):3832–3845, 2011. doi: 10.1016/j.jsv.2011.03.022. Cited on page(s) 8, 9, 181
- [8] H. L. Atkins. Continued development of the discontinuous Galerkin method for computational aeroacoustic applications. In *Proceedings of*

- the 3rd AIAA/CEAS Aeroacoustics Conference, Atlanta (GA), USA, 12-14 May 1997*, 1997. Cited on page(s) 11, 12, 130
- [9] H. L. Atkins and C.-W. Shu. Quadrature-free implementation of discontinuous Galerkin method for hyperbolic equations. *AIAA J.*, 36(5):775–782, 1998. doi: 10.2514/2.436. Cited on page(s) 23
- [10] M. Baldauf. Stability analysis for linear discretisations of the advection equation with Runge-Kutta time integration. *J. Comput. Phys.*, 227(13):6638–6659, 2008. doi: 10.1016/j.jcp.2008.03.025. Cited on page(s) 28
- [11] F. Bassi and S. Rebay. A high-order accurate discontinuous finite element method for the numerical solution of the compressible Navier-Stokes equations. *J. Comput. Phys.*, 131(2):267–279, 1997. doi: 10.1006/jcph.1996.5572. Cited on page(s) 113
- [12] F. Bassi and S. Rebay. High-order accurate discontinuous finite element solution of the 2D Euler equations. *J. Comput. Phys.*, 138(2):251–285, 1997. doi: 10.1006/jcph.1997.5454. Cited on page(s) 130, 131
- [13] F. Bassi, A. Crivellini, S. Rebay, and M. Savini. Discontinuous Galerkin solution of the Reynolds-averaged Navier-Stokes and  $k\text{-}\omega$  turbulence model equations. *Comput. Fluids*, 34(4-5):507–540, 2005. doi: 10.1016/j.compfluid.2003.08.004. Cited on page(s) 113
- [14] M. Bauer, J. Dierke, and R. Ewert. Application of a discontinuous Galerkin method to predict airframe noise. In *Proceedings of the 15th AIAA/CEAS Aeroacoustics Conference, Miami (FL), USA, 11-13 May 2009*, 2009. Cited on page(s) 11, 12, 125, 126
- [15] J. Berland, C. Bogey, and C. Bailly. Low-dissipation and low-dispersion fourth-order Runge-Kutta algorithm. *Comput. Fluids*, 35(10):1459–1463, 2006. doi: 10.1016/j.compfluid.2005.04.003. Cited on page(s) 40, 43, 82, 187
- [16] M. Bernacki and S. Piperno. A dissipation-free time-domain discontinuous Galerkin method applied to three dimensional linearized Euler equations around a steady-state non-uniform inviscid flow. *J. Comput. Acoust.*, 14(4):445–467, 2006. doi: 10.1142/S0218396X0600313X. Cited on page(s) 11
- [17] M. Bernardini and S. Pirozzoli. A general strategy for the optimization of Runge-Kutta schemes for wave propagation phenomena. *J. Comput. Phys.*, 228(11):4182–4199, 2009. doi: 10.1016/j.jcp.2009.02.032. Cited on page(s) 81, 82, 83, 84, 85, 86, 186

- [18] P. J. Bismuti and D. A. Kopriva. Solution of acoustic scattering problems by a staggered-grid spectral domain decomposition method. In Tam and Hardin [130], pages 69–78. NASA Conference Paper Nr. 3352. Cited on page(s) 9
- [19] L. S. Blackford, J. Demmel, J. Dongarra, I. Duff, S. Hammarling, G. Henry, M. Heroux, L. Kaufman, A. Lumsdaine, A. Petitet, R. Pozo, K. Remington, and R. C. Whaley. An updated set of basic linear algebra subprograms (BLAS). *ACM Trans. Math. Softw.*, 28:135–151, June 2002. doi: <http://doi.acm.org/10.1145/567806.567807>. Cited on page(s) 121
- [20] C. P. A. Blom. *Discontinuous Galerkin Method on Tetrahedral Elements for Aeroacoustics*. PhD thesis, University of Twente, 2003. Cited on page(s) 11, 12, 30, 39, 107
- [21] J. P. Boyd. *Chebyshev and Fourier Spectral Methods*. Dover books on mathematics. Dover Publications, 2001. ISBN 9780486411835. Cited on page(s) 7
- [22] J. C. Butcher. *The numerical analysis of ordinary differential equations*. John Wiley & Sons, Ltd, Chichester, England, 2003. ISBN 0-471-96758-0. Cited on page(s) 27, 28, 89
- [23] M. Calvo, J. M. Franco, and L. Rández. Minimum storage Runge-Kutta schemes for computational acoustics. *Computers Math. Applic.*, 45(1-3): 535–545, 2003. ISSN 0898-1221. doi: 10.1016/S0898-1221(03)80035-4. Cited on page(s) 28, 82
- [24] M. Calvo, J. M. Franco, and L. Rández. A new minimum storage Runge-Kutta scheme for computational acoustics. *J. Comput. Phys.*, 201(1): 1–12, 2004. doi: 10.1016/j.jcp.2004.05.012. Cited on page(s) 40, 43, 82, 86, 187
- [25] M. H. Carpenter and C. A. Kennedy. Fourth-order 2N-storage Runge-Kutta schemes. Technical Memorandum NASA-TM-109112, NASA Langley Research Center, 1994. Cited on page(s) 40, 43, 82, 86, 187
- [26] N. Chevaugeon and J.-F. Remacle. Efficient discontinuous Galerkin methods for solving acoustic problems. In *Proceedings of the 11th AIAA/CEAS Aeroacoustics Conference, Monterey (CA), USA, 23-25 May 2005*, 2005. Cited on page(s) 7
- [27] N. Chevaugeon, K. Hillewaert, X. Gallez, P. Ploumhans, and J.-F. Remacle. Optimal numerical parameterization of discontinuous Galerkin method applied to wave propagation problems. *J. Comput. Phys.*, 223(1):188–207, 2007. doi: 10.1016/j.jcp.2006.09.005. Cited on page(s) 180

- [28] C. B. Christophe Bogey and D. Juvé. Computation of flow noise using source terms in linearized Euler's equations. *AIAA J.*, 40(2):235–243, 2002. doi: 10.2514/2.1665. Cited on page(s) 6
- [29] B.-T. Chu and L. S. G. Kovásznyai. Non-linear interactions in a viscous heat-conducting compressible gas. *J. Fluid Mech.*, 3(5):494–514, 1958. doi: 10.1017/S0022112058000148. Cited on page(s) 110
- [30] B. Cockburn and C.-W. Shu. TVB Runge-Kutta local projection discontinuous Galerkin finite element method for conservation laws II: General framework. *Math. Comput.*, 52(186):411–435, 1989. Cited on page(s) 12, 36
- [31] B. Cockburn and C.-W. Shu. The Runge-Kutta local projection  $p^1$ -discontinuous-Galerkin finite element method for scalar conservation laws. *RAIRO Modél. Math. Anal. Numér.*, 25(3):337–361, 1991. Cited on page(s) 12, 36
- [32] B. Cockburn and C.-W. Shu. Runge-Kutta discontinuous Galerkin methods for convection-dominated problems. *J. Sci. Comput.*, 16(3):173–261, 2001. doi: 10.1023/A:1012873910884. Cited on page(s) 12, 19, 21, 36, 39, 40, 41
- [33] B. Cockburn, S. Hou, and C.-W. Shu. The Runge-Kutta local projection discontinuous Galerkin finite element method for conservation laws. IV: The multidimensional case. *Math. Comput.*, 54(190):545–581, 1990. Cited on page(s) 28, 36
- [34] T. Colonius. Modeling artificial boundary conditions for compressible flow. *Annu. Rev. Fluid Mech.*, 36(1):315–345, 2004. doi: 10.1146/annurev.fluid.36.050802.121930. Cited on page(s) 115
- [35] T. Colonius and S. K. Lele. Computational aeroacoustics: progress on nonlinear problems of sound generation. *Prog. Aerosp. Sci.*, 40:345–416, 2004. doi: 10.1016/j.paerosci.2004.09.001. Cited on page(s) 4, 5, 6, 7, 10, 11
- [36] N. Curle. The influence of solid boundaries upon aerodynamic sound. *Proc. R. Soc. A*, 231:505–514, 1955. Cited on page(s) 4
- [37] W. De Roeck. *Hybrid Methodologies for the Computational Aeroacoustic Analysis of Confined, Subsonic Flows*. PhD thesis, K.U. Leuven, 2007. Cited on page(s) 6, 107, 155
- [38] P. Delorme, P. Mazet, C. Peyret, and Y. Ventribout. Computational aeroacoustics applications based on a discontinuous Galerkin method.

- C.R. Mec.*, 333(9):676–682, 2005. doi: 10.1016/j.crme.2005.07.007. Cited on page(s) 11, 12
- [39] F. D. Denia, J. Albelda, F. J. Fuenmayor, and A. J. Torregrosa. Acoustic behaviour of elliptical chamber mufflers. *J. Sound Vibrat.*, 241(3):401–421, 2001. doi: 10.1006/jsvi.2000.3289. Cited on page(s) 145
- [40] S. Dequand. *Duct Aeroacoustics: from Technological Applications to the Flute*. PhD thesis, Technische Universiteit Eindhoven, 2000. Cited on page(s) 3
- [41] N. S. Dickey, A. Selamet, and M. S. Ciray. An experimental study of the impedance of perforated plates with grazing flow. *J. Acoust. Soc. Am.*, 110(5):2360–2370, 2001. doi: 10.1121/1.1400736. Cited on page(s) 152, 156
- [42] M. Dumbser and C.-D. Munz. ADER discontinuous Galerkin schemes for aeroacoustics. *C.R. Mec.*, 333(9):683–687, 2005. doi: 10.1016/j.crme.2005.07.008. Cited on page(s) 11
- [43] J. D. Eldredge, D. J. Bodony, and M. Shoeybi. Numerical investigation of the acoustic behavior of a multi-perforated liner. In *Proceedings of the 13th AIAA/CEAS Aeroacoustics Conference, Rome, Italy, 21-23 May 2007*, 2007. Cited on page(s) 153
- [44] B. Engquist and S. Osher. One-sided difference approximations for nonlinear conservation laws. *Math. Comput.*, 36(154):321–351, 1981. Cited on page(s) 40
- [45] M. Escobar. *Finite Element Simulation of Flow-Induced Noise using Lighthill’s Acoustic Analogy*. PhD thesis, Universität Erlangen-Nürnberg, 2007. Cited on page(s) 10
- [46] R. Ewert and W. Schröder. Acoustic perturbation equations based on flow decomposition via source filtering. *J. Comput. Phys.*, 188(2):365–398, 2003. doi: 10.1016/S0021-9991(03)00168-2. Cited on page(s) 6
- [47] G. G. F. Lörcher and C. Munz. The space-time discontinuous Galerkin method for the solution of unsteady compressible Navier-Stokes equations. In *Proceedings of the 13th AIAA/CEAS Aeroacoustics Conference, Rome, Italy, 21-23 May 2007*, 2007. Cited on page(s) 12
- [48] J. E. Ffowcs Williams. Aeroacoustics. *J. Sound Vibrat.*, 190(3):387–398, 1996. doi: 10.1006/jsvi.1996.0070. Cited on page(s) 4

- [49] J. E. Ffowcs Williams and D. L. Hawkings. Sound generated by turbulence and surfaces in arbitrary motion. *Phil. Trans. R. Soc. A*, 264(1151):321–342, 1969. Cited on page(s) 4
- [50] T. Fogarty and R. J. LeVeque. High-resolution finite volume methods for acoustics in periodic or random media. *J. Acoust. Soc. Am.*, 106:17–28, 1999. Cited on page(s) 9
- [51] C. Geuzaine and J.-F. Remacle. Gmsh: A 3-D finite element mesh generator with built-in pre- and post-processing facilities. *International Journal for Numerical Methods in Engineering*, 79(11):1309–1331, 2009. doi: 10.1002/nme.2579. Cited on page(s) 121, 131
- [52] J. Golliard. *Noise of Helmholtz-resonator Like Cavities Excited by a Low Mach-number Turbulent Flow*. PhD thesis, Université de Poitiers, 2002. Cited on page(s) 152, 155, 156, 157, 158, 159, 163, 164, 165, 166, 167, 168, 169
- [53] S. Gottlieb, C.-W. Shu, and E. Tadmor. Strong stability-preserving high-order time discretization methods. *SIAM Rev.*, 43(1):89–112, 2001. doi: 10.1137/S003614450036757X. Cited on page(s) 41, 43, 86
- [54] S. M. Grace, K. P. Horan, and M. S. Howe. The influence of shape on the Rayleigh conductivity of a wall aperture in the presence of grazing flow. *J. Fluids Struct.*, 12(3):335–351, 1998. doi: 10.1006/jfls.1997.0145. Cited on page(s) 153
- [55] R. Hagmeijer, C. Blom, and H. Hoeijmakers. Wave-speed analysis of discontinuous Galerkin finite element method for aeroacoustics. In *Proceedings of the V European Conference on Computational Fluid Dynamics (ECCOMAS CFD 2010), Swansea (Wales), UK, 4-7 September 2010*, 2010. Cited on page(s) 11, 129
- [56] J. A. Hamilton and R. J. Astley. Acoustic propagation on irrotational mean flows using time-domain finite and infinite elements. *AIAA J.*, 43: 124–134, 2005. doi: 10.2514/1.45353. Cited on page(s) 7
- [57] J. Hesthaven. From electrostatics to almost optimal nodal sets for polynomial interpolation in a simplex. *SIAM J. Numer. Anal.*, 35:655–676, 1998. Cited on page(s) 25
- [58] J. Hesthaven and T. Warburton. Nodal high-order methods on unstructured grids: I. time-domain solution of Maxwell’s equations. *J. Comput. Phys.*, 181(1):186–221, 2002. doi: 10.1006/jcph.2002.7118. Cited on page(s) 25, 26, 120

- [59] J. S. Hesthaven and C. H. Teng. Stable spectral methods on tetrahedral elements. *SIAM J. Sci. Comput.*, 21:2352–2380, December 1999. doi: 10.1137/S1064827598343723. Cited on page(s) 25
- [60] J. S. Hesthaven and T. Warburton. *Nodal discontinuous Galerkin Methods: Algorithms, Analysis, and Applications*, volume 54 of *Texts in Applied Mathematics*. Springer Verlag, New York, USA, 2008. ISBN 978-0-387-72065-4. doi: 10.1007/978-0-387-72067-8. Cited on page(s) 25, 26, 31, 113, 115, 119, 120
- [61] F. Hindenlang. Personal communication, 2010. Cited on page(s) 68
- [62] C. Hirsch, C. Lacor, and H. Deconinck. Convection algorithms based on a diagonalization procedure for the multidimensional Euler equations. In *Proceedings of the 8th Computational Fluid Dynamics Conference, Honolulu (HI), USA, 9-11 June 1987*, pages 667–676, 1987. Cited on page(s) 111
- [63] K. Hong and J. Kim. Natural mode analysis of hollow and annular elliptical cylindrical cavities. *J. Sound Vibrat.*, 183(2):327–351, 1995. doi: 10.1006/jsvi.1995.0257. Cited on page(s) 145
- [64] M. S. Howe. Edge, cavity and aperture tones at very low Mach numbers. *J. Fluid Mech.*, 330:61–84, 1997. doi: 10.1017/S0022112096003606. Cited on page(s) 152, 159
- [65] M. S. Howe. Influence of wall thickness on Rayleigh conductivity and flow-induced aperture tones. *J. Fluids Struct.*, 11(4):351–366, 1997. doi: 10.1006/jfls.1997.0087. Cited on page(s) 152
- [66] M. S. Howe. Low Strouhal number instabilities of flow over apertures and wall cavities. *J. Acoust. Soc. Am.*, 102(2, Part 1):772–780, 1997. doi: 10.1121/1.419903. Cited on page(s) 152
- [67] M. S. Howe, M. I. Scott, and S. R. Sipcic. The influence of tangential mean flow on the Rayleigh conductivity of an aperture. *Proc. R. Soc. A*, 452:2303–2317, 1996. Cited on page(s) 152, 157, 159, 164, 166, 167, 168
- [68] M. Y. Hsi and F. Périé. Computational aeroacoustics for prediction of acoustic scattering. In Tam and Hardin [130], pages 111–117. NASA Conference Paper Nr. 3352. Cited on page(s) 9
- [69] F. Q. Hu and H. L. Atkins. Eigensolution analysis of the discontinuous Galerkin method with nonuniform grids: I. one space dimension. *J. Comput. Phys.*, 182(2):516–545, 2002. doi: 10.1006/jcph.2002.7184. Cited on page(s) 30

- [70] F. Q. Hu and H. L. Atkins. Two-dimensional wave analysis of the discontinuous Galerkin method with non-uniform grids and boundary conditions. In *Proceedings of the 8th AIAA/CEAS Aeroacoustics Conference, Breckenridge (CO), USA, 17-19 June 2002*, 2002. Cited on page(s) 11, 129
- [71] F. Q. Hu, M. Y. Hussaini, and J. L. Manthey. Low-dissipation and low-dispersion Runge-Kutta schemes for computational acoustics. *J. Comput. Phys.*, 124(1):177–191, 1996. doi: 10.1006/jcph.1996.0052. Cited on page(s) 40, 43, 82, 86, 187, 188
- [72] F. Q. Hu, M. Hussaini, and P. Rasetarinera. An analysis of the discontinuous Galerkin method for wave propagation problems. *J. Comput. Phys.*, 151(2):921–946, 1999. doi: 10.1006/jcph.1999.6227. Cited on page(s) 11, 129
- [73] X. Huang and X. Zhang. A fourier pseudospectral method for some computational aeroacoustics problems. *Int. J. Aeroacoust.*, 5(3):279–294, 2006. Cited on page(s) 9
- [74] A. Jameson. Solution of the Euler equations for two dimensional transonic flow by a multigrid method. *Appl. Math. Comput.*, 13(3-4):327–355, 1983. doi: 10.1016/0096-3003(83)90019-X. Cited on page(s) 41, 43, 86
- [75] X. Jing, X. Sun, J. Wu, and K. Meng. Effect of grazing flow on the acoustic impedance of an orifice. *AIAA J.*, 39(8):1478–1484, 2001. doi: 10.2514/2.1498. Cited on page(s) 153
- [76] S. K. and Lele. Compact finite difference schemes with spectral-like resolution. *J. Comput. Phys.*, 103(1):16–42, 1992. doi: 10.1016/0021-9991(92)90324-R. Cited on page(s) 10
- [77] L. F. Kallivokas and J. Bielak. Time-domain analysis of transient structural acoustics problems based on the finite element method and a novel absorbing boundary element. *J. Acoust. Soc. Am.*, 94:3480–3492, 1993. doi: 10.1121/1.407202. Cited on page(s) 10
- [78] A. Kanevsky, M. H. Carpenter, D. Gottlieb, and J. S. Hesthaven. Application of implicit-explicit high order Runge-Kutta methods to discontinuous-Galerkin schemes. *J. Comput. Phys.*, 225(2):1753–1781, 2007. doi: 10.1016/j.jcp.2007.02.021. Cited on page(s) 12
- [79] L. Kapa. *Numerical prediction of noise production and propagation*. PhD thesis, Université Libre de Bruxelles, 2011. Cited on page(s) 10

- [80] R. Kirby and A. Cummings. The impedance of perforated plates subjected to grazing gas flow and backed by porous media. *J. Sound Vibrat.*, 217(4):619–636, 1998. doi: 10.1006/jsvi.1998.1811. Cited on page(s) 152
- [81] A. Kirkegaard. *Frequency Domain Linearized Navier-Stokes Equations Methods for Low Mach Number Internal Aeroacoustics*. PhD thesis, K ungliga Tekniska H ogskolan (KTH), Stockholm, 2011. Cited on page(s) 153, 159
- [82] G. Kooijman, A. Hirschberg, and J. Golliard. Acoustical response of orifices under grazing flow: Effect of boundary layer profile and edge geometry. *J. Sound Vibrat.*, 315(4-5):849–874, 2008. doi: 10.1016/j.jsv.2008.02.030. Cited on page(s) 152, 155, 156, 159, 169
- [83] D. A. Kopriva. Spectral solution of acoustic wave-propagation problems. In *Proceedings of the 13th AIAA Aeroacoustics Conference, Tallahassee (FL), USA, 22-24 Oct. 1990*, 1990. Cited on page(s) 9
- [84] D. A. Kopriva. A conservative staggered-grid Chebyshev multidomain method for compressible flows. ii. a semi-structured method. *J. Comput. Phys.*, 128(2):475–488, 1996. doi: 10.1006/jcph.1996.0225. Cited on page(s) 9
- [85] D. A. Kopriva and J. H. Kalias. Solution of acoustic workshop problems by a spectral multidomain method. In J. C. Hardin, J. R. Ristorcelli, and C. K. W. Tam, editors, *ICASE/LaRC Workshop on Benchmark Problems in Computational Aeroacoustics*, pages 117–124, 1995. NASA Conference Publication 3300. Cited on page(s) 9
- [86] D. A. Kopriva and J. H. Kalias. A conservative staggered-grid Chebyshev multidomain method for compressible flows. *J. Comput. Phys.*, 125(1):244–261, 1996. doi: 10.1006/jcph.1996.0091. Cited on page(s) 9
- [87] H. O. Kreiss and L. Wu. On the stability definition of difference approximations for the initial boundary value problem. *Appl. Numer. Math.*, 12(1-3):213–227, 1993. doi: 10.1016/0168-9274(93)90119-C. Cited on page(s) 31
- [88] L. Krivodonova and M. Berger. High-order accurate implementation of solid wall boundary conditions in curved geometries. *J. Comput. Phys.*, 211(2):492–512, 2006. doi: 10.1016/j.jcp.2005.05.029. Cited on page(s) 130, 131

- [89] E. J. Kubatko, J. J. Westerink, and C. Dawson. Semi discrete discontinuous Galerkin methods and stage-exceeding-order, strong-stability-preserving Runge-Kutta time discretizations. *J. Comput. Phys.*, 222(2):832–848, 2007. doi: 10.1016/j.jcp.2006.08.005. Cited on page(s) 28, 36, 37
- [90] E. J. Kubatko, C. Dawson, and J. J. Westerink. Time step restrictions for Runge-Kutta discontinuous Galerkin methods on triangular grids. *J. Comput. Phys.*, 227(23):9697–9710, 2008. doi: 10.1016/j.jcp.2008.07.026. Cited on page(s) 28, 36, 37
- [91] K. A. Kurbatskii and R. R. Mankbadi. Review of computational aeroacoustics algorithms. *Int. J. Comput. Fluid Dyn.*, 18(6):533–546, 2004. doi: 10.1080/10618560410001673542. Cited on page(s) 7, 10, 11
- [92] S.-H. Lee and J.-G. Ih. Empirical model of the acoustic impedance of a circular orifice in grazing mean flow. *J. Acoust. Soc. Am.*, 114(1):98–113, 2003. doi: 10.1121/1.1581280. Cited on page(s) 152
- [93] M. J. Lighthill. On sound generated aerodynamically. I. general theory. *Proc. R. Soc. A*, 211(1107):564–587, 1952. doi: 10.1098/rspa.1952.0060. Cited on page(s) 3, 4
- [94] M. J. Lighthill. On sound generated aerodynamically. II. turbulence as a source of sound. *Proc. R. Soc. A*, 222(1148):1–32, 1954. Cited on page(s) 3, 4
- [95] M. J. Lighthill. Flow noise science - a citation-classic commentary on sound generated aerodynamically. *C.C./Eng. Tech. Appl. Sci.*, 22(38):11, 1991. Cited on page(s) 3
- [96] M. J. Lighthill. Final panel discussion. In J. C. Hardin and M. Y. Hussaini, editors, *Computational Aeroacoustics*. Springer-Verlag, 1993. ISBN 9780387940748. Cited on page(s) 4
- [97] L. Liu, X. Li, and F. Q. Hu. Nonuniform time-step Runge-Kutta discontinuous Galerkin method for computational aeroacoustics. *J. Comput. Phys.*, 229(19):6874–6897, 2010. doi: 10.1016/j.jcp.2010.05.028. Cited on page(s) 11
- [98] D. P. Lockard, K. S. Brentner, and H. L. Atkins. High-accuracy algorithms for computational aeroacoustics. *AIAA J.*, 33:246–251, 1995. doi: 10.2514/3.12436. Cited on page(s) 10
- [99] R. H. Loh and W. H. Lin. Numerical solutions to the third CAA workshop benchmark problems. In J. C. Hardin, D. Huff, and C. K. W. Tam, editors,

- Third Computational Aeroacoustics Workshop on Benchmark Problems*, pages 295–308, 2000. NASA Conference Paper Nr. 2000-209790. Cited on page(s) 9
- [100] M. Lukáčová-Medvid'ová, G. Warnecke, and Y. Zahaykah. Finite volume evolution Galerkin (FVEG) methods for three-dimensional wave equation system. *Appl. Numer. Math.*, 57(9):1050–1064, 2007. doi: 10.1016/j.apnum.2006.09.011. Cited on page(s) 9
- [101] C. Malmary, S. Carbonne, Y. Aurégan, and V. Pagneux. Acoustic impedance measurement with grazing flow. In *Proceedings of the 7th AIAA/CEAS Aeroacoustics Conference, Maastricht, The Netherlands, 28-30 May 2001*, 2001. Cited on page(s) 152
- [102] P. Martinez-Lera, Q. Schram, S. Foeller, R. Kaess, and W. Polifke. Identification of the aeroacoustic response of a low Mach number flow through a t-joint. *J. Acoust. Soc. Am.*, 126(2):582–586, 2009. doi: 10.1121/1.3159604. Cited on page(s) 153
- [103] J. L. Mead and R. A. Renaut. High order methods for problems in computational aeroacoustics, mathematical and numerical aspects of wave propagation. In A. DeSanto, editor, *Proceedings of the Fourth International Conference on Mathematical and Numerical Aspects of Wave Propagation*, pages 597–599, 1998. Cited on page(s) 9
- [104] J. L. Mead and R. A. Renaut. Optimal Runge-Kutta methods for first order pseudospectral operators. *J. Comput. Phys.*, 152(1):404–419, 1999. doi: 10.1006/jcph.1999.6260. Cited on page(s) 40, 41, 43, 82, 86, 187
- [105] F. Mechel. *Formulas of Acoustics*. Springer Reference. Springer, 2008. ISBN 9783540768326. Cited on page(s) 166, 167
- [106] S. Mendez and J. D. Eldredge. Acoustic modeling of perforated plates with bias flow for large-eddy simulations. *J. Comput. Phys.*, 228:4757–4772, July 2009. doi: 10.1016/j.jcp.2009.03.026. Cited on page(s) 153
- [107] M. Munjal. *Acoustics of ducts and mufflers with application to exhaust and ventilation system design*. Wiley-Interscience publication. Wiley, 1987. ISBN 9780471847380. Cited on page(s) 153
- [108] G. Nakiboğlu, S. P. C. Belfroid, J. Golliard, and A. Hirschberg. On the whistling of corrugated pipes: effect of pipe length and flow profile. *J. Fluid Mech.*, 672:78–108, 2011. doi: 10.1017/S0022112010005884. Cited on page(s) 153

- [109] D. V. Nance and L. N. Sankar. Low dispersion finite volume schemes in the resolution of vortex shedding noise. In *Proceedings of the 36th Aerospace Sciences Meeting and Exhibit, Reno (NV), USA, 15-19 Jan. 1998*, 1998. Cited on page(s) 9
- [110] S. Osher and F. Solomon. Upwind difference schemes for hyperbolic systems of conservation laws. *Math. Comput.*, 38(158):339–374, 1982. Cited on page(s) 40
- [111] J. Palaniappan, R. B. Haber, and R. L. Jerrard. A spacetime discontinuous Galerkin method for scalar conservation laws. *Comput. Methods Appl. Mech. Eng.*, 193(33-35):3607–3631, 2004. doi: 10.1016/j.cma.2004.01.028. Cited on page(s) 12
- [112] K. S. Peat, J.-G. Ih, and S.-H. Lee. The acoustic impedance of a circular orifice in grazing mean flow: Comparison with theory. *J. Acoust. Soc. Am.*, 114(6):3076–3086, 2003. doi: 10.1121/1.1621865. Cited on page(s) 152
- [113] K. S. Peat, R. Sugimoto, and J. L. Horner. The effects of thickness on the impedance of a rectangular aperture in the presence of a grazing flow. *J. Sound Vibrat.*, 292(3-5):610–625, 2006. doi: 10.1016/j.jsv.2005.08.012. Cited on page(s) 153, 159
- [114] S. Pirozzoli. Performance analysis and optimization of finite-difference schemes for wave propagation problems. *J. Comput. Phys.*, 222(2):809–831, 2007. doi: 10.1016/j.jcp.2006.08.006. Cited on page(s) 81, 82, 83
- [115] C. Prax, F. Golanski, and L. Nadal. Control of the vorticity mode in the linearized Euler equations for hybrid aeroacoustic prediction. *J. Comput. Phys.*, 227(12):6044–6057, 2008. doi: 10.1016/j.jcp.2008.02.022. Cited on page(s) 6
- [116] J. Qiu, M. Dumbser, and C.-W. Shu. The discontinuous Galerkin method with Lax-Wendroff type time discretizations. *Comput. Methods Appl. Mech. Eng.*, 194(42-44):4528–4543, 2005. doi: 10.1016/j.cma.2004.11.007. Cited on page(s) 11
- [117] J. Ramboer, T. Broeckhoven, S. Smirnov, and C. Lacor. Optimization of time integration schemes coupled to spatial discretization for use in CAA applications. *J. Comput. Phys.*, 213(2):777–802, 2006. doi: 10.1016/j.jcp.2005.08.033. Cited on page(s) 31
- [118] P. P. Rao. *High Order Unstructured Grid Methods for Computational Aeroacoustics*. PhD thesis, Pennsylvania State University, 2004. Cited on page(s) 11, 12

- [119] P. Rasetarinera, D. A. Kopriva, and M. Y. Hussaini. Discontinuous spectral element solution to aeroacoustic problems. In J. C. Hardin, D. Huff, and C. K. W. Tam, editors, *Third Computational Aeroacoustics Workshop on Benchmark Problems*, pages 103–115, 2000. NASA Conference Paper Nr. 2000-209790. Cited on page(s) 11, 12
- [120] J. Rayleigh. *The Theory of Sound*. MacMillan, 1896. Cited on page(s) 152, 153
- [121] S. C. Reddy and L. N. Trefethen. Stability of the method of lines. *Numer. Math.*, 62(2):235–267, 1992. doi: 10.1007/BF01396228. Cited on page(s) 31
- [122] Y. Reymen. *3D High-Order Discontinuous Galerkin Methods for Time-Domain Simulation of Flow Noise Propagation*. PhD thesis, Katholieke Universiteit Leuven, 2008. Cited on page(s) 12, 112, 120
- [123] Y. Reymen, M. Baelmans, and W. Desmet. Efficient implementation of tam and auriault’s time-domain impedance boundary condition. *AIAA J.*, 46(9):2368–2376, 2008. doi: 10.2514/1.35876. Cited on page(s) 131, 181
- [124] S. J. Ruuth. Global optimization of explicit strong-stability-preserving Runge-Kutta methods. *Math. Comput.*, 75(253):183–207, 2006. Cited on page(s) 41, 43, 86, 187
- [125] J. H. Seo and Y. J. Moon. Linearized perturbed compressible equations for low Mach number aeroacoustics. *J. Comput. Phys.*, 218(2):702–719, 2006. doi: 10.1016/j.jcp.2006.03.003. Cited on page(s) 6
- [126] D. Stanescu. *A multidomain spectral method for computational aeroacoustics*. PhD thesis, Concordia University, 1999. Cited on page(s) 9
- [127] D. Stanescu and W. G. Habashi. 2N-storage low dissipation and dispersion Runge-Kutta schemes for computational acoustics. *J. Comput. Phys.*, 143(2):674–681, 1998. doi: 10.1006/jcph.1998.5986. Cited on page(s) 40, 43, 82, 86
- [128] T. Suzuki and S. K. Lele. Green’s functions for a source in a boundary layer: direct waves, channelled waves and diffracted waves. *J. Fluid Mech.*, 477:129–173, 2003. doi: 10.1017/S0022112002003099. Cited on page(s) 125
- [129] K. Takeda and C. Shieh. Cavity tones by computational aeroacoustics. *Int. J. Comput. Fluid Dyn.*, 18(6):439–454, 2004. doi: 10.1080/10618560410001673461. Cited on page(s) 153

- [130] C. Tam and J. Hardin, editors. *Second Computational Aeroacoustics Workshop on Benchmark Problems*, 1997. NASA Conference Paper Nr. 3352. Cited on page(s) 133, 229, 233
- [131] C. K. Tam and J. C. Webb. Dispersion-relation-preserving finite difference schemes for computational acoustics. *J. Comput. Phys.*, 107(2):262–281, 1993. doi: 10.1006/jcph.1993.1142. Cited on page(s) 10, 121, 123
- [132] C. K. W. Tam. Computational aeroacoustics: An overview of computational challenges and applications. *International Journal of Computational Fluid Dynamics*, 18(6), 2004. doi: 10.1080/10618560410001673551. Cited on page(s) 11
- [133] C. K. W. Tam. Recent advances in computational aeroacoustics. *Fluid Dyn. Res.*, 38(9):591–615, 2006. doi: 10.1016/j.fluiddyn.2006.03.006. Cited on page(s) 4, 7, 10
- [134] C. K. W. Tam, K. A. Kurbatskii, K. K. Ahuja, and R. J. G. Jr. A numerical and experimental investigation of the dissipation mechanisms of resonant acoustic liners. *J. Sound Vibrat.*, 245(3):545–557, 2001. doi: 10.1006/jsvi.2001.3571. Cited on page(s) 153
- [135] C. K. W. Tam, H. Ju, and B. E. Walker. Numerical simulation of a slit resonator in a grazing flow under acoustic excitation. *J. Sound Vibrat.*, 313(3-5):449–471, 2008. doi: 10.1016/j.jsv.2007.12.018. Cited on page(s) 153
- [136] D. Tonon. *Aeroacoustics of shear layers in internal flows: closed branches and wall perforations*. PhD thesis, Technische Universiteit Eindhoven, 2011. Cited on page(s) 152
- [137] I. Touloupoulos and J. A. Ekaterinaris. Characteristic boundary conditions for the numerical solution of Euler equations by the discontinuous Galerkin methods. In J. C. F. Pereira and A. Sequeira, editors, *Proceedings of the V European Conference on Computational Fluid Dynamics (ECCOMAS CFD 2010), Lisbon, Portugal, 14-17 June 2010*, 2010. Cited on page(s) 111
- [138] T. Toulorge, Y. Reymen, and W. Desmet. A 2D discontinuous Galerkin method for aeroacoustics with curved boundary treatment. In *Proceedings of the International Conference on Noise and Vibration Engineering (ISMA 2008), Leuven, Belgium, 15-17 September 2008*, 2008. Cited on page(s) 133, 136

- [139] K. Tselios and T. Simos. Optimized Runge-Kutta methods with minimal dispersion and dissipation for problems arising from computational acoustics. *Phys. Lett. A*, 363(1-2):38–47, 2007. doi: 10.1016/j.physleta.2006.10.072. Cited on page(s) 40, 43, 82, 86, 187
- [140] J. J. W. van der Vegt and H. van der Ven. Space-time discontinuous Galerkin finite element method with dynamic grid motion for inviscid compressible flows: I. general formulation. *J. Comput. Phys.*, 182(2): 546–585, 2002. doi: 10.1006/jcph.2002.7185. Cited on page(s) 12
- [141] G. Wang, L. N. Sankar, and H. Tadghighi. Prediction of rotorcraft noise with a low-dispersion finite volume scheme. In *Proceedings of the 37th Aerospace Sciences Meeting and Exhibit, Reno (NV), USA, 11-14 Jan. 1999*, 1999. Cited on page(s) 9
- [142] M. Wang, J. B. Freund, and S. K. Lele. Computational prediction of flow-generated sound. *Annu. Rev. Fluid Mech.*, 38(1):483–512, 2006. doi: 10.1146/annurev.fluid.38.050304.092036. Cited on page(s) 3, 4, 6, 7, 11
- [143] T. Warburton and T. Hagstrom. Taming the CFL number for discontinuous Galerkin methods on structured meshes. *SIAM J. Numer. Anal.*, 46:3151–3180, 2008. doi: 10.1137/060672601. Cited on page(s) 180
- [144] V. L. Wells and R. A. Renaut. Computing aerodynamically generated noise. *Annu. Rev. Fluid Mech.*, 29(1):161–199, 1997. doi: 10.1146/annurev.fluid.29.1.161. Cited on page(s) 3, 4, 9
- [145] R. C. Whaley and A. Petitet. Minimizing development and maintenance costs in supporting persistently optimized BLAS. *Software Pract. Exper.*, 35(2):101–121, February 2005. Cited on page(s) 121
- [146] J. H. Williamson. Low-storage Runge-Kutta schemes. *J. Comput. Phys.*, 35(1):48–56, 1980. doi: 10.1016/0021-9991(80)90033-9. Cited on page(s) 28, 82, 97
- [147] D. Wirasaet, S. Tanaka, E. J. Kubatko, J. J. Westerink, and C. Dawson. A performance comparison of nodal discontinuous Galerkin methods on triangles and quadrilaterals. *Int. J. Numer. Meth. Fluids*, 64(10-12):1336–1362, 2010. doi: 10.1002/fld.2376. Cited on page(s) 180
- [148] B. Yue and M. N. Guddati. Dispersion-reducing finite elements for transient acoustics. *J. Acoust. Soc. Am.*, 118(4):2132–2141, 2005. doi: 10.1121/1.2011149. Cited on page(s) 10
- [149] T. Zhang and Z. Li. Optimal error estimate and superconvergence of the DG method for first-order hyperbolic problems. *J. Comput. Phys.*, 235(1):144–153, 2010. doi: 10.1016/j.cam.2010.05.023. Cited on page(s) 28



# Curriculum Vitae

## PERSONAL DATA

Thomas Toulorge  
33 Years Old  
French Nationality  
E-mail: thomas.toulorge@gmail.com

## EDUCATION

**2007–2012 KU Leuven, Belgium.**

Ph.D. in Mechanical Engineering.

**Autumn 2003** Graduated from the École Centrale de Lille and from KTH.

T.I.M.E. double-degree programme.

**2001–2003 KTH, Stockholm, Sweden.**

Royal Institute of Technology (Kungliga Tekniska Högskolan).

Specialization in Aeronautics and Astronautics.

**1999–2001 École Centrale de Lille, France.**

Graduate engineering school.

**1997–1999 Mathématiques Supérieures / Mathématiques spéciales.**

Lycée Victor Hugo, Caen, France.

Post-secondary-school advanced mathematics, physics and chemistry classes in preparation for the competitive entrance to French engineering schools.

**July 1997** Scientific Baccalauréat.

## PROFESSIONAL EXPERIENCE

### **2007–2011 KU Leuven** (Leuven, Belgium)

Research assistant. Research on high-order discontinuous Galerkin methods: investigation of stability and accuracy properties, derivation of optimized Runge-Kutta time integration schemes, study of high-order boundary conditions, application to aeroacoustics. Participation in the European Marie-Curie project “AETHER”. Teaching activities: student tutoring.

### **2004–2007 INTA** (Madrid, Spain)

Research engineer in the field of CFD. Development of finite volume codes for compressible flows, design and implementation of prediction tools for laminar-turbulent transition, application to aeronautics. Development of a Lattice-Boltzmann code for incompressible flows. Involvement in national (PROFIT) as well as European (FP6, GARTEUR) research projects. Responsible for a project financed by the aeronautical industry.

### **April–Nov. 2003 INTA** (Madrid, Spain)

8-month Master’s thesis work. Implementation of the dynamic mesh capability into a CFD code: moving mesh algorithm, ALE formulation of the Euler equations, implicit time integration scheme (dual time stepping).

### **April–July 2001 GANIL** (Caen, France)

11-week training period. Development of a software contributing to the tuning of a cyclotron.

### **Jan. & July 2000 Philips Semiconductors** (Caen, France)

Two-month training period. Work on the computer system supervising the conditions of production.

# List of Publications

## International peer reviewed journal articles

1. T. Toulorge, W. Desmet, Optimal Runge-Kutta Schemes for Discontinuous Galerkin Space Discretizations Applied to Wave Propagation Problems, *Journal of Computational Physics*, Vol. 231, Issue 4, pp. 2067–2091, 2012.
2. T. Toulorge, W. Desmet, CFL Conditions for Runge-Kutta Discontinuous Galerkin Methods on Triangular Grids, *Journal of Computational Physics*, Vol. 230, Issue 12, pp. 4657–4678, 2011.
3. T. Toulorge, W. Desmet, Curved Boundary Treatments for the Discontinuous Galerkin Method Applied to Aeroacoustic Propagation, *AIAA Journal*, Vol. 48, Nr. 2, pp. 479–489, 2010.

## Full papers in proceedings of international conferences

1. T. Toulorge, W. Desmet, Spectral Properties of Discontinuous Galerkin Space Operators on Curved Meshes, In *Spectral and High Order Methods for Partial Differential Equations, Lecture Notes in Computational Science and Engineering: Vol. 76, International Conference on Spectral and High Order Methods, Trondheim, Norway, 22–26 June 2009*, pp. 495–502, Springer, 2010.
2. T. Toulorge, W. Desmet, Time Stepping and Linear Stability of Runge-Kutta Discontinuous Galerkin Methods on Triangular Grids, In *Proceedings of the V European Conference on Computational Fluid Dynamics (ECCOMAS CFD 2010), Lisbon, Portugal, 14–17 June 2010*, 2010.
3. T. Toulorge, W. Desmet, Time Stepping with Runge-Kutta Discontinuous Galerkin Methods on Triangular Grids, In *Proceedings of the 16th*

*AIAA/CEAS Aeroacoustics Conference, Stockholm, Sweden, 7–9 June 2010*, AIAA Paper Nr. 2010-3986, 2010.

4. W. De Roeck, T. Toulorge, W. Desmet, A Linear Network Representation for the Determination of the Acoustic Properties of Lined Ducts Carrying a Non-Uniform Mean Flow, In *Proceedings of the International Congress on Sound and Vibration (ICSV16), Krakow, Poland, 5–9 July 2009*, 2009.
5. T. Toulorge, W. Desmet, Curved Boundary Treatments for the Discontinuous Galerkin Method Applied to Aeroacoustic Propagation, In *Proceedings of the 15th AIAA/CEAS Aeroacoustics Conference, Miami, USA, 11–13 May 2009*, AIAA Paper Nr. 2009-3176, 2009.
6. T. Toulorge, Y. Reymen, W. Desmet, A 2D Discontinuous Galerkin Method for Aeroacoustics with Curved Boundary Treatment, In *Proceedings of the International Conference on Noise and Vibration Engineering, Leuven, Belgium, 15–17 Sept. 2008*, 2008.



Arenberg Doctoral School of Science, Engineering & Technology  
Faculty of Engineering  
Department of Mechanical Engineering  
Division Production engineering, Machine design and Automation (PMA)  
Celestijnenlaan 300B - Box 2420  
B-3001 Heverlee

KATHOLIEKE UNIVERSITEIT  
**LEUVEN**

ASSOCIATIE  
K.U. LEUVEN